

Investigating the Interaction between π -Conjugated Organic Molecules and Metal Surfaces with Photoemission Tomography

Xiaosheng Yang

Information

Band / Volume 71

ISBN 978-3-95806-584-0

Forschungszentrum Jülich GmbH
Peter Grünberg Institut (PGI)
Quantum Nanoscience (PGI-3)

Investigating the Interaction between π -Conjugated Organic Molecules and Metal Surfaces with Photoemission Tomography

Xiaosheng Yang

Schriften des Forschungszentrums Jülich
Reihe Information / Information

Band / Volume 71

ISSN 1866-1777

ISBN 978-3-95806-584-0

Bibliografische Information der Deutschen Nationalbibliothek.
Die Deutsche Nationalbibliothek verzeichnet diese Publikation in der
Deutschen Nationalbibliografie; detaillierte Bibliografische Daten
sind im Internet über <http://dnb.d-nb.de> abrufbar.

Herausgeber und Vertrieb: Forschungszentrum Jülich GmbH
Zentralbibliothek, Verlag
52425 Jülich
Tel.: +49 2461 61-5368
Fax: +49 2461 61-6103
zb-publikation@fz-juelich.de
www.fz-juelich.de/zb

Umschlaggestaltung: Grafische Medien, Forschungszentrum Jülich GmbH

Druck: Grafische Medien, Forschungszentrum Jülich GmbH

Copyright: Forschungszentrum Jülich 2021

Schriften des Forschungszentrums Jülich
Reihe Information / Information, Band / Volume 71

D 82 (Diss. RWTH Aachen University, 2021)

ISSN 1866-1777
ISBN 978-3-95806-584-0

Vollständig frei verfügbar über das Publikationsportal des Forschungszentrums Jülich (JuSER)
unter www.fz-juelich.de/zb/openaccess.



This is an Open Access publication distributed under the terms of the [Creative Commons Attribution License 4.0](https://creativecommons.org/licenses/by/4.0/), which permits unrestricted use, distribution, and reproduction in any medium, provided the original work is properly cited.

Acknowledgments

There are many people I must thank for their help and contributions to this work. I would like to thank my PhD advisor Stefan Tautz for giving me an opportunity to write the thesis on such an interesting topic. I am greatly obliged for the scientific supervision and encouragement I have received from him during the time in Peter Grünberg Institut (PGI-3), Forschungszentrum Jülich. Grateful thanks are extended to Sergey Subach for his kind and professional guidance in and out of the lab. The time we spent together during multiple visits to synchrotrons was truly enjoyable.

The data presented in this work is a result of the collaborative links between Jülich and other groups in Berlin, Bonn, Graz, etc. I am indebted to those who contributed to fruitful experiments and discussions, among others, Christine Brülke, Larissa Egger, Anja Haags, Felix Hajek, Timo Heepenstrick, Michael Hollerer, Philipp Hurdax, Georg Koller, Ina Krieger, Marcel Meyer, François Posseik, Michael Ramsey, Moritz Sokolowski, Petra Tegeder, and Simon Weiß. I wish to show my gratitude to Peter Puschnig and his group members, Dominik Brandstetter, Jana Fuchsberger, Christian Kern, Daniel Lüftner, Mathias Schwendt, and Martin Unzog, of the University of Graz for making output data of the quantum chemical calculations available, and for the friendly invitation for a short research stay in Austria.

I acknowledge numerous experimental supports from our technicians in the institute, Franz-Peter Coenen, Claudia Funk, and Helmut Stollwerk, and from beamline scientists at different synchrotrons, including Metrology Light Source of Physikalisch-Technische Bundesanstalt, Germany (Alexander Gottwald, Hendrik Kaser, Hans Kirschner, Mathias Richter), Diamond Light Source, UK (David Duncan, Pardeep Kumar Thakur, Tien-Lin Lee), and Elettra Sincrotrone Trieste, Italy (Vitaliy Feyer, Matteo Jugovac, Giovanni Zamborlini).

Also, I would like to thank all the members of PGI-3 for various scientific and non-scientific discussions, relaxing coffee breaks, and the pleasant working atmosphere in the institute. Finally, my heartfelt thanks go to my family and friends who have always supported me over the years. Thank you very much! Herzlichen Dank!

Abstract

Photoemission tomography (PT) is a combined experimental and theoretical technique applied to molecule–metal interfaces which uses angle-resolved photoemission spectroscopy over a wide angular range, while the photoelectron angular distributions in reciprocal space (momentum maps, or called k -maps) are interpreted in terms of the molecular orbital structure of the initial state. This thesis uses PT to investigate various aspects of the interaction between π -conjugated organic molecular adsorbates and metal surfaces:

PT was successfully used to identify the exact products of chemical reactions at surfaces and their local bonding. The measured k -maps confirm a modification of the orbital structure of dibromo-bianthracene on Cu(110) in the thermal reaction and the fully hydrogenated bisanthene is found to be the correct reaction intermediate.

To decouple molecular adsorbates from the metal substrate, PT was employed to gauge whether charge is transferred through the interface. Oxygen adsorbed on the Cu(100) surface immobilizes the surface electrons in the Cu–O covalent bonds, thus achieving electronic and physical decoupling of perylene-tetracarboxylic-dianhydride as determined by combined results of PT and normal incidence X-ray standing waves.

A special example of an electronically inhomogeneous unary molecular layer on a metal surface is showcased in the saturated monolayer of tetracene on Ag(110). With the help of PT, two highest occupied molecular orbital peaks in the photoemission spectra were found, indicating that two molecular species coexist in the tetracene layer—while one molecule remains neutral, another is charged.

Finally, we applied PT to study photoelectron angular distributions for highly-hybridized molecule–metal systems, monolayers of p-sexiphenyl, p-quinquephenyl, and pentacene on Cu(110) and on Ag(110), respectively. In k -maps measured for the lowest unoccupied molecular orbital, PT has identified the scattering of either the Shockley surface states or the states around the projected bulk band gap. The scattering vectors can be directly related to reciprocal lattice vectors of the overlayer structure.

Kurzfassung

Photoemissionstomographie (PT) ist eine kombinierte experimentelle und theoretische Technik, die auf Molekül-Metall-Grenzflächen angewandt wird. Dabei wird winkelaufgelöste Photoemissionsspektroskopie über einen weiten Winkelbereich verwendet, während die Photoelektronen-Winkelverteilungen im reziproken Raum (Impulskarten oder k -Karten genannt) in Bezug auf die Molekülorbitalstruktur des Anfangszustands interpretiert werden. Diese Arbeit nutzt PT, um verschiedene Aspekte der Wechselwirkung zwischen π -konjugierten organischen molekularen Adsorbaten und Metalloberflächen zu untersuchen:

PT wurde erfolgreich eingesetzt, um die genauen Produkte chemischer Reaktionen an Oberflächen und deren lokale Bindung zu identifizieren. Die gemessenen k -Karten bestätigen eine Modifikation der Orbitalstruktur von Dibromobianthracen auf Cu(110) in der thermischen Reaktion und das vollständig hydrierte Bisanthen erweist sich als das richtige Zwischenprodukt.

Zur Entkopplung molekularer Adsorbate von dem Metallsubstrat wurde PT eingesetzt, um zu messen, ob Ladung durch die Grenzfläche übertragen wird. An der Cu(100)-Oberfläche adsorbierter Sauerstoff immobilisiert die Oberflächenelektronen in den kovalenten Cu–O Bindungen, wodurch eine elektronische und physikalische Entkopplung von Perylentetracarbonsäuredianhydrid erreicht wird. Dies wurde durch kombinierte Ergebnisse aus PT und senkrecht einfallenden stehenden Röntgenwellen bewiesen.

Ein besonderes Beispiel für eine elektronisch inhomogene einkomponentige Moleküllage auf einer Metalloberfläche ist die gesättigte Schicht von Tetracen auf Ag(110). Mithilfe von PT wurden zwei Peaks des höchsten besetzten Molekülorbitals in den Photoemissionsspektren gefunden, was darauf hindeutet, dass zwei molekulare Spezies in der Tetracenschicht koexistieren. Dabei verbleibt ein Molekül neutral und ein anderes wird geladen.

Außerdem wurde PT angewandt, um Photoelektronen-Winkelverteilungen von hochhybridisierten Molekül-Metall-Systemen, wie einzelne Lagen aus *p*-Sexiphenyl, *p*-Pentaphenyl und Pentacen auf Cu(110) bzw. Ag(110), zu untersuchen. In den gemessenen k -Karten des niedrigsten unbesetzten Molekülorbitals, hat PT die Streuung von entweder Shockley-Oberflächenzuständen oder der Zustände um die projizierte Volumenbandlücke identifiziert. Die Streuvektoren können direkt auf die reziproken Gittervektoren der Überschichtstruktur bezogen werden.

Contents

Acknowledgments	i
Abstract	iii
Kurzfassung	v
List of Acronyms	xi
List of Figures and Tables	xiii
List of Own Publications	xvii
1 Motivation of the Thesis	1
2 Introduction to Photoemission Tomography	3
2.1 Molecular Orbitals	3
2.2 Photoemission Spectroscopy	7
2.3 Photoemission Tomography	10
2.3.1 Quantum-Mechanical Description of Photoemission	11
2.3.2 Plane Wave Final State Approximation	12
2.3.3 Applications of Photoemission Tomography	18
2.3.4 Recent Progress	30
2.3.5 Comparison with Other Methods	31
3 Instruments and Complementary Methods	33
3.1 Hemispherical Electron Analyzer	33
3.2 Photoemission Electron Microscopy	34
3.2.1 LEED	35
3.2.2 LEEM/PEEM	36
3.2.3 NanoESCA	37
3.3 Toroidal Electron Analyzer	39
3.4 Normal Incidence X-Ray Standing Waves	43
3.5 Density Functional Theory Calculations	45

4 Bonded or Not: In-Situ Identification of Surface Reaction Intermediates	49
4.1 Introduction	49
4.2 Identification of Reaction Intermediates	49
4.3 Thermal Reaction of DBBA on Cu(110)	50
4.3.1 Density of States	51
4.3.2 Momentum Maps	52
4.3.3 Electronic Structure Calculations	54
4.3.4 Comparison with Literature	59
4.4 Conclusion	63
5 Charged or Not: Decoupling of Molecules at Metal Surfaces	65
5.1 Introduction	65
5.2 Approaches to Decouple Molecules from Metal	65
5.3 Dielectric Interlayer	66
5.3.1 MgO Thin Film on Ag(100)	67
5.3.2 5A/MgO/Ag(100)	68
5.3.3 PTCDA/MgO/Ag(100)	69
5.4 Surface Reconstruction	71
5.4.1 Oxygen-Reconstructed Cu(100)	72
5.4.2 PTCDA on Oxygen-Reconstructed Cu(100)	73
5.5 2D Materials	82
5.5.1 hBN Growth on Cu(111)	83
5.5.2 PTCDA/hBN/Cu(111)	83
5.6 Conclusion	85
6 Equally Charged or Not: Coexisting Charge States in a Unary Organic Monolayer Film	87
6.1 Introduction	87
6.2 Charge Transfer Scenarios at Molecule–Metal Interfaces	87
6.3 Tetracene on Cu(110)/Ag(110)	88
6.3.1 Literature Review	88
6.3.2 Sample Preparation	89
6.3.3 Density of States	89
6.3.4 DFT Calculations	90
6.3.5 Momentum Maps	92
6.3.6 UPS Results	97
6.4 Discussion	100
6.5 Conclusion	101

7 Scattered or Not: Momentum-Resolved Hybridization of Molecular and Metal States	103
7.1 Introduction	103
7.2 Experimental Details	105
7.3 Clean Cu(110) and Ag(110)	105
7.4 6P/5P/5A on Cu(110)	108
7.4.1 6P/Cu(110) and 5P/Cu(110)	110
7.4.2 5A/Cu(110)	116
7.5 6P/5P/5A on Ag(110)	123
7.6 Discussion	126
7.7 Conclusion	130
8 Summary and Outlook	131
A Data Analysis Software—Mozi	135
B Data Analysis Software—Neso	141
C Sensitivity of PT for Geometric Information	145
D Photon-Energy Dependence of PT	149
Bibliography	159

List of Acronyms

4A	tetracene
5A	pentacene
5P	p-quinquephenyl
6P	p-sexiphenyl
6T	sexithiophene
AFM	atomic force microscopy
ARPES	angle-resolved photoemission spectroscopy
BZ	Brillouin zone
DBBA	10,10'-dibromo-9,9'-bianthracene
DFT	density functional theory
DOS	density of states
EA	electron affinity
E_b	binding energy
EDC	energy distribution curve
E_F	Fermi level
E_{kin}	kinetic energy
E_{pass}	pass energy
E_{vac}	vacuum level
FCT	fractional charge transfer
FT	Fourier transform
GGA	generalized gradient approximation
GNR	graphene nanoribbon
GWA	GW approximation
hBN	hexagonal boron nitride
HOMO	highest occupied molecular orbital
HSE	Heyd–Scuseria–Ernzerhof
IAC	independent-atomic-center
ICT	integer charge transfer
IP	ionization potential
LEED	low energy electron diffraction
LEEM	low energy electron microscopy
LUMO	lowest unoccupied molecular orbital

List of Acronyms

MCP	multichannel plates
ML	monolayer
MO	molecular orbital
NEXAFS	near edge X-ray absorption fine structure
NIXSW	normal incidence X-ray standing waves
NTCDA	1,4,5,8-naphthalene tetracarboxylic dianhydride
PBE	Perdew–Burke–Ernzerhof
Pc	phthalocyanine
pDOS	projected density of states
PEEM	photoemission electron microscopy
Φ	work function
ψ_f	final state
ψ_i	initial state
PT	photoemission tomography
PTCDA	3,4,9,10-perylene tetracarboxylic dianhydride
RDS	reflectance difference spectroscopy
ROI	region of interest
RT	room temperature
SAM	self-assembled monolayer
SBZ	surface Brillouin zone
SOMO	singly occupied molecular orbital
SPA-LEED	spot profile analysis low energy electron diffraction
STM	scanning tunneling microscopy
SUMO	singly unoccupied molecular orbital
TPP	tetraphenylporphyrin
UHV	ultra high vacuum
UPS	ultraviolet photoemission spectroscopy
vdW	van der Waals
XPS	X-ray photoemission spectroscopy

List of Figures and Tables

List of Figures

2.1	5A molecule	5
2.2	PTCDA molecule	7
2.3	Photoemission spectroscopy	9
2.4	Inelastic mean free path as a function of the electron energy	10
2.5	Relationship between the molecular orbital in real and reciprocal space and the measured k -maps	14
2.6	Geometry factor	16
2.7	Geometry factor and its influence on the theoretical HOMO of 5A	17
2.8	Structure models of PTCDA ML phases on low-index Ag surfaces and corresponding theoretical LUMO k -maps	19
2.9	Theoretical HOMO k -map contributed by two 5A molecules	20
2.10	5A ML on Cu(110)	23
2.11	PT deconvolution procedure for PTCDA/Ag(110)	24
2.12	Measurement of PTCDA LUMO as a function of photon energy	26
2.13	5A(022) films on p(2 × 1) oxygen-reconstructed Cu(110) surface	28
2.14	PTCDA ML on Cu(100)	29
2.15	k -maps of PTCDA LUMO and HOMO measured with different experimental methods	32
3.1	Hemispherical electron analyzer	34
3.2	Working principle of LEED	35
3.3	Photoemission electron microscope	38
3.4	Toroidal electron analyzer	40
3.5	Two measurement modes of the toroidal electron analyzer	41
3.6	Comparison of NanoESCA and toroidal electron analyzer	42
3.7	Normal incidence X-ray standing waves	44
4.1	Surface reaction of DBBA on Au(111) and Cu(110)	51
4.2	Bandmaps and EDCs of DBBA on Cu(110)	52
4.3	Experimental and theoretical k -maps of DBBA	53
4.4	DFT calculation of DBBA adsorption structures before annealing	55
4.5	DFT calculation of DBBA adsorption structures after annealing	57

List of Figures and Tables

4.6	Chemical structure and simulated k -maps for bisanthene, $C_{28}H_{12}$, and $C_{28}H_8$ on Cu(110)	60
4.7	STM image and DFT calculations for reaction intermediate of DBBA on Cu(110)	61
4.8	Chemical structure and simulated STM images for bisanthene, $C_{28}H_{12}$, and $C_{28}H_8$ on Cu(110)	62
4.9	XPS of reaction intermediate and fitting models for reaction intermediate of DBBA on Cu(110)	63
5.1	ARPES results of 5A/Ag(100) and 5A/MgO/Ag(100)	67
5.2	Energy level alignment for 5A/Ag(100) and 5A/MgO/Ag(100)	69
5.3	Photoemission results of PTCDA/MgO/Ag(100)	70
5.4	Surface reconstruction of copper	72
5.5	LEED model and image of clean Cu(100) and oxygen-reconstructed Cu(100)	73
5.6	LEED model and image of PTCDA/O/Cu(100)	74
5.7	Photoemission results of PTCDA on oxygen-reconstructed Cu(100)	76
5.8	XPS spectra before and after PTCDA deposition on oxygen-reconstructed Cu(100)	77
5.9	Normalized photoelectron yields before and after PTCDA deposition on oxygen-reconstructed Cu(100)	79
5.10	Sphere model of PTCDA/O/Cu(100)	79
5.11	Electron densities and change in electron potential energy for PTCDA/Cu(100) and PTCDA/O/Cu(100)	81
5.12	ARPES data of hBN/Cu(111) and of PTCDA/hBN/Cu(111)	84
6.1	EDCs measured for 5A and 4A on Ag(110) and Cu(110)	90
6.2	DFT simulations for two exemplary structures of 4A/Ag(110)	91
6.3	Experimental and simulated k -maps for 5A/Cu(110) and 5A/Ag(110)	93
6.4	Experimental and simulated k -maps for 4A/Cu(110) and 4A/Ag(110)	94
6.5	Photoemission results of 4A/Ag(110) in three different preparations	96
6.6	Coverage-dependent UPS spectra of 4A/Ag(110)	98
7.1	Photoemission results of clean Cu(110)	106
7.2	Photoemission results of clean Ag(110)	107
7.3	Structure models and LEED images of 6P, 5P, and 5A on Cu(110)	109
7.4	EDCs measured for 6P, 5P, and 5A on Cu(110) and Ag(110)	110
7.5	6P ML on Cu(110)	113
7.6	5P ML on Cu(110)	114
7.7	5A ML on Cu(110)	115

7.8	Bandmaps measured through critical points for clean Cu(110), 6P/Cu(110), 5P/Cu(110), and 5A/Cu(110)	117
7.9	Enlarged sections of corrected experimental k -maps for clean Cu(110), 6P/Cu(110), 5P/Cu(110), and 5A/Cu(110)	118
7.10	Enlarged sections of as-obtained experimental k -maps for clean Cu(110), 6P/Cu(110), 5P/Cu(110), and 5A/Cu(110)	119
7.11	Bandmaps of 6P/Cu(110)	120
7.12	Bandmaps of 5P/Cu(110)	121
7.13	Bandmaps of 5A/Cu(110)	122
7.14	Structure models and LEED images of 6P, 5P, and 5A on Ag(110)	125
7.15	k -maps of 6P, 5P, and 5A on Ag(110)	127
7.16	Bandmaps measured through critical points for clean Ag(110), 6P/Ag(110), 5P/Ag(110), and 5A/Ag(110)	128
7.17	Bandmaps of 6P, 5P, and 5A on Ag(110) and selected k -maps	129
A.1	Screenshot of MOZI	136
B.1	Screenshot of NESO	142
B.2	Dispersion correction in NESO	143
C.1	Theoretical k -maps of HOMO for 4A with different tilting around molecules' long axis	146
C.2	Theoretical k -maps of HOMO and LUMO for 4A with in-plane misalignment	147
D.1	Calibrated photon yield at U125 insertion device beamline, PTB	150
D.2	Photon-energy dependent theoretical k -maps of LUMO and HOMO for PTCDA molecules using the toroidal electron analyzer	151
D.3	Photon-energy dependent data of PTCDA/Ag(110), after Weiß et al.	154
D.4	Photon-energy dependent data of 5A/Ag(100)	155
D.5	Photon-energy dependent data of bisanthene/Cu(110)	156
D.6	Photon-energy dependent data of PTCDA/Ag(110), after Graus et al.	157

List of Tables

2.1	Parameters of different polarizations	17
4.1	Total energies and adsorption energies of as-deposited DBBA on Cu(110)	56
4.2	Total energies and adsorption energies of reaction intermediates of DBBA on Cu(110)	58

List of Figures and Tables

5.1	Coherent positions, coherent fractions, and adsorption heights of different chemical species in PTCDA/O/Cu(100)	80
6.1	List of publications on 4A/Ag(110)	100

List of Own Publications

- D. Lüftner, S. Weiß, X. Yang, P. Hurdax, V. Feyer, A. Gottwald, G. Koller, S. Soubatch, P. Puschnig, M. G. Ramsey, and F. S. Tautz, “Understanding the photoemission distribution of strongly interacting two-dimensional overlayers”, *Phys. Rev. B* **96**, 125402 (2017).
- X. Yang, I. Krieger, D. Lüftner, S. Weiß, T. Heepenstrick, M. Hollerer, P. Hurdax, G. Koller, M. Sokolowski, P. Puschnig, M. G. Ramsey, F. S. Tautz, and S. Soubatch, “On the decoupling of molecules at metal surfaces”, *Chem. Commun.* **54**, 9039 (2018).
- S. Weiß, D. Gerbert, A. Stein, A. K. Schenk, X. Yang, C. Brülke, R. Kremring, S. Feldmann, F. C. Bocquet, M. Gille, S. Hecht, M. Sokolowski, P. Tegeder, S. Soubatch, and F. S. Tautz, “Dependence of the adsorption height of graphenelike adsorbates on their dimensionality”, *Phys. Rev. B* **98**, 075410 (2018).
- C. Brülke, T. Heepenstrick, I. Krieger, B. Wolff, X. Yang, A. Shamsaddinlou, S. Weiß, F. C. Bocquet, F. S. Tautz, S. Soubatch, and M. Sokolowski, “Quantitative analysis of the electronic decoupling of an organic semiconductor molecule at a metal interface by a monolayer of hexagonal boron nitride”, *Phys. Rev. B* **99**, 121404 (2019).
- L. Egger, B. Kollmann, P. Hurdax, D. Lüftner, X. Yang, S. Weiß, A. Gottwald, M. Richter, G. Koller, S. Soubatch, F. S. Tautz, P. Puschnig, and M. G. Ramsey, “Can photoemission tomography be useful for small, strongly-interacting adsorbate systems?”, *New J. Phys.* **21**, 043003 (2019).
- X. Yang, L. Egger, P. Hurdax, H. Kaser, D. Lüftner, F. C. Bocquet, G. Koller, A. Gottwald, P. Tegeder, M. Richter, M. G. Ramsey, P. Puschnig, S. Soubatch and F. S. Tautz, “Identifying surface reaction intermediates with photoemission tomography”, *Nat. Commun.* **10**, 3189 (2019).
- X. Yang, L. Egger, J. Fuchsberger, M. Unzog, D. Lüftner, F. Hajek, P. Hurdax, M. Jugovac, G. Zamborlini, V. Feyer, G. Koller, P. Puschnig, F. S. Tautz, M. G. Ramsey, and S. Soubatch, “Coexisting charge states in a unary organic monolayer film on a metal”, *J. Phys. Chem. Lett.* **10**, 6438 (2019).
- P. Hurdax, M. Hollerer, L. Egger, G. Koller, X. Yang, A. Haag, S. Soubatch, F. S. Tautz, M. Richter, A. Gottwald, P. Puschnig, M. Sterrer, and M. G. Ramsey, “Controlling the electronic and physical coupling on dielectric thin films”, *Beilstein J. Nanotechnol.* **11**, 1492 (2020).

List of Own Publications

- A. Haags, A. Reichmann, Q. Fan, L. Egger, H. Kirschner, T. Naumann, S. Werner, T. Vollgraff, J. Sundermeyer, L. Eschmann, X. Yang, D. Brandstetter, F. C. Bocquet, G. Koller, A. Gottwald, M. Richter, M. G. Ramsey, M. Rohlfing, P. Puschnig, J. M. Gottfried, S. Soubatch, and F. S. Tautz, “Kekulene: on-surface synthesis, orbital structure, and aromatic stabilization”, *ACS Nano* **14**, 15766 (2020).
- L. Egger, M. Hollerer, C. S. Kern, H. Herrmann, P. Hurdax, A. Haags, X. Yang, A. Gottwald, M. Richter, S. Soubatch, F. S. Tautz, G. Koller, P. Puschnig, M. G. Ramsey, and M. Sterrer, “Charge-promoted self-metalation of porphyrins on an oxide surface”, *Angew. Chem., Int. Ed.* **60**, 5078 (2021).
- R. Wallauer, M. Raths, K. Stallberg, L. Münster, D. Brandstetter, X. Yang, J. Güdde, P. Puschnig, S. Soubatch, C. Kumpf, F. C. Bocquet, F. S. Tautz, and U. Höfer, “Tracing orbital images on ultrafast time scales”, *Science* **371**, 1056 (2021).
- D. Brandstetter, X. Yang, D. Lüftner, F. S. Tautz, and P. Puschnig, “kMap.py: A Python program for simulation and data analysis in photoemission tomography”, *Comput. Phys. Commun.* **263**, 107905 (2021).

1 Motivation of the Thesis

The miniaturization of semiconductor devices in the last few decades has created a long-standing booming technology sector. Today, further efforts are being made to tackle new major challenges such as building a quantum computer using novel physical phenomena. Still, many aspects in the understanding of physical properties of interfaces (“the interface is the device”—Herbert Kroemer) are in the exploration stage. Precise experimental and theoretical descriptions of complex surface structures are always difficult (“God made the bulk; surfaces were invented by the devil”—Wolfgang Pauli). Fortunately, innovative tools are continuously developed to advance science and engineering. In the subfield that studies the molecule–metal interface, one of these tools is photoemission tomography (PT), the central topic of this thesis.

PT is a combined experimental and theoretical approach that uses the angular distribution of electrons which are photoemitted from oriented molecular layers on crystalline metal surfaces. For such quasi-two-dimensional systems, scanning tunneling microscopy (STM) has been repeatedly employed to investigate the structures of molecular orbitals (MOs) [1], especially the frontier orbitals of molecules that comprise the main determinants of their chemical, optical, and electronic properties [2]. Instead, PT is an ensemble-averaging method that is based on angle-resolved photoemission spectroscopy (ARPES). PT can directly relate the Fourier transform (FT) of measured photoelectron angular distributions (momentum maps, or called k -maps) to specific MOs in initial states under the approximation to treat the photoemission final states as plane waves. With this convenient relationship, heavy quantum mechanical *ab initio* calculations of photoemission cross sections of complex molecule–metal interfaces can be greatly simplified to considering only a single molecule, if the number of molecular orientations existing in the adsorbate layer is limited.

First applied in one dimension on crystalline multilayer films formed by π -conjugated molecules [3–6], Puschnig et al. [7] have shown that PT also works perfectly on two-dimensional systems. The value of PT is further exploited for various applications, mainly in investigating the electronic and geometric structures of organic molecular monolayers [8–42]. Further refining this method, algorithms were developed to extract the lost phase information of MO from the measured ARPES intensity distribution [43–45], three-dimensional MOs in real space were reconstructed from purely experimental photoemission data [46, 47], a damping

1 Motivation of the Thesis

term was included in plane wave final states to account for the strongly interacting substrate [48, 49], and the list continues. The accuracy and precision of the PT method have been proved by accumulating results in the past decade.

This thesis uses PT to perform quantitative electronic structure studies on the chemical interaction of π -conjugated organic molecular adsorbates with the metal surfaces, to address the questions whether they are bonded, whether there is charge transfer, whether all molecules are charged equally, and whether scattering within the adsorbate layer occurs. First, [Chapter 2](#) offers a concise introduction to PT and an overview of its diverse application scenarios. In [Chapter 3](#), several experimental techniques that are useful for PT studies are described and compared. One of the prerequisites for PT is to map ARPES intensity distributions in a large reciprocal range, for this purpose the NanoESCA ([Section 3.2.3](#)) and the toroidal electron analyzer ([Section 3.3](#)) are preferred. [Chapter 4](#) shows cases that PT applied in the thermal reaction of a precursor molecule on Cu(110) can successfully determine the reaction intermediate in atomic resolution, which is more precise and reliable than the STM results. [Chapter 5](#) compares three different approaches to decouple molecules from metal surfaces and [Chapter 6](#) demonstrates a special case that the charged and uncharged tetracene molecules co-exist in the monolayer on Ag(110), in both chapters the PT method is used to quantify the charge transfer through the molecule–metal interface. [Chapter 7](#) shows that the theoretical calculations for PT based on isolated molecules can be insufficient but remain useful in the interpretation of photoelectron angular distributions for highly-hybridized molecule–metal systems.

2 Introduction to Photoemission Tomography

Photoemission tomography (PT), sometimes also termed “photoemission orbital tomography”, “molecular orbital tomography”, or “photoelectron tomography”, is a combined experimental and theoretical approach to image molecular orbitals by sectioning the photoelectron distribution in reciprocal space, reminiscent of the X-ray computed tomography scan in medical use. Instead of gaining knowledge about one’s abdominal or cardiac anatomy, here surface scientists are interested in molecular orbitals by evaluating angle-resolved photoemission data. It is based on the plane wave final state approximation proposed by Gadzuk [50–52] in the 1970s, which was revisited by Puschnig et al. [7] in 2009 and has since achieved great success in explaining the photoemission results in various organic molecular systems with those predicted by density functional theory (DFT). Various applications, such as identification of spectral features in ultraviolet photoemission spectroscopy (UPS), extraction of molecular orientations, deconvolution of individual orbital contributions, and real-space orbital reconstruction, have made PT an interesting and powerful technique in the toolkit of surface scientists.

2.1 Molecular Orbitals

In one-electron systems, e.g. hydrogen-like atoms, the wave function of a single electron $\varphi(\mathbf{x})$ contains a spatial as well as a spin coordinate $\mathbf{x} = (\mathbf{r}, \sigma)$. Then $|\varphi(\mathbf{x})|^2$ corresponds to the probability density of finding the electron at a certain spatial position, known as electron density. Molecules, as many-electron systems, have N -electron wave functions $\Psi(\mathbf{x}_1, \dots, \mathbf{x}_N)$ depending on the coordinates of all electrons $\mathbf{x}_1, \dots, \mathbf{x}_N$. Molecular orbitals (MOs), however, are no longer uniquely defined by nature, but serve as an *approximation* to $\Psi(\mathbf{x}_1, \dots, \mathbf{x}_N)$. For instance, within the simple Hartree–Fock model, the wave function of a molecule with N electrons is approximated by the antisymmetrized product of N single-particle

2 Introduction to Photoemission Tomography

wave functions, referred to as Slater determinant [53–55]:

$$\Psi(\mathbf{x}_1, \dots, \mathbf{x}_N) \approx \Phi_A(\mathbf{x}_1, \dots, \mathbf{x}_N) = \frac{1}{\sqrt{N!}} \begin{vmatrix} \varphi_1(\mathbf{x}_1) & \varphi_2(\mathbf{x}_1) & \cdots & \varphi_N(\mathbf{x}_1) \\ \varphi_1(\mathbf{x}_2) & \varphi_2(\mathbf{x}_2) & \cdots & \varphi_N(\mathbf{x}_2) \\ \vdots & \vdots & \ddots & \vdots \\ \varphi_1(\mathbf{x}_N) & \varphi_2(\mathbf{x}_N) & \cdots & \varphi_N(\mathbf{x}_N) \end{vmatrix}, \quad (2.1)$$

where single-particle wave functions $\varphi_i(\mathbf{x})$ for $i = 1, 2, \dots, N$ are solutions of the Hartree–Fock equations.

Since MOs are merely mathematical constructs to produce an approximation, there are different definitions of orbitals. A few examples: Kohn–Sham orbitals are obtained from self-consistent calculations within the framework of density functional theory (DFT) for the ground state density (cf. Section 3.5) [56]; natural orbitals are eigenfunctions of the one-body reduced density matrix in complete active space self-consistent-field theory (CASSCF) [35, 57]; Dyson orbitals are evoked when interpreting results of various spectroscopic and scattering experiments, which are defined as overlaps between initial N -electron states (Ψ_i) and final states with $N \pm 1$ electrons (Ψ_f) [55, 57, 58]:

$$\Phi_D^{\text{anion}}(\mathbf{x}) = \sqrt{N+1} \langle \Psi_f^{N+1} | \Psi_i^N \rangle, \quad (2.2)$$

or

$$\Phi_D^{\text{cation}}(\mathbf{x}) = \sqrt{N} \langle \Psi_f^{N-1} | \Psi_i^N \rangle. \quad (2.3)$$

The term “orbital” is widely used in the interpretation of experimental results. Zuo et al. [59] claimed a direct observation of the copper d-orbital in cuprite with X-ray diffraction. Brion et al. [60] achieved the imaging of the spherically averaged orbital electron density of several molecules in gas-phase by electron momentum spectroscopy. Itatani et al. [61] reconstructed the molecular orbital of N_2 including the phase with high harmonics generation of intense femtosecond laser pulses. Using scanning tunneling microscopy (STM), often on an inert decoupling alkali halide film (e.g. NaCl, KCl), one is able to map the orbital structures of molecules, the most cited example is pentacene [1, 62] (see Fig. 2.1).

These experimental studies, however, have been critically discussed for years [53, 55, 57, 58, 64–66]. There are mainly two aspects that need to be addressed. First, if an orbital concept such as Kohn–Sham orbitals is used to express the N -electron ground state wave function $\Psi(\mathbf{x}_1, \dots, \mathbf{x}_N)$, the single-particle orbitals do not describe the behavior of any individual electron in the many-electron system. The state (energy and spatial distribution) of a single electron can principally only be determined if one excites the system, i.e. removes one electron or adds one electron to the system. The appropriate orbital concept for such one-electron excitation is the Dyson orbital. It turns out that in many

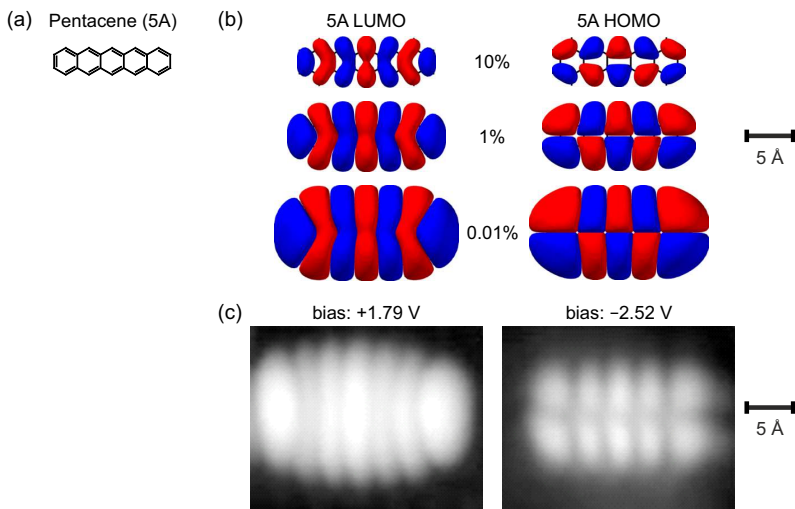


Figure 2.1: Pentacene (5A). (a) Molecular structure. (b) DFT-calculated LUMO and HOMO of 5A in gas-phase represented at different isosurface levels—10%, 1%, and 0.01% of the maximum of $|\psi(x, y, z)|$ [63]. (c) Constant-current STM images of 5A on NaCl thin film on Cu(111) with different bias voltages, reproduced from Ref. [1]. Positive bias means electrons tunneling from the tip into the LUMO, negative bias means electrons tunneling out of the HOMO.

case Dyson orbitals look quite similar to e.g. Kohn–Sham orbitals, but the proper quantity is the Dyson orbital.

The second aspect concerns the fact that an orbital is a single-particle wave function and therefore a complex physical quantity. Only its absolute value can be observed, that is the electron density. For example, in STM, the voltage bias V induces a tunneling current I at a particular space point and the differential tunneling conductance is proportional to the local density of states (DOS) of the surface material ρ_s :

$$\frac{dI}{dV} \propto \rho_s(E_F - eV). \quad (2.4)$$

Thus, STM provides real-space images of the electron density of the Dyson orbitals that connect the neutral molecules with their respective anions and cations [55]. The energy levels measured by dI/dV , however, will only be roughly approximated by the lowest unoccupied molecular orbital (LUMO) and highest occupied molecular orbital (HOMO) energies of the isolated molecule, which are from the ground state calculations [66].

2 Introduction to Photoemission Tomography

In this thesis, we deal with the photoemission experimental data where Dyson orbitals should be the correct description. Because of the fact that Dyson orbitals often closely resemble one-electron Kohn–Sham orbitals calculated from DFT [22, 67], the simple one-electron picture is used for gas-phase (isolated) molecules throughout this thesis [e.g. Fig. 2.1(b) and Fig. 2.2(b)]. If the substrate is included in DFT calculations, more advanced approaches are used, see Section 3.5. The detailed quantum-mechanical description of photoemission involved in this thesis is introduced in Section 2.3.

To end this section, we briefly introduce the main objects of study— π -conjugated organic molecules on metal surfaces. Like benzene and graphene, neighboring carbon atoms of π -conjugated systems overlap their p_z orbitals across a σ bond forming delocalized π orbitals (sp^2 hybridization) beneath and above the molecular plane. In this thesis the following π -conjugated molecules often appear: 3,4,9,10-perylene tetracarboxylic dianhydride (PTCDA), tetracene (4A), pentacene (5A), p-quinquephenyl (5P), and p-sexiphenyl (6P), where oligomers of acene and phenyl are abbreviated as “A” and “P”, respectively, with the digit indicating the number of units.

Of interest are often frontier orbitals of molecules—LUMO and HOMO, which are prime determinants of molecules’ chemical, optical, and electronic properties [2]. The second lowest unoccupied (second highest occupied) MO is then named as LUMO+1 (HOMO–1), and so on. An example of the molecular orbitals of PTCDA is shown in Fig. 2.2. Here, MOs are represented as an isosurface,¹ see Fig. 2.2(b), where different colors (red/blue) indicate the sign of the wave function. The LUMO (HOMO) level in organic semiconductors is in analogy to the valence band maximum (conduction band minimum) in inorganic semiconductors [68]. For research or practical device applications, thin films of organic molecules in contact with a metal surface, instead of molecular single crystals, are often investigated. Regarding the thermodynamic equilibrium of electrons throughout the interface, measurements of the LUMO/HOMO position and the Fermi level (E_F) are crucial to understand the electronic structure [69].

When a molecule approaches a metal surface, the image potential created by the image charge reduces the gap between frontier orbitals (polarization effect). Taking a look at the example in Fig. 2.2(c), the image potential of PTCDA on Ag(111) reduces the gap by approximately 2.4 eV, which consequently shifts down (up) the initial gas-phase LUMO (HOMO) level. Additionally, the push-back effect, also referred to as cushion/pillow effect [70–72], reduces the surface dipole and decreases the work function. This can result in an energy alignment that positions the LUMO below the Fermi level, leading to charge transfer from the metal substrate to the molecule and hybridization of molecule/metal states. In

¹In this thesis the isosurface is chosen at, if not specified, 10% of the maximum of $|\psi(x, y, z)|$.

2.2 Photoemission Spectroscopy

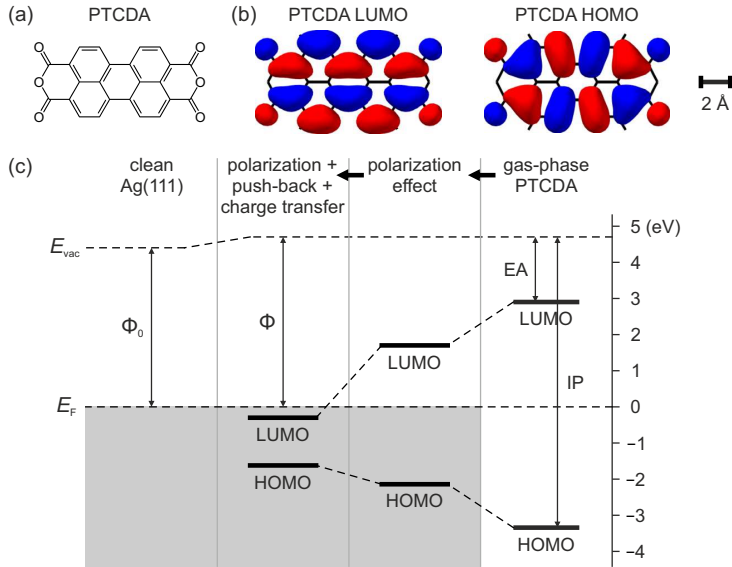


Figure 2.2: 3,4,9,10-perylene tetracarboxylic dianhydride (PTCDA). (a) Molecular structure. (b) DFT-calculated LUMO and HOMO of PTCDA in gas phase [63]. (c) Schematic partitioning of the energy level alignment of PTCDA on Ag(111) surface. Φ_0 : work function of clean Ag(111), Φ : work function when PTCDA is adsorbed on the substrate, E_F : Fermi level, E_{vac} : vacuum level, EA: electron affinity, IP: ionization potential. After Fig. 9 of Ref. [24].

this case the LUMO becomes occupied, so-called former LUMO (f-LUMO). This charge transfer in turn mitigates the push-back effect, and can even lead to an increase of the work function if the charge transfer is large enough, such as in the case of PTCDA/Ag [24, 73].

2.2 Photoemission Spectroscopy

Photoemission spectroscopy, particularly ultraviolet photoemission spectroscopy (UPS), is the most used technique to study the valence band structure of solids. For organic semiconductors and insulators, UPS is generally not performed on single crystal samples due to their low electrical conductivity and the charging effect upon photoemission, but on thin films on conductive substrate [74]. As shown in Fig. 2.3, the photoemission process for an electron in organic adsorbates

2 Introduction to Photoemission Tomography

on a metal substrate from initial state (ψ_i) to final state (ψ_f) follows the energy conservation [75–77]:

$$E_{\text{kin}} = h\nu - E_{\text{b}} - \Phi_{\text{s}}, \quad (2.5)$$

where E_{kin} is the kinetic energy of the photoemitted electron, $h\nu$ is the photon energy, E_{b} is the binding energy, and Φ_{s} is the work function (Φ) of the sample. The resulting spectrum right at the sample surface, shown on the left side of Fig. 2.3(a), contains the following features: onset of the photoemission signal at the Fermi edge, primary peaks related to occupied frontier orbitals, valence band from the metal substrate and a sloping background originating from secondary electrons. The valence band is best investigated with lower energies (typically < 100 eV for ultraviolet) due to the better energy and momentum resolution, reduced beam damage and higher cross-section for excitation. However, to access a larger range of core-level electronic states [not drawn in Fig. 2.3(a)], higher-energy X-ray (1–10 keV) is instead used—X-ray photoemission spectroscopy (XPS). XPS is widely used for determining the surface composition, because the core-level states are characteristic of the chemical species, which is needed for the X-ray standing wave technique, see Section 3.4.

Typical photoemission spectrum has a sharp cutoff at $E_{\text{kin}} = 0$, which can be used for the measurement of the sample work function [75]. It is worth noting that when measuring E_{kin} the contact potential, $\Phi_{\text{s}} - \Phi_{\text{a}}$, i.e. the work function difference between sample and analyzer, has to be taken into account. The Fermi levels of sample and analyzer (metallic) are equilibrated through electrical connections, e.g. the same grounding. Usually the analyzer work function Φ_{a} is smaller than the sample work function Φ_{s} , so that the photoelectrons are accelerated to the analyzer [77]. This results in that the measured kinetic energies of photoelectrons are shifted by $\Phi_{\text{s}} - \Phi_{\text{a}}$:

$$E_{\text{kin}} = h\nu - E_{\text{b}} - \Phi_{\text{s}} + (\Phi_{\text{s}} - \Phi_{\text{a}}) = h\nu - E_{\text{b}} - \Phi_{\text{a}}. \quad (2.6)$$

These photoelectrons hit surfaces in the analyzer generating secondary electrons of the analyzer itself by impact, shown pink in the spectrum on the right side of Fig. 2.3(a). The superposition of secondary electrons from these two kinds of origin makes it difficult to determine the secondary edge of the sample. The solution is to apply an additional sample bias of several eV, see e.g. Ref. [77] for details. Photoemission data in this thesis are presented using binding energies E_{b} , recalculated from the Fermi level E_{F} of metal substrates, for the energy scale.

If an angle-resolved electron analyzer is utilized, i.e. using angle-resolved photoemission spectroscopy (ARPES),² the parallel and perpendicular momenta of the

²Initially called ARUPS (angle-resolved UPS). As the photon energies used are often beyond the ultraviolet range thanks to the development of synchrotron radiation, now the acronym ARPES is more common.

2.2 Photoemission Spectroscopy

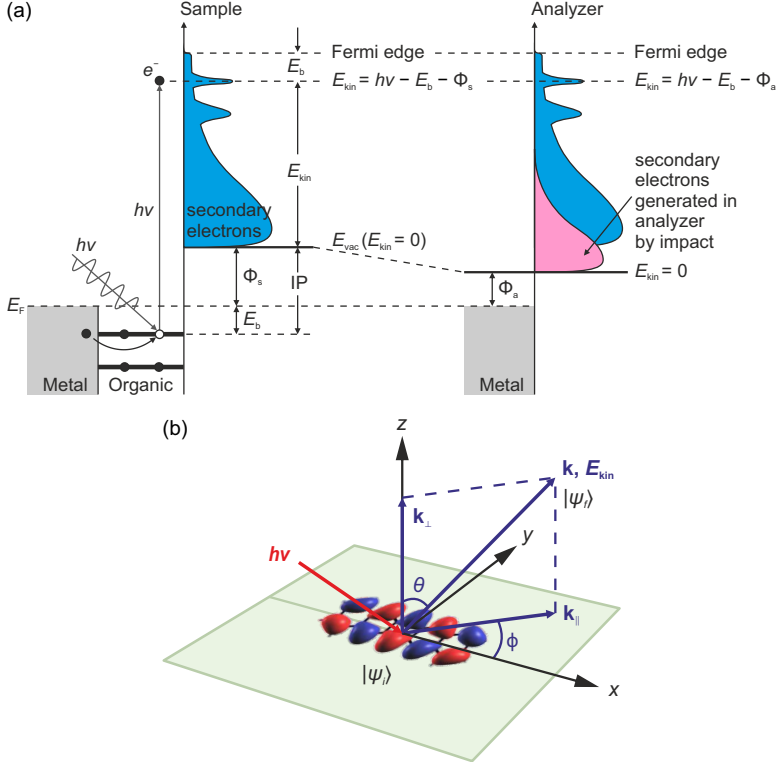


Figure 2.3: Photoemission spectroscopy. (a) Scheme of the UPS process of organic molecules on metal substrate. Adapted from Refs. [69, 77]. E_F : Fermi level, E_b : binding energy referred to E_F , E_{vac} : vacuum level, E_{kin} : kinetic energy, Φ_s (Φ_a): work function of sample (analyzer), IP: ionization potential. The kinetic energy scale at sample surface (left) is compared to that at analyzer channeltron (right). See text for details. (b) Standard ARPES geometry. The incident photon with energy $h\nu$ excites an electron from the initial state ψ_i (here 5A HOMO as example) to the final state ψ_f characterized by the momentum vector \mathbf{k} and the kinetic energy E_{kin} . θ (ϕ): polar (azimuth) angle of the photoemitted electron's direction. \mathbf{k}_{\parallel} (\mathbf{k}_{\perp}): in-plane (out-of-plane) component of \mathbf{k} .

outgoing electron are determined by:

$$k_{\parallel} = \sqrt{2m_e E_{kin}/\hbar^2} \sin \theta, \quad (2.7)$$

$$k_{\perp} = \sqrt{2m_e E_{kin}/\hbar^2} \cos \theta, \quad (2.8)$$

2 Introduction to Photoemission Tomography

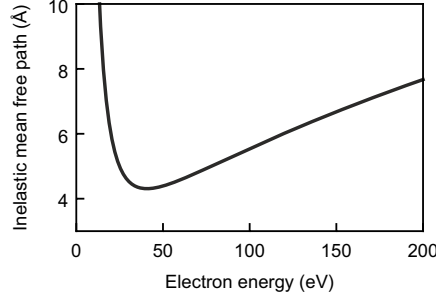


Figure 2.4: Inelastic mean free path λ as a function of the electron energy. Empirical parameters $c_1 = 1430$ and $c_2 = 0.54$ for elements [78] are used to express λ in units of Å.

or further converting k_{\parallel} into two components k_x and k_y :

$$k_x = k_{\parallel} \cos \phi, \quad (2.9)$$

$$k_y = k_{\parallel} \sin \phi, \quad (2.10)$$

where θ and ϕ are the polar and azimuth angles under which the electrons leave the surface, respectively, see Fig. 2.3(b). A convenient conversion relation between k_{\parallel} and E_{kin} is:

$$k_{\parallel} [\text{Å}^{-1}] \approx 0.51 \sqrt{E_{\text{kin}} [\text{eV}]} \sin \theta. \quad (2.11)$$

One important consideration of using electron spectroscopy for surface analysis is the high surface sensitivity. In the kinetic energy range of interest, 10 to 100 eV, the mean free path λ for inelastic photoelectrons is only a few Ångstroms [75] (see Fig. 2.4). The empirical “universal curve” can be used to have a reasonable estimation of λ [78]:

$$\lambda = c_1 E^{-2} + c_2 \sqrt{E}, \quad (2.12)$$

where E is the electron energy, c_1 and c_2 are material parameters. Therefore, photoemission spectroscopy is suited to probe the near-surface region, where the main contribution of the total photoemission intensity originates from. This also requires an atomically clean surface under ultra high vacuum (UHV) condition to avoid contamination.

2.3 Photoemission Tomography

Common experimental methods for imaging MOs, i.e. obtaining their distribution either in real or reciprocal space, mentioned in Section 2.1 are either limited

to very small molecules, e.g. laser-aligned simple gas-phase molecules for imaging with ARPES, or strongly demanding experimental conditions, e.g. flat-lying molecules electronically decoupled from substrate at cryogenic temperatures and in UHV for imaging with STM. In the following, photoemission tomography (PT), an easy and robust technique for reconstructing MOs of adsorbed molecules and many more applications beyond, is introduced as a powerful alternative.

2.3.1 Quantum-Mechanical Description of Photoemission

Equation (2.5) in Section 2.2 is merely an energy conservation relation. In order to understand the angular distribution of measured photoemission intensities, a quantum-mechanical description of photoemission is needed. The transition probability $w_{i,f}$ for an optical excitation between an N -electron initial (ground) state (Ψ_i^N) and a final state (Ψ_f^N) with one photoelectron, which directly relates to the measured photoemission intensity $I(\mathbf{k}, E_{\text{kin}})$, can be described by Fermi's golden rule derived from time-dependent first-order perturbation theory [75]:

$$I(\mathbf{k}, E_{\text{kin}}) \propto w_{i,f} = \frac{2\pi}{\hbar} \left| \langle \Psi_f^N | H' | \Psi_i^N \rangle \right|^2 \delta(E_f^N - E_i^N - h\nu), \quad (2.13)$$

where E_i^N and E_f^N are the initial and final state energies of the N -particle system and H' is a small perturbation.

Using SI units, the perturbation (interaction) Hamiltonian in the most general form is [79, 80]:

$$H' = \frac{e}{2m_e} (\mathbf{P} \cdot \mathbf{A} + \mathbf{A} \cdot \mathbf{P}) + \frac{e^2}{2m_e} \mathbf{A}^2 - e\Pi, \quad (2.14)$$

where \mathbf{A} and Π are the vector and scalar potentials of the incident electromagnetic field, $\mathbf{P} = -i\hbar\nabla$ is the momentum operator. Operating with $(\mathbf{P} \cdot \mathbf{A} + \mathbf{A} \cdot \mathbf{P})$ on a wave function Ψ one gets:

$$\begin{aligned} (\mathbf{P} \cdot \mathbf{A} + \mathbf{A} \cdot \mathbf{P})\Psi &= \mathbf{P} \cdot \mathbf{A}\Psi + \mathbf{A} \cdot \mathbf{P}\Psi \\ &= -i\hbar(\nabla \cdot \mathbf{A}\Psi + \mathbf{A} \cdot \nabla\Psi) \\ &= -i\hbar[(\nabla \cdot \mathbf{A})\Psi + \mathbf{A} \cdot (\nabla\Psi) + \mathbf{A} \cdot \nabla\Psi] \\ &= -i\hbar[(\nabla \cdot \mathbf{A})\Psi + 2\mathbf{A} \cdot \nabla\Psi]. \end{aligned} \quad (2.15)$$

Choosing $\Pi = 0$ and using the Coulomb gauge ($\nabla \cdot \mathbf{A} = 0$), the perturbation Hamiltonian H' becomes:

$$H' = \frac{e}{m_e} \mathbf{A} \cdot \mathbf{P} + \frac{e^2}{2m_e} \mathbf{A}^2. \quad (2.16)$$

Neglecting two-photon processes ($\mathbf{A}^2 = 0$), H' is simplified to:

$$H' = \frac{e}{m_e} \mathbf{A} \cdot \mathbf{P}. \quad (2.17)$$

2 Introduction to Photoemission Tomography

In Eq. (2.13), N -electron final state Ψ_f^N is composed of the ionized molecule with $N - 1$ electrons and the emitted photoelectron. In practice, the *sudden approximation* removes the photoelectron instantaneously and the ionized molecule changes its effective potential discontinuously. This allows for expressing Ψ_f^N as an antisymmetrized product of two separate states:

$$\Psi_f^N(\mathbf{x}_1, \dots, \mathbf{x}_N) = \sum_{i=1}^N \frac{(-1)^{i+1}}{\sqrt{N}} \Psi^{N-1}(\mathbf{x}_1, \dots, \mathbf{x}_{i-1}, \mathbf{x}_{i+1}, \dots, \mathbf{x}_N) \varphi(\mathbf{x}_i), \quad (2.18)$$

where φ is the wave function of the photoelectron and Ψ^{N-1} is the eigenfunction of the $(N - 1)$ -electron Hamiltonian that describes the singly ionized molecule. Due to the difficulty of calculating the many-particle matrix element, it is simplified into the form of a single-particle matrix element (with the many-body momentum operator $\mathbf{P} = \sum_{i=1}^N \mathbf{p}_i$, see detailed derivation in Ref. [22]):

$$\langle \Psi_f^N | \mathbf{A} \cdot \mathbf{P} | \Psi_i^N \rangle = \langle \psi_f | \mathbf{A} \cdot \mathbf{p} | \psi_i \rangle = \langle \varphi(\mathbf{x}) | \mathbf{A} \cdot \mathbf{p} | \Phi_D(\mathbf{x}) \rangle, \quad (2.19)$$

where the single-particle initial (ψ_i) and final (ψ_f) state are treated as the Dyson orbital for cation [Eq. (2.3)] and the wave function of the photoelectron, respectively.

Finally, Eq. (2.13) is rewritten as:

$$I(\mathbf{k}, E_{\text{kin}}) \propto |\langle \psi_f | \mathbf{A} \cdot \mathbf{p} | \psi_i \rangle|^2 \delta(E_b + \Phi + E_{\text{kin}} - h\nu), \quad (2.20)$$

where Eq. (2.5) is included to reformulate the delta function. In this way, the photoemission intensity is described with one-electron matrix elements in a simplified picture. As we are not interested in strongly correlated systems or the line shape in spectra where less approximations above are valid [76], for the molecules dominated by dynamical rather than static correlation the initial state—Dyson orbital—is closely related to e.g. Kohn–Sham orbitals [57]. Detailed discussions about computing Dyson orbitals can be found in Refs. [22, 81]. In this thesis, the Kohn–Sham orbitals calculated from DFT are sufficient to describe the initial states. Our main concerns lie with the intensity distribution of photoemission and the only question left is the description of the final state, see the next section.

2.3.2 Plane Wave Final State Approximation

The simplest model to describe the final state of a photoelectron in Eq. (2.20) is the plane wave, proposed by Gadzuk [50–52]: $\psi_f \propto e^{i\mathbf{k} \cdot \mathbf{r}}$, which is characterized by its momentum \mathbf{k} and the direction \mathbf{r} in which the photoelectron leaves the sample.

Using $\mathbf{p} = -i\hbar\nabla$ and exploiting the Hermitian character of ∇ , Eq. (2.20) can be rewritten as follows [22, 82]:

$$\begin{aligned} I(\mathbf{k}, E_{\text{kin}}) &\propto |\langle \psi_f | \mathbf{A} \cdot \mathbf{p} | \psi_i \rangle|^2 = \left| - \int \psi_i^*(\mathbf{r}) \mathbf{A} \cdot i\hbar\nabla e^{i\mathbf{k}\cdot\mathbf{r}} d^3r \right|^2 \\ &= \hbar^2 |\mathbf{A} \cdot \mathbf{k}|^2 \left| \int \psi_i^*(\mathbf{r}) e^{i\mathbf{k}\cdot\mathbf{r}} d^3r \right|^2 \\ &= \hbar^2 |\mathbf{A} \cdot \mathbf{k}|^2 \left| \int \psi_i(\mathbf{r}) e^{-i\mathbf{k}\cdot\mathbf{r}} d^3r \right|^2. \end{aligned} \quad (2.21)$$

Notice that the integral above is the Fourier transform (FT) of $\psi_i(\mathbf{r})$ —the initial state wave function in reciprocal space: $\tilde{\psi}_i(\mathbf{k})$. Therefore we get:

$$I(\mathbf{k}, E_{\text{kin}}) \propto |\mathbf{A} \cdot \mathbf{k}|^2 |\tilde{\psi}_i(\mathbf{k})|^2. \quad (2.22)$$

Equation (2.22) has a simple, easy-to-calculate form that the angle-resolved photoemission intensity is proportional to the square of the product of the FT of the initial state wave function and the factor $\mathbf{A} \cdot \mathbf{k}$.

This relationship is of great advantage as shown in Fig. 2.5: applying FT on an orbital $\psi_i(\mathbf{r})$ of interest, one could directly compare the measured photoelectron distribution (*momentum map*, or called *k-map*) with the intersection of its FT, $\tilde{\psi}_i(\mathbf{k})$, and a hemisphere of radius $k = \sqrt{2m_e E_{\text{kin}}}/\hbar$ (Ewald sphere construction) [7]. Due to the fact that molecular orbitals could be sliced in the momentum space for a chosen kinetic energy E_{kin} , this experimental technique is referred to as “photoemission tomography”.

There are two things to bear in mind while applying photoemission tomography using Eq. (2.22): (1) the plane wave final state approximation is used and (2) there is an additional factor $\mathbf{A} \cdot \mathbf{k}$ related to the experimental geometry.

2.3.2.1 Relation to IAC approximation

The preceding argument (1) has been noted by several authors that the plane wave final state approximation may fail to describe the observed photoemission intensity of some clean or adsorbate-covered surfaces or only reveals qualitative similarities [83–86]. This has led to the development of the independent-atomic-center (IAC) approximation [87, 88], where the initial state is decomposed into atomic eigenfunctions which build up the initial molecular orbitals. For the final state the spherical wave approximation is used and single or multiple intramolecular scattering can be included in this model. Ueno and his colleagues at Chiba University were one of the pioneers to employ the IAC model for quantitative studies of the electronic structure of conjugated molecules [89–95].

2 Introduction to Photoemission Tomography

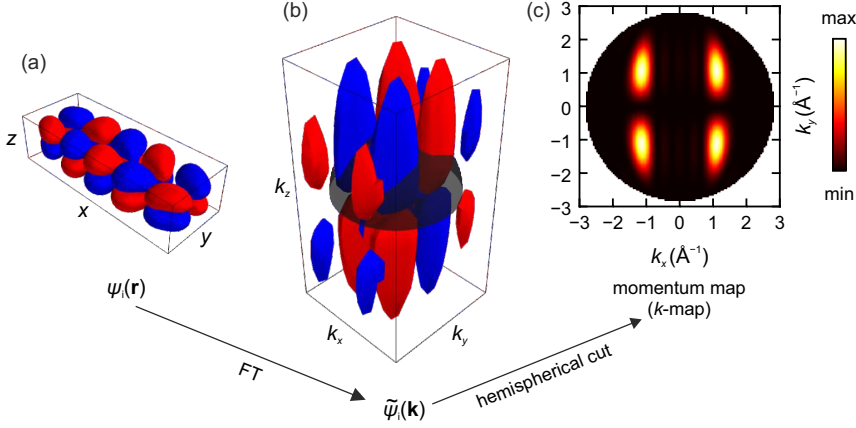


Figure 2.5: Relationship between the molecular orbital in real space $\psi_i(\mathbf{r})$ and reciprocal space $\tilde{\psi}_i(\mathbf{k})$ and the measured momentum maps (k -maps). (a) Calculated HOMO of isolated 5A (cf. Fig. 2.1). x and y coordinates are parallel to the long and short molecular axis, respectively, and z is perpendicular to the molecular plane. (b) FT of 5A HOMO. A hemisphere with radius $k = \sqrt{2m_e E_{\text{kin}}}/\hbar$ ($E_{\text{kin}} = 30 \text{ eV}$) is shown in gray. (c) Absolute value of the HOMO FT on the hemisphere. Calculations with the help of Ref. [63] and MOZI (Appendix A).

The more complicated mathematical form of the IAC model can be considerably simplified, if the initial molecular orbital is composed of atomic orbitals of the same character, say, the π orbital of a planar aromatic molecule built by the same p_z orbitals of carbon atoms. In this case the photoemission amplitude at the detector is reduced to [7, 87, 96]:

$$\alpha(\mathbf{R}, E_{\text{kin}}) = \frac{N_{p_z}(\hat{R}, E_{\text{kin}})}{\tilde{\phi}_{p_z}(\mathbf{k})} \tilde{\psi}_i(\mathbf{k}), \quad (2.23)$$

where \mathbf{R} is the position on the detector, $\hat{R} = \mathbf{k}/k$ is the unit vector in the direction of momentum \mathbf{k} , N_{p_z} is the “atomic factor” as a function of \hat{R} and kinetic energy E_{kin} , $\tilde{\phi}_{p_z}$ and $\tilde{\psi}_i$ are the FT of the p_z orbital and of the initial molecular orbital, respectively.

The similarity of Eqs. (2.22) and (2.23) is noteworthy. In fact, as Goldberg et al. [97] and Scheffler et al. [98] have pointed out, the factor $N_{p_z}/\tilde{\phi}_{p_z}$ in Eq. (2.23) can be shown to become independent of the emission direction (θ, ϕ) when the \mathbf{A} vector is parallel to the direction of the photoelectron, $\mathbf{A} \parallel \mathbf{k}$. For this special geometry, the photoemission intensity resulting from the IAC approximation reduces exactly

to the intensity given by the plane wave final state approximation. Moreover, the factor $N_{p_z}/\widehat{\phi}_{p_z}$ essentially has an overall weak angular dependence on emission direction [87, 96, 99]. Despite critically viewed by some (cf. the review article by Bradshaw and Woodruff [100]), it will be shown in Section 2.3.3 that in many systems the plane wave final state approximation suffices under the following conditions, summarized by Puschnig et al. [96]:

- π orbital emissions from large planar molecules.
- An experimental geometry in which the angle between the polarization vector \mathbf{A} and the direction of the emitted electron \mathbf{k} is small.
- Molecules consisting of many light atoms (H, C, N, O) and final state scattering effects are negligible.

But even these are not particularly stringent and as yet all reported examples of IAC and plane wave approximation results are practically the same.

2.3.2.2 Geometry factor

The idea of relating angle-resolved photoemission intensity with the FT of the initial state wave function is very appealing, but additional factors should be taken into consideration. First, the experimental geometry factor $|\mathbf{A} \cdot \mathbf{k}|^2$ has a major impact on the photoelectron distribution. Second, this factor is deduced from a plane wave of fully free electrons and a less oversimplified (although still simple) model has been equivalently introduced by Moser [101] and Lüftner et al. [48] that changes $|\mathbf{A} \cdot \mathbf{k}|^2$ to $|\mathbf{A} \cdot (i\mathbf{k} - \mathbf{e}_\perp/\lambda)|^2$: an evanescent plane wave described with the inelastic mean free path λ [cf. Eq. (2.12)] to incorporate the damping inside the solid (\mathbf{e}_\perp : unit vector for surface normal). More specifically, the final state can be written as [48]:

$$|\psi_f\rangle = \begin{cases} e^{i\mathbf{k} \cdot \mathbf{r}} e^{(z-z_0)/\lambda}, & \text{if } z < z_0 \\ e^{i\mathbf{k} \cdot \mathbf{r}}, & \text{if } z \geq z_0 \end{cases} \quad (2.24)$$

where along the z direction, i.e. the surface normal, the plane wave is exponentially damped inside the substrate ($z < z_0$), while the region above the substrate is treated by a pure plane wave.

Figure 2.6 shows the standard ARPES geometry for a p-polarized light incident in the y - z plane. The polarization vector \mathbf{A} can be written as:

$$\mathbf{A} = e^{i\eta} \begin{pmatrix} \cos \xi \\ e^{i\delta} \cos \alpha \sin \xi \\ e^{i\delta} \sin \alpha \sin \xi \end{pmatrix}, \quad (2.25)$$

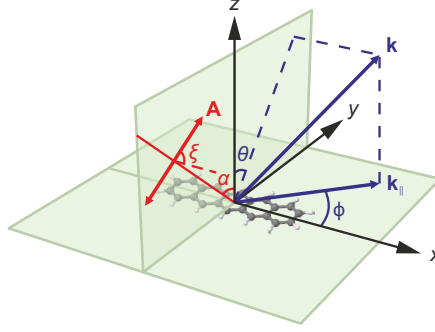


Figure 2.6: \mathbf{A} and \mathbf{k} in ARPES geometry with y - z as the incidence plane. Polarization vector \mathbf{A} and photoelectrons' momentum vector \mathbf{k} are marked in red and blue, respectively. α : angle of incidence. ξ : ratio between the principle components of \mathbf{A} ($\xi = \pi/2$ for p-polarized light as illustrated here). θ (ϕ): polar (azimuth) angle of the photoelectrons. \mathbf{k}_{\parallel} : in-plane component of the momentum vector \mathbf{k} .

where $e^{i\eta}$ is the phase term which will be canceled out through the modulus square, ξ and δ are the ratio and the relative phase between the principle components of \mathbf{A} , α is the angle of incidence. With the help of Stokes parameters (S_0 , S_1 , S_2 , and S_3 , see compilation in Table 2.1) one can rewrite the geometry factor [101]:

$$\begin{aligned} \left| \mathbf{A} \cdot \left(i\mathbf{k} - \frac{\mathbf{e}_{\perp}}{\lambda} \right) \right|^2 &= \frac{S_0}{2} \left(k_x^2 + k'^2 + \frac{\sin^2 \alpha}{\lambda^2} \right) + \frac{S_1}{2} \left(k_x^2 - k'^2 - \frac{\sin^2 \alpha}{\lambda^2} \right) \\ &+ S_2 k_x k' - S_3 k_x \frac{\sin \alpha}{\lambda}, \end{aligned} \quad (2.26)$$

where $k' = k_y \cos \alpha + k_z \sin \alpha$.

How does the geometry factor influence the photoelectron distribution? Using the geometry shown in Fig. 2.6, Fig. 2.7(a) depicts the calculated geometry factors according to Eq. (2.26) within a photoemission horizon of kinetic energy 30 eV and angle of incidence $\alpha = 65^\circ$. Appreciable difference is shown between different polarizations of the incident light:

- The geometry factor with p polarization (p pol.) is overall larger than the geometry factor with other polarizations. The maximum point is actually corresponding to the geometry where $\mathbf{A} \parallel \mathbf{k}$ as noted in discussions about the IAC approximation in the last section.³

³To fulfill $\mathbf{A} \parallel \mathbf{k}$: $k_x = 0$ and $\theta = 90^\circ - \alpha$ [cf. Eq. (2.11)].

	p pol.	s pol.	c+ pol.	c- pol.
ξ	$\pi/2$	0	$\pi/4$	$\pi/4$
δ	0	0	$\pi/2$	$-\pi/2$
S_0	1	1	1	1
S_1	1	-1	0	0
S_2	0	0	0	0
S_3	0	0	1	-1

Table 2.1: Parameters of different polarizations: linear polarized (p and s) and circular polarized (c+: right-hand and c-: left-hand). ξ and δ are the ratio and the relative phase between the principle components of \mathbf{A} , respectively. $S_0, S_1, S_2,$ and S_3 are Stokes parameters.

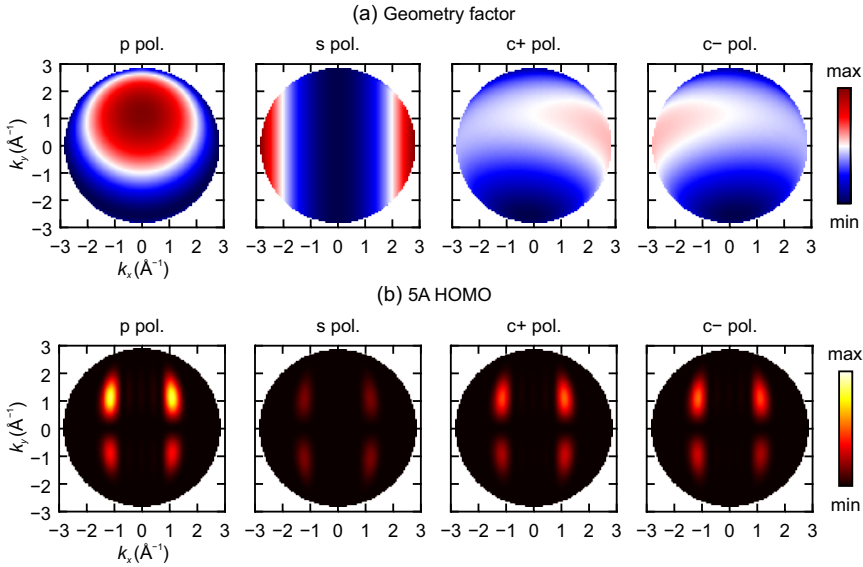


Figure 2.7: Geometry factor and its influence on the theoretical HOMO of 5A with different polarizations of the incident light. (a) Calculated distribution of geometry factor in the momentum space. (b) Product of the geometry factor and the squared FT of theoretical 5A gas-phase HOMO (cf. k -map in Fig. 2.5). $E_{\text{kin}} = 30\text{ eV}$, angle of incidence $\alpha = 65^\circ$ (cf. geometry in Fig. 2.6), inelastic mean free path λ is estimated as in Fig. 2.4. Calculations with the help of Ref. [63] and MOZI (Appendix A).

2 Introduction to Photoemission Tomography

- The geometry factor with s polarization (s pol.) has no dependence on k_y and its maximum is only on the edge, where $|k_x|$ is larger than 2.5\AA^{-1} . In most regions in the middle the intensity is highly suppressed.
- The geometry factors with circular polarizations (c+ and c- pol.) show in the most regions a medium level of intensity. Different from linear polarizations, there is an asymmetry in the k_x direction: c+ pol. has slightly increased intensities on the right $k_x > 0$ side and c- pol. on the left $k_x < 0$ side.⁴ Note that if no damping term related to λ is included in the calculation, this asymmetry cannot be observed [31], as Eq. (2.26) in the limit $\lambda \rightarrow \infty$ reveals.

As an example, the product of the geometry factor and the theoretical k -map of 5A HOMO (cf. Fig. 2.5) is displayed in Fig. 2.7(b), which is supposed to be comparable to the measured photoemission intensity in experiment. On the whole, each polarization is able to maintain the characteristics of the HOMO main lobes, but with varying intensity distributions: p pol. enhances the intensity at $k_y > 0$ (forward emission) while the intensity at $k_y < 0$ (backward emission) is lower. s pol. shows symmetrized intensity for forward and backward emissions and has the lowest intensity among the four polarizations. Although the difference between c+ and c- pol. is minimal, it has been attempted to derive the phase symmetry of molecular orbitals with the circular dichroism [20].

2.3.3 Applications of Photoemission Tomography

This section briefly reviews the various applications of photoemission tomography based on the plane wave final state approximation. Reviews by Puschnig and Ramsey [2], Puschnig et al. [96], Offenbacher et al. [27], and Woodruff [102] provide further insights into this topic.

2.3.3.1 Extraction of Molecular Orientations

The attractive idea of photoemission tomography [Eq. (2.22)] that directly relates the ARPES intensity to the initial state wave function (molecular orbital) has been introduced for a single molecule in Sections 2.3.1 and 2.3.2. In practice, it is easy to apply PT to a molecular monolayer (ML) system having all molecules in the same orientation. But what if the molecules in a ML have multiple azimuthal orientations?

⁴The right-hand/left-hand (c+/c-) circularly polarization is defined from the point of view of the source. The opposite handedness convention is also seen in the literature.

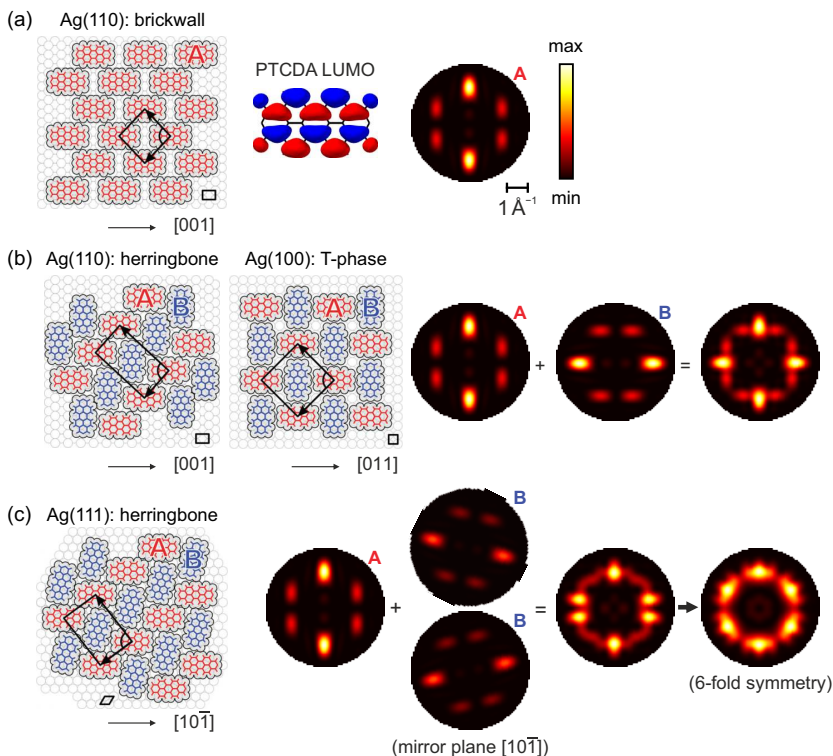


Figure 2.8: Structure models of PTCDA ML phases on low-index Ag surfaces and corresponding theoretical LUMO k -maps. (a) Brickwall phase on Ag(110), real-space distribution and k -map of PTCDA LUMO. (b) Herringbone phase on Ag(110) and T-phase on Ag(100), k -map constructed by two perpendicular orientations. (c) Herringbone phase on Ag(111), k -map constructed by considering a mirror plane and the sixfold surface symmetry. Images of structure models are adapted from Ref. [24]. Calculations with the help of Ref. [63] and MOZI (Appendix A).

Different phases of PTCDA ML on three low-index silver surfaces—Ag(100), Ag(110), and Ag(111) summarized by Willenbockel et al. [24] provide a good example, see Fig. 2.8. On Ag(110), the brickwall phase has only one molecular orientation. In this case, the theoretical LUMO k -map calculated from a single PTCDA molecule in gas phase (geometry factor not included) is sufficient to predict the expected momentum distribution from the ML. The second possibility for PTCDA

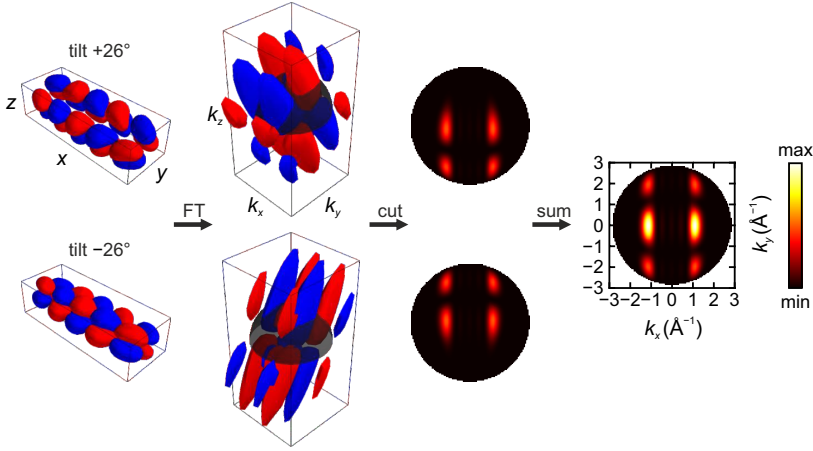


Figure 2.9: Theoretical HOMO k -map contributed by two 5A molecules with out-of-plane tilt angle $\pm 26^\circ$. For comparison see Fig. 2.5. Calculations with the help of Ref. [63] and MOZI (Appendix A).

on Ag(110) is a herringbone phase, which contains two inequivalent molecules [marked as A and B in Fig. 2.8(b)] in the unit cell whose azimuthal orientations are nearly perpendicular to each other, same as the T-phase on Ag(100). The k -map is nothing else than the sum of contributions from A and B. The herringbone phase of PTCDA on Ag(111) is more complicated as the surface has a sixfold symmetry and due to the combination of two molecules in the unit cell an additional mirror plane has to be considered [Fig. 2.8(c)]: the A-molecule is aligned along $[10\bar{1}]$ and the B-molecule is rotated by $\pm 77^\circ$ relative to A; the sum of these contributions has to be superimposed by the sixfold symmetry to produce the expected k -map.

Experimental ARPES results show good agreements with the calculated k -maps (cf. Fig. 2 of Ref. [24]), proving that PT as an area-averaging technique is useful if all orientation domains are properly considered. On the other hand, one could also infer the molecular orientations by comparing the measured k -maps with the theoretical ones based on the single molecule. The photoemission distribution from the corresponding clean substrate, e.g. the Fermi surface [103, 104], could serve as a good reference to determine the relative orientation between adsorbate and substrate.

The above discussion illustrates how PT determines the in-plane molecular orientation in a flat ML [12, 18, 21, 23, 33]. In fact, as already shown by Puschnig

et al. [7], PT can also be employed to obtain the molecular tilt angle with respect to the substrate: the crystalline 5A(022) films on the $p(2 \times 1)$ oxygen-reconstructed Cu(110) surface (cf. Fig. 5.4) have 5A molecules with their long axis parallel to the surface plane and the π face tilted out of plane by $\pm 26^\circ$. Taking this geometry into account, the hemispherical cut shown in Fig. 2.5 has to be applied to the FT of tilted molecular orbitals, see Fig. 2.9: The superposition of two contributions of tilt angles $\pm 26^\circ$ has two main and four minor lobes, losing the nodal plane along $k_y = 0$ for flat-lying 5A molecules.

In practice, one could compare the experimental results and a series of theoretical k -maps with varying tilt angle and find the minimum of the squared difference which corresponds to the geometry closest to experiments. Typically, the sensitivity of PT to tilt angle is within 5° [7] (see also Appendix C). PT has been successfully applied to molecular systems with out-of-plane orientations [17, 29, 30, 32, 37, 41]. For instance, Reinisch et al. [17, 30] reported that upon caesium doping the 6P LUMO k -map on Cu(110) could be explained by a one-to-one mix of $\pm 22^\circ$ and $\pm 75^\circ$ tilted molecules; Huempfer et al. [32] found via PT analysis that the picene ML on Ag(100) has a two-molecule unit cell, one is flat-lying and the other is tilted by 45° .

2.3.3.2 Identification of Spectral Features in UPS

As introduced in Section 2.2, UPS is well established and widely used in determining surface electronic structures. However, the interpretation of experimental UPS results can be difficult, particularly for adsorbates with strong interactions involving peak broadening, level splitting, or intermolecular dispersing bands [23]. Commonly, DOS from *ab initio* electronic structure calculations are cited to interpret UPS data. This could be problematic, as approximations for the exchange-correlation effects can strongly influence the prediction of adsorption geometries and the electronic structure of interfaces [10]. PT, being capable of mapping the angular distribution of the wave function for each UPS peak, is an ideal technique to unambiguously identify the energy levels of molecular orbitals.

This advantage is nicely exemplified in the case of 5A ML adsorbed on Cu(110) surfaces [105]. Yamane et al. [106] concluded that the photoemission results suggest a strong hybridization between 5A and the substrate. UPS results and DFT calculations by Ferretti et al. [107] also pointed at a chemisorptive picture. However, Müller et al. [108] later reported only partial LUMO occupation by comparing the ARPES experimental results with projected density of states (pDOS) calculations [Fig. 2.10(a)]. This erroneous assignment of energy levels was corrected by Ules et al. [23] where the PT study provides a *momentum-space view* at each binding energy position: two kinds of treatment for exchange correlation effects [Perdew–Burke–Ernzerhof (PBE) functional of generalized gradient

approximation (GGA) and Heyd–Scuseria–Ernzerhof (HSE) hybrid functional], see Fig. 2.10(b), give completely different HOMO positions. The HOMO feature is considerably shifted to larger binding energies in HSE, while the LUMO position just below the Fermi level is hardly changed. Note that the GGA results in Fig. 2.10(a,b) are qualitatively identical. Relying on the pDOS calculation mistakenly leads to assigning the peak at 0.9 eV to be HOMO instead of LUMO [107]. The momentum maps in Fig. 2.10(c) provide an intuitive view at two binding energies. Not only the one-to-one correspondence between theoretical and experimental k -maps makes the level assignment clear, the additional information of momentum space distribution enables an easier interpretation of the azimuthal dependence of photoemission intensity: when measured along the $[1\bar{1}0]$ direction the intensity is mainly contributed by the main lobe of LUMO; the HOMO is instead captured when measured at 45° away from $[1\bar{1}0]$.

As a powerful tool to convincingly make orbital assignments, PT has been successfully applied to many molecular ML systems, such as 5A [27, 29, 34, 36, 44, 45], 6P [17, 27, 30, 34, 41], picene [32], PTCDA [8, 15, 24, 35, 48, 109], 1,4,5,8-naphthalene tetracarboxylic dianhydride (NTCDA) [16, 42], coronene [13, 49], metal phthalocyanine (Pc) [18, 21, 33, 38], metal tetraphenylporphyrin (TPP) [37], to name a few examples. On the other hand, the understanding of heteromolecular films (ML comprising two or more types of molecules) [19, 26, 28, 39] and bilayer systems [12, 40] have also benefited from a PT analysis.

2.3.3.3 Deconvolution of Individual Orbital Contributions

Following the discussion about UPS spectra in Fig. 2.10, it is concluded that PT enables a more reliable peak assignment than binding energy arguments based on calculated pDOS. In cases where the difference of orbital energies is even smaller than the experimental energy resolution (typically 100–150 meV) and more than one orbital contributes under one spectral peak, PT can be applied following a deconvolution procedure in k -space [10]:

$$r^2 = \int \left[I(E, k_x, k_y) - \sum_i a_i(E) |\tilde{\psi}_i(k_x, k_y)|^2 \right]^2 dk_x dk_y, \quad (2.27)$$

where the sum of least squares r^2 of the experimental data $I(E, k_x, k_y)$ and several theoretical k -maps $|\tilde{\psi}_i(k_x, k_y)|^2$ is minimized in the integration over k_x and k_y . The resulting fit coefficients $a_i(E)$ thus reflect the energy-resolved DOS projected onto each molecular orbital i .

This deconvolution procedure was applied first on the PTCDA brickwall phase on Ag(110) [Fig. 2.8(a)]. Three molecular features, denoted as M1, M2, and M3, were found in the measured bandmap (cf. Fig. 3.5) at binding energies of 0.8, 1.9,

2.3 Photoemission Tomography

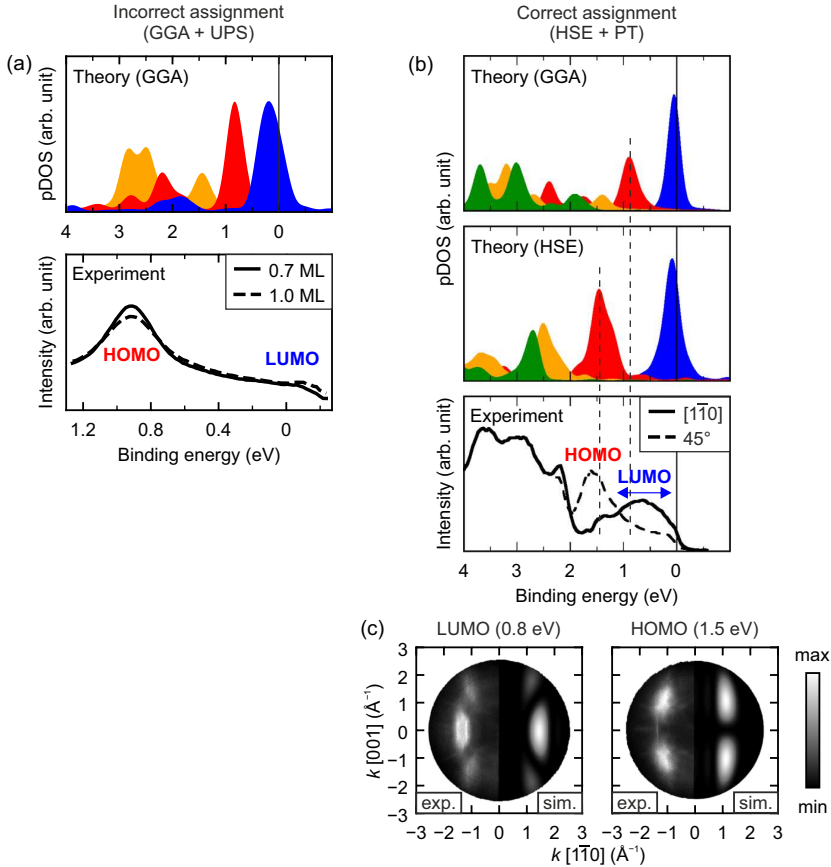


Figure 2.10: 5A ML on Cu(110). (a) DFT calculation of pDOS for 5A on Cu(110) using the PBE-GGA functional; photoemission spectra as a function of the 5A coverage (integrated in an azimuthal section between $[1\bar{1}0]$ and $[1\bar{1}0] + 20^\circ$). Adapted from Müller et al. [108]. (b) DFT calculation of pDOS for 5A on Cu(110) using the PBE-GGA functional and HSE hybrid functional; photoemission spectra of the 5A ML along $[1\bar{1}0]$ and $[1\bar{1}0] + 45^\circ$. Dotted vertical lines are for comparing different HOMO positions predicted by PBE-GGA and HSE. (c) Experimental k -maps at two binding energies compared to theoretical LUMO/HOMO. (b) and (c) are adapted from Ules et al. [23].

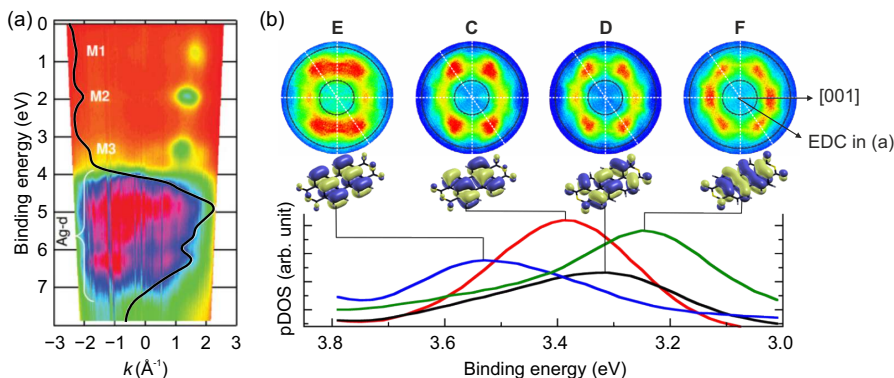


Figure 2.11: PT deconvolution procedure for the PTCDA/Ag(110) brickwall phase. (a) Experimental bandmap along the emission plane at 32° away from the [001] azimuth. Black line shows the k -integrated energy distribution curve (EDC). Adapted from Ref. [10]. (b) pDOS for orbitals C, D, E, and F deconvoluted by PT. Measured k -maps and corresponding calculated orbitals are marked at the peak of each pDOS spectrum. Adapted from Ref. [35].

and 3.4 eV between the silver d-band and the Fermi level [10], see Fig. 2.11(a). The k -maps measured at M1 and M2 were determined by PT analysis to be the filled LUMO (due to charge transfer [110]) and HOMO, respectively. For the M3 feature, however, there are four possible candidates—orbitals C, D, E, and F with increasing binding energies from free molecules’ GGA and GW approximation (GWA) calculations—in a small binding energy range of ~ 500 meV. Solving the linear fit problem in Eq. (2.27), the DOS spectra projected onto C–F could be plotted as shown in Fig. 2.11(b). Surprisingly, upon molecular adsorption the energetic order of E_b is completely altered: $E > C > D > F$, the orbital F turns out to have the highest E_b in calculation but the lowest E_b in experiment.

For PTCDA ML on different low-index silver surfaces—Ag(100), Ag(110), and Ag(111), it was found by PT deconvolution that the E_b order of the orbitals is the same. It is well-known that the energetic ordering of Kohn–Sham orbitals of organic molecules must be taken with care [111]. In many cases, an optimal choice for exchange-correlation has been shown to improve the orbital order [112]. However, in the present case of the four orbitals C–F it turns out that all state-of-the-art approaches for compensating the underestimated correlation energy all failed in predicting the correct ordering [35], presumably due to the deficiency in the correlation functional to account for static correlations [113]. This highlights the importance of PT as a complementary method to utilize information embedded

in the k -space distribution and as a benchmark for *ab initio* electronic structure calculations.

Significantly, the deconvolution in PT has shown the capability to resolve site-specific electronic structures. For instance, two inequivalent PTCDA molecules in the unit cell of the herringbone phase on Ag(110) exhibit only slight energy differences for the LUMO and HOMO, 90 meV and 40 meV, respectively [15]; likewise, for the herringbone phase on Ag(111) these values are 170 meV and 40 meV, respectively [11] (cf. structure models in Fig. 2.8). Photoemission results on complicated heteromolecular structures, such as PTCDA–CuPc, NTCDA–CuPc [28], and PTCDA–SnPc [39], can also be deconvoluted by PT to determine the energy ordering for each relevant molecule.

2.3.3.4 Real-Space Orbital Reconstruction

The success of applying Eq. (2.22) to interpret the experimental k -maps by the FT of initial-state wave functions tempts the next challenge—reconstructing molecular orbitals in real space from purely experimental photoemission data by performing an inverse FT. The first issue to address is the “phase problem”: the detectable quantity in experiment, the photoemission intensity distribution $I(\mathbf{k}, E_{\text{kin}})$, loses inherently the phase information of the wave function $\psi_i(\mathbf{k})$.

In simple systems, one may infer the phase distribution from the parity of the wave function. For example, the 6P HOMO (LUMO) investigated by Puschnig et al. [7] is odd (even) along the molecule’s long axis. By adding different or same signs according to the symmetry, one could make a rough phase estimation and subsequently perform the inverse FT to obtain (a slice of) real-space orbitals. Wießner et al. [20] claim that dichroism photoemission measurements on the model system PTCDA/Ag(110) can reveal the phase information. This is, however, also assisted by DFT calculations when making the symmetry arguments.

More generally, there are two kinds of phase retrieval procedure without any symmetry consideration. The first was performed by Lüftner et al. [43] via a procedure similar to the Gerchberg–Saxton algorithm [114] where FT is iteratively performed back and forth between reciprocal and real space. Starting from a random initial guess of the phase, the phase information could be reproducibly obtained when proper constraints, such as the wave function distribution limited within the molecule’s van der Waals (vdW) boundary, are applied in each iteration. The second procedure was proposed by Kliuiev et al. [44, 45] in analogy to treatments in coherent diffraction imaging where the shrinkwrap algorithm is employed and no *a priori* information about the molecule such as its size is required.

With the abundant toolbox available for analyzing PT data in 2D, further efforts have been made which measure photoemission data as a function of photon energy

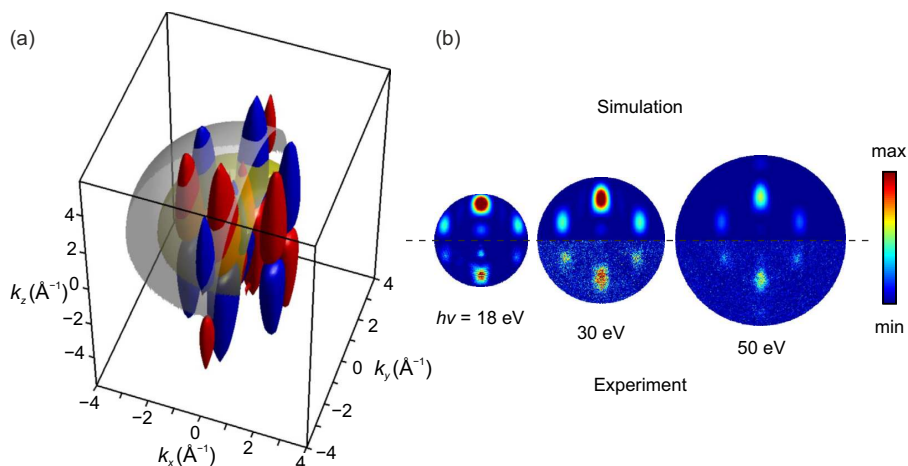


Figure 2.12: Measurement of the PTCDA LUMO as a function of photon energy. (a) PTCDA LUMO illustrated in momentum space with two hemispherical cuts corresponding to E_{kin} of 29.7 eV and 58.1 eV, respectively. (b) Simulated and measured k -maps of the PTCDA LUMO at various photon energies. Adapted from Ref. [46].

to reconstruct molecular orbitals in 3D [46, 47, 115]. It was first performed on the model system of a brickwall ML PTCDA on Ag(110), see Fig. 2.12. Compared to the illustration in Fig. 2.5 where only one single photon energy is used, multiple hemispherical cuts at various kinetic energies facilitate a full three-dimensional rendering of the molecular orbital in momentum space. After performing the inverse FT, the real-space orbitals are allowed to be reconstructed from purely experimental data. The main technical difficulty here is the precise photon flux measurement between different optical configurations in the synchrotron beamline for covering a broad photon energy range [116].

2.3.3.5 Intra- and Intermolecular Band Dispersion

Prior to applying the plane wave final state approximation on various molecular ML systems as introduced in previous sections, it was first successfully applied to thick multilayer molecular films [3–6]. The crystalline multilayer films formed by large π -conjugated molecules, such as pentacene (5A), p-sexiphenyl (6P), and sexithiophene (6T), can be grown up to micrometer size on an atomically controlled anisotropic substrate. This allows not only *ex situ* diffraction measurement to

determine the sample's structural information, but also allows both intra- and intermolecular band dispersion to be measured *in situ* with photoemission [2]. One-dimensional FT of the theoretical π orbitals of the isolated molecule gave a good description of measured ARPES spectra in terms of k -position, k -width, and relative intensities, see the following example of 5A(022) films on $p(2 \times 1)$ oxygen-reconstructed Cu(110) surface [4].

In 5A(022) films on the $p(2 \times 1)$ -O Cu(110) surface (cf. Fig. 5.4), as shown in Fig. 2.13(a), the 5A molecules have their long axis parallel to the close-packed Cu–O [001] direction (x -direction). The bandmap measured along x [Fig. 2.13(c)] shows two molecular π bands, containing five (upper) and six (lower) orbitals, respectively. All molecular orbitals are symmetric around the Γ point and their energy and momentum are in agreement with calculations for an isolated 5A molecule, see maximum positions in the FT of calculated orbitals indicated by a symbol (\times for the upper band and $+$ for the lower band). The two-band structure of the 5A π orbitals can be understood as follows: the isolated 5A molecule has 22 carbon atoms, 11 fully occupied p_z -derived orbitals give rise to five orbitals from the pairs of apex carbons and six from the linking and end carbon pairs [4], see Fig. 2.13(b). This is contrary to infinite systems such as a hypothetical infinitely long acene, whose intramolecular band would be continuous with infinite number of orbitals. The discrepancy between 5A films and the hypothetical system is also reflected at the Brillouin zone (BZ) boundary expected for an infinite polymer at π/a , with a being the inter-ring spacing. The highest orbital of upper band (HOMO) has its maximum evidently smaller than π/a . This can be seen in the wave function of HOMO shown in Fig. 2.13(b) where the maxima are not centered on the apex atom positions and their spacings are slightly larger than a , therefore the weight of the Fourier components moves inwards to Γ .

Perpendicular to the molecular axis (along y -direction), the measured bandmap [Fig. 2.13(d)] shows continuous intensity over the full range of momentum. In fact, periodic variations in energy are visible with turning points at π/b (b is the lateral spacing) corresponding to the BZ boundary of the 5A crystal along y , see the weak HOMO dispersion and the band dispersion in the energy region around $E_b \sim 5$ eV. The observed bands reflecting the crystal periodicity along y suggest an intermolecular band dispersion, while the two discontinuous π bands along x as discussed above demonstrate an intramolecular band dispersion.

In the ML regime, intermolecular band dispersion in monolayers has also been observed. Wießner et al. calculated LUMO and HOMO dispersion for molecular ML (PTCDA [14] and NTCDA [16]) adsorbed on metal. They found that the bandwidths are of the same magnitude (~ 200 meV) compared to that of corresponding freestanding ML, suggesting a minor enhancement of the intermolecular dispersion by the substrate. For systems with stronger molecule–substrate interactions,

2 Introduction to Photoemission Tomography

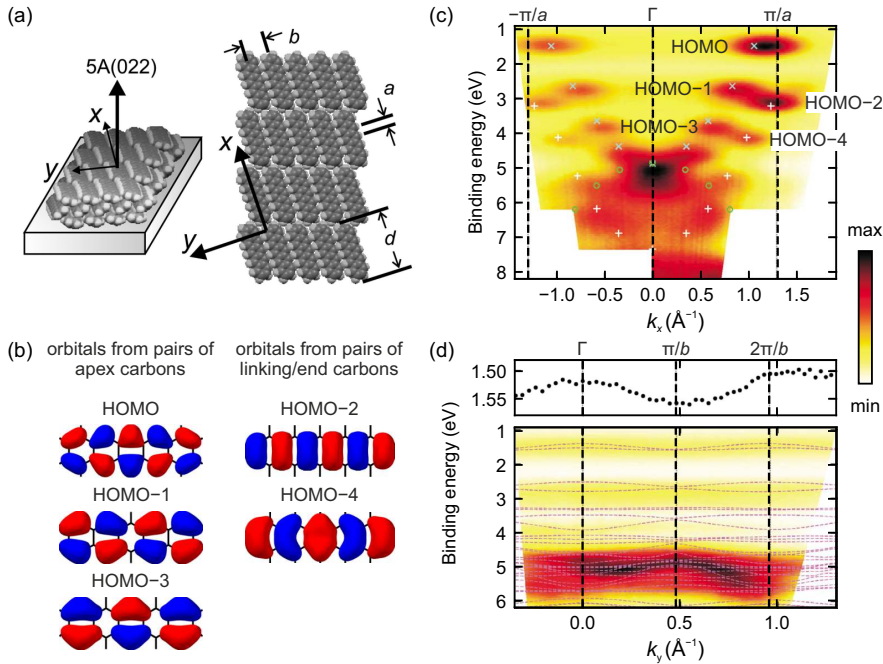


Figure 2.13: 5A(022) films on $p(2 \times 1)$ oxygen-reconstructed Cu(110) surface. (a) Stacking model (left) and top view (right) of multilayer 5A film with (022) orientation. Inter-ring spacing $a = 2.35 \text{ \AA}$, lateral spacing $b = 6.41 \text{ \AA}$, and inter-plane spacing $d = 14.77 \text{ \AA}$ are indicated. (b) Calculated molecular orbitals of gas-phase pentacene. (c) Photoemission bandmap measured within the emission plane along x -direction (molecular axis). The two π bands are marked with \times (upper) and $+$ (lower). The σ band is marked with \circ . (d) Photoemission bandmap measured within the emission plane along y -direction (perpendicular to molecular axis). Calculated band structure for bulk 5A is overlaid as dashed lines. The inset on the top shows the center of a Gaussian peak fit of the HOMO emissions. Adapted from Ref. [4].

a modification of the experimental k -map of molecules on substrate in comparison to the calculated one of an isolated molecule can indicate the substrate-induced intermolecular dispersion. For instance, see Fig. 2.10(c), within the LUMO major lobe the experimental k -map of 5A on Cu(110) [23] shows a weak splitting of the emission along $k_{[1\bar{1}0]}$, seen as double vertical stripes along $k_{[001]}$. The distance between these two stripes corresponds to the BZ of the 5A overlayer along the [001]

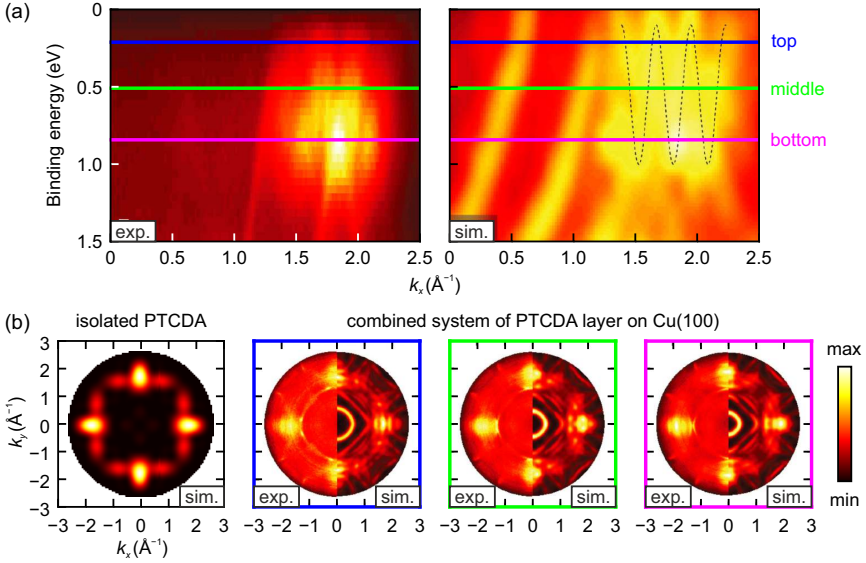


Figure 2.14: PTCDA ML on Cu(100). (a) Experimental and simulated bandmap. Dotted line guides the eye for the band dispersion. Horizontal blue/green/magenta lines indicate the energy where the corresponding k -maps in (b) are measured. (b) Simulated k -map for LUMO of isolated PTCDA and comparisons between experimental (left halves) and simulated (right halves) k -maps at the binding energies as marked in (a). Adapted from Ref. [48].

direction.

The 5A/Cu(110) example above has an incommensurate overlayer structure, therefore the whole molecule–substrate system could not be calculated and only a freestanding 5A layer with the corresponding unit cell was modeled instead (cf. Fig. 5 of Ref. [23]). Better quantitative studies [48, 49] have included the substrate in simulation for commensurate molecular ML by introducing a damped plane wave final state [cf. Eq. (2.24)]. In Fig. 2.14(a), the bandmap of PTCDA on Cu(100) [48] displays a strongly oscillating (magnitude of 1.1 eV), dispersive substructure within the LUMO region. Over the whole range of dispersion the LUMO pattern in k -maps can be clearly recognized and well reproduced by simulation [Fig. 2.14(b)].

2.3.4 Recent Progress

Section 2.3.2 discussed the conditions for validity of the plane wave final state approximation, especially “large planar (lying-down) molecules containing low-atomic number elements” seems to be a general requirement for PT [100]. But what size is large enough and what if the studied molecules are not planar? There have been recently some case studies in this regard:

Egger et al. [117] investigated a small and strongly interacting system: benzene adsorbed on Pd(110). Compared to larger molecules, benzene has two different characteristics: (1) lack of quasi-periodicity in its orbital structure and (2) commensurability of all carbon atoms in the systems to the substrate. The first will cause the k -map to be less distinct and the second may result in stronger scattering effects. The PT results revealed two π states (binding energies larger than Pd d-band) with a small energy-splitting of 0.3 eV, which was not previously observed. The DFT calculation showed that this is due to the lifting of degeneracy of the top-most π state. The corresponding k -maps of benzene/Pd(110), although not as clear as in PT studies for larger molecules, were able to identify these two states [117]. The small molecular size and the reasonably strong molecule–metal interaction have increased the deviations between measured and simulated k -maps, but PT remains applicable for a wide range of molecule–metal systems.

The classic football-like C_{60} fullerene was used for testing whether PT is applicable to non-planar molecules [118, 119]. Metzger et al. [118] prepared a ML of C_{60} with one unique azimuthal orientation on Ag(110) and achieved a good agreement between the measured two-fold symmetric k -maps and the simulation. Between two simulation methods—plane-wave and IAC (Section 2.3.2.1) based, they found only small differences in the relative intensities. Haag et al. [119] studied a thicker film (5 ML) of C_{60} on Ag(111), which shows an atomic crystal-like band structure with delocalized π -like valence states and strongly localized σ states at larger binding energies. The k -maps measured at both states can be well described by PT simulations considering a plane-wave final state. The major difference to planar molecules such as PTCDA is that the expected k -map of C_{60} illustrates a complex intensity distribution with strong photon-energy dependence (see Fig. S6 of Ref. [119]), i.e. the FT of C_{60} molecular orbitals does not appear as lobes perpendicular to the (k_x, k_y) plane as in the PTCDA/Ag(110) case, where the k -map pattern is nearly independent of the photon energy (cf. Fig. 2.12).

PT has also been employed to explore other diverse aspects in physics and chemistry, e.g. the electron–phonon coupling [120] and the aromaticity [121]. Graus et al. [120] identified three HOMO photoemission peaks for coronene ($C_{24}H_{12}$) on Au(111): one prominent peak at 1.55 eV, and two smaller peaks at 1.75 eV and 1.95 eV that correspond to vibronic excitations. By comparing the k -maps measured at these energies to simulated ones, the different k -map patterns were at-

tributed to a distortion of coronene molecules caused by one specific vibration that couples to the photoionization. Haags et al. [121] investigated the long-debated nature of the π bonding within kekulene ($C_{48}H_{24}$) by using PT for an ordered kekulene layer synthesized on Cu(111). Compared to previous experimental studies that discussed kekulene’s aromaticity on the basis of structural properties such as C–C bond lengths, PT can be used to directly access aromaticity through the spatial distribution of electronic states and exclude the proposed superaromaticity model.

2.3.5 Comparison with Other Methods

Many examples have manifested that PT, combined with theoretical calculations for the electronic structure and the plane wave final state approximation, is becoming a powerful tool to study both the surface electronic and geometric structure of molecules. The “observation” of orbitals with PT requires neither cryogenic temperatures nor controlled tip state as in scanning probe methods for atomic and orbital resolution. Instead, a large detectable k -space range is crucial for the applications of PT, which makes use of information in the *whole* k -space available at a given excitation energy to provide an unambiguous assignment of molecular orbitals. Typically, the π orbitals of planar organic molecules (like PTCDA, 5A, 6P and similar) have their major lobes appearing between $k_{\parallel} = 1 \text{ \AA}^{-1}$ and 2 \AA^{-1} . This means that the photon energy being used should not be too low (typically $> 15 \text{ eV}$), otherwise the major orbital lobes may appear beyond the photoemission horizon, see e.g. Fig. 2.12.

Taking the photoemission experiments on the LUMO and HOMO of PTCDA brickwall ML on Ag(110) as an example, the red line in the center of Fig. 2.15(a) illustrates the available k -range at photoemission along the surface normal with a standard hemispherical electron analyzer, e.g. with $\pm 15^\circ$ acceptance and He I α (21.2 eV) excitation. It is noteworthy that at this geometry the LUMO and HOMO are not distinguishable. Photoemission experiments provide an easy distinction between LUMO and HOMO only if the detection angle is away from the normal, say at around $(k_x, k_y) = (0 \text{ \AA}^{-1}, 1.5 \text{ \AA}^{-1})$, the two molecular orbitals can be clearly identified, observed as one and two lobes, respectively. To measure a full k -map with a conventional hemispherical electron analyzer, the sample has to be tilted and rotated, which means long measurement times and possible radiation damage. Therefore to date, the most convenient spectroscopic instruments to obtain k -maps for PT are the k -resolved photoemission electron microscope and the toroidal electron analyzer, the latter covering the largest k -range in momentum space (Fig. 2.15). These will be further discussed in Chapter 3.

Regarding the determination of surface geometric structure, PT also has its

2 Introduction to Photoemission Tomography

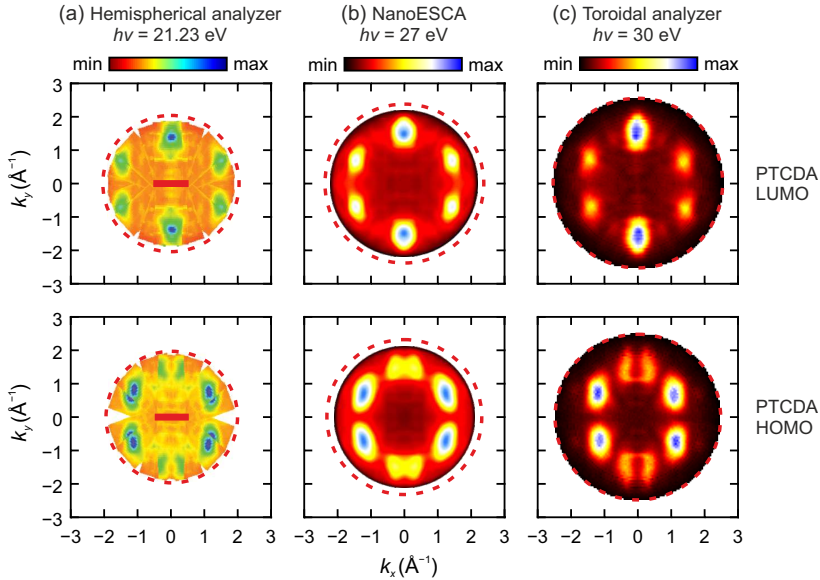


Figure 2.15: k -maps of PTCDA LUMO and HOMO measured with three kinds of experimental methods. (a) Hemispherical electron analyzer [8], (b) Photoemission electron microscope [20], and (c) Toroidal electron analyzer [10]. The photon energies used in each methods are labeled and the ideal accessible k -range are marked in red dashed circle. Work function $\Phi = 4.45\text{ eV}$ and binding energy $E_b = 0.8\text{ eV}$ (LUMO) and 1.9 eV (HOMO) are used for estimating the k -range using Eq. (2.11). The red line in (a) shows the detectable k -range at normal emission for $\pm 15^\circ$ acceptance angle of the analyzer (cf. Fig. 3.1).

advantages compared to other methods. If, as is sometimes the case, molecules are tilted with respect to the surface, the interpretation of scanning probe results is rather difficult. The common technique for determining molecular orientations is near edge X-ray absorption fine structure (NEXAFS) spectroscopy, which however can only yield an *average* tilt angle with an uncertainty of $\sim 10^\circ$. PT's approach, as introduced in Section 2.3.3.1, not only has a better precision ($< 5^\circ$) but can also treat the cases where multiple orientations exist, or even orientations involving different molecule species (cf. Section 2.3.3.3).

3 Instruments and Complementary Methods

This chapter covers three types of apparatus for applying the PT technique: hemispherical electron analyzer, photoemission electron microscope, and toroidal electron analyzer. In addition, the complementary experimental method of normal incidence X-ray standing waves (NIXSW) employed in this thesis and density functional theory (DFT), which is used for data interpretation, are briefly explained.

3.1 Hemispherical Electron Analyzer

The ARPES technique (Section 2.2) measures the energy and position of photoelectrons to determine experimentally the electronic band structure of crystals. Nowadays, the standard instrument for ARPES is the hemispherical electron analyzer with energy resolution down to < 5 meV and kinetic energy range up to 10 keV, see its schematic structure shown in Fig. 3.1. Upon the photon-induced excitation, electrons are collected into the focusing electrostatic lenses. For ARPES, the lens system is set to the angular multiplexing mode in which the emission angle distribution is imaged onto the entrance slit of the energy dispersion hemisphere. The lens system is set to match the kinetic energy of electrons to the so-called pass energy E_{pass} of the energy analyzer—the kinetic energy E_{kin} of the electron at the center of the detected energy window when it passes through the energy dispersing element consisting of two hemispheres (see dashed trajectories in Fig. 3.1) [122].

The electrons passing through the entrance slits follow trajectories that are bent in the 180° radial electrostatic field between two concentric hemispheres. Inside the analyzer, the electrons are dispersed depending on their E_{kin} ; the ones with higher E_{kin} have trajectory with larger radii. Finally, on the 2D detector, normally assembled by multichannel plates (MCP) and a phosphorous screen, the electron distribution as a function of angle and energy is captured with a camera located outside of the UHV chamber. The energy window simultaneously covered by the detector is normally around 8% of E_{pass} , with the resolution of a few meV [122, 123]. The angular window covered is limited by the acceptance angle of the en-

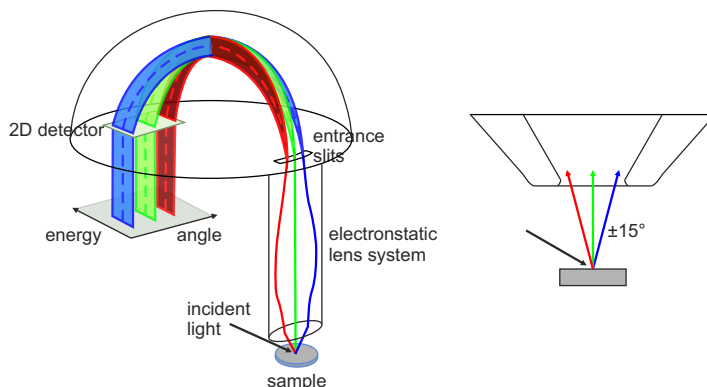


Figure 3.1: Hemispherical electron analyzer. Left: Schematic structure. The photoelectrons’ trajectories at three different polar angles are shown in red, green and blue. Dashed trajectories correspond to the electrons at the center of the detected energy window having the pass energy E_{pass} . Adapted from drawing by Ponor, CC BY-SA 4.0, via Wikimedia Commons. Right: $\pm 15^\circ$ acceptance angle of the entrance lens at normal emission geometry.

trance lens, with the resolution of a few tenths of degree.

The result of transforming from real space (polar angle of $\pm 15^\circ$) into momentum space (k_{\parallel}) is exemplified in Fig. 2.15(a). Of course, it is not always the normal emission that is measured and the sample is tilted (rotated) to access different areas in k -space radially (azimuthally). That is the reason why the measured k -map in this example resembles a sliced pizza [8]. PT measurements with hemispherical analyzer are time-consuming and the calibration of the k -scale can be inaccurate, the latter being visible in Fig. 2.15(a) where the major lobe of the PTCDA HOMO from different measurement series does not overlap very well. For this reason, hemispherical analyzers are not used for the PT studies in this thesis.

3.2 Photoemission Electron Microscopy

Photoemission electron microscopy (PEEM) images electrons emitted from a surface by photoexcitation either in real or reciprocal space. To obtain an easy understanding, a few foundational experimental methods need to be briefly introduced.

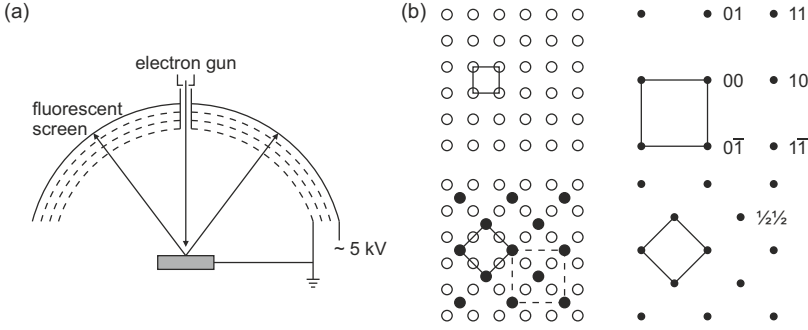


Figure 3.2: Working principle of LEED. (a) Schematic LEED optics. Electrons from the electron gun hit the sample and get scattered in straight line in the field-free region. Dashed lines stand for the grid screens responsible for blocking in-elastically scattered electrons and low energy electrons. Electrons passing through the filtering grids fall on the fluorescent screen for detection. (b) Examples of surface structure in real space (left) and reciprocal space (right). Top: (100) surface of an fcc crystal; bottom: the same surface with superstructure $(\sqrt{2} \times \sqrt{2})R45^\circ$. Solid rectangles represent the unit cell. The overlayer structure can alternatively be denoted as $c(2 \times 2)$ (dashed rectangle). Adapted from Ref. [102].

3.2.1 LEED

Low energy electron diffraction (LEED) is a conventional diffraction method to investigate the surface structure of single crystals. A typical schematic LEED optics is shown in Fig. 3.2(a): an electron beam of energy defined by the potential of the electron gun bombards the sample target; the low-energy (20–300 eV) electrons have corresponding wavelengths of 1–3 Å and mean free paths below 10 Å, hence being highly surface-sensitive. The incident and scattered wavevectors, \mathbf{k} and \mathbf{k}' , for a bulk material fulfill the Laue condition:

$$\mathbf{k}' = \mathbf{k} + \mathbf{G}_{hkl}, \quad (3.1)$$

where \mathbf{G}_{hkl} is a reciprocal lattice vector and (h, k, l) are Miller indices. For the diffraction from a surface (truncated bulk), this condition is reduced to:

$$\mathbf{k}'_{\parallel} = \mathbf{k}_{\parallel} + \mathbf{G}_{hk}. \quad (3.2)$$

Subsequently, crystal truncation rods of the surface cell are indexed as (hk) . The lattice of an adsorbed phase with a unit cell larger than the surface cell is called

a *superlattice*; the associated structure a *superstructure*, which is referenced according to (hk) . In this work, of interest are molecule monolayers on low-index metal fcc substrates, which often form adsorbate superstructures described using a matrix notation:

$$\begin{pmatrix} \mathbf{a}' \\ \mathbf{b}' \end{pmatrix} = M \begin{pmatrix} \mathbf{a} \\ \mathbf{b} \end{pmatrix} = \begin{pmatrix} M_{11} & M_{12} \\ M_{21} & M_{22} \end{pmatrix} \begin{pmatrix} \mathbf{a} \\ \mathbf{b} \end{pmatrix}, \quad (3.3)$$

where \mathbf{a} , \mathbf{b} and \mathbf{a}' , \mathbf{b}' are unit cell vectors of the substrate and overlayer, respectively. If these two meshes can establish a rational relationship via M , the structure of surface is called *commensurate*, otherwise *incommensurate*. In the example shown in Fig. 3.2(b) the superstructure matrix is $\begin{pmatrix} 1 & -1 \\ 1 & 1 \end{pmatrix}$. The equivalent representation using Wood's notation is $(\sqrt{2} \times \sqrt{2})R45^\circ$ which means $\|\mathbf{a}'\|/\|\mathbf{a}\| = \|\mathbf{b}'\|/\|\mathbf{b}\| = \sqrt{2}$ and both \mathbf{a}' and \mathbf{b}' are rotated by 45° with respect to \mathbf{a} and \mathbf{b} , respectively. Alternatively the notation can also be $c(2 \times 2)$ ("c" for "centered"). Similarly, an overlayer with lattice structure directly related to the substrate, $\mathbf{a}' = m\mathbf{a}$ and $\mathbf{b}' = n\mathbf{b}$, is denoted as $p(m \times n)$ ("p" for "primitive"). For complete nomenclature one may refer to standard textbooks, e.g. Woodruff [102], Ibach [124], Oura et al. [125].

3.2.2 LEEM/PEEM

Similar to conventional LEED, low energy electron microscopy (LEEM) also uses an electron gun as source, while achieving the lateral spatial resolution as low as 50 \AA (with aberration-correction down to $\sim 20 \text{ \AA}$) [102]. Because of the difficulty to build electron optics at typical LEED energies, the electron optics of LEEM operate at much higher energies (10–20 keV) and the primary electrons of this energy are at first retarded before reaching the surface and then again accelerated after being diffracted. This potential applied between the objective lens and the sample is called "extractor voltage". The key characteristic of LEEM optics, see Fig. 3.3(a), is the ability to either detect the real-space image or the diffraction pattern by varying the strength of the intermediate lens, the latter being μ LEED which is useful for surface domains study. The modern design of LEEM equipment is either Y- or T-shaped with a magnetic separator to split incident and scattered electrons.

Compared to LEEM, photoemission electron microscopy (PEEM) simply replaces the electron source with photons because the same optics is also capable of imaging electrons from photoemission. In fact, the commercially available LEEM is at the same time a PEEM when a lab light source is used or the equipment is installed at a synchrotron, so-called LEEM/PEEM system. With PEEM, one measures in diffraction mode the angular distribution of the photoelectrons, just

as what ARPES does. Because of being site-specific on the sample surface down to a few square micrometers (comparable to domain size of adsorbates), it is also referred to as μ ARPES [42].

3.2.3 NanoESCA

In this thesis (Chapters 6 and 7), another kind of PEEM, NanoESCA from Scienta Omicron, was employed at Elettra synchrotron, Trieste, Italy. NanoESCA is derived from traditional PEEM, and consists of two hemispherical electron analyzers [127, 128]. It allows the following three operation modes [129, 130], see numbered electron paths in Fig. 3.3(b):

1. Standard PEEM mode: real-space image from all photoelectrons which pass through the PEEM column (imaging mode) and get detected on a 2D detector.
2. Channeltron mode (spectroscopy mode): photoelectrons pass through the PEEM column (imaging mode) and are energy-filtered by the first hemispherical analyzer. These electrons are counted by the channeltron detector (electron multiplier) while the spatial information is neglected. Scanning the filtering energy one obtains an energy distribution spectrum of a selected, small region of interest (ROI) of size down to 6 μ m.
3. Energy-filtered PEEM mode: photoelectrons pass through the PEEM column (diffraction mode) and through two hemispherical analyzers, forming a k -space image on a 2D detector. The first hemispherical analyzer provides the energy filtering, while the second one compensates the aberrations of the first one, achieving good energy (< 200 meV) and lateral (< 100 nm) resolution [131].

For the PT applications in this work, the energy-filtered PEEM mode is used. Ramping the allowed kinetic energy of electrons through the analyzer, a three-dimensional data cube $I(E_{\text{kin}}, k_x, k_y)$ was recorded. To calibrate the k -scale, one utilizes the known parabolic relation between the photoemission horizon (maximal parallel momentum k_{\parallel}) and the kinetic energy E_{kin} with the help of Eq. (2.11): $k_{\parallel, \text{max}} [\text{\AA}^{-1}] \approx 0.51 \sqrt{E_{\text{kin}} [\text{eV}]} \sin 90^\circ = 0.51 \sqrt{E_{\text{kin}} [\text{eV}]}$: the settings of analyzer are swept such that the detected kinetic energy increasing from $E_{\text{kin}} = 0 \text{ eV}$. With rising kinetic energy, the photoemission horizon expands and its radius k_{\parallel} as a function of E_{kin} can be used to calibrate the k -space scale. The accuracy of such calibration can be cross-checked using the known structures in k -space, for instance imaging a Cu(111) sample at the Fermi level the distance $\overline{M}-\overline{M}$ is 2.84\AA^{-1} [132]. The field of view in k -space depends on the microscope settings. The pass energy

3 Instruments and Complementary Methods

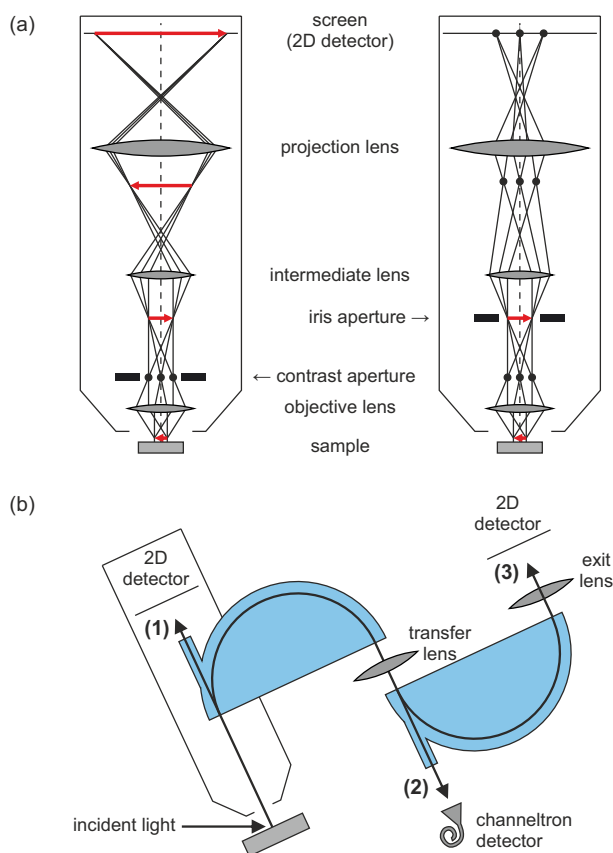


Figure 3.3: Photoemission electron microscope. (a) Schematic imaging optics of an electron microscope in imaging mode (left) and diffraction mode (right). (Intermediate) image plane and diffraction plane are indicated by red arrows and black dots, respectively. After Fig. 4.24 of Ref. [102]. (b) Schematic structure of NanoESCA: PEEM combined with two hemispherical electron analyzers (shown in light blue), incident angle 65° . Numbered arrows represent different operation modes, see text for details. Adapted from Ref. [126].

and extractor voltage used were 50 eV and 12 kV, respectively, resulting in an accessible k_{\parallel} range of around $\pm 2.0 \text{ \AA}^{-1}$. For a specific molecular orbital at a certain E_b , k -maps are repeatedly recorded at the corresponding E_{kin} to increase the signal-to-noise ratio, while the sample position is laterally scanned throughout

the measurement in order to avoid beam damage due to high-intensity photons at the synchrotron.

If the k -maps are measured in small kinetic energy steps for the $I(E_{\text{kin}}, k_x, k_y)$ data cube, it is possible to retrieve bandmaps, $I(E_{\text{kin}}, k_{\parallel})$, along a chosen direction out of the data cube $I(E_{\text{kin}}, k_x, k_y)$. An important step in this analysis process is to take the device energy dispersion into consideration, which is intrinsically introduced by the two hemispherical analyzers in series [Fig. 3.3(b)]. This energy dispersion results in a slightly “bent” Fermi edge along the k_y direction (the other perpendicular direction k_x remains intact). As mentioned above, with the NanoESCA PEEM, a k -map with high-resolution is obtained by averaging dozens of maps, $I(k_x, k_y)$, with the same analyzer settings, i.e. at the fixed E_{kin} . In this case, the minor (below 100 meV) instrument-intrinsic energy dispersion is always present such that at larger $|k_y|$ the E_{kin} of electrons is slightly overestimated. Therefore, there are two types of k -maps that can be presented:

1. The as-obtained ones that contain an inhomogeneous distribution of E_{kin} as described above, where the high k -space resolution is preferred.
2. The corrected ones of chosen E_{kin} that are extracted from the $I(E_{\text{kin}}, k_x, k_y)$ data cube using the numerical procedure described in Appendix B, where it is guaranteed that all points in the k -map correspond to the same E_{kin} .

For analyzing data measured with the NanoESCA, a Python-based program NESO was written during this thesis, see Appendix B.

3.3 Toroidal Electron Analyzer

PT results in this thesis (Chapters 4 and 5) were also obtained using the toroidal electron analyzer, a second version of angle-resolved photoemission spectrometer [123] designed and built by J. Riley and R. Leckey of La Trobe University, Australia. Now owned and operated by Peter Grünberg Institut (PGI-3), Forschungszentrum Jülich and stationed on the U125 insertion device beamline at the Metrology Light Source of Physikalisch-Technische Bundesanstalt (PTB), Berlin, Germany [116], the toroidal electron analyzer can measure photoemission data within an energy window whose width is $\sim 8\%$ of the pass energy simultaneously for polar angles in the range -90° to 90° .

The structure of the toroidal analyzer is shown in Fig. 3.4. The sample is located vertically on a five-axes (x , y , z , polar θ , and in-plane azimuthal rotation ϕ) manipulator on the symmetry axis of the analyzer. The input lens and the slit in front of the sample have a dual purpose: to re-focus electrons from the sample onto the entrance slit to the toroidal sector, where the electrons’ trajectory gets bent between the energy dispersive elements—“toroids”, see Fig. 3.4(a), and to reduce

3 Instruments and Complementary Methods

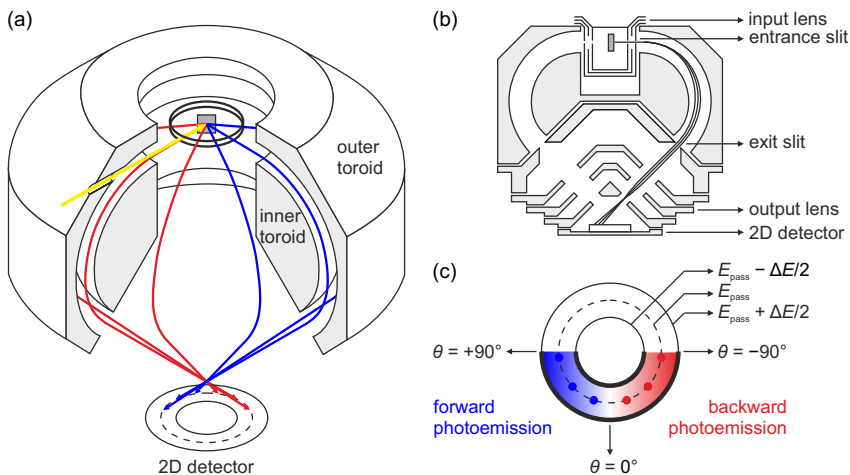


Figure 3.4: Toroidal electron analyzer. (a) Isometric section view of the analyzer structure. Incoming photons (yellow) incident on the sample (gray) excite electrons in forward (blue) and backward (red) emission, whose trajectories are bent between the inner and outer toroids and fall onto the 2D detector at the bottom. (b) Cross-section illustration of the analyzer structure. (c) Bottom view of the 2D detector where the detectable (kinetic energy E_{kin} , polar angle θ) range is shown between two thick black arcs. After Refs. [123, 133].

their energy to match the selected pass energy of the sector [123]. The electrons within the energy window $\Delta E \sim 8\% E_{\text{pass}}$ pass through the ring-shape exit slit and are accelerated toward a ring-like 2D detector (assembled by MCP and phosphorous screen, illumination from which is recorded by CCD camera), the radial and azimuthal position of arrival on the detector thus being a measure of the kinetic energy and emission angle, respectively, see Fig. 3.4(b,c). More specifically, in the snapshot of the camera image transferred to the acquisition computer, the user defines two circular arcs using the LabVIEW-based measurement software. The average radius of these two corresponds to electrons with the selected pass energy and the difference in kinetic energy of electrons on these two arcs is the energy window ΔE . The measurement software then performs digitization between the two arcs to get an intensity distribution as a function of kinetic energy and polar angle, $I(E_{\text{kin}}, \theta)$. This intensity distribution can also be measured while the sample is azimuthally rotated, obtaining a 3D data cube, $I(E_{\text{kin}}, \theta, \phi)$.

The most prominent advantage of the toroidal electron analyzer is that all polar angles, in the range -90° to 90° , can be measured at the same time without tilting

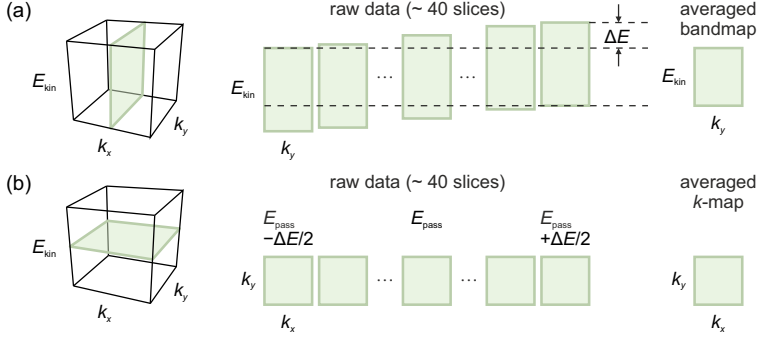


Figure 3.5: Two measurement modes of the toroidal electron analyzer. (a) Bandmap: the sample position is unchanged and the pass energy scanned, obtaining a raw data cube of $I(E_{\text{kin}}, k_{\parallel})$ where k_{\parallel} is the chosen azimuthal direction. The E_{kin} range of two neighboring data slices differ by $\Delta E/(\text{number of slices})$, ΔE being the energy window. (b) k -map: the sample is rotated and the pass energy fixed, obtaining a raw data cube of $I(k_x, k_y)$. The center data slice has E_{kin} corresponding to the pass energy. E_{kin} of two neighboring data slices differ by $\Delta E/(\text{number of slices})$.

the sample, thus saving plenty of time and preserving the incidence geometry. There are two kinds of measurements which can be performed with this analyzer: one is the *bandmap* where the sample's azimuthal angle is fixed but the kinetic energy is scanned, the other is the *k-map* where the kinetic energy is fixed and the measurement is performed for each azimuthal rotation step of the sample to create a projection of the measurement hemisphere (cf. Fig. 2.5). Essentially, these two modes correspond to different ways of slicing in the $I(E_{\text{kin}}, \theta, \phi)$ data cube or, after transforming into reciprocal space, the $I(E_{\text{kin}}, k_x, k_y)$ data cube, see Fig. 3.5. In practice, the final results are presented as an averaged bandmap or k -map and only those data slices of interest are taken into account. For the k -map mode, often it is unnecessary to rotate the sample full 360° if the expected momentum map has n -fold rotational symmetry ($n > 1$). The symmetrization of an incomplete k -map is performed in the data process to build the whole k -map.

In our experiments p-polarized ultraviolet light with angle of incidence $\sim 40^\circ$ was used. Compared to the k -map data taken with the same polarization on the NanoESCA introduced in the preceding section, the main difference is the incidence geometry effect ($|\mathbf{A} \cdot \mathbf{k}|^2$ factor, cf. Section 2.3.2.2). The NanoESCA collects photoelectrons emitted by the sample in all directions at the same time, therefore the intensity of the upper half (forward emission direction as in common practice)

3 Instruments and Complementary Methods

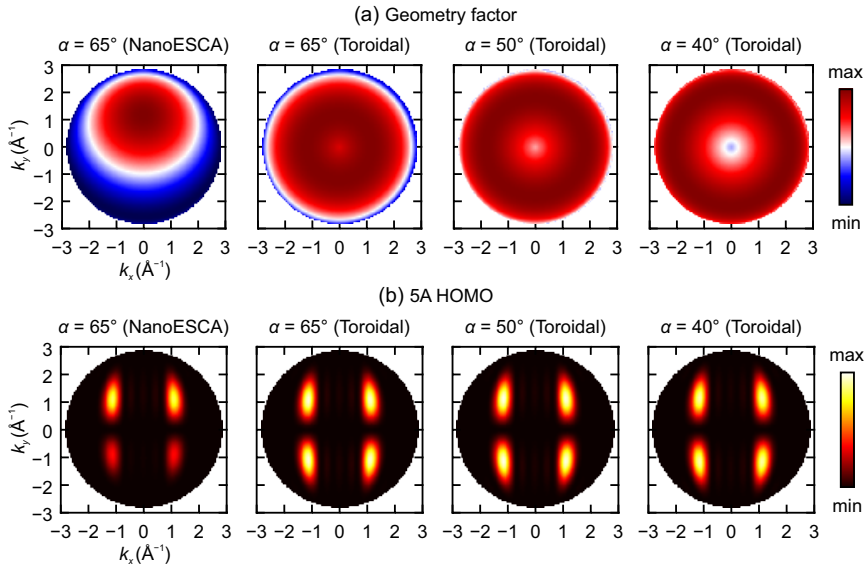


Figure 3.6: Comparison of NanoESCA and toroidal electron analyzer in terms of the geometry factor and its influence on the theoretical HOMO of 5A (p polarization). (a) Calculated geometry factor in momentum space (forward emission for toroidal electron analyzer). (b) Product of the geometry factor and the squared FT of theoretical 5A HOMO (cf. k -map in Fig. 2.5). $E_{\text{kin}} = 30$ eV, angle of incidence $\alpha = 65^\circ$ for NanoESCA and $\alpha = 65^\circ, 50^\circ,$ and 40° for toroidal electron analyzer. For comparison see also Fig. 2.7. Calculations with the help of Ref. [63] and MOZI (Appendix A).

of the k -map is always higher compared to the bottom half, see Fig. 3.6. With the toroidal electron analyzer, the k -map is measured with sample rotation because only photoelectrons emitted in the incidence plane can pass through the entrance slit. As a consequence, the geometry factor is always circularly symmetric, if measured with toroidal electron analyzer (Fig. 3.6). At each azimuthal orientation of sample (rotation step), electrons of all polar angles are detected, hence one can choose to use *either* the positive (forward emission) *or* negative polar half (backward emission) to create the k -map.⁵

This difference is shown in Fig. 3.6(a): different from the NanoESCA, the geometry factor for the toroidal electron analyzer is circularly symmetric. For an

⁵In this thesis, if not specified, forward emission is used to present k -maps while using the toroidal electron analyzer.

angle of incidence between 40° and 65° shown here, the expected photoemission distribution, i.e. the product of the geometry factor and the squared FT of theoretical molecular orbital are qualitatively identical, see Fig. 3.6(b). This is due to the fact that the major emissions from the frontier molecular π states of the molecules discussed in this work are found between $k_{\parallel} = 1 \text{ \AA}^{-1}$ and 2 \AA^{-1} where the geometry factor has a weak radial (polar angle) dependence, see e.g. the homogeneous plot in Fig. 3.6(a) for $\alpha = 50^\circ$. As a result, calculated k -maps of isolated molecules often suffice to be compared to the measured ones with the toroidal electron analyzer, without applying a geometric factor. As a side note, k -maps measured with p-polarized light on NanoESCA need to be symmetrized to reduce the geometry factor effect if only compared to the calculation of isolated molecules, unless the $|\mathbf{A} \cdot \mathbf{k}|^2$ factor is specifically taken into account in calculations [20, 44].

For analyzing data measured with the toroidal electron analyzer, a Python-based program MOZI was written during this thesis, see Appendix A.

3.4 Normal Incidence X-Ray Standing Waves

The normal incidence X-ray standing waves (NIXSW) technique was employed in Chapter 5 to study the geometric structural properties of surfaces. As a complementary experimental method, it measures the molecules' adsorption height with high accuracy (typically $< 0.05 \text{ \AA}$), which is directly related to the bonding strength between molecule and substrate. For detailed description of this technique, one may refer to Woodruff [102, 134], Zegenhagen and Kazimirov [135], and Bocquet et al. [80].

In NIXSW, X-rays hit the sample crystal at the three-dimensional Bragg conditions and the interference between the incident and reflected light results in a standing wave, whose periodicity is identical to the scatterer plane spacing as illustrated in Fig. 3.7(a). In the experiments performed at the beamline I09 of the Diamond Light Source, Didcot, UK [Fig. 3.7(b)], the incoming p-polarized light (1) is perpendicular to the optical axis of the Scienta EW4000 hemispherical analyzer (cf. Section 3.1); the sample is tilted by $\alpha = 3.5^\circ$ from the ideal normal incidence so that the reflected light reaches the fluorescent screen (2) for measuring the reflection intensity; the detection angle ϕ between the incident light and the emitted photoelectrons (3) is used to apply angle-dependent non-dipolar corrections [137, 138] in the data analysis. At such geometry, total reflectivity is observed in a finite range of photon energy around the Bragg energy E_{Bragg} ,

$$E_{\text{Bragg}} = \frac{hc}{2d_{hkl} \cos \alpha}, \quad (3.4)$$

where (h, k, l) are Miller indices, d_{hkl} the scatterer plane spacing, and c the speed

3 Instruments and Complementary Methods

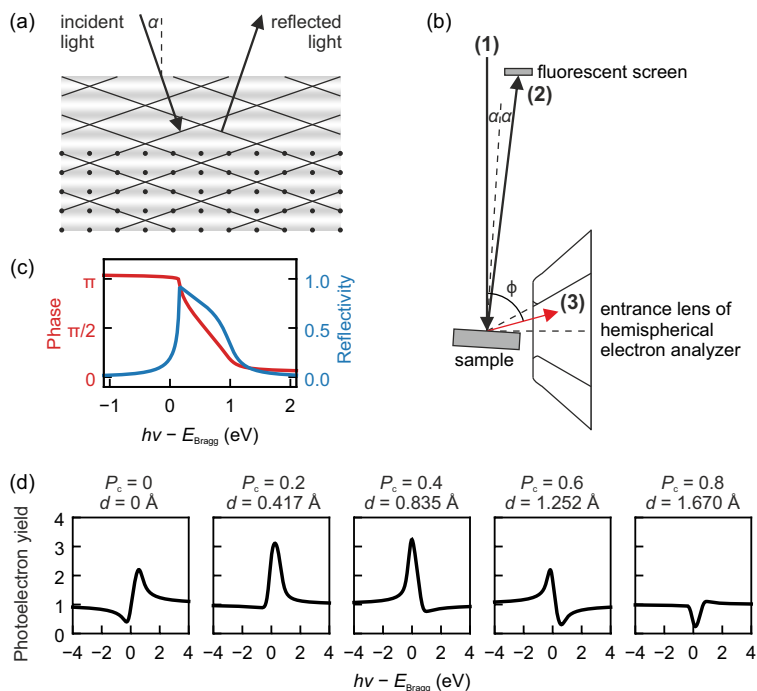


Figure 3.7: NIXSW. (a) Incident and Bragg-reflected X-ray beams form a standing wave whose intensity is shown as light and dark stripes. α : angle of incidence. After Fig. 1 of Ref. [136]. (b) Experimental geometry of NIXSW experiment at Diamond Light Source. See text for details. (c) Theoretical phase and reflectivity and (d) theoretical photoelectron yield for different coherent positions P_c and corresponding heights d with respect to the scatterer plane for the (111) Bragg reflection of the Cu(111) substrate ($\alpha = 3.5^\circ$, $E_{\text{Bragg}} = 2975.85\text{ eV}$, $d_{111} = 2.087\text{ \AA}$), calculated with the TORRICELLI program [80].

of light. This reflectivity curve is called the Darwin curve, see Fig. 3.7(c). Within this finite range, the phase of the standing wave field shifts by π , i.e. the antinodal planes move from on the scatterer planes to the midpoint between them.

Essentially, the NIXSW experiments probe the following quantities: the intensity of the incident photon beam $I_0(h\nu)$ (for normalization), the reflectivity $R(h\nu)$, and the XPS spectra (cf. Section 2.2) of the chemical species of interest as a function of photon energy. The latter is measured by the hemispherical electron ana-

lyzer in order to retrieve the photoelectron yield Y , which is given by:

$$Y = 1 + R_S + 2F_c \sqrt{R_S} \cos(\varphi_S - 2\pi P_c), \quad (3.5)$$

where R_S and φ_S are the theoretical reflectivity and phase of the sample, F_c and P_c are two structural fitting parameters—coherent fraction and coherent position, respectively. F_c indicates the level of vertical order of the species, between zero (complete disorder) and unity (all species on the same height). P_c gives the mean position of the species, also between zero and unity, with respect to the Bragg plane of the crystal. The adsorption height of the species is then given by $(n + P_c)d_{hkl}$, where $n = 0, 1, 2, \dots$. The choice of n is rationalized by considering the common sense, or typical reference systems, e.g. a monolayer of molecules adsorbed on a metal substrate as investigated in Chapter 5.

The shape of the photoelectron yield curve is highly sensitive to F_c and P_c , see Fig. 3.7(d), thus offering the possibility to determine F_c and P_c with high accuracy. However, Eq. (3.5) is a simplified form based on the dipole approximation. In practice, the non-dipolar corrections need to be included during the fitting [137, 138] with experimentally or theoretically determined parameters [139, 140]. In addition, at most synchrotrons a double-crystal monochromator, typically with two Si(111) single crystals, is used to achieve small energy bandwidth of the incident beam and large transmission only for a narrow range of photon energies. Therefore, in the final fit model for the photoelectron yield, the monochromator reflectivities R_M need to be cross-correlated with the sample reflectivity R_S and a Gaussian broadening term is included to account for the energy and angle distributions of the incident beam, see the relevant formalism developed in Refs. [80, 141].

The key characteristic of NIXSW in the scope of this thesis is the high accuracy in determining the adsorption height in a chemically selective way. Taking PTCDA as an example, the carboxylic and anhydride oxygen atoms as well as the carbon atoms directly bound to oxygen and the remaining carbon atoms in the backbone all appear at different peak positions in XPS, see Section 5.4.2 for details. Fitting the yield curve (area under each XPS peak as a function of photon energy) results in different P_c for different components, thus different adsorption heights [142]. As a side note, NIXSW is also applicable to determine the lateral adsorption structure via triangulation, i.e. using several different Bragg reflections [143].

3.5 Density Functional Theory Calculations

This section gives a general description of DFT calculations employed in this thesis for molecular electronic structure. All theoretical calculations in this work

3 Instruments and Complementary Methods

have been performed by Prof. P. Puschnig and his group of the University of Graz, Austria, at the Vienna Scientific Computing (VSC) cluster and at the High Performance Computing (HPC) center in Graz.

In a nutshell, DFT provides a rigorous framework to reduce the interacting many-electron problem to an effective system of non-interacting electrons. In this thesis, the many-electron system in question is either isolated (gas-phase) molecules or molecules adsorbed on a substrate. Within the framework of DFT, different levels of simulation can be performed [56]:

For gas-phase molecules, the Kohn–Sham equation—single-electron Schrödinger equation with an effective potential v_{eff} —is solved with the ABINIT code [144] or the NWChem code [145]:

$$\left[-\frac{\hbar^2}{2m}\nabla^2 + v_{\text{eff}}(\mathbf{r}) \right] \psi_i(\mathbf{r}) = \varepsilon_i \psi_i(\mathbf{r}), \quad (3.6)$$

where ε_i are the energies of the Kohn–Sham orbitals ψ_i . For illustration, such a Kohn–Sham orbital for $i = N$, that is the HOMO, is shown as an isosurface, for instance in Fig. 2.5. For exchange-correlation effects, the generalized gradient approximation (GGA) [146] for v_{eff} is employed. The simulated momentum maps of the isolated molecule are obtained as FT of the respective Kohn–Sham orbitals [7] (cf. Fig. 2.5).

For molecules adsorbed on a substrate, the code suitable for periodic boundary conditions, Vienna Ab-initio Simulation Package (VASP) [147, 148], is used. Here instead of one single molecule, one needs to model the whole system by including both the substrate and the adsorbed molecule(s) within a unit cell. To fulfill the three-dimensional periodic boundary conditions, a commensurate superstructure (cf. Section 3.2.1) is necessary and the system of interest is placed in a three-dimensional unit cell, with a vacuum layer of $\sim 15\text{--}30\text{\AA}$ inserted between the slabs—so-called “repeated-slab approach” [149]. To avoid spurious electrical fields, a dipole layer is added in the vacuum region [150].

The DFT software packages are characterized by their basis sets for solving Eq. (3.6) while expanding the Kohn–Sham orbitals $\psi_i(\mathbf{r})$ into:

$$\psi_i(\mathbf{r}) = \sum_j c_j^{(i)} \varphi_j(\mathbf{r}), \quad (3.7)$$

where $\varphi_j(\mathbf{r})$ are the known basis functions. Considering the translational symmetry, a natural choice of $\varphi(\mathbf{r})$ is the plane wave $e^{i\mathbf{G}\cdot\mathbf{r}}$, where \mathbf{G} is a reciprocal lattice vector. Doing so, the DFT calculations are simplified and easy to transform between real and momentum space. For k -point sampling, a Monkhorst–Pack grid [151] is used and a first-order Methfessel–Paxton smearing [152] of 0.1 eV is utilized. In practice, the plane wave expansion is truncated by a cut-off wave

3.5 Density Functional Theory Calculations

number G_{cut} in momentum space, characterized by the cut-off kinetic energy $E_{\text{cut}} = G_{\text{cut}}^2/2$. In the calculations discussed in this thesis, the cut-off kinetic energy was set to $\sim 500\text{eV}$. In order to achieve the convergence of the results in a reasonable time scale, simple plane waves are not enough to account for the rapid oscillations of the wave functions close to the atomic nuclei. This is why a pseudo-potential scheme is needed, which was the projector augmented wave approach [153] in the results reported in this thesis.

For unknown adsorption geometry, the most favorable adsorption site is determined by testing different possible adsorption sites and performing local geometry optimizations in which the one or two topmost substrate layers and all molecular degrees of freedom are allowed to relax until forces are below a certain threshold, e.g. $0.01\text{eV}\text{\AA}^{-1}$. Additionally, van der Waals interactions between substrate and adsorbed molecules have been included according to the Tkatchenko–Scheffler vdW-surf method [154, 155].

4 Bonded or Not: In-Situ Identification of Surface Reaction Intermediates

4.1 Introduction

In this chapter, the chemical state of chemically synthesized bisanthene from DBBA on Cu(110) is accurately determined by the PT method.

Part of the results shown in this chapter have been published in the following journal article: X. Yang, L. Egger, P. Hurdax, H. Kaser, D. Lüftner, F. C. Bocquet, G. Koller, A. Gottwald, P. Tegeder, M. Richter, M. G. Ramsey, P. Puschnig, S. Soubatch, and F. S. Tautz, “Identifying surface reaction intermediates with photoemission tomography”, *Nat. Commun.* **10**, 3189 (2019) [156].

4.2 Identification of Reaction Intermediates

The determination of reaction pathways is a key issue in chemistry. Identifying the reaction intermediate—a molecular entity with a lifetime appreciably longer than a molecular vibration that is formed from the reactants and reacts further to give the products of a chemical reaction [157]—helps in understanding how a reaction takes place. This has led to the development of various approaches in analytical chemistry, from the classical wet chemistry to the modern variants, e.g. ion spectroscopy and nuclear magnetic resonance spectroscopy.

Surface reactions are particularly challenging because the reactants, intermediates, and products are all adsorbed on the surface and many methods used for gas or liquid phase are inapplicable at surfaces. Typical surface science techniques indeed provide some useful insights in this case: non-contact atomic force microscopy (AFM) can be used to observe the molecular backbone structure and thus identify an intermediate [158]; vibrational modes in infrared spectroscopy [159] or chemical shifts in core level spectroscopy [160] could infer the presence or absence of specific bonds. These observations sometimes suffice but does not always guarantee the identification of an adsorbed species. Especially, the degree of hydrogenation of a given molecule is often difficult to determine, as standard surface

science techniques, e.g. AFM, are not sensitive to hydrogen at the periphery and only indirect conclusions are possible.

Here, PT is proposed to address this issue because the object of PT studies—molecular orbitals—are extremely sensitive to the composition and chemical structure, which also includes the molecular periphery where adsorbates react with the substrate. In combination with DFT calculations, it should be possible to unambiguously detect if the hydrogen abstraction takes place at the surface, provided that the intermediates are stable with infinite lifetime before the next reaction step is induced by an external stimulus. This is illustrated in the following example: the thermally induced reaction of dibromo-bianthracene to graphene which is shown to proceed via a fully hydrogenated bisanthene intermediate.

4.3 Thermal Reaction of DBBA on Cu(110)

The controlled synthesis of graphene nanoribbons (GNRs) is vital for fabricating nanoscale devices. Recently, the atomically precise bottom-up approach, either in solution or on surface, has attracted attention due to its reproducibility and well-defined, controllable structure. Particularly, the surface-mediated reaction of oligomer precursors has been extensively exploited. By using different precursor molecules, the resulting nanoribbons can be of armchair or chevron type, with different widths, and with oxygen or nitrogen doping [161–163]. One popular precursor molecule is 10,10'-dibromo-9,9'-bianthracene (DBBA, $C_{28}H_{16}Br_2$), see Fig. 4.1.

The DBBA molecules are composed of two anthracene groups twisted with respect to each other and two boron atoms. Upon annealing, DBBA molecules on the Au(111) surface evolve in several steps [Fig. 4.1(a)]: first at 200 °C, the boron substituents are removed (dehalogenation) and intermolecular covalent bonds are formed through radical addition (C–C coupling); at 400 °C, dehydrogenation reaction takes place and forms the 7-armchair graphene nanoribbon (cyclodehydrogenation) [161]. Similar results were reported also on Cu(111), but the nanoribbon is obtained at lower temperature (250 °C) due to the more reactive surface and shows a chiral shape instead of armchair [164]. To obtain a better alignment, the vicinal Au(788) surface was used to guide the growth of GNR on the terraces [165].

The thermal reaction of DBBA on Cu(110) is different to that on Cu(111), see Fig. 4.1(b): Simonov et al. [166] reported that the Cu(110) surface with increased reactivity forbids the formation of nanoribbon but results in “nanographenes”, bisanthene [phenanthro(1,10,9,8-opqra)perylene, $C_{28}H_{14}$]. Further annealing at higher temperatures above 700 °C (cf. supporting information of Ref. [166]) causes the decomposition of nanographenes with subsequent formation of graphene is-

4.3 Thermal Reaction of DBBA on Cu(110)

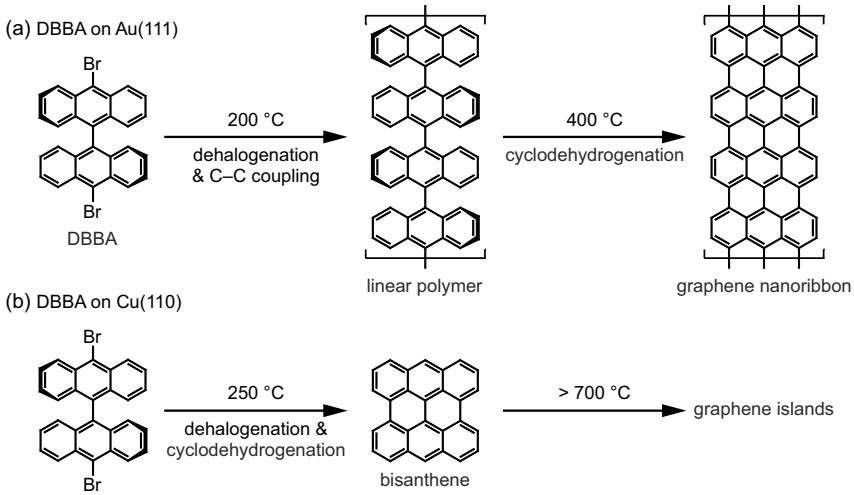


Figure 4.1: Surface reaction of 10,10'-dibromo-9,9'-bianthracene (DBBA) on (a) Au(111) and (b) Cu(110).

lands. Thus the overall reaction is: intact DBBA adsorbed on Cu(110) \rightarrow chemical intermediate formed after annealing at 250 °C \rightarrow graphene formed at > 700 °C. However, Simonov et al. suggested that the intermediate has partly dehydrogenated zigzag edges bonded to the underlying copper atoms based on STM, XPS results and adsorption energy calculations. It will be shown in the following by the PT studies that the thermally induced reaction of DBBA on Cu(110) at 250 °C produces a fully hydrogenated bisanthene intermediate instead.

4.3.1 Density of States

The Cu(110) crystal was cleaned by Ar⁺ sputtering cycles at 1 keV followed by annealing at 800 K. DBBA was evaporated from a Knudsen-type molecular evaporator (Kentax GmbH) at 185 °C onto the Cu(110) surface kept at room temperature (RT). The molecular flux was calibrated using a quartz microbalance to obtain the nominal thickness of one ML.

First, the electronic structure of the as-deposited molecules was measured with the toroidal electron analyzer (cf. Section 3.3). EDCs in the valence band range between the Fermi level and the onset of the copper d-band emissions are shown in Fig. 4.2(a,c): At least two adsorbate-related features are discernible, one at approximately 0.15 eV and another between 1.0 eV and 1.5 eV. However, the pre-

4 In-Situ Identification of Surface Reaction Intermediates

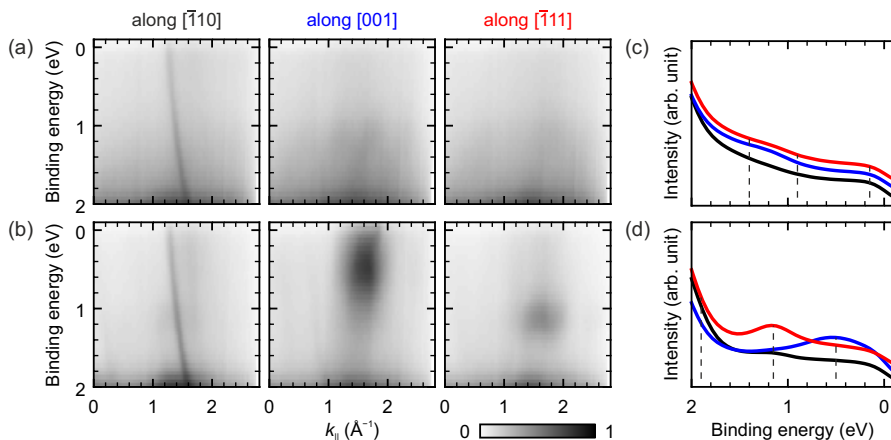


Figure 4.2: Bandmaps (a,b) and EDCs (c,d) of DBBA on Cu(110) along different azimuths before (a,c) and after (b,d) annealing at 250°C. For the EDCs, the photoelectron intensity was integrated between $k_{\parallel} = 0 \text{ \AA}^{-1}$ and 2.5 \AA^{-1} . The dashed lines mark energies corresponding to experimental k -maps in Fig. 4.3(a,b). After Fig. 2 of Ref. [156], with added images.

cise binding energies of these broad features are difficult to determine. Moreover, the anisotropy between the EDCs recorded at the two principal azimuths of the substrate is much weaker than for other organic monolayers on metal (110) surfaces [3, 7, 10]. Nevertheless, Section 4.3.2 below will show that the angular distribution of photoelectrons exhibits a two-fold symmetry and thus points to a well-defined orientation of the as-deposited species.

After annealing the sample at 250°C, the EDCs are clearly modified, see Fig. 4.2(b,d). Three molecular emissions are found, one of them almost completely concealed by the rising flank of the Cu d-band. The other two appear at 0.5 eV and 1.15 eV as well-defined peaks. The anisotropy between the two azimuths is now pronounced, suggesting a high degree of molecular orientation after annealing.

4.3.2 Momentum Maps

On the basis of the experimental EDC, the nature of the molecular emissions, both before and after annealing, remains unclear. At the binding energies in question, corresponding momentum maps were measured by the toroidal analyzer, see Fig. 4.3.

4.3 Thermal Reaction of DBBA on Cu(110)

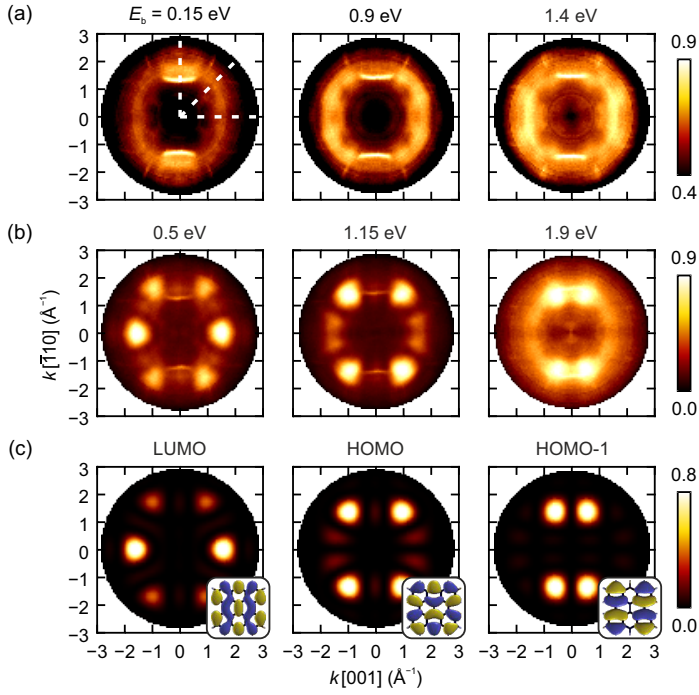


Figure 4.3: Photoelectron distributions. Experimental k -maps of DBBA (a) before and (b) after annealing measured at chosen binding energies. White dashed lines in the first k -map indicate the azimuths where the bandmaps in Fig. 4.2(a,b) are measured. (c) Theoretical k -maps of LUMO, HOMO, and HOMO-1 orbitals of a bisanthene [63]. Corresponding real-space orbitals are shown in insets. After Fig. 3 of Ref. [156].

Before Annealing

For the as-deposited species, the k -maps measured at 0.15, 0.9 and 1.4 eV below the Fermi level are dominated by diffuse patterns that are superimposed on sharp features from Cu sp -band emissions [Fig. 4.3(a)]. These patterns are two-fold symmetric and clearly vary with binding energy, indicating that they must originate from well-defined and distinct molecular orbitals, in spite of the indistinct density of states in Fig. 4.2(c).

After Annealing

After annealing to 250 °C, the momentum maps appear more defined [Fig. 4.3(b)]. In agreement with the EDCs in Fig. 4.2(d), this suggests a higher degree of orientation and indicates the presence of only one surface species. Most importantly, however, the changes in the k -maps prove a significant modification of the orbital structure, indicating that a thermally activated surface reaction to a new species has occurred.

A plausible candidate for this reaction intermediate is bisanthene (cf. Fig. 4.1). The calculated k -maps of LUMO, HOMO, and HOMO–1 of bisanthene in the gas phase, depicted in Fig. 4.3(c), match very well the three measured patterns at 0.5, 1.15, and 1.9 eV, respectively. Thus it gives strong evidence that during the annealing at 250 °C on Cu(110), DBBA undergoes dehalogenation and cyclodehydrogenation during which the adsorbate planarizes and the π -conjugation expands to the entire fused carbon backbone. The momentum maps in Fig. 4.3(b,c) further reveal that, first, the central C–C bond of bisanthene is oriented along the $\bar{1}10$ direction of the Cu(110) surface, and second, bisanthene chemisorbs on Cu(110). The latter is proven by the charge transfer into the formerly unoccupied LUMO, which makes this orbital observable in PT.

4.3.3 Electronic Structure Calculations

In order to interpret the measured k -maps Fig. 4.3(a), electronic structure calculations for DBBA monolayers adsorbed on Cu(110) are performed in the repeated-slab approach (cf. Section 3.5). The metallic substrate is modeled by five Cu layers with lattice parameter $a_{\text{Cu}} = 3.61 \text{ \AA}$ and a vacuum layer of at least 15 \AA . The epitaxial matrices used for the species before and after annealing are $\begin{pmatrix} 4 & 0 \\ 1 & 6 \end{pmatrix}$ and $\begin{pmatrix} 4 & 0 \\ 2 & 5 \end{pmatrix}$, respectively. All structures discussed below have been locally relaxed, but the atomic positions in the three Cu layers at the bottom of the slab are frozen. To account for the van der Waals interactions between Cu(110) surface and adsorbed molecules, the Tkatchenko–Scheffler vdW-surf method was used [154, 155].

Note that the electronic structure calculations in this section have been performed by Prof. P. Puschnig of the University of Graz, Austria (cf. Section 3.5).

Before Annealing

For the as-deposited DBBA/Cu(110), three possible adsorption geometries were tested, see Fig. 4.4(a). Structure #1 is identical to the adsorption geometry suggested by Simonov et al. [166] who calculated the adsorption energy to be

4.3 Thermal Reaction of DBBA on Cu(110)

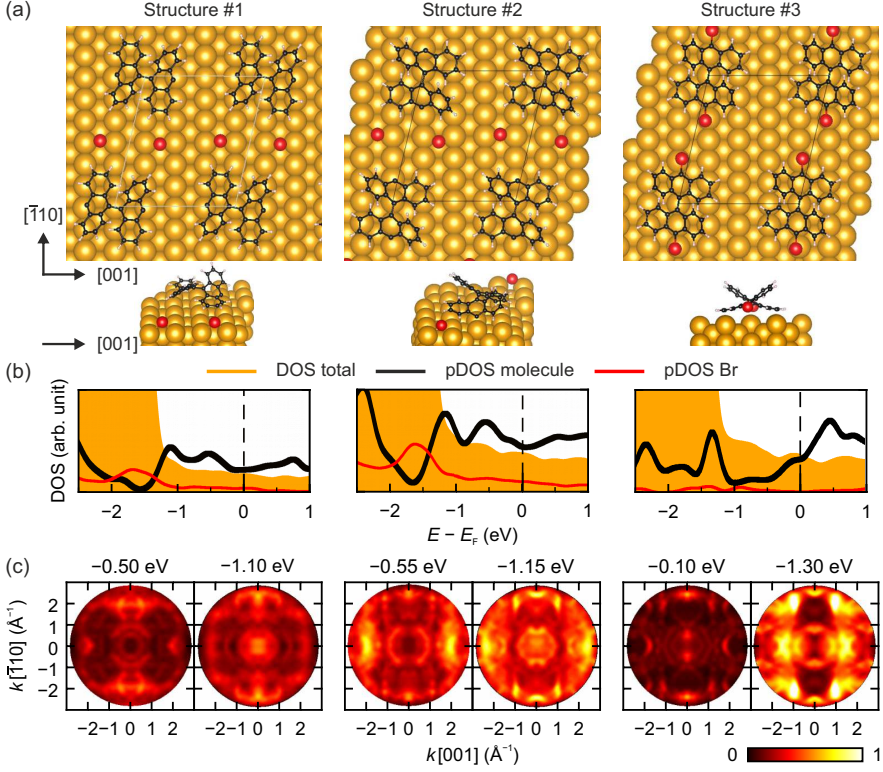


Figure 4.4: DFT calculation of DBBA adsorption structures before annealing. (a) Top view and side view of the relaxed adsorption structure. (b) Total DOS (orange) and pDOS (magnified scale) for the molecule (black) and the Br atoms (red). (c) Simulated k -maps at chosen energies. After Fig. S2–S4 of Ref. [156]. Calculations by P. Puschnig.

–3.27 eV. Adsorption energies are calculated as:

$$E_{\text{ad}} = E_{\text{total}} - (E_{\text{total, DBBA}} + E_{\text{total, Cu(110)-slab}}), \quad (4.1)$$

where $E_{\text{total, DBBA}}$ and $E_{\text{total, Cu(110)-slab}}$ are total energies when only one of the two subsystems—freestanding DBBA film and Cu(110) substrate slab—is calculated; E_{total} is the total energy of the substrate with adsorbates relaxed. Negative E_{ad} corresponds to a bonding situation, while positive values indicate repulsion. The calculated values (Table 4.1) thus contain contributions of the intermolecular

4 In-Situ Identification of Surface Reaction Intermediates

Structure	Composition	E_{total} (eV)	E_{ad} (eV)
DBBA (gas phase)	$\text{C}_{28}\text{H}_{16}\text{Br}_2$	-315.01658	
Cu(110)-slab	Cu_{120}	-478.44739	
DBBA/Cu(110) structure #1	$\text{Cu}_{120}\text{C}_{28}\text{H}_{16}\text{Br}_2$	-796.73309	-3.269
DBBA/Cu(110) structure #2	$\text{Cu}_{120}\text{C}_{28}\text{H}_{16}\text{Br}_2$	-797.05866	-3.595
DBBA/Cu(110) structure #3	$\text{Cu}_{120}\text{C}_{28}\text{H}_{16}\text{Br}_2$	-795.73354	-2.270

Table 4.1: Total energies E_{total} and adsorption energies E_{ad} of as-deposited DBBA on the Cu(110) surface. After Table S1 of Ref. [156]. Calculations by P. Puschnig.

interaction as well as of the molecule–substrate interaction in the superstructure [167].

Azimuthally rotating the molecules by 90° such that the zig-zag edges of the molecule are aligned perpendicular to the Cu rows results in structure #2. It is energetically more favorable and exhibits an adsorption energy of -3.60eV . Finally, an adsorption geometry with intact DBBA (Br atoms attached to the molecule) is denoted as structure #3. It turns out to be the least favorable structure with $E_{\text{ad}} = -2.27\text{eV}$.

Figure 4.4(b,c) shows the DOS/pDOS (cf. Section 2.3.3.2) and simulated k -maps for these three structures. Note that none of these three structures can explain the experimentally observed k -maps in Fig. 4.3(a). The possibility that more than one configuration of the adsorbed species co-exist is also supported by both the diffuseness of k -maps and the indistinctiveness of EDCs. The PT study for such three-dimensional species is extremely sensitive to the exact molecular geometry and would require the development of a global search algorithm to identify the as-deposited species, which is beyond the scope of this work.

After Annealing

While the agreement between angular photoelectron distributions of gas-phase bisanthene and the measured patterns [Fig. 4.3(b,c)] is good, there are deviations, which could in principle point to small modifications of bisanthene, such as (partial) dehydrogenation. Therefore, the exact chemical state of the reaction intermediate is not yet clear. At the level of van der Waals-corrected DFT, the following three molecular species are considered:

- Fully hydrogenated bisanthene ($\text{C}_{28}\text{H}_{14}$)
- Partially zig-zag-edge-dehydrogenated $\text{C}_{28}\text{H}_{12}$

4.3 Thermal Reaction of DBBA on Cu(110)

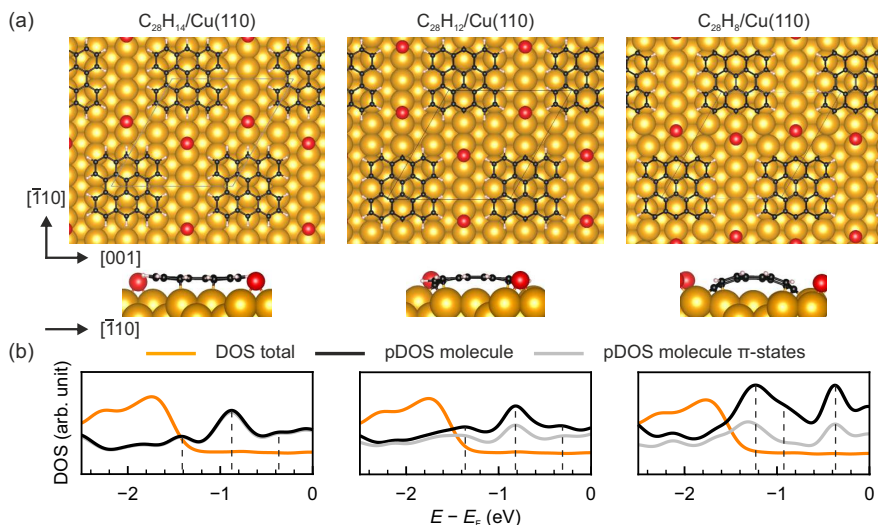


Figure 4.5: DFT calculation of DBBA adsorption structures after annealing. (a) Top view and side view of the relaxed adsorption structure. (b) Total DOS (orange) and pDOS (magnified scale) for the molecule (black) and the molecular π -states (gray). After Fig. S5–S7 of Ref. [156]. Calculations by P. Puschnig.

- Fully zig-zag-edge-dehydrogenated $C_{28}H_8$

The latter two would form covalent bonds with the Cu surface through dehydrogenated C atoms, see Fig. 4.5(a) and Fig. 4.6.

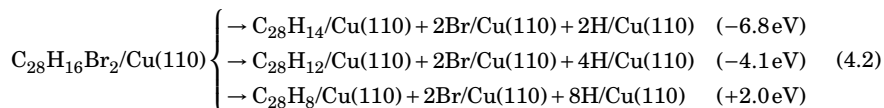
For each molecular species, four high-symmetry adsorption sites have been considered: hollow, long bridge, short bridge, and top sites. The total energies and adsorption energies of these candidates for reaction intermediates are summarized in Table 4.2. Adsorption energies have been calculated as $E_{ad} = E_{total} - (E_{total, gas-phase molecule} + E_{total, Cu(110)-slab} + 2Br)$. Note that the detached Br atoms are now considered as a part of the substrate together with the Cu(110) slab. In all three cases, the molecules are oriented with their central C–C bond along the $[\bar{1}10]$ direction of the Cu(110) surface [cf. Fig. 4.5(a)]. Bisanthene favors the short bridge ($E_{ad} = -5.26$ eV) adsorption site, while $C_{28}H_{12}$ and $C_{28}H_8$ both prefer the top site with adsorption energies of -8.01 eV and -12.72 eV, respectively. The latter value indicates $C_{28}H_8$ to be the most stable intermediate and in agreement with the adsorption energy given by Simonov et al. [166]. However, this adsorption energy disregards the energy needed to split the C–H bonds. When computing

4 In-Situ Identification of Surface Reaction Intermediates

Structure	Composition	Site	E_{total} (eV)	E_{ad} (eV)
Cu(110)-slab	Cu ₁₀₀		-398.32704	
Cu(110)-slab + 2Br	Cu ₁₀₀ Br ₂		-405.31483	
bisanthene (gas phase)	C ₂₈ H ₁₄		-305.62265	
bisanthene/Cu(110) + 2Br	Cu ₁₀₀ Br ₂ C ₂₈ H ₁₄	H	-714.48437	-3.547
bisanthene/Cu(110) + 2Br	Cu ₁₀₀ Br ₂ C ₂₈ H ₁₄	LB	-713.83354	-2.896
bisanthene/Cu(110) + 2Br	Cu ₁₀₀ Br ₂ C ₂₈ H ₁₄	SB	-716.19721	-5.260
bisanthene/Cu(110) + 2Br	Cu ₁₀₀ Br ₂ C ₂₈ H ₁₄	T	-714.97503	-4.038
C ₂₈ H ₁₂ (gas phase)	C ₂₈ H ₁₂		-292.65724	
C ₂₈ H ₁₂ /Cu(110) + 2Br	Cu ₁₀₀ Br ₂ C ₂₈ H ₁₂	H	-702.88498	-4.913
C ₂₈ H ₁₂ /Cu(110) + 2Br	Cu ₁₀₀ Br ₂ C ₂₈ H ₁₂	LB	-702.56425	-4.592
C ₂₈ H ₁₂ /Cu(110) + 2Br	Cu ₁₀₀ Br ₂ C ₂₈ H ₁₂	SB	-705.49124	-7.519
C ₂₈ H ₁₂ /Cu(110) + 2Br	Cu ₁₀₀ Br ₂ C ₂₈ H ₁₂	T	-705.98567	-8.014
C ₂₈ H ₈ (gas phase)	C ₂₈ H ₈		-266.79873	
C ₂₈ H ₈ /Cu(110) + 2Br	Cu ₁₀₀ Br ₂ C ₂₈ H ₈	H	-681.81636	-9.703
C ₂₈ H ₈ /Cu(110) + 2Br	Cu ₁₀₀ Br ₂ C ₂₈ H ₈	LB	-683.06676	-10.953
C ₂₈ H ₈ /Cu(110) + 2Br	Cu ₁₀₀ Br ₂ C ₂₈ H ₈	SB	-684.63227	-12.519
C ₂₈ H ₈ /Cu(110) + 2Br	Cu ₁₀₀ Br ₂ C ₂₈ H ₈	T	-684.83779	-12.724

Table 4.2: Total energies E_{total} and adsorption energies E_{ad} of reaction intermediates of DBBA on the Cu(110) surface at hollow (H), long bridge (LB), short bridge (SB), and top (T) sites. After Table S2 of Ref. [156]. Calculations by P. Puschnig.

the full chemical reaction energies for the three intermediates,



where the reaction energies are shown in the parenthesis. It demonstrates that the fully hydrogenated bisanthene (C₂₈H₁₄) is the most energetically favorable intermediate.

The calculated pDOS shown in Fig. 4.5(b) contains peaks which can be associated with the states observed in the experimental EDC in Fig. 4.2(d). There is, however, no clear fingerprint which could be used to unambiguously identify the exact nature of the reaction intermediate. Yet, it is interesting to note that the contribution of π -states to the total pDOS gradually decreases from intact bisanthene to C₂₈H₈ [Fig. 4.5(b)]. This is caused by the strong concave distortion of

the dehydrogenated bisanthene derivatives, see side views in Fig. 4.5(a), resulting from chemical bonds that are formed between unsaturated edge carbons and the Cu(110) surface [163].

It is reasonable to assume that the strong molecular distortion apparent in the pDOS will modify the corresponding orbital structure significantly. Therefore, momentum maps from the *combined* adsorbate/substrate system including the local bonds at the edges are simulated, see Fig. 4.6. For each chemical species, the simulated k -maps are shown at three representative binding energies, as indicated by the dashed lines in the pDOS curves of Fig. 4.5(b). Profound differences in the k -maps for the three species demonstrate a striking sensitivity of PT to the hydrogen saturation of molecular edges. Dehydrogenation alters the patterns and moreover leads to increasingly more diffuse emissions signatures, most likely because the local bonds of the dehydrogenated carbon atoms with the Cu(110) mix substrate states into the molecular wave functions.

The comparison of the simulated k -maps with the experimental ones [Fig. 4.3(b)] excludes the two dehydrogenated species ($C_{28}H_{12}/C_{28}H_8$) and leads to the conclusion that the fully hydrogenated bisanthene is the sought-after reaction intermediate. Note that the agreement of k -maps of the adsorbed bisanthene [Fig. 4.6(a)] with experiments is better than that of the gas-phase simulations [Fig. 4.3(c)]. Nevertheless, the close resemblance of these two demonstrates that its orbital structure suffers only minor changes upon adsorption, despite the former LUMO being filled and involved in the bonding of the molecule to the metal.

4.3.4 Comparison with Literature

The PT and DFT results above have identified fully-hydrogenated bisanthene ($C_{28}H_{14}$) as the reaction intermediate. This is in contrast to the conclusion made by Simonov et al. that dehydrogenated $C_{28}H_8$ is the intermediate [166]. In Section 4.3.3, it is shown that the reaction energies, which take into account the energy necessary to detach hydrogen atoms from DBBA, should be used to find the most energetically favorable intermediate. Otherwise, adsorption energy calculations only would lead to the same conclusion made by Simonov et al. However, in their paper $C_{28}H_8$ was also suggested by STM and XPS results. These results and corresponding conclusion will be critically discussed below.

STM

At the bias of $-0.1V$ [Fig. 4.7(a)], Simonov et al. observed an STM contrast that resembles the LUMO shape of intact bisanthene. Based on their DFT results [Fig. 4.7(b)], they assigned the corresponding electronic level to the third state

4 In-Situ Identification of Surface Reaction Intermediates

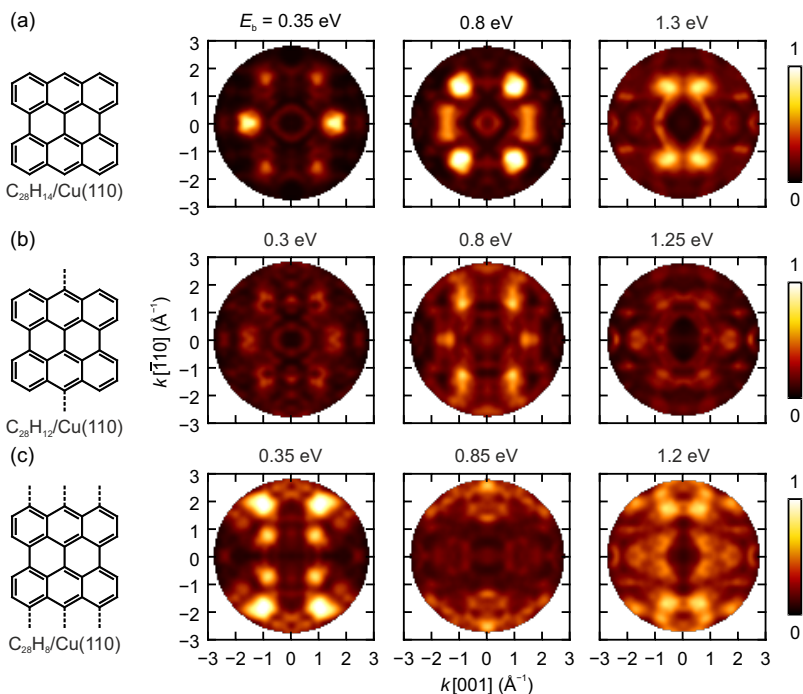


Figure 4.6: Chemical structure and simulated k -maps for (a) bisanthrene, (b) $C_{28}H_{12}$, and (c) $C_{28}H_8$ on the Cu(110) surface. Dashed lines in the chemical structures mark the localized chemical bonds of dehydrogenated carbon atom with copper atoms. The binding energies of k -maps are corresponding to the dashed lines in Fig. 4.5(b). After Fig. 4 of Ref. [156]. Calculations by P. Puschnig.

below the Fermi level (HOMO-2) of $C_{28}H_8$ on Cu(110). This assignment, however, implies at least two additional occupied levels (HOMO and HOMO-1) to be located in a narrow binding energy interval of 0.1 eV. This is ruled out by the PT results (Sections 4.3.2 and 4.3.3) that the former LUMO of $C_{28}H_{14}$ is the closest occupied molecular state to the Fermi level.

In order to make the direct and fair comparison, STM contrast simulations are carried out in the framework of the Tersoff–Hamann approximation [168] using the DFT results presented in Section 4.3.3 for three orbitals and three possible reaction intermediates in question, see Fig. 4.8. It is clear that the simulated STM image corresponding to the former LUMO of hydrogenated $C_{28}H_{14}/Cu(110)$ with the bias of -0.35 V [Fig. 4.8(a)], i.e. just below the Fermi level, resembles the

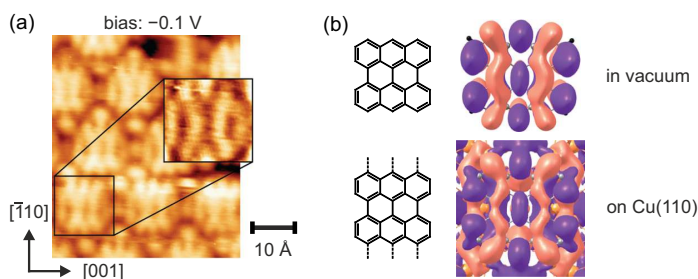


Figure 4.7: STM image and DFT calculations shown by Simonov et al. [166]. (a) STM image taken at -0.1 V and 500 pA. (b) Calculated real-space illustration for LUMO of bisanthene in vacuum and HOMO-2 of $C_{28}H_8$ on the Cu(110) surface. See text for discussion. After Fig. 7 of Ref. [166].

STM results of Simonov et al. much better than any of the images corresponding to the dehydrogenated $C_{28}H_8/Cu(110)$ [Fig. 4.8(c)]. This supports the conclusions from photoemission tomography that $C_{28}H_{14}$ is the reaction intermediate instead.

XPS

Conventionally, core-level spectroscopy like XPS is used for identifying the exact chemical state of a molecule (cf. Section 2.2). In their work Simonov et al. have successfully applied XPS to prove that a reaction of DBBA upon annealing on Cu(110) takes place, as the XPS spectra before and after annealing are evidently different, see Fig. 6(a,b) of Ref. [166]. But these spectral changes have left space for interpretation and discussion:

- Simonov et al. *a priori* assumed a dehydrogenated state and fit the experimental spectrum, including a peak with a shoulder, with three components. Using the spectrum of 7-armchair GNRs on Cu(111) as a reference [Fig. 6(c) of Ref. [166]], the core and hydrogenated carbon peaks were shifted differently (by approx. 100 meV and 200 meV respectively) to higher binding energies, which is difficult to justify.
- A zoom into the experimental XPS spectrum of Simonov et al. at the shoulder clearly shows that the three-component fitting is in fact not very accurate [Fig. 6(b) of Ref. [166]].

In order to check the stringency of the three-component model, XPS measurements were independently carried out at the I09 beamline of Diamond Light Source with a Scienta EW4000 electron analyzer. Fig. 4.9 shows the C 1s soft XPS

4 In-Situ Identification of Surface Reaction Intermediates

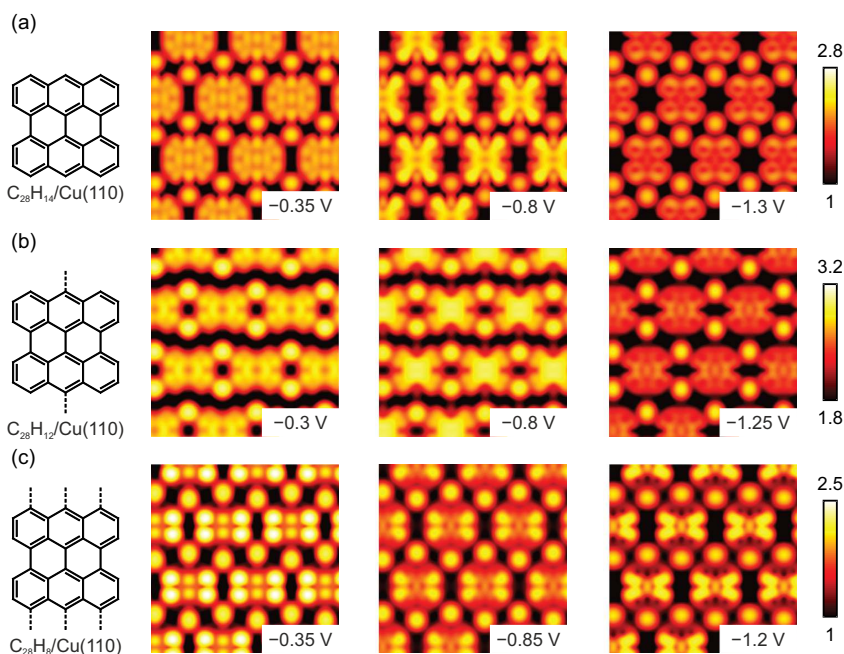


Figure 4.8: Chemical structure and simulated constant-current STM images for (a) bisanthrene, (b) $C_{28}H_{12}$, and (c) $C_{28}H_8$ on the Cu(110) surface. Note the Br adatoms are also included in simulations. Bias voltages are shown in the inset. The color code reflects the height of the tip (in Å) above the surface. After Fig. S8 of Ref. [156]. Calculations by P. Puschnig.

spectrum measured after annealing of DBBA on Cu(110) at 250°C and fitted with two- ($C_{28}H_{14}$) and three-component ($C_{28}H_8$) models. The areas under the component lines correspond to the stoichiometry of $C_{28}H_{14}$ and $C_{28}H_8$ on Cu(110), see inset drawings. The relative binding energies of the components of the two- and three-component models are fixed following the models in literature for graphene nanoribbons on Cu(111) [Fig. 6(c) of Ref. [166]] and nanographene on Cu(110) [Fig. 6(b) of Ref. [166]], respectively. Notably, there is no apparent difference in the fitting quality between the two models, which reveals the restricted capability of XPS to resolve differences in the exact chemical state of the reaction intermediate in question.

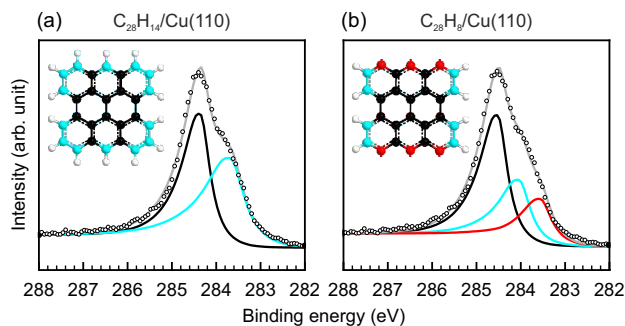


Figure 4.9: XPS of reaction intermediate and fitting models. Fitting of the XPS spectrum measured at 500 eV photon energy using (a) two- and (b) three-component models according to Simonov et al. [166]. White dots represent experimental data (identical in both panels). Black, cyan, and red curves correspond to core, hydrogenated, and bonded-to-copper carbon atoms, respectively. Gray curve is the fitting envelop. After Fig. S9 of Ref. [156]. Courtesy of S. Subach.

4.4 Conclusion

In this chapter, PT is presented as a precise method to identify the reaction intermediate to be fully hydrogenated bisanthene ($C_{28}H_{14}$) in the test case of surface-assisted thermal reaction of DBBA on Cu(110). The direct chemical bonds between the bisanthene carbon atoms and the underlying copper substrate are missing, although a charge transfer has occurred from the metal to the molecule. The ability of PT to image orbitals in the reciprocal space (Section 2.3.3) makes it particularly sensitive to the exact chemical state of surface reaction species. While conventional experimental techniques such as STM and XPS can be inconclusive for this purpose, PT can differentiate the chemistry of the molecular periphery, i.e. the degree of (de-)hydrogenation, as well as determine the occupation of the frontier orbitals.

As PT is neither constrained by the need for cryogenic temperatures nor to planar surface species, it will be a powerful companion to atomic force microscopy and other state-of-the-art surface science methods in the study of reaction pathways at surfaces. Its major restrictions are those of vacuum and conductive substrates inherent to ARPES.

5 Charged or Not: Decoupling of Molecules at Metal Surfaces

5.1 Introduction

In this chapter, a study of the decoupling mechanisms of molecules on metal surfaces is presented using PT, combined with NIXSW experiments and DFT calculations.

Part of the results shown in this chapter have been published in the following journal articles: X. Yang, I. Krieger, D. Lüftner, S. Weiß, T. Heepenstrick, M. Hollerer, P. Hurdax, G. Koller, M. Sokolowski, P. Puschnig, M. G. Ramsey, F. S. Tautz, and S. Soubatch, “On the decoupling of molecules at metal surfaces”, *Chem. Commun.* **54**, 9039 (2018) [109] and C. Brülke, T. Heepenstrick, I. Krieger, B. Wolff, X. Yang, A. Shamsaddinlou, S. Weiß, F. C. Bocquet, F. S. Tautz, S. Soubatch, and M. Sokolowski, “Quantitative analysis of the electronic decoupling of an organic semiconductor molecule at a metal interface by a monolayer of hexagonal boron nitride”, *Phys. Rev. B* **99**, 121404 (2019) [169].

5.2 Approaches to Decouple Molecules from Metal

Organic semiconductors have gained much attention in research and device development in the last two or three decades. It is essential to have fundamental understanding of the electronic properties and processes in organic materials, thus model systems, mainly organic molecules on well-structured metal surfaces, have been investigated. However, the intrinsic electronic and structural properties of molecules are easily perturbed by the metallic support beneath [109]. Various strategies have been proposed in order to decouple organic molecules from metal surfaces, including:

- “Molecular landers”: synthesized molecule with functionalized peripheries as spacers which lift the molecular core from the metal surface, like a spacecraft [170].

5 Decoupling of Molecules at Metal Surfaces

- Organic decoupling layers: films of vertically-standing organic molecules, most often used are e.g. alkanethiol self-assembled monolayers (SAMs) [171].
- Post-synthetic intercalation: exposure to iodine vapor after the synthesis of covalent polyphenylene networks on the silver substrate leads to intercalation [172].
- Alkali dopants: doping of alkali element such as cesium and potassium results in reduced electronic coupling between adsorbed molecules and the substrate [34, 173].

These approaches, however, have their limits in terms of wide applications or preparation feasibility. In the following, three popular decoupling methods—dielectric interlayer, surface reconstruction, and 2D materials—are discussed in more detail.

5.3 Dielectric Interlayer

Thin dielectric layers on metals form the basis for microelectronic and storage applications, but they are also of interest for fundamental research [36]. On the one hand, thin dielectric layers have very different chemical and physical properties from their bulk counterparts. For example, the space-charge effect is avoided with reduced thickness and electron-based methods can be utilized to study the dielectric material. On the other hand, a thin decoupling dielectric interlayer between a metal substrate and adsorbed molecules has enabled various STM experiments, such as orbital imaging [1, 174] (cf. Fig. 2.1) and charge-state switching [175, 176].

These STM experiments used thin alkali halide films, most often NaCl which is easy to fabricate and optimize. Other alternatives include KCl, KBr, CaF, RbI, etc. Actually, the choice of NaCl may not be ideal because the phonons in NaCl films could couple and broaden electronic states of the adsorbate [1].

A second set of materials for the interlayer is metal oxide, often grown in oxygen atmosphere, e.g. the surface oxide of NiAl(110) [177]. The preparation of metal oxide thin films is more difficult because of the challenge to obtain a good epitaxy [178]. However, it is found that metal oxide thin films do not necessarily serve as passivating layers, but can change the electron energy level alignment for adsorbates such that charge transfer is promoted [179, 180] due to large changes in work function Φ . This was recently discussed in detail for 5A (cf. Fig. 2.1) adsorbed on a thin MgO film on Ag(100) by Hollerer et al. [36], which is reviewed in the following subsections to have an overview of relevant physical phenomena for a dielectric interlayer.

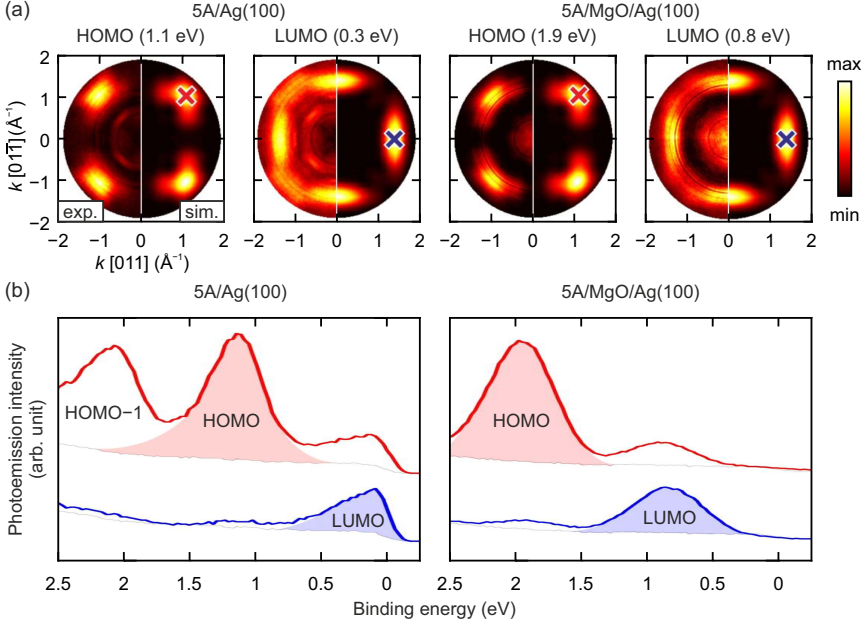


Figure 5.1: ARPES results of 1 ML 5A on Ag(100) and on 2 ML MgO(100) on Ag(100). (a) Experimental (left halves) and simulated (right halves) k -maps at different binding energies for HOMO and LUMO. (b) EDC spectra measured at k -positions of the HOMO (red) and LUMO (blue) intensity maxima, shown as red/blue crosses in (a). The peak areas of the HOMO/LUMO emission features are drawn as red/blue shades. The background is estimated using the spectra taken at normal emission. After Fig. 6 of Ref. [36].

5.3.1 MgO Thin Film on Ag(100)

For MgO, one atomic layer (half a unit cell) is referred to as one ML [181]. Hollerer et al. [36] have prepared a bilayer of MgO(100) on Ag(100) following the recipe from Pal et al. [182]: depositing magnesium in an oxygen background of 1×10^{-6} mbar at a rate of 0.5 ML/min while keeping the sample at 300 °C. In this work, the same preparation procedure was followed. MgO(100) grown on Ag(100) in this way has a good epitaxial relationship where Mg atoms occupy the hollow sites, i.e. continuing the Ag fcc lattice ($a = 4.079 \text{ \AA}$), while O atoms occupy the top sites [183].

5.3.2 5A/MgO/Ag(100)

Hollerer et al. [36] investigated 5A directly adsorbed on Ag(100) and compared it to the case when there is a 2 ML thin MgO film in between. In contrast to 5A on fcc (110) surfaces where all molecules have the same orientation along a high-symmetry direction [23], one ML of 5A on Ag(100) has ordered domains with their long axis aligned parallel to either $[01\bar{1}]$ or $[011]$. The 5A molecules on 2 ML MgO/Ag(100) also have orientations parallel to $[01\bar{1}]$ and $[011]$, the difference to 5A directly adsorbed on Ag(100) is that on MgO/Ag(100) the molecules are better immobilized.

Both systems have been studied using PT, measured with the toroidal electron analyzer (cf. Section 3.3), see Fig. 5.1. Because of the above-mentioned molecular orientations, two isolated 5A molecules with perpendicular orientations are considered for the simulated k -maps [compare Fig. 2.10(c) where only one orientation exists]. For 5A/Ag(100), HOMO and HOMO-1 peaks are clearly visible at the HOMO emission maximum direction, while at the LUMO emission maximum direction there is only a truncated LUMO peak at the Fermi edge. For 5A/MgO/Ag(100), both HOMO and LUMO peaks are shifted to higher binding energies and the diminished Fermi edge points at the presence of the MgO layer. The interesting aspect here is that the LUMO peak area with respect to HOMO has slightly increased: it is concluded that the HOMO/LUMO intensity ratio for 5A/Ag(100) is 2 : 0.7, while for 5A/MgO/Ag(100) it is approximately 2 : 1 [36].

The different energy level alignments have been rationalized with fractional charge transfer (FCT) for 5A/Ag(100) and integer charge transfer (ICT) for the case with the MgO(100) interlayer, respectively, see Fig. 5.2. For 5A directly adsorbed on the Ag(100) surface [Fig. 5.2(a)], the molecules undergoes the polarization effect (reduces the LUMO-HOMO gap), the push-back effect (decreases the work function), and also the charge transfer from metal to molecule (increases the work function), similar to the PTCDA/Ag(111) case introduced in Fig. 2.2(c). The net effect on the work function depends on the electron donating (e.g. tetrathiafulvalene) or accepting (e.g. PTCDA, 5A) character of the adsorbed molecules and its magnitude compared to the Pauli push-back [184]. Here a fractional number of electrons per molecule is transferred as a result of highly polarized hybrid orbitals formed at the interface—FCT, whose amount can only be approximated [Fig. 5.2(c)]. In this 5A/Ag(100) example, the peak area at the theoretical LUMO/HOMO maximum is utilized. Noticeably, the charge transfer is accompanied by “Fermi-level pinning” where the Fermi level of the substrate aligns with the partially filled band (LUMO) of the adsorbate layer.

Turning to the 5A/MgO/Ag(100) case, the first major difference is a strongly decreased work function by the formation of 2 ML MgO coverage due to the push-back effect (from 4.3 eV to 2.6 eV). The subsequently adsorbed one ML of 5A, how-

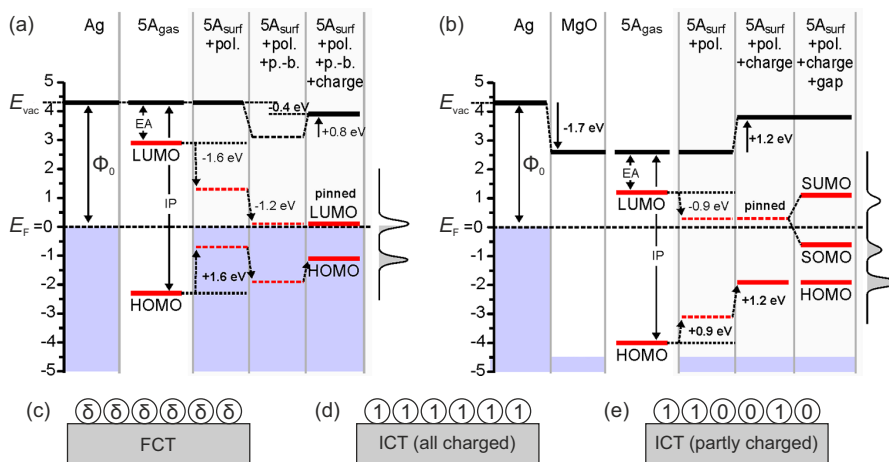


Figure 5.2: Partitioning of the energy level alignment for (a) 5A/Ag(100) and (b) 5A/MgO/Ag(100). Different contributions are abbreviated as: polarization (pol.), push-back (p.-b.), charging (charge), and gap opening (gap). The curves on the right side schematically show the measured spectra. After Fig. 7 of Ref. [36]. Schematic drawing of different charge transfer modes at organic/inorganic interfaces: (c) fractional, (d) all integer-charged, and (e) partly integer-charged.

ever, does not have a similar impact due to its physical separation from metal. For the same reason, the charge transfer is not facilitated by the hybridization between adsorbate and substrate, but via tunneling through the MgO dielectric barrier with an integer amount of charge. The conclusion of ICT [Fig. 5.2(d)] is supported by the finding that the HOMO/LUMO intensity ratio stays constant at 2 : 1 while Φ increases linearly with the 5A coverage. STS measurements also confirmed that the LUMO is singly occupied—split into singly occupied molecular orbital (SOMO) and singly unoccupied molecular orbital (SUMO). A scenario where only part of the molecules receive integer charge [the others remain neutral, see Fig. 5.2(e)] is excluded because a second HOMO peak is not observed and because of the 2 : 1 ratio of HOMO/LUMO.

5.3.3 PTCDA/MgO/Ag(100)

A submonolayer of PTCDA (crucible temperature 580K) was deposited on 2 ML MgO on Ag(100) (preparation recipe described in Section 5.3.1) kept at RT and

5 Decoupling of Molecules at Metal Surfaces

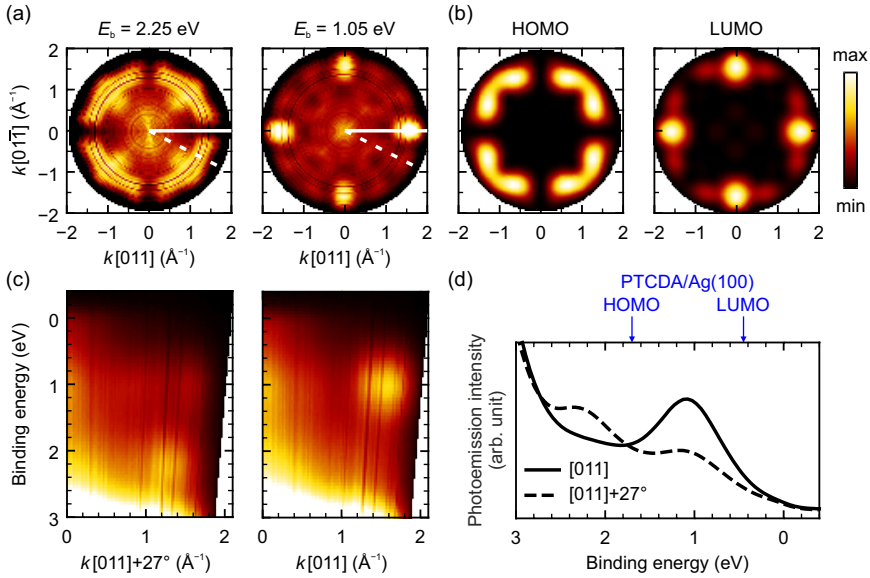


Figure 5.3: PTCDA on MgO on Ag(100). (a) Experimental k -maps measured at binding energies of 2.25 eV and 1.05 eV. White dashed and straight lines illustrate the azimuths used for bandmaps in (c) and integrated EDCs in (d). (b) Theoretical HOMO and LUMO k -maps of two perpendicularly oriented PTCDA molecules [63]. (c) Bandmaps of forward emission in two azimuths, along $[011]$ and 27° away from $[011]$. (d) EDCs of PTCDA/MgO/Ag(100) integrated between $k_{\parallel} = 1.1 \text{\AA}^{-1}$ and 1.8\AA^{-1} along the two azimuths mentioned above. Blue arrows on top depict the binding energies of photoemission resonances of PTCDA HOMO and LUMO on clean Ag(100) [24]. After Fig. 1 of Ref. [109] with added images.

studied by PT with the toroidal electron analyzer (cf. Section 3.3). First, judging by the measured k -maps shown in Fig. 5.3(a), the molecular orientations of PTCDA on the MgO bilayer are also identical to the 5A case, i.e. the long molecular axis parallel to $[01\bar{1}]$ and $[011]$. Therefore, in Fig. 5.3(b) the theoretical k -maps consider two perpendicularly oriented PTCDA molecules, see also Fig. 2.8(b). Apart from some substrate contributions, the measured k -maps at binding energies of 2.25 eV and 1.05 eV resemble the k -space fingerprints of the PTCDA HOMO and LUMO, respectively. Thus the conclusion is that the LUMO of PTCDA deposited on a thin insulating layer of MgO grown on Ag(100) receives charge from the metal, similar to the 5A/MgO/Ag(100) case [36].

Two bandmaps were measured at azimuths where the HOMO and LUMO maxima in theoretical k -maps are expected, i.e. along [011] and 27° away from [011], respectively, see Fig. 5.3(c). Two photoemission resonances are observed at binding energies of 2.25 eV and 1.05 eV, revealing two molecular levels between the Fermi level and the onset of the MgO states. In Fig. 5.3(d), the difference in relative intensities of the two EDCs taken in different orientations indicates a strong angular anisotropy of photoemission, which is typical for ordered organic layers. For instance, along the [011] azimuth the LUMO feature dominates while the HOMO feature is hardly visible.

Moreover, considering the energy level alignment of the molecule/insulator/metal stack we observe both HOMO and LUMO emissions shift to higher binding energies by 0.56 eV and 0.59 eV, respectively, in comparison with PTCDA on pristine Ag(100) [24]. Thus, although the dielectric interlayer physically decouples the molecule from the metal substrate (as hinted by the diminished Fermi edge), it does not prevent charge transfer. Therefore, one cannot consider dielectric interlayers *per se* as decoupling layers. As suggested by Hollerer et al. [36], it is the dramatic lowering of the work function ($\Delta\Phi = -1.7$ eV) due to the push-back by the dielectric layer that promotes the integer charge transfer (ICT), see Section 5.3.2.

5.4 Surface Reconstruction

Surface reconstruction is typical for covalently bonded semiconductors and some 5d-transition metals [124]. It occurs in cases where the dangling bonds of a cleaved single crystal surface become saturated, e.g. Si(111) (7×7), or another material is adsorbed on the single crystal, e.g. by oxidation. Surface reconstructions are expressed in the same way as superstructures (see Section 3.2.1), i.e. in reference to unit cell base vectors of the truncated bulk.

On copper surfaces, the reconstruction resulting from oxygen adsorption has been the subject of many studies [185]. In terms of manipulating the coupling between adsorbate and metal substrate, the Cu(110) $p(2 \times 1)$ -O reconstruction has been used [186–188], see Fig. 5.4(a). Compared to clean Cu(110), Cu(110) $p(2 \times 1)$ -O provides not only a pronounced corrugation with close-packed Cu–O rows oriented along [001] which guide the molecules' growth, but also a chemically less reactive surface [186]. The weak electronic interaction between one ML of 6P and Cu(110) $p(2 \times 1)$ -O was confirmed by UPS [186] and reflectance difference spectroscopy (RDS) [188] studies. Tsukahara et al. [187] reported that iron phthalocyanine (FePc) molecules on the $p(2 \times 1)$ -O surface preserve the triplet spin state as in the bulk, which is switched to singlet on the clean Cu(110) surface.

Similar decoupling results have been reported on various surface reconstruc-

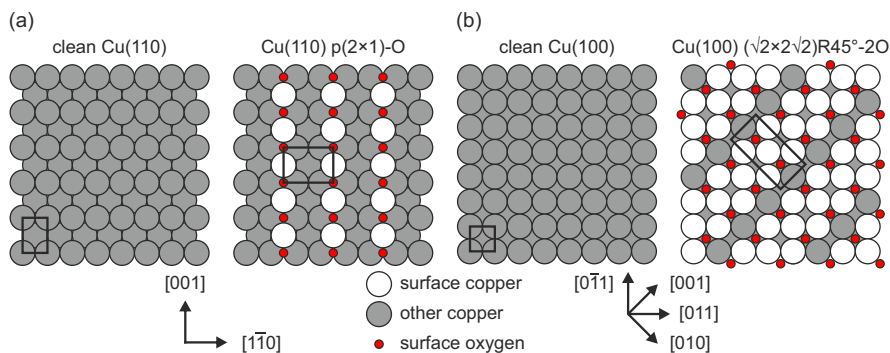


Figure 5.4: Surface reconstruction of copper. (a) Clean Cu(110) and Cu(110) $p(2 \times 1)$ -O added-row reconstruction. (b) Clean Cu(100) and Cu(100) $(\sqrt{2} \times 2\sqrt{2})R45^\circ$ -2O missing-row reconstruction. Unit cells are shown in rectangles.

tions, and not limited to oxidized surfaces, e.g. Cu(110) $c(6 \times 2)$ -O [189], Fe(100) $p(1 \times 1)$ -O [190], Ni(111) $p(2 \times 2)$ -O [191], Cu(100) $(3\sqrt{2} \times \sqrt{2})R45^\circ$ -2Sn (surface Sn alloying) [192], Cu(110) $p(2 \times 3)$ -N [193], and Cu(100) $c(2 \times 2)$ -N [194] (copper nitride layer). In the following sections, a ML of PTCDA on the Cu(100) $(\sqrt{2} \times 2\sqrt{2})R45^\circ$ -2O reconstruction is investigated with PT and NIXSW techniques, combined with DFT calculations.

5.4.1 Oxygen-Reconstructed Cu(100)

A Cu(100) $(\sqrt{2} \times 2\sqrt{2})R45^\circ$ -2O missing-row reconstruction was prepared by exposing the Cu(100) surface to ~ 750 Langmuir of O_2 (oxygen background 5×10^{-7} mbar, 33 min) at the temperature of 500 K [195–197] and confirmed by the appearance of $1/4$ superstructure reflexes in the LEED pattern. Due to the fact that the Cu(100) surface has four-fold symmetry, naturally the missing rows could be either along [001] or [010]. This symmetry is also visible in LEED from the fact that $(1/4, \pm 1/4)$ spots both exist, see the spots marked by red arrows in Fig. 5.5.

Note that the oxygen reconstruction of Cu(100) has been a much debated research topic since the 1980s. Different oxygen adsorption structures [185, 195–200] have been suggested. A more recent summary was done by Duan et al. [201], where it is established that the $(\sqrt{2} \times 2\sqrt{2})R45^\circ$ -2O missing-row reconstructed structure is energetically most favored; at lower oxygen exposures the oxygen adsorption prefers the hollow site, forming the $c(2 \times 2)$ unit cell, i.e. $(\sqrt{2} \times \sqrt{2})R45^\circ$ [cf. Fig. 3.2(b)]. According to their DFT study, the changes relative to the bulk interlayer spacing between the i -th and j -th top copper layers, Δ_{ij} , are: $\Delta_{12} = +4.4\%$,

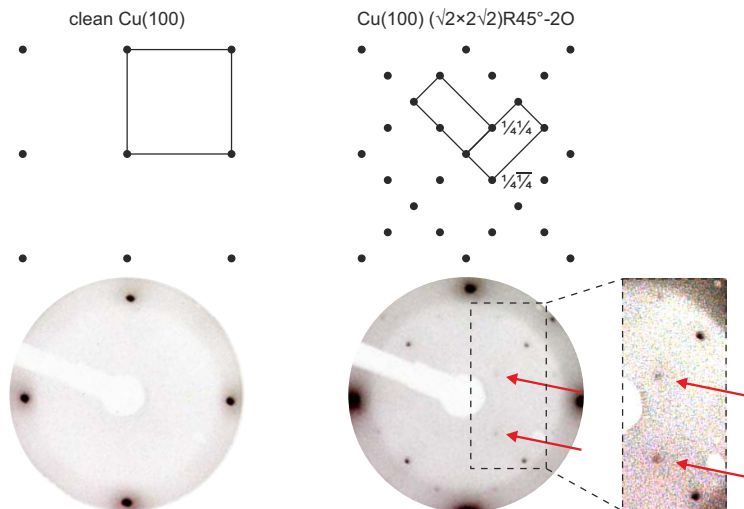


Figure 5.5: LEED model and LEED image of clean Cu(100) and Cu(100) $(\sqrt{2} \times 2\sqrt{2})R45^\circ-2O$ missing-row reconstruction. Reciprocal unit cells are shown in rectangles. Inlet: enlarged view with increased contrast. LEED measurement was performed at the beamline I09 of the Diamond Light Source, Didcot, UK. Electron energy 66eV.

$\Delta_{23} = +2.2\%$, and $\Delta_{34} = +1.1\%$, respectively.⁶ Thus, the topmost copper layer is relaxed outward by approximately 7.7% of the Bragg distance (0.14 Å), which will be later used in the discussion of NIXSW results.

5.4.2 PTCDA on Oxygen-Reconstructed Cu(100)

A submonolayer of PTCDA (crucible temperature 580 K, 20 min) was deposited on the oxygen-reconstructed Cu(100) $(\sqrt{2} \times 2\sqrt{2})R45^\circ-2O$ surface kept at RT [referred as PTCDA/O/Cu(100) in short from now on].

Noticeably, the prepared PTCDA/O/Cu(100) has a different molecular orientation than what was reported by Gärtner et al. [202], see the LEED comparison in Fig. 5.6. In their STM and LEED work, the longer vector of the PTCDA unit cell on the oxygen-reconstructed Cu(100) makes an angle of 6° with respect to [001]. The molecules orient themselves in a herringbone-like pattern, i.e. they adopt an

⁶Note that there is a typo in Table I of Ref. [201]: “MR $(2\sqrt{2} \times 2\sqrt{2})R45^\circ$ ” should be “MR $(\sqrt{2} \times 2\sqrt{2})R45^\circ$ ”.

5 Decoupling of Molecules at Metal Surfaces

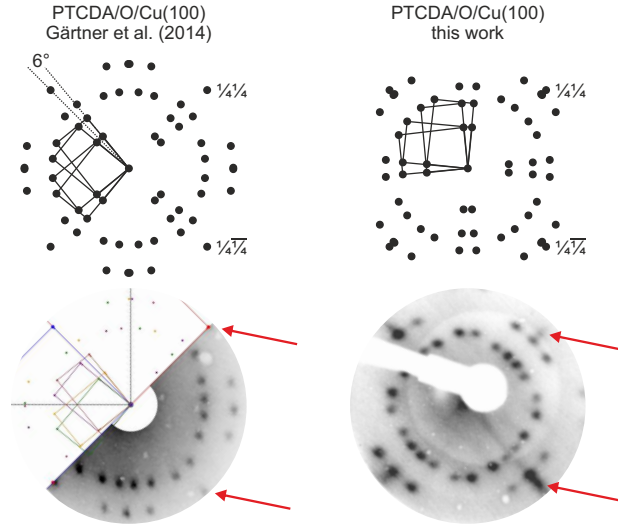


Figure 5.6: LEED model and LEED image of PTCDA/O/Cu(100) in Gärtner et al. [202] and this work. Left: 16 eV, at 220 K, after Fig. 2(b) in Ref. [202]. Right: 14.8 eV, RT, measured at the beamline I09 of the Diamond Light Source, Didcot, UK. Reciprocal unit cells are shown in rectangles.

angle of 90° with respect to each other. The LEED spots can be explained by four symmetry-equivalent domains of the incommensurate PTCDA superstructure and the $(1/4, \pm 1/4)$ spots of the Cu(100) $(\sqrt{2} \times 2\sqrt{2})R45^\circ\text{-}2O$ reconstruction remain visible. The $(\pm 1, 0)$ and $(0, \pm 1)$ LEED spots of PTCDA cannot be detected (16 spots which are closest to the origin in LEED model), which the authors argued to be a consequence of the $p2gg$ symmetry of PTCDA.

In this work, the prepared PTCDA/O/Cu(100) sample has similar LEED features, except that the spots related to the PTCDA layer are rotated by 45° , which is shown by the unmoved $(1/4, \pm 1/4)$ spots of the Cu(100) $(\sqrt{2} \times 2\sqrt{2})R45^\circ\text{-}2O$ reconstruction (see the spots pointed at by red arrows in the LEED images). One assumption to explain this discrepancy is the different sample preparation by Gärtner et al. [202]: on the one hand, they used less oxygen (sample kept at 470 K, oxygen background 1×10^{-6} mbar for 8 min, corresponding to ~ 360 Langmuir); on the other hand, a post-annealing of the sample at 700 K for 10 min was performed. Note that other than the 45° rotation, the two superstructures in Fig. 5.6 are not

exactly identical.⁷ Nevertheless, the size and shape of the unit cell does not allow any significantly different arrangement or orientation of the molecules, i.e. for the PTCDA/O/Cu(100) sample prepared in this work the long molecular axis of PTCDA aligns along the substrate's missing row directions—[001] and [010], with possibly a small misalignment ($< 10^\circ$). In the analysis of PT results below, the experimental k -maps are compared to the calculation that considers a minor misorientation of $\pm 6^\circ$ as in Gärtner et al. [202]. The limited resolution of the experimental k -maps prevents us from fitting a definite result of misalignment, but a misalignment larger than 10° is unlikely and it does not hamper our data interpretations.

PT Results

The EDCs integrated along different azimuths of the PTCDA/O/Cu(100) surface shown in Fig. 5.7(d) have essentially the same profile, with only one pronounced resonance near the top of the Cu d-band, at $E_b = 2.25$ eV, and a shoulder at 1.45 eV. The k -map measured at 2.25 eV [Fig. 5.7(a)] shows a pattern which, despite strong emission in the center, reasonably resembles the theoretical prediction [Fig. 5.7(b)] for the HOMO of a PTCDA monolayer on the Cu(100) ($\sqrt{2} \times 2\sqrt{2}$)R45°-2O surface where molecules align along the substrate's two high symmetry directions with a minor misorientation of $\pm 6^\circ$. At lower binding energies the momentum maps show no distinct structure and, significantly, no pattern that can be associated to the predicted LUMO map. Note that when deposited directly on Cu(100), the PTCDA molecule exhibits a filled LUMO with strong intermolecular dispersion enhanced by molecule-substrate interactions (band width ~ 1 eV, cf. Fig. 2.14) [48]. Clearly, the oxygen adsorbed on Cu(100) has prevented charge transfer from the metal into the molecule and hence indeed has "isolated" the molecular from metallic states.

NIXSW Results

In order to check whether this electronic decoupling goes along with an actual physical separation of the molecule from the surface, NIXSW experiments (cf. Section 3.4) for PTCDA/O/Cu(100) were performed. Prior to the actual NIXSW measurement, XPS spectra before and after PTCDA deposition were acquired for Cu 3s, O 1s, and C 1s core levels to partition contributions from different chemi-

⁷The unit cells in this work and in Gärtner et al. [202] are $\begin{pmatrix} 0.6 & 5.2 \\ -8.2 & 0.8 \end{pmatrix}$, $a_1 = 13.38 \text{ \AA}$, $a_2 = 21.06 \text{ \AA}$, $\gamma = 91.0^\circ$ and $\begin{pmatrix} -3.7 & 3.0 \\ 4.8 & 5.8 \end{pmatrix}$, $a_1 = 12.2 \text{ \AA}$, $a_2 = 19.3 \text{ \AA}$, $\gamma = 90.6^\circ$, respectively. Both are almost rectangular.

5 Decoupling of Molecules at Metal Surfaces

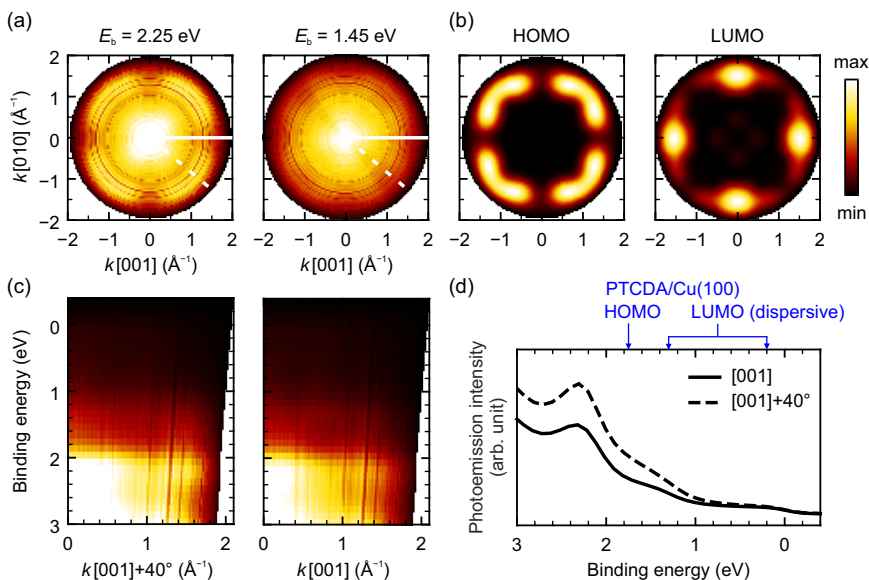


Figure 5.7: PTCDA on oxygen-reconstructed Cu(100) ($\sqrt{2} \times 2\sqrt{2}$)R45°-2O. (a) Experimental k -maps measured at binding energies of 2.25 eV and 1.45 eV. White dashed and straight lines illustrate the azimuths used for bandmaps in (c) and integrated EDCs in (d). (b) Theoretical HOMO and LUMO k -maps of PTCDA molecules with misorientation of $\pm 6^\circ$ to missing-row directions, see text for details [63]. (c) Bandmaps of forward emission in two azimuths, along [001] and 40° away from [001]. (d) EDCs of PTCDA/MgO/Ag(100) integrated between $k_{\parallel} = 1.1 \text{\AA}^{-1}$ and 1.8\AA^{-1} along the two azimuths mentioned above. Blue arrows on top depict the binding energies of photoemission resonances of PTCDA HOMO and LUMO on clean Cu(100) [48]. After Fig. 1 of Ref. [109] with added images.

cal components, see Fig. 5.8. The XPS spectra for oxygen and carbon are shown in Fig. 5.8(b-d): O_{carb} and O_{an} stand for carboxylic and anhydride oxygens of PTCDA, O_{surf} for oxygen atoms in the ($\sqrt{2} \times 2\sqrt{2}$)R45° superstructure, and C_1 and C_{234} for functional and perylene backbone carbons of PTCDA [Fig. 5.8(a)].

The fitting models for these XPS spectra were developed in accordance with the literature [143, 203, 204]:

- O 1s: the binding energy offset between the carboxylic satellite and the carboxylic main peak is fixed at 2.17 eV, while the offset between the anhydride satellite and the anhydride main peak is fixed to 2.20 eV. The carboxylic and

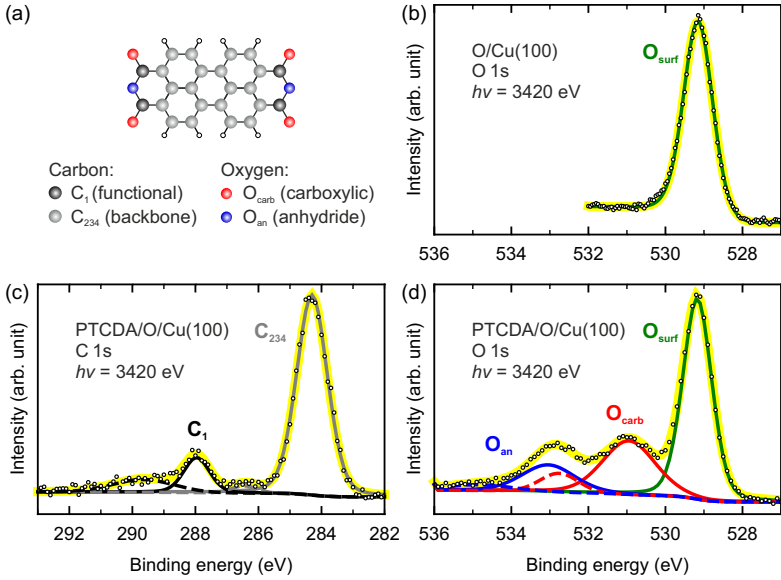


Figure 5.8: Off-Bragg XPS spectra before and after PTCDA deposition on oxygen-reconstructed Cu(100). (a) Ball-and-stick model of the PTCDA molecule, see also Fig. 2.2(a). After Fig. 1 of Ref. [109]. (b) O 1s spectra of oxygen-reconstructed Cu(100) ($\sqrt{2} \times 2\sqrt{2}$)R45°-2O. XPS spectra of PTCDA deposited on oxygen-reconstructed Cu(100) ($\sqrt{2} \times 2\sqrt{2}$)R45°-2O for (c) C 1s and (d) O 1s. In (b–d), raw data are shown as open circles; the fitted components are color-coded as in (a) and oxygen on the copper surface is shown in green; dashed lines show the satellite lines and yellow lines show the fit envelope. After Fig. 2 of Ref. [109] with additional plot.

anhydride main peaks are set to possess the same full width at half maximum. The area constraints between carboxylic and anhydride (also for their satellites) fulfill the stoichiometric ratio 2 : 1. The O_{surf} component has been fitted by only one main peak, see Fig. 5.8(b,d).

- C 1s: the four-peak fitting models developed by Schöll et al. [203] and Mercurio et al. [204] could not be applied here due to insufficient statistics. Hence, instead of fitting three components under the larger peak for the backbone carbons at about 284.3 eV, see Fig. 5.8(c), only a single component called C_{234} was used. The binding energy offsets between the C_1 satellite and the C_1 main peak is fixed at 1.57 eV, between the C_{234} satellite and the C_{234}

5 Decoupling of Molecules at Metal Surfaces

main peak at 2.15 eV.

- Line shape: the main peaks were modeled by Voigt functions with 20% Lorentzian and 80% Gaussian contribution (“SGL(20)” in the XPS analysis software CasaXPS) [205], while the satellite peaks are fitted by pure Gaussian functions (“SGL(0)” in CasaXPS) [141].

In the NIXSW experiments, the Bragg reflection from the copper (200) plane ($d_{200} = 1.807 \text{ \AA}$) was employed, which corresponds to a Bragg energy of 3436.22 eV in the experimental geometry with a tilt angle $\alpha = 3.5^\circ$ against normal incidence (see introduction of NIXSW in Section 3.4). Photoelectron yields from Cu 3s, O 1s, and C 1s core levels were recorded as a function of photon energies around the Bragg energy and fitted in order to extract the height of the corresponding atoms above the crystal Bragg planes. The yield signal was integrated over the acceptance angle of analyzer and angle-dependent non-dipolar correction parameters [137, 138, 143] were calculated for a weighted average of the detection angles (74.8°). The fits of photoelectron yield data were performed with the TORRICELLI program [80], see Fig. 5.9.

Coherent positions P_c and coherent fractions F_c [cf. Eq. (3.5)], averaged over three data sets, are given in Table 5.1. The adsorption heights d of different chemical species in the table are quoted relative to the topmost Cu layer, which is relaxed outward by approximately 0.14 \AA , see Section 5.4.1. Note that the height of O_{surf} before PTCDA adsorption is in good agreement with experiments using LEED $I-V$ analysis [195] (0.1 \AA) and photoelectron diffraction [197] (0.2 \AA to 0.3 \AA). It changes only marginally after PTCDA adsorption. The O_{surf} atoms are located 0.18 \AA above the topmost Cu layer, see Fig. 5.10. This is only consistent with a hollow site on the Cu(100) surface. Thus, as expected from the known structure of the $(\sqrt{2} \times 2\sqrt{2})R45^\circ$ reconstruction, O_{surf} has negligible influence on the surface topography.

All chemical components related to PTCDA, including O_{carb} , O_{an} , C_1 , and C_{234} , have very similar adsorption heights ($\Delta d = 0.16 \text{ \AA}$). This shows that the molecule is hardly distorted upon adsorption, which hints at an effective physical separation from the substrate surface. For comparison, Δd for PTCDA/Cu(100) is twice as large (0.32 \AA) [143], and even for PTCDA/Cu(111) $\Delta d = 0.23 \text{ \AA}$ [206] is larger than what is observed here. The distance of 3.16 \AA between the PTCDA carbon backbone and the O_{surf} atoms is very close to the sum of carbon (1.75 \AA) and oxygen (1.50 \AA) vdW-radii. An even more complete separation is observed between the carbon backbone and the topmost copper atoms, where no overlap of their vdW-radii (1.40 \AA for Cu) is present. These findings prove that PTCDA interacts extremely weakly with the oxygen-reconstructed Cu(100) $(\sqrt{2} \times 2\sqrt{2})R45^\circ$ -2O surface, in sharp contrast to the cases of PTCDA on Au(111) [207], Ag(111) [206, 208],

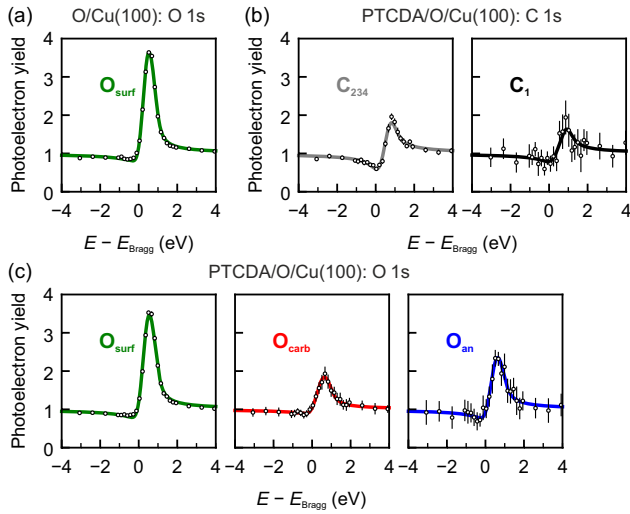


Figure 5.9: Normalized photoelectron yields for (a) O 1s before PTCDA deposition, (b) C 1s and (c) O 1s after PTCDA deposition on oxygen-reconstructed Cu(100) ($\sqrt{2} \times 2\sqrt{2}$)R45°-2O. Raw data are shown as open circles with error bars. Line fits are color-coded as in Fig. 5.8. After Fig. 2 of Ref. [109] with additional plots.

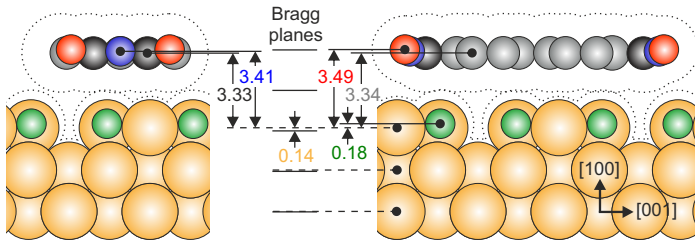


Figure 5.10: Sphere model of PTCDA/O/Cu(100) (side view). The vertical distances are given in Å. Different chemical species are color-coded as in Fig. 5.8. The covalent radii and vdW-radii of surface atoms and adsorbates are drawn as spheres and dotted line, respectively. Note that the lateral registry of molecules is arbitrarily chosen due to the incommensurate superstructure. After Fig. 3 of Ref. [109].

	P_c	F_c	d (Å)
O/Cu(100)			
O _{surf}	0.180(4)	1.16(7)	0.19(1)
PTCDA/O/Cu(100)			
O _{surf}	0.18(1)	1.13(3)	0.18(1)
O _{carb}	0.01(1)	0.41(1)	3.49(2)
O _{an}	0.96(1)	0.52(2)	3.41(2)
C ₁	0.92(2)	0.73(8)	3.33(2)
C ₂₃₄	0.927(3)	0.79(1)	3.342(5)

Table 5.1: Coherent positions P_c and coherent fractions F_c from the NIXSW analysis and adsorption heights d of different chemical species with respect to the topmost copper layer. The adsorption height d with respect to the Bragg plane is given by $(n + P_c)d_{200}$ where $n = 0$ for O_{surf}, $n = 1$ for O_{an}, C₁, and C₂₃₄, $n = 2$ for O_{carb}. After Table S1 of Ref. [109].

Ag(100) [142], Cu(111) [206], Ag(110) [142, 204], and Cu(100) [143], for which the adsorption heights of the carbon backbone decrease from 3.27 Å to 2.46 Å and are always smaller than the sum of vdW-radii of carbon and the corresponding substrate atom.

DFT Results

The PT and NIXSW results above prompt us to ask why the incorporation of oxygen into the Cu(100) surface leads to this simultaneous electronic and physical decoupling.

The first thing to notice is that it cannot be solely due to the increase of the work function induced by the oxygen coverage, because compared to the clean Cu(100) surface, the Cu(100) ($\sqrt{2} \times 2\sqrt{2}$)R45°-2O missing-row reconstruction increases the work function by approximately 0.3 eV [201, 209, 210] to ~4.9 eV—roughly the same as that of clean Cu(111) [211], where a strong chemical interaction accompanied by an occupation of the PTCDA LUMO has been observed [212]. Clearly, there must be an additional mechanism in operation. When a molecule approaches a surface, Pauli repulsion pushes back the spill-out electrons in front of the surface. This push-back effect commonly leads to a reduction of the work function and a concomitant change in level alignment, see e.g. Fig. 2.2. One hypothesis is that the oxygen in the reconstructed surface does not only raise the work function, but also effectively immobilizes electrons at the surface in localized covalent Cu–O bonds: The electrons of metal atoms now involved in covalent

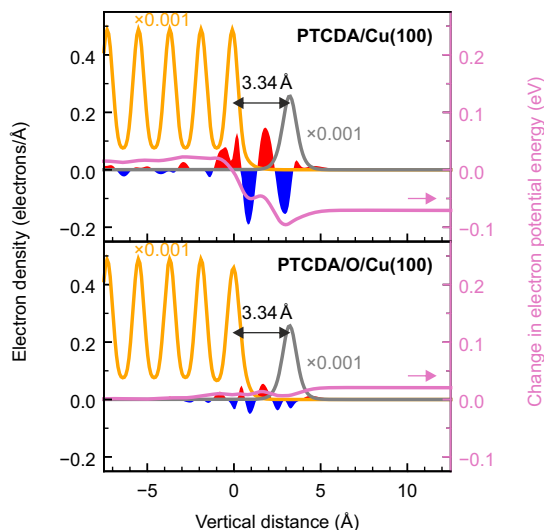


Figure 5.11: Plane-averaged electron density of the substrate (orange) and adsorbed PTCDA (light gray), electron density difference (red/blue) and change in electron potential energy (purple) as a function of the vertical z -direction. The origin of vertical distance is set to be at the topmost copper layer and negative z stands for the substrate. The slightly weaker peak for the topmost copper layer in PTCDA/O/Cu(100) is due to the surface reconstruction. After Fig. 4 of Ref. [109]. Calculations by P. Puschnig.

bonding with oxygen atoms lose their free-electron character. As a consequence, the displacement of the substrate's electronic charge arising from the push-back effect due to the electrons of the adsorbate is suppressed. Therefore, the adsorbed molecules experience additional repulsion preventing both a close approach of PTCDA to the surface and the reduction of the work function upon PTCDA adsorption.

To test this hypothesis, DFT calculations (cf. Section 3.5) were performed for PTCDA on clean Cu(100) and PTCDA on oxygen-reconstructed Cu(100) ($\sqrt{2} \times 2\sqrt{2}$)R45°-2O at the adsorption height experimentally determined on the second system (3.34 Å), see Fig. 5.11. The charge redistribution upon PTCDA adsorption, shown as red (blue) areas for regions of electron accumulation (depletion), are calculated with the charge density difference $\Delta\rho$ [21]:

$$\Delta\rho(\mathbf{r}) = \rho_{\text{full}}(\mathbf{r}) - [\rho_{\text{molecule}}(\mathbf{r}) + \rho_{\text{substrate}}(\mathbf{r})], \quad (5.1)$$

where the charge densities of two subsystems, isolated molecule layer ρ_{molecule}

5 Decoupling of Molecules at Metal Surfaces

(PTCDA) and isolated substrate $\rho_{\text{substrate}}$ [clean Cu(100) or oxygen-reconstructed Cu(100) ($\sqrt{2} \times 2\sqrt{2}$)R45°-2O], and the charge density of the full system ρ_{full} are calculated separately. The results are then plane-averaged, i.e. along x, y , and the associated changes in the electron potential energy is obtained by integrating $\Delta\rho(z)$ twice along z according to the one-dimensional Poisson's equation [167].

For PTCDA/Cu(100), there is a strong signature of the push-back effect, resulting in a significant reduction of the work function as hinted by the potential drop (purple curve), although the adsorption height in the calculation is substantially larger than in equilibrium (2.46 Å). In reality, the effect for PTCDA/Cu(100) would be even larger. Conversely, only minor charge rearrangements take place when PTCDA adsorbs on the oxygen-reconstructed Cu(100) ($\sqrt{2} \times 2\sqrt{2}$)R45°-2O surface, with an almost unchanged electron potential energy upon approach of the molecule. As a consequence, the work function remains high on this surface even after PTCDA adsorption and serves as an effective barrier for charge exchange between the metal and the molecule.

In summary, the oxygen pre-coverage on Cu(100) electronically decouples PTCDA from the substrate in the sense that there is no charge transfer to the molecule, and that at the same time the molecule is also physically well separated from the substrate. Such electronic surface hardening by the formation of covalent bonds within the uppermost surface layer is anticipated to be a general mechanism for promoting electronic decoupling and physical separation of molecular adsorbates from the substrate.

5.5 2D Materials

Recently, 2D materials have been identified as another alternative for decoupling molecules from a metal substrate, especially hexagonal boron nitride (hBN) due to its chemical stability and electrical insulation property (wide band gap of ~6 eV). A monolayer hBN sheet on a metal substrate varies from being flat and weakly bonded on e.g. Cu(111), Ag(111), to being highly corrugated (often with Moiré patterns due to lattice mismatch) and stronger bonded on e.g. Ir(111), Rh(111), depending on the reactivity of the chosen metal substrate [213]. For the molecular adsorbates deposited on hBN/Ir(111) [214] and hBN/Rh(111) [215, 216], the molecule-metal interaction on the pore of the Moiré pattern is enhanced compared to elsewhere, which is also accompanied with the tendency that the adsorbates laterally get trapped in those pores. On hBN/Cu(111), some studies have shown that the deposited molecular adsorbates on top of it are electronically unperturbed by the underlying metallic states [217, 218].

Similarly, the passivation of the surface has been realized with graphene on iridium [219] and with epitaxial graphene on SiC [220, 221], or even just with a

closed monolayer of hexabenzocoronene on gold [222]. In the following sections, some ARPES results of PTCDA on hBN/Cu(111) are shown for comparing with other decoupling mechanisms introduced in this chapter.

5.5.1 hBN Growth on Cu(111)

A monolayer of hBN on Cu(111) is grown by dosing liquid borazine from a cooled glass tube through a leak valve while keeping the copper crystal at 800–820 °C in vacuum. Typically, the base pressure is in the order of 1×10^{-10} mbar, and the pressure during borazine dosing is kept at 1.5×10^{-6} mbar. The borazine in the glass tube needs to be continuously cooled to approximately -4 °C to minimize degradation [213]. Upon adsorption of borazine on the hot Cu(111), the precursor molecules undergo thermal decomposition and form the boron nitride nanosheets.

A quantitative characterization of the hBN/Cu(111) system was done by Brülke et al. [213]. NIXSW results show that boron and nitrogen atoms in the hBN layer have large adsorption heights, 3.25 Å and 3.22 Å respectively, with respect to the topmost Cu(111) layer, i.e. the hBN layer is extremely flat and well separated from Cu(111). Spot profile analysis low energy electron diffraction (SPA-LEED) images of hBN/Cu(111) have a star-like diffraction pattern around the specular (0,0) spot, which is due to the multiple scattering of electrons and the lattice mismatch between Cu(111) and hBN (the latter by 2.2% smaller at 300 K).

5.5.2 PTCDA/hBN/Cu(111)

A monolayer and a bilayer of PTCDA (crucible temperature 580 K) were deposited on the hBN/Cu(111) surface kept at RT, respectively. The ARPES results of these two systems are shown in Fig. 5.12, with hBN/Cu(111) as a reference. The band dispersion of hBN/Cu(111) is similar to that of graphene [223]: two concave parabolas of σ -band with the same top (see the region marked with a red rectangle) and a convex parabola of π -band at $\bar{\Gamma}$, the latter can be observed in the angle-integrated spectra at ~ 8.8 eV in Fig. 5.12(b). Upon the deposition of PTCDA, several flat bands with almost no dispersion emerge, see the bandmaps of PTCDA ML and PTCDA bilayer on hBN/Cu(111) in Fig. 5.12(a). The binding energies of these flat bands are at about 3.8, 4.9, 5.5, 6.2, and 7.8 eV, which can be assigned to PTCDA due to their similarity with the gas-phase PTCDA spectrum [224], see dashed lines in Fig. 5.12(b).

In the binding energy region between the copper d-bands and the Fermi level ($E_b < 2.0$ eV), only a continuous intensity exists, in contrast to the case without an hBN interlayer where a filled LUMO peak is visible in this region [212]. The band dispersion before and after the PTCDA coverage mainly differs in the intensity of the above-mentioned flat bands of PTCDA, see Fig. 5.12(a). The lack

5 Decoupling of Molecules at Metal Surfaces

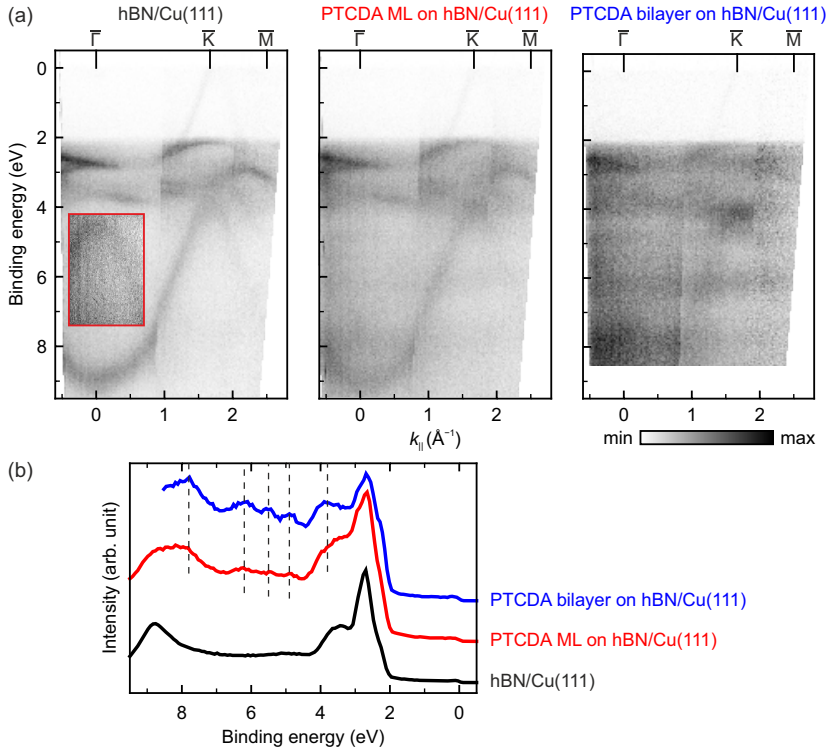


Figure 5.12: ARPES data of hBN/Cu(111) and of PTCDA on hBN/Cu(111). (a) Band dispersion measured along the $\bar{\Gamma}$ - \bar{K} direction of the Brillouin zone of hBN. The region marked with a red rectangle has an enhanced contrast to show the two concave parabolas of σ -band. (b) Angle-integrated spectra between $\bar{\Gamma}$ and \bar{K} ($\sim 1.67 \text{\AA}^{-1}$). Dashed lines in (b) highlight the positions of PTCDA flat bands with almost no dispersion upon molecule adsorption. Photoemission spectra were measured using He II α excitation (40.81 eV) in 45° incidence with a hemispherical electron analyzer (Scienta R4000) at Peter Grünberg Institut (PGI-3), Forschungszentrum Jülich.

of charge transfer is also evidenced by the work function measurements, derived from the secondary electron cutoff: the work function of Cu(111) upon the hBN coverage changes by $\Delta\Phi = -0.50 \text{ eV}$, showing that hBN suppresses the spill-out of the copper states; after the PTCDA deposition the work function is only slightly decreased, by less than 0.05 eV , due to the push-back effect (cf. Section 2.1).

The NIXSW experiments show that the perylene backbone carbons of PTCDA has adsorption height of 3.37 Å on hBN/Cu(111) [169], which is even slightly larger than that on oxygen-reconstructed Cu(100) ($\sqrt{2} \times 2\sqrt{2}$)R45°-2O surface (3.34 Å, cf. Section 5.4.2). This large adsorption height (largest for PTCDA backbone reported so far, see Fig. 4 of Brülke et al. [169]) reconciles the weak electronic interaction between PTCDA and copper.

5.6 Conclusion

In Sections 5.3, 5.4, and 5.5, three decoupling methods using a dielectric interlayer, a surface reconstruction, and a 2D material are discussed. With PTCDA as the probing molecule, three systems including PTCDA/MgO/Ag(100), PTCDA on oxygen-reconstructed Cu(100) ($\sqrt{2} \times 2\sqrt{2}$)R45°-2O, and PTCDA/hBN/Cu(111), respectively, are tested. The dielectric interlayer does not necessarily prevent the charge transfer from metal to molecule, if the work function is strongly lowered by the dielectric. The latter two methods could in general prevent the charge transfer, with different mechanisms: the oxygen pre-coverage results in the formation of covalent bonds between the oxygen and surface atoms so that the surface metal electrons are immobilized and the molecular adsorbates are electronically decoupled; the 2D material (here hBN as an example) physically separates molecules from the metal substrate and the spill-out of metallic states is strongly suppressed.

To choose which way to decouple molecules at metal surfaces depends on various aspects. One needs to consider the feasibility of sample preparation, e.g. different thickness of the MgO dielectric interlayer shows work function values of a wide range, which in turn opens the possibility to vary the strength of charge transfer by controlling the prepared thickness [225]. The surface reconstruction is only applicable on certain type of surfaces via oxidization or other methods. Because of the surface reconstruction, the structure may be utilized to guide the growth of molecular adsorbates so that all molecules align in the same direction for PT studies. Similar effect can be expected for 2D materials on some surfaces where the interlayer is not perfectly flat and molecules are attracted into the pores of its Moiré pattern.

6 Equally Charged or Not: Coexisting Charge States in a Unary Organic Monolayer Film

6.1 Introduction

In this chapter, the electronic and geometric structure of tetracene films on Ag(110) and Cu(110) is studied with PT and compared to that of pentacene.

Part of the results shown in this chapter have been published in the following journal article: X. Yang, L. Egger, J. Fuchsberger, M. Unzog, D. Lüftner, F. Hajek, P. Hurdax, M. Jugovac, G. Zamborlini, V. Feyer, G. Koller, P. Puschnig, F. S. Tautz, M. G. Ramsey, and S. Soubatch, “Coexisting charge states in a unary organic monolayer film on a metal”, *J. Phys. Chem. Lett.* **10**, 6438 (2019) [226].

6.2 Charge Transfer Scenarios at Molecule–Metal Interfaces

In Fig. 2.2, the electronic structure of the molecule–metal interface was briefly introduced. The following processes will occur when a molecule adsorbs on a metallic surface: First, the molecule gets physically attracted by non-covalent van der Waals interactions [227]. Then, the ionization potential (IP) and electron affinity (EA) levels of the molecule are renormalized due to the proximity of the metal because of polarization effects [24, 32, 228, 229]. Once the electronic wave functions of the molecule and the metal start to overlap, hybridized states arise at the interface [106, 230–235]. If the level alignment permits, charges can be transferred, resulting in the population of formerly unoccupied molecular states or the depopulation of formerly occupied ones. Many examples of such charge transfers are known [37, 90, 106, 110, 236–242].

If either the adsorption configuration or the molecular environment varies from one molecule to another, the amount of transferred charge can vary laterally as well. This is schematically illustrated in Fig. 5.2(c–e) for three different charge transfer modes—fractional charge transfer (FCT), homogeneous integer charge

transfer (ICT), and inhomogeneous integer charge transfer. However, the so far reported electronically inhomogeneous interfaces exhibit only a marginal variation of the electronic levels [15, 110] or have been observed in binary monolayers where the competition between two molecular acceptors (PTCDA–CuPc) results in preferential charge transfer to the stronger one (PTCDA) leaving the second species (CuPc) neutral [19]. An alternative scenario has been recently predicted theoretically: a thin insulating film on a metal [36, 243] or the doping of ZnO [244] substrates has been suggested to trigger inhomogeneously charged ICT and to lead to the formation of a molecular layer consisting of alternating charged and uncharged molecules [Fig. 5.2(e)].

But to the best of current knowledge, an experimental realization of the coexistence of different charge states in a unary organic film, i.e. a film containing only one type of molecule, on a metal substrate has not yet been reported. In the following, a ML of tetracene on Ag(110) is shown to consist of molecules with negative and neutral charge states, thus being the first experimental demonstration of unequal charge states in a unary organic monolayer film.

6.3 Tetracene on Cu(110)/Ag(110)

6.3.1 Literature Review

In the case of tetracene (4A) on Cu(110) and Ag(110) there is a delicate balance between weak intermolecular and interfacial interactions. This leads to multiple structural motifs [245–250] and may be the reason for the difficult reproducibility of experimental results and discrepancies in data interpretation:

In an early study of 4A/Cu(110), Yannoulis et al. [251] found an upright standing orientation of molecules. Later, it was suggested that the molecular plane is actually parallel to the substrate [245, 247]. Beyond the first ML, a poorly controlled coverage of 4A caused by its high vapor pressure may lead to structural transformations and a reorientation of the molecules in the first layer [245, 247]. On Ag(110), where the molecule–substrate interaction is weaker than on copper, various structures of 4A have been reported [246, 248, 249]. A recent coverage-dependent study by Takasugi and Yokoyama [250] of 4A/Ag(110) showed several structural transformations occurring up to 1 ML. The molecules, however, always have their molecular axes parallel to the substrate and the interface registry is reportedly commensurate.

The complicated and diverse structural organization of the interface is mirrored by controversial interpretations of its electronic structure. Recent UPS studies of 4A on Cu(110) and Ag(110) have attempted to correlate observed photoemission spectra to the DOS obtained from DFT calculations [247, 249]. However, the

assignment of photoemission peaks is often merely inferred and even with the assistance of DFT calculations the interpretation of UPS spectra is not reliable. PT, with the k -space resolution, allows the unambiguous and straightforward energy level assignment (see Section 2.3.3.2). Meanwhile, the geometric structure of molecular orientation can also be correctly determined by PT (see Section 2.3.3.1).

6.3.2 Sample Preparation

The Cu(110) and Ag(110) substrates were cleaned by Ar⁺ sputtering cycles and annealing at 800 K. A ML of pentacene (5A) was prepared at RT by exposure corresponding to a layer thickness of 4 Å. The preparation of tetracene/metal samples is experimentally challenging because of tetracene’s high vapor pressure. Therefore, here a ML of tetracene is considered to be the saturation coverage originating from the tetracene background vapor from the Knudsen-type evaporator. It is known that the growth of tetracene films on silver is self-limiting to 1 ML and the second layer is unstable at RT [252]. During tetracene accumulation on Ag(110) from the tetracene background vapor, the sequence of tetracene adsorption layers with increasing submonolayer coverage was recorded for UPS studies.

6.3.3 Density of States

The PT experiments were performed with the NanoESCA PEEM at Elettra synchrotron, Trieste, Italy (see Section 3.2.3). In the energy-filtered PEEM mode, p-polarized light (photon energy 35 eV⁸, angle of incidence 65°) was used to record the three-dimensional data cube $I(E_{\text{kin}}, k_x, k_y)$. Experiments were performed on two pairs of Ag and Cu crystals mounted along two perpendicular high symmetry directions such that the plane of incidence included the [001] or [1 $\bar{1}$ 0] azimuths. Integrating intensities corresponding to a fixed E_{kin} over the entire available k_{\parallel} range (around $\pm 2.0 \text{ \AA}^{-1}$) results in angle-integrated EDCs. To avoid beam damage to the molecular layer due to the high-intensity focused photon beam, the sample position was laterally scanned throughout the measurement.

In Fig. 6.1 the EDCs are shown for pentacene and tetracene on Ag(110) and Cu(110), where pentacene is discussed in the following as a reference. The emissions of 5A are in agreement with earlier PT studies which have identified the orbitals and molecular orientations [23]. On Cu(110), the 5A molecules lie flat on the surface and parallel to [1 $\bar{1}$ 0] as has been observed in STM [253]. The emissions down to 1.2 eV below the Fermi level E_{F} arise from the former LUMO, populated

⁸Note that there is an error in Methods section of Ref. [226]: “photon energy 30 eV” should be “photon energy 35 eV”.

6 Coexisting Charge States in a Unary Organic Monolayer Film

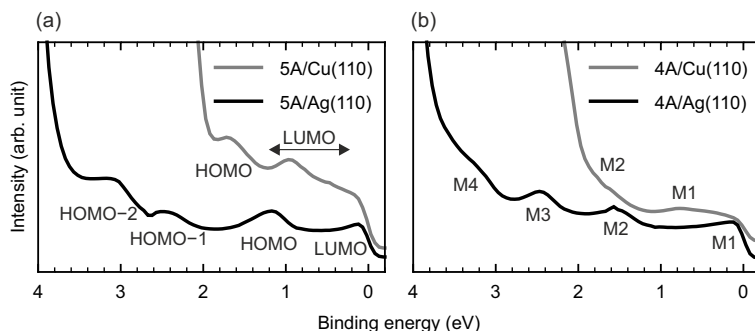


Figure 6.1: Angle-integrated energy distribution curves measured for (a) pentacene (5A) and (b) tetracene (4A) on Ag(110) and Cu(110). The orbital assignment for 5A is adopted from Ref. [23]. For 4A the emissions are numbered in order of increasing binding energy with respect to the Fermi level as M1, M2, M3, and M4. After Fig. 1 of Ref. [226].

due to charge donation from the metal and strongly dispersing due to substrate-assisted intermolecular dispersion [23]. The emission at 1.7 eV corresponds to the HOMO of pentacene. On Ag(110), the 5A molecules lie across the atomic rows of the surface and parallel to the [001] azimuth. The interaction is weaker than on copper, the LUMO is only fractionally occupied and is observed at E_F , while the HOMO, HOMO-1, and HOMO-2 emissions are at 1.2, 2.4, and 3.1 eV [23, 43]. Not only have these been identified from angular distributions, but also from the real-space reconstructions of the orbitals [43].

The EDCs of the saturated monolayer of 4A on Cu(110) and Ag(110) [Fig. 6.1(b)] resemble those of 5A [Fig. 6.1(a)]. Thus it is tempting to assign the electronic levels of 4A similar to 5A. Surprisingly, in the following it will be shown that this would lead to a wrong interpretation in case of 4A/Ag(110), as its geometric and electronic structure is very different.

6.3.4 DFT Calculations

While the properties of 5A on both surfaces are well-established, they are still debated for 4A/Ag(110) [246, 248–250]. As a first attempt to clarify the case, DFT calculations were performed on several models corresponding to different structural motifs and coverages reported in literature. For all tested cases, the peak positions in the pDOS are similar and can be adequately assigned to experimentally observed M1, M2, and M3 emissions. Two representative cases are shown in

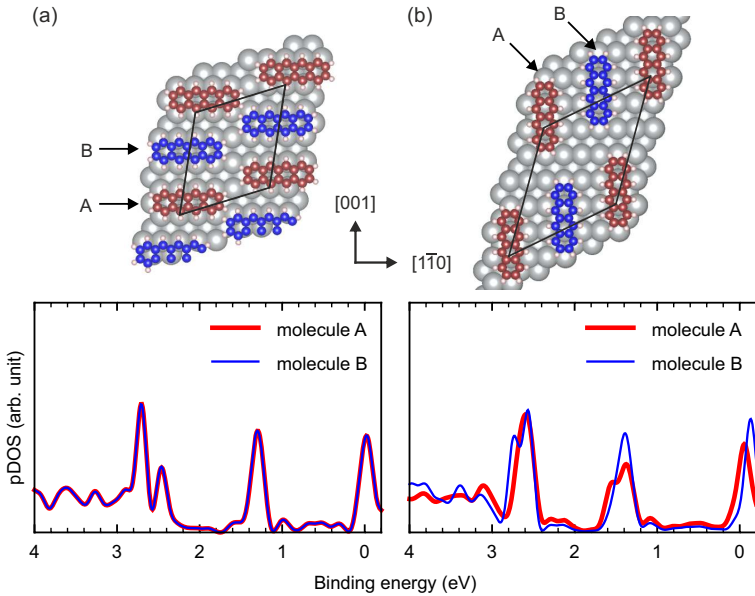


Figure 6.2: Molecular supercell and projected density of states (pDOS) in DFT simulations for two exemplary structures of 4A/Ag(110): (a) 4A along the $[1\bar{1}0]$ direction, (b) 4A along the $[001]$ direction. The pDOS of two sets of molecules in the unit cell (marked as molecule A and B) is drawn as red and blue lines, respectively. After Fig. 1 of Ref. [226]. Courtesy of M. Unzög.

Fig. 6.2. Fig. 6.2(a) displays the structurally relaxed $\begin{pmatrix} 5 & 1 \\ 1 & 4 \end{pmatrix}$ superstructure with two molecules per unit cell. The molecules' long axes are oriented parallel to the atomic rows ($[1\bar{1}0]$ direction) as observed by Takasugi and Yokoyama [250] for coverages beyond 0.8ML. The starting configuration of this calculation had the two molecules in the unit cell at different heights; however, the molecules equalize their heights and achieve identical pDOS upon structural relaxation. Fig. 6.2(b) represents the structure suggested by Huang et al. [248]. This $\begin{pmatrix} 6 & 2 \\ 2 & 5 \end{pmatrix}$ unit cell includes two molecules oriented across the atomic rows with slightly different heights. Here relaxation did not result in the same heights and the LUMO of the molecule further away from the surface remains unoccupied, while the molecule closer to the substrate is slightly charged. Thus DFT suggests the presence of two electronically inequivalent molecular species in this supercell.

It is worth noting that DFT, in the case of 4A/Ag(110), first fails to make a definitive prediction for the interface structure and electronic properties because variations in the adsorption energy among structurally very different models are minor, and second, the pDOS calculations show only negligible variations beyond the sensitivity of conventional UPS. The first finding agrees with the multiplicity of structures reported for 4A/Ag(110) and experimental results which are sensitive to preparation conditions. The second finding demands for more advanced spectroscopic methods to reveal the electronic structure.

6.3.5 Momentum Maps

In Fig. 6.3 and Fig. 6.4(a,b), the experimental k -maps for photoemission peaks denoted in Fig. 6.1 are compared to theoretical ones simulated for corresponding isolated molecules.

6.3.5.1 Pentacene on Cu(110)/Ag(110)

Fig. 6.3 reveals a good agreement between experiment and simulation for 5A on Cu(110) and on Ag(110) [23]. Note that the geometry factor (Section 2.3.2.2) of p-polarized incident light results in the asymmetry of intensity distributions. The well-defined patterns of experimental k -maps prove that for both cases the molecules in the monolayer are parallel to each other.

Because the substrate is not taken into account in the simulations, there are deviations between the experimental and theoretical k -maps. For instance, the structure within the main emission lobes of the 5A LUMO on Cu(110) caused by intermolecular dispersion [14, 23, 32, 49] is not reproduced in simulations for free molecules. These secondary effects, however, do not prevent an unambiguous assignment of each emission to a particular molecular orbital. This in turn allows the extraction of geometric information regarding the orientation of the molecules on the surface with high sensitivity (Appendix C). Comparison with the simulated k -maps confirms that 5A adsorbs strictly flat and along the $[1\bar{1}0]$ direction on Cu(110) and along $[001]$ on Ag(110).

6.3.5.2 Tetracene on Cu(110)/Ag(110)

The k -maps of 4A HOMO and LUMO on Cu(110) have good agreement with the simulations [Fig. 6.4(a)], except for the structure within the main LUMO lobes due to intermolecular dispersion, see preceding Section 6.3.5.1. Compared to 5A/Ag(110), the PT results of 4A/Ag(110) in three different preparations are more complicated, showing a coverage-dependent reorientation behavior.

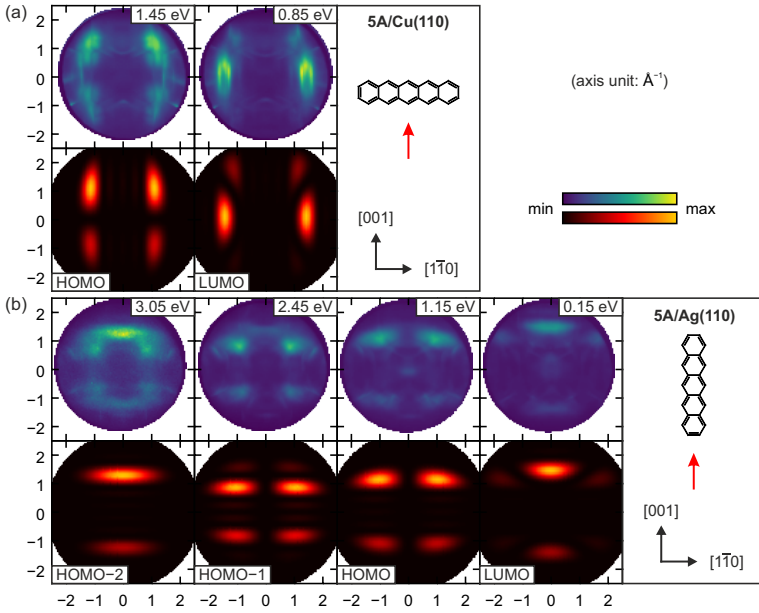


Figure 6.3: Experimental (upper row) and simulated (lower row) k -maps for (a) 5A/Cu(110) and (b) 5A/Ag(110). Experimental k -maps are taken at E_b (insets) corresponding to the peaks in Fig. 6.1(a). Simulated k -maps of the isolated 5A molecules are calculated corresponding to the sketches on the right showing the assigned molecular orientations with respect to the incident light (red arrow) and the substrate [63]. After Fig. 2 of Ref. [226].

Before discussing the molecular orientations, noticeable differences from three preparations of 4A/Ag(110) can be seen in the EDC spectra [Fig. 6.5(a)]: at low coverage, a small peak appears at 2.4 eV; at moderate coverage, the peak at 2.4 eV grows higher and the second peak at 1.5 eV appears as a broader shoulder on the low binding energy side; at saturation coverage, the second peak at 1.5 eV is clearly visible and the LUMO peak can be seen just below the Fermi level at 0.1 eV [the same curve as in Fig. 6.1(b)].

Analysis of the corresponding k -maps in the following shows that the peak just below the Fermi level, at 0.1 eV, resembles the 4A LUMO simulation [M1 as in Fig. 6.1(b)], indicating charge transfer at the interface. The peaks at 2.4 eV and 1.5 eV both have the HOMO character, i.e. maxima at $(k_{[1\bar{1}0]}, k_{[001]}) = (1.0 \text{\AA}^{-1}, 1.0 \text{\AA}^{-1})$. Due to the order of their appearance on exposure

6 Coexisting Charge States in a Unary Organic Monolayer Film

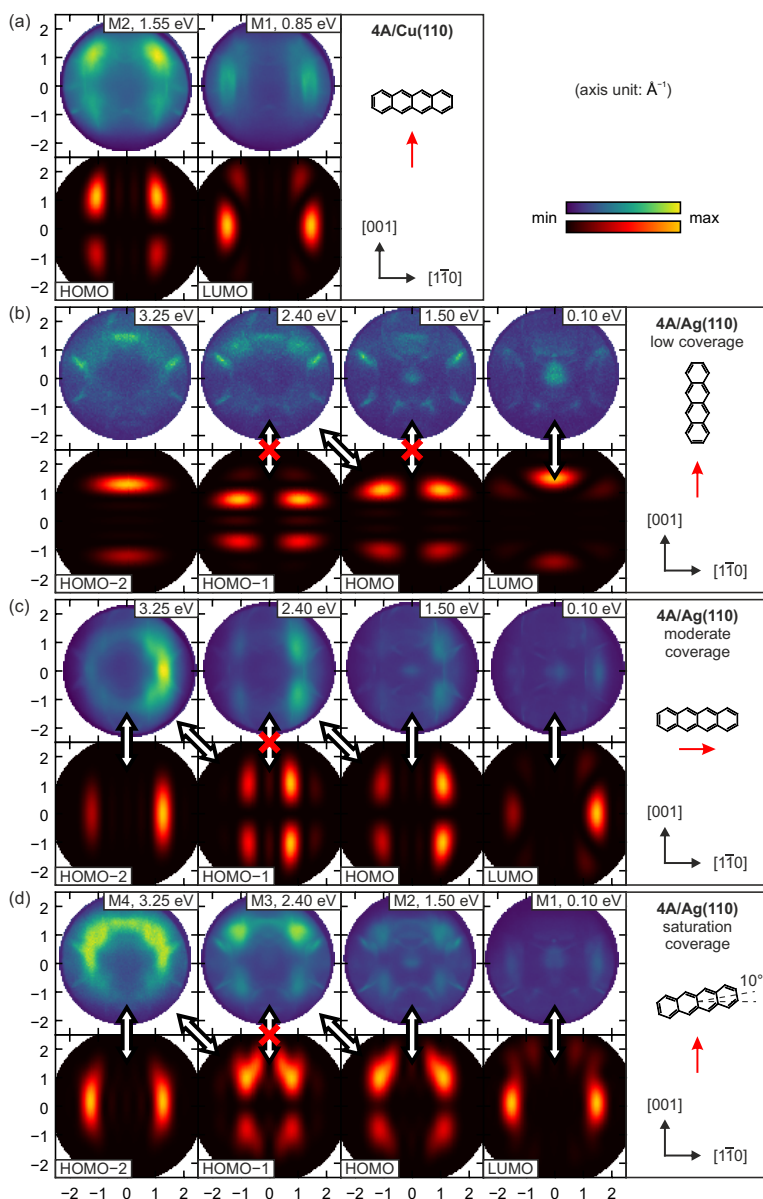


Figure 6.4: Experimental (upper row) and simulated (lower row) k -maps for (a) 4A/Cu(110), saturation coverage; (b–d) 4A/Ag(110), low (b), moderate (c), and saturation (d) coverage. Experimental k -maps are taken at E_b (insets) corresponding to the peaks in Fig. 6.1(b). Simulated k -maps of the isolated 4A molecules are calculated corresponding to the sketches on the right showing the assigned molecular orientations with respect to the incident light (red arrow) and the substrate [63]. After Fig. 2 and Fig. S4 of Ref. [226].

the two HOMO emissions are referred to as HOMO_A and HOMO_B [M3 and M2 as in Fig. 6.1(b)], respectively.

Fig. 6.4(b–d) shows the comparison between experimental k -maps at binding energies of 0.10, 1.50, 2.40, and 3.25 eV and simulations of LUMO, HOMO, HOMO–1, and HOMO–2 (The full series of experimental k -maps are shown in Fig. S5–S7 of Ref. [226]), which yields the molecular orientation as a function of coverage:

- At low coverage [Fig. 6.4(b)], only the HOMO pattern of the A molecule is clearly recognized at 2.40 eV binding energy; its intensity distribution reveals that molecules are aligned flat and parallel to the [001] direction. Importantly, only substrate emissions are detected at 1.50 eV, proving the absence of B molecules on the surface. The LUMO is expected to be occupied; however, due to low intensity, it is barely visible in the experimental k -map at 0.10 eV. The experimental k -map at 3.25 eV may contain intensity corresponding to HOMO–2 and HOMO–1, but this overlaps with relatively strong substrate emissions.
- At moderate coverage [Fig. 6.4(c)], the intensity patterns observed at binding energies of 0.10, 1.50, 2.40, and 3.25 eV clearly resemble the k -maps of, respectively, LUMO, HOMO_B, HOMO_A, and joint contributions of HOMO–1 and HOMO–2. Thus two electronically distinct 4A species are present on the surface. Orientations of experimentally observed patterns point at re-orientation of molecules from along [001] at low coverage to along [110] at moderate coverage.
- At saturation coverage [Fig. 6.4(d)], the assignment of the observed intensity distributions is similar to that at the moderate coverage [Fig. 6.4(c)]. However, the modifications of the HOMO_A and HOMO_B main lobes suggest a $\pm 10^\circ$ azimuthal misalignment of the molecules (cf. simulations in Fig. C.2).

The observed behavior in the orientation of the 4A molecules with increasing coverage up to the saturated ML at room temperature ([001] \rightarrow [110] \rightarrow [110] misaligned) is in agreement with that reported for 0.70, 0.85, and 0.94 molecule/nm² in the STM study of Takasugi and Yokoyama [250].

Coming back to the electronic structure of 4A/Ag(110): in Fig. 6.4(b–d), the correlation (or lack of correlation) between simulation and experiment is indicated by double-headed white arrows (or white arrows with red cross). Normally, one would expect to observe HOMO, HOMO–1, HOMO–2, ... below the Fermi level, with increasing binding energy. If charge transfer takes place, then also LUMO is also observable in a photoemission experiment. However, the anomaly here is that two emission peaks, separated by 0.9 eV, both have HOMO character (HOMO_A and

6 Coexisting Charge States in a Unary Organic Monolayer Film

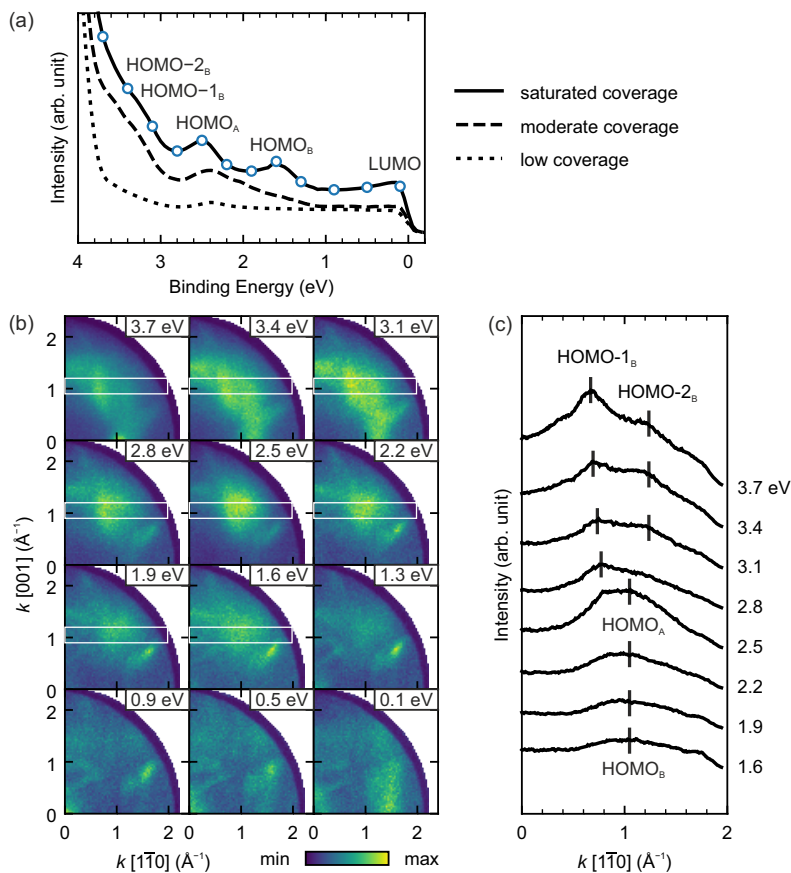


Figure 6.5: Photoemission results of 4A/Ag(110). (a) Angle-integrated EDC spectra in three different preparations. The intensity is normalized between the three preparations. (b) Segments of the k -maps for saturated ML 4A/Ag(110) at binding energies marked in (a) with empty circles. (c) Photoemission intensities integrated in the area marked in (b) with white rectangles. k -space positions of the maxima of corresponding molecular orbitals are marked with vertical bars. After Fig. S3 and Fig. 3 of Ref. [226].

HOMO_B, or M3 and M2). The k -maps of 3.25 eV at moderate and saturation coverage appear to have joint contributions of HOMO-1 and HOMO-2. This is clear when the experimental k -maps are more accurately analyzed, see Fig. 6.5(b,c).

Using a set of experimental k -maps of 4A/Ag(110) corresponding to the EDC of the saturation coverage [Fig. 6.5(a)], it is obvious that as E_b increases from 1.3 eV to 2.5 eV all k -maps show similar patterns characteristic for the 4A HOMO. Then at about $E_b = 2.8$ eV the intensity pattern changes from the 4A HOMO to that of the 4A HOMO-1 as indicated by a shift of the lobes from 1.0 \AA^{-1} to 0.8 \AA^{-1} along $k_{[1\bar{1}0]}$ [Fig. 6.5(c)]. Beyond 3.1 eV the HOMO-2 emission dominates, although the HOMO-1 contribution is still noticeable. Thus the HOMO-1 level can be identified in the k -maps, although due to its location at the Ag d-band onset it is difficult to discern in the EDC.

The remaining question is, what exactly is the origin of the 0.9 eV energy splitting of the 4A HOMO? There are two possible scenarios that could lead to it: either it is a real state splitting caused by interfacial or intermolecular interactions, or it is due to the presence of two electronically different tetracene species. The first can be ruled out, because such a large level splitting would require an exceptionally strong interaction, while tetracene is known to interact only relatively weakly with noble metals. Note that even more chemically active molecules (e.g. 5A, PTCD [15]) do not exhibit such strong level splitting on Ag(110). Moreover, DFT does not indicate any splitting for the HOMO for either 4A or 5A. Therefore, the two HOMOs in Fig. 6.4(c,d) should belong to different 4A species.

6.3.6 UPS Results

To find out the two 4A species that give rise to the two energetically distinct HOMOs, the coverage-dependent evolution of the electronic properties of 4A/Ag(110) is further analyzed with UPS (Section 2.2). The experiments were performed with a hemispherical Scienta SES-200 analyzer by L. Egger, F. Hajek, and Prof. M. G. Ramsey of the University of Graz, Austria. Here the change of the work functions $\Delta\Phi$, measured using the secondary electron cutoff (Section 2.2) in normal emission, was utilized for the indirect estimation of the tetracene coverage. After the saturation of 4A coverage at RT is reached, i.e. when the UPS spectrum and the work function Φ do not change with increasing exposure time any more, the sample was cooled down to liquid nitrogen temperature (here around 100 K) to produce a multilayer for comparison with the monolayer.

Fig. 6.6(a) shows spectra measured with He I α excitation for the clean Ag surface (green curve, work function $\Phi = 4.35$ eV), sub-ML 4A film (blue curve, change of the work function $\Delta\Phi = -0.15$ eV), saturated ML (red curve, $\Delta\Phi = -0.6$ eV), and multilayer film condensed at 100 K (black curve). The strong emissions from the Ag d-band decrease with exposure, but still dominate even for saturated monolayer of 4A. For the ML sample three emissions are observed at 1.5, 2.5, and 3.2 eV in agreement with PT measurements. At sub-ML coverages, it is evident

6 Coexisting Charge States in a Unary Organic Monolayer Film

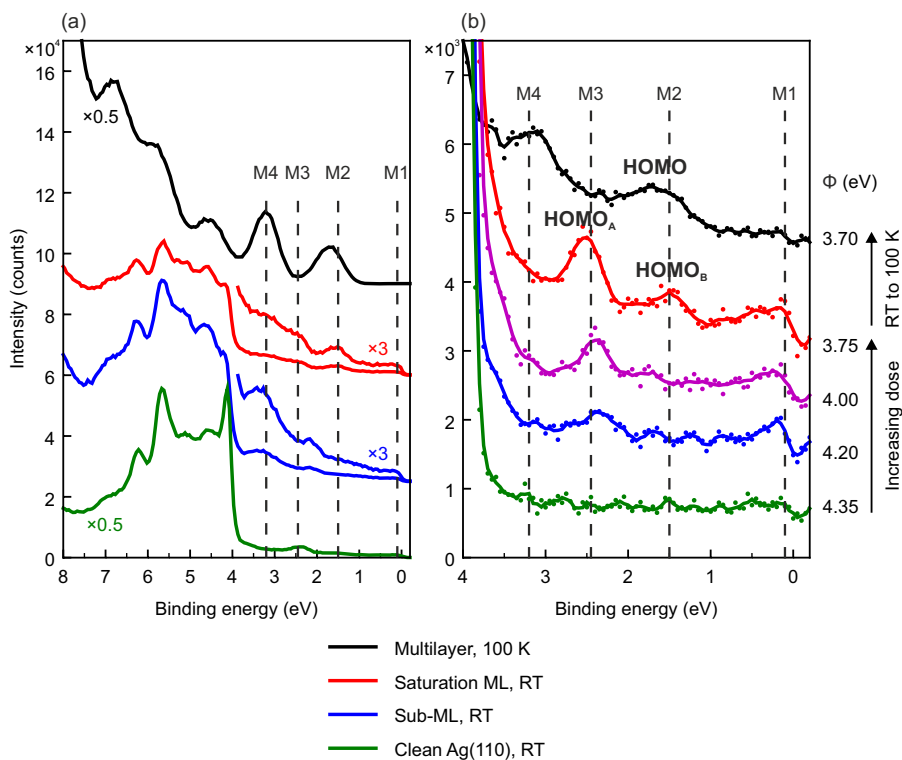


Figure 6.6: Coverage-dependent UPS spectra of 4A/Ag(110). (a) He I α excitation (21.22 eV), angle of emission 45°. (b) He II α excitation (40.81 eV), angle of emission 30°. The change of work function is listed beside the curves. After Fig. 4 of Ref. [226]. Measurement performed by L. Egger, F. Hajek, and M. G. Ramsey.

that the HOMO-related emission at 1.5 eV is not observed. An unambiguous assignment of the features above 2 eV to the adsorbate, however, is not possible due to parasitic emissions from the Ag d-band excited by the He I β line [cf. Fig. 6.6(a), green curve, peak at 2.4 eV].

To avoid this parasitic emission, UPS measurements using He II α light were performed [Fig. 6.6(b)]. On increasing exposure of 4A, a photoemission resonance first appears and grows at 2.4 eV, then only beyond about half of the saturation coverage ($\Delta\Phi \sim -0.35$ eV) the 1.5 eV HOMO emission appears. Note that this evolution of spectra is in good agreement to the EDC curves of the coverage-dependent

PT results [Fig. 6.5(a)] which show that the two energetically well separated HOMOs appear once the molecules adopt the [110] orientation [Fig. 6.5(b–d)].

As mentioned in preceding Section 6.3.5.2, these two HOMO emissions are referred to as HOMO_A and HOMO_B, respectively, according to the order of their appearance. Importantly, the E_b of HOMO_A changes only marginally after the second resonance, i.e. HOMO_B, appears. This additionally proves that HOMO_A and HOMO_B belong to two different molecular species, because otherwise the level splitting should have significantly affected its binding energy. HOMO_A (appearing first) can be assigned to dilute 4A sub-ML and associated with molecules having a fractional occupation of the LUMO. As HOMO_B appears later and with an energy close to the HOMO of the multilayer (Fig. 6.5, black curves), it is intuitively tempting to assign it to a bilayer species.

However, a number of observations speak against the bilayer assumption and testify that it is due to a second, but electronically neutral, species within the first monolayer:

- First, the work function continues to decrease as HOMO_B grows. Generally, for molecular film growth on metals, $\Delta\Phi$ is dominated by the push-back effect (Section 2.1) and thus saturates on completion of the first monolayer [24].
- Second, the HOMO_A emission is not attenuated on the appearance of HOMO_B, suggesting that the B molecules are not on top of the A molecules.
- Third, the suppression of the Ag emissions for the saturated tetracene is similar to that of the 4 Å wetting monolayer of pentacene on the Ag surface.
- Finally, the PT results show that the B species lies with its aromatic plane parallel to the substrate (significant tilting of 4A can be excluded, cf. Fig. C.1), while beyond the first ML rod-like aromatic molecules adopt tilted geometries, as the intermolecular interactions favor for the bulk-like structure [3, 7]. In particular, tetracene on Ag(111) tends to adopt out-of-plane geometry beyond the first ML [229].

Interestingly, although there are two distinct HOMO resonances originating from different 4A molecules, only one weak emission attributed to the former LUMO is observed, see Fig. 6.1(b). Moreover, the binding energy of HOMO_B matches that of 4A multilayer. Thus the conclusion is that the B species remains uncharged and, correspondingly, the 4A ML on Ag(110) includes two electronically inequivalent species, charged and uncharged, representing a specific case of an electronically inhomogeneous, unary molecular film of two coexisting charge states.

Author	Year	Methods	Orientation of tetracene's long axis
Lu et al. [246]	2005	STM	[001]
Huang et al. [248]	2008	STM, DFT	[001]
Tao et al. [249]	2015	UPS, DFT	prefers [001]
Takasugi and Yokoyama [250]	2016	STM	[001] \rightarrow $[\bar{1}\bar{1}0] \rightarrow [\bar{1}\bar{1}0] \pm 10^\circ$
Liang et al. [254]	2020	STM, DFT	$[\bar{1}\bar{1}2]$

Table 6.1: List of publications on 4A/Ag(110). See the text for more remarks.

6.4 Discussion

The finding of two coexisting charge states is quite novel and its reason can, at present, only be speculated upon. One suggestion is that the charge transfer to the LUMOs of the dilute ML molecules leads to a surface dipole that increases the local work function in their vicinity, such that the energy alignment for additional tetracene molecules is not conducive to charge transfer to them. Presumably, pentacene does not show this phenomena due to its higher electron affinity.

In the literature, various assignments of molecular orientation for 4A on Ag(110) have been made, see the summary in Table 6.1. The STM studies by Lu et al. [246] and Huang et al. [248] and the UPS study by Tao et al. [249] all suggested that the tetracene's long axis is along the [001] direction. The conclusion made by the latter, however, merely relied on DFT calculations of different adsorption sites, and the efforts to relate the UPS spectra directly with calculated pDOS can be problematic (see e.g. Section 2.3.3.2). Takasugi and Yokoyama [250] performed a coverage-dependent STM study and showed the reorientation behavior, in agreement with the PT results presented in Section 6.3.5.

One intriguing possibility to explain the coexisting charging states of 4A on Ag(110): Huang et al. [248] reported at coverage of 0.67 molecule/nm² there are two molecules in the unit cell, where the neighboring 4A molecules were imaged with alternating bright and dim STM contrast. This was assigned to be two distinct adsorption heights and could be in agreement with the PT result of charged and uncharged molecules in the moderate/saturation coverage, but the orientation observed in this thesis is $[\bar{1}\bar{1}0]/[\bar{1}\bar{1}0] \pm 10^\circ$ instead. Recently, in a follow-up publication by the same group, Liang et al. [254] clarified that the conclusion of different heights are incorrect due to incomplete DFT calculations for describing the long-range electron correlations. With the vdW interaction included, their new STM/DFT results have given a $[\bar{1}\bar{1}2]$ orientation, which is $\sim 35^\circ$ away from [001].

The alternating bright and dim STM contrast taken at -1.5V bias⁹ therein could be related to the PT results in this thesis: one would expect uncharged molecules appear HOMO-like ($E_b = 1.5\text{eV}$ of HOMO_B) and charged molecules ($E_b = 2.4\text{eV}$ of HOMO_A) appear LUMO-like, provided that the submolecular resolution is observable at all. The STM imaging of HOMO/LUMO for 4A should be different judging by the existence or non-existence of a nodal plane along the molecular long axis, see the similar example for 5A in Fig. 2.1. However, the authors concluded that the STM contrast is bright and dark HOMOs in agreement with their DFT simulations and the molecular orientation is different from this work and their previous work.

Note the STM work by Takasugi and Yokoyama [250] showed no differences of adjacent molecules in all reported structures. Whether charged and uncharged molecules can be differentiated in STM depends on tip and bias conditions, which are very different in the STM works reported so far. To completely elucidate the coexisting charge states and their appearances in STM imaging, more rigorous (probably coverage-dependent) studies are needed.

A similar competition for the donated charge between adsorbed molecular species was recently reported for binary (or called heteromolecular) monolayer of PTCDA–CuPc [19] with the dominant charge transfer to PTCDA accompanied by equalizing the adsorption heights of the two species.

6.5 Conclusion

Summarizing, the electronic and structural properties of tetracene and pentacene on Ag(110) and Cu(110) were studied using conventional and k -space resolved photoemission. On copper, both oligoacenes adsorb similarly, forming monolayers of flat-lying molecules oriented along the $[1\bar{1}0]$ azimuth. Both tetracene and pentacene are charged on Cu(110), with the former LUMO exhibiting substrate-enhanced intermolecular dispersion.

In contrast, on Ag(110) tetracene and pentacene monolayers behave qualitatively differently. While pentacene lies across the atomic rows of the substrate, tetracene's orientation changes in a coverage-dependent manner. The difference in electronic properties is even more intriguing. Pentacene/Ag(110) represents an example of the common situation of charge transfer at the molecule/metal interface with the former LUMO of all molecules fractionally occupied because of electron donation from metal. Unlike that, for tetracene, PT and coverage-dependent conventional UPS clearly prove the presence of two electronically inequivalent molecular species in the saturated monolayer—charged and uncharged. This

⁹To avoid confusion, here the conventional bias signs (positive for LUMO and negative for HOMO, see Fig. 2.1) are used, in opposite to the assignments in Liang et al. [254].

6 Coexisting Charge States in a Unary Organic Monolayer Film

makes the tetracene/Ag(110) a unique example of an electronically inhomogeneous unary molecular monolayer on a metal surface.

7 Scattered or Not: Momentum-Resolved Hybridization of Molecular and Metal States

7.1 Introduction

The hybridization of adsorbate molecules' orbitals at a metal surface is of significance to the understanding of molecule–metal surface electronic properties. To address the extent to which particular molecular states are modified upon bonding with metal states, it is convenient to start the discussion with a thick layer (several hundreds Å) of molecular films. On low-index metal surfaces, the tiled molecular crystallites can be grown in a controlled way, enabling the investigation of intra- and intermolecular band dispersion, see [Section 2.3.3.5](#). For a thick layer of molecular films, the influence of the metal substrate can be neglected, as conventional photoemission methods probe only the near-surface region of a few Å. In the examples of pentacene (5A) [4] or p-sexiphenyl (6P) [3] thick layers on a metal, depending on the measurement direction, the band structure can be related to the periodicity of molecular crystallite for intermolecular band dispersion or to the inter-ring spacing for intramolecular band dispersion. The momentum maps (k -maps) measured in angle-resolved photoemission experiments can be directly compared to the FT of DFT calculations which are based on isolated gas-phase molecules, an approach which is termed PT [7].

Decreasing the thickness of the molecular overlayer down to the monolayer region, the structure of molecular orbitals will be modified through the molecule–metal hybridization. In general, the energy levels of molecular π states are broadened in the interaction with metallic states, especially delocalized sp -bands of the substrate. This broadening is also accompanied by the HOMO–LUMO gap reduction and a possible (partial) orbital filling or emptying through charge transfer (see [Section 6.2](#)). These modifications are mostly discussed only concerning the energy level alignment as the figure of merit from a device point of view. Even within the PT approach, when a momentum-space view (k -map) is used to iden-

tify which orbital is located at which energy, calculations based on isolated gas-phase molecules already suffice in many cases, see e.g. [Chapters 4, 5, and 6](#). For instance, the sp-band of a metal fcc (110) substrate appears as two stripes along $\bar{X}\text{--}\bar{S}$ in the k -map measured for the Fermi surface, but it does not greatly distort the photoemission pattern of a certain orbital.

However, the full picture is that the molecular states are always (to certain extent) modified upon bonding with metallic states. The influence of the metal on molecular states can take the following shapes:

1. Modification of the momentum structures of the molecular orbital (corresponding to deformation of the real-space structure).
2. (Substrate-mediated) intermolecular dispersion, i.e. coupling of neighboring molecular orbitals (through the substrate).
3. k -dependent hybridization: molecular and metal states can hybridize, but this needs overlap not only in energy and real space, but also in reciprocal k -space.

This is studied by e.g. symmetry analysis [\[255\]](#), resonant photoemission [\[256\]](#), and recently PT with damped plane wave final states ([Section 2.3.2.2](#)) [\[48, 49\]](#). In the PT approach, the DFT calculations have considered not only single molecules, but a full overlayer–substrate system in the unit cell, which convincingly addressed the strong intermolecular dispersion of the molecules' LUMO that appear in the k -maps. The last point (3) was addressed by Berkebile et al. [\[9\]](#) where the bonding of 6P with the Cu(110) surface with a strong hybridization was studied, without including substrate in calculations. For the complete, commensurate ML coverage of 6P on Cu(110), there are evident deviations of the k -distribution of LUMO from that of the free molecule. These deviations demonstrate a hybridization of the molecular orbital and metal states around the copper bulk energy gap, whose k -positions are directly related to the 6P overlayer periodicity. This shows that for molecule–metal hybridization to occur, not only do states require overlap in energy and real space, but also in momentum.

In this chapter, we revisit the momentum-resolved molecule–metal bonding by investigating six similar oligomer systems, p-sexiphenyl (6P), p-quinquephenyl (5P), and pentacene (5A) on Cu(110) and on Ag(110), respectively. The difference between these systems and features in a broader range of k -space than that reported by Berkebile et al. [\[9\]](#) are discussed in detail.

7.2 Experimental Details

The Cu(110) and Ag(110) substrates were cleaned by Ar⁺ sputtering cycles and annealing at 800K. 4Å thick layers were grown by sublimating molecular material at 550K (6P), 500K (5P), and 475K (5A), respectively, for suitable time while the sample was kept at RT.

The PT experiments were performed with the NanoESCA PEEM at Elettra synchrotron, Trieste, Italy (Section 3.2.3). In the energy-filtered PEEM mode, p-polarized light (photon energy 35eV, angle of incidence 65°) was used to record the three-dimensional data cube $I(E_{\text{kin}}, k_x, k_y)$. Experiments were performed on two pairs of Ag and Cu crystals mounted along two perpendicular high symmetry directions such that the plane of incidence included the [001] or [1 $\bar{1}$ 0] azimuths. Note, to avoid beam damage of the molecular layer due to the high-intensity focused photon beam, the sample position was laterally scanned throughout the measurement.

To ease the comparison, for all k -maps in this chapter the incidence direction is from the negative side to the positive side along the y -axis. As a result of the geometry factor of p-polarized incident light, the k -maps show an asymmetry where the intensity of the upper half is higher, see Fig. 3.6.

7.3 Clean Cu(110) and Ag(110)

A stack of k -maps were measured for the clean Cu(110) and Ag(110) surfaces, respectively, between the Fermi level and the metal d-band, see Figs. 7.1 and 7.2. Because the k -maps were measured in small binding energy steps (0.025eV or 0.05eV), bandmaps can be retrieved with the instrument-intrinsic energy dispersion taken into account, see Section 3.2.3. For clean Cu(110) and Ag(110), at photon energy 35eV, the E_{kin} scales are shifted by approximately 0.1eV at $k_y = \pm 2\text{Å}^{-1}$ compared to that at $k_y = 0\text{Å}^{-1}$. As discussed in Section 3.2.3, two types of k -maps can thus be presented, the as-obtained ones with higher signal-to-noise ratio and the corrected ones. The latter one has a lower k -space resolution, but guarantees that all points in the k -map correspond to the same E_{kin} , which is important for our discussions about the surface states later on. Note, all k -maps presented in this chapter have been corrected for this parasitic energy dispersion unless otherwise specified.

First, the Fermi surface maps for the clean Cu(110) are shown in Fig. 7.1(a). The surface Brillouin zone (SBZ) is drawn with the symmetry points $\bar{\Gamma}$, \bar{X} , \bar{Y} , and \bar{S} labeled. The Shockley surface state is located at \bar{Y} , $(k_{[001]}, k_{[1\bar{1}0]}) = (\pm 0.87\text{Å}^{-1}, 0\text{Å}^{-1})$, with its major axis along the \bar{Y} - \bar{S} . The Shockley surface state is observed as a parabola in the bandmap along \bar{Y} - \bar{S} direction and possesses a dispersion from the

7 Momentum-Resolved Hybridization of Molecular and Metal States

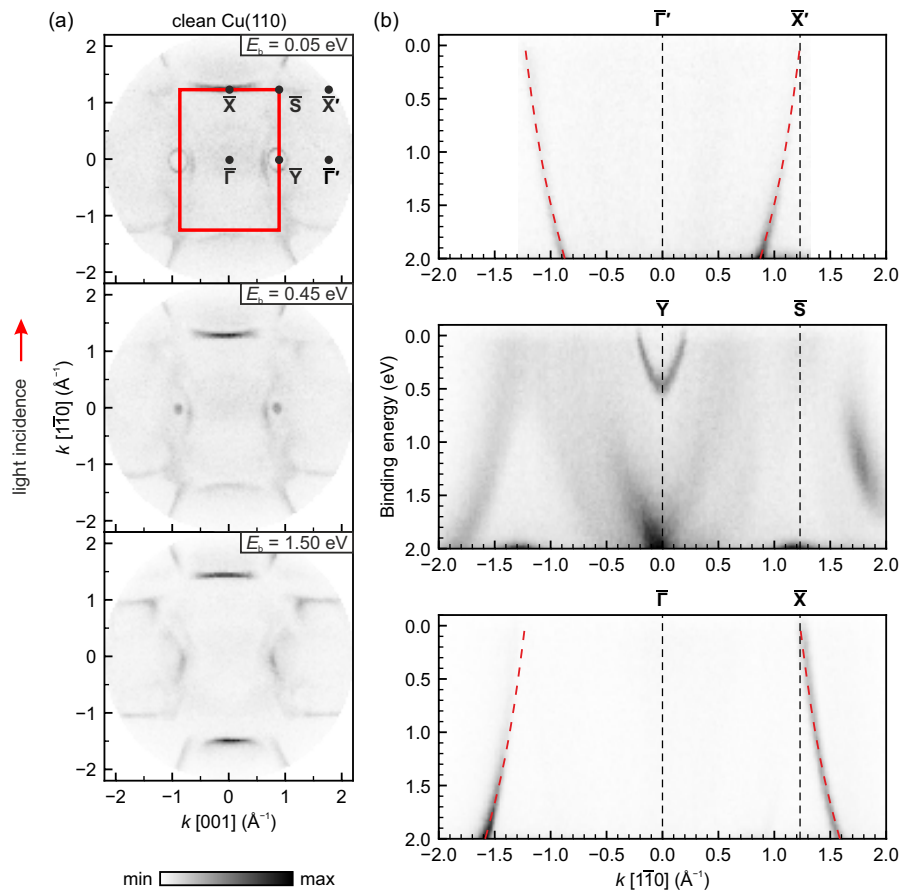


Figure 7.1: Photoemission results of the clean Cu(110) surface. (a) k -maps measured at $E_b = 0.05$ eV, 0.45 eV, and 1.50 eV. The first one (Fermi surface) shows the Shockley surface state at \bar{Y} . The SBZ of the Cu(110) surface is drawn as a rectangle. (b) Bandmaps measured along $[1\bar{1}0]$ through different high-symmetry points, $\bar{\Gamma}$, \bar{Y} , and $\bar{\Gamma}$. Dispersive sp-bands are marked with red dashed lines.

Fermi level E_F down to $E_b = \sim 0.45$ eV [257, 258], see Fig. 7.1(b). Besides that, the main feature is the dispersive sp-band between E_F and $E_b = \sim 2.0$ eV, marked as red dashed lines in the bandmap along $\bar{\Gamma}$ - \bar{X} and along $\bar{\Gamma}'$ - \bar{X}' (prime symbol

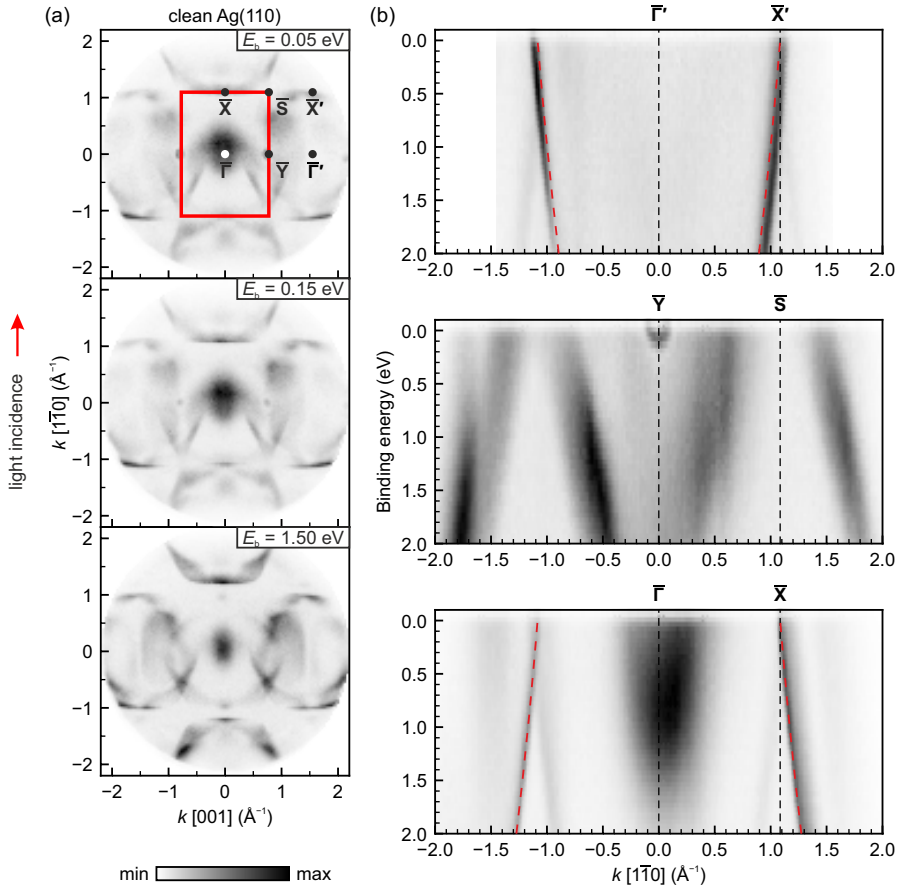


Figure 7.2: Photoemission results of the clean Ag(110) surface. (a) k -maps measured at $E_b = 0.05$ eV, 0.15 eV, and 1.50 eV. The first one (Fermi surface) shows the Shockley surface state at \bar{Y} . The SBZ of the Cu(110) surface is drawn as a rectangle. (b) Bandmaps measured along $[\bar{1}\bar{1}0]$ through different high-symmetry points, $\bar{\Gamma}$, \bar{Y} , and \bar{S} . Dispersive sp -bands are marked with red dashed lines.

represents the neighboring SBZ).

The photoemission results of the clean Ag(110) surface are similar to that of Cu(110), see Fig. 7.2. The main differences are: (1) the SBZ of Ag(110) is smaller compared to Cu(110) because of a different lattice constant (4.079 Å vs. 3.597 Å),

as are the $\bar{\Gamma}$ - \bar{X} and $\bar{\Gamma}$ - \bar{Y} distances, (2) the Shockley surface state at \bar{Y} is located lower in binding energy, bottom of which is at around $E_b = \sim 0.1$ eV [259], and (3) additionally, there is a prominent intensity appearing at $\bar{\Gamma}$. The origin of the latter is not yet resolved, but may be assigned to an s-like substrate contribution [8].

7.4 6P/5P/5A on Cu(110)

LEED

The structures of the prepared 6P/Cu(110), 5P/Cu(110), and 5A/Cu(110) samples are summarized in Fig. 7.3. 6P/Cu(110) possesses a highly ordered $c(22 \times 2)$ structure when the ML is completed [9, 186, 260]. Similarly, the superstructure of 5P/Cu(110) is also centered, $c(18 \times 2)$, slightly smaller than the one of 6P/Cu(110). Various structures for an overlayer of the shorter 5A molecule on Cu(110) have been reported [23, 245, 253, 261–264]. In accordance with the literature, 5A/Cu(110) prepared in this work has a structure close to $p(7 \times 2)$, but the long-range order is less defined as hinted by the diffuse LEED reflexes.

According to the LEED models and images, the real-space monolayer structure of each case is displayed in Fig. 7.3(c). The 6P, 5P, and 5A molecules all lie flat on the surface with their long axes parallel to $[\bar{1}\bar{1}0]$, the orientation of these systems will be verified later in the measured k -maps. For flat-lying molecules possessing the same orientation, the appearance of their molecular orbitals are easily predicted by PT with help of the plane wave final state approximation (Section 2.3.2) in the theoretical k -maps, as shown in Fig. 7.3(d).

EDC

In Fig. 7.4(a), the EDCs integrated for all k values from the data cube $I(E_b, k_x, k_y)$ are shown for 6P, 5P, and 5A on Cu(110). The populated former LUMO of 5A has a strong intermolecular dispersion, resulting in a broad feature size, in agreement with earlier PT studies [23]. For 6P and 5P, the LUMO is also occupied upon adsorption, but the peak just below the Fermi level is relatively sharp. Because of the intense copper d band at binding energies larger than 2.0 eV, the HOMO is the only other emission peak observable, at about 1.7 eV to 1.8 eV for all three molecules.

At chosen energies close to the Fermi level, k -maps were measured to investigate whether and how the Shockley surface state is altered upon the adsorption of molecules. These energies are marked as short vertical lines in Fig. 7.4(a). It will be shown in the following that these states were identified as the former LUMO using PT.

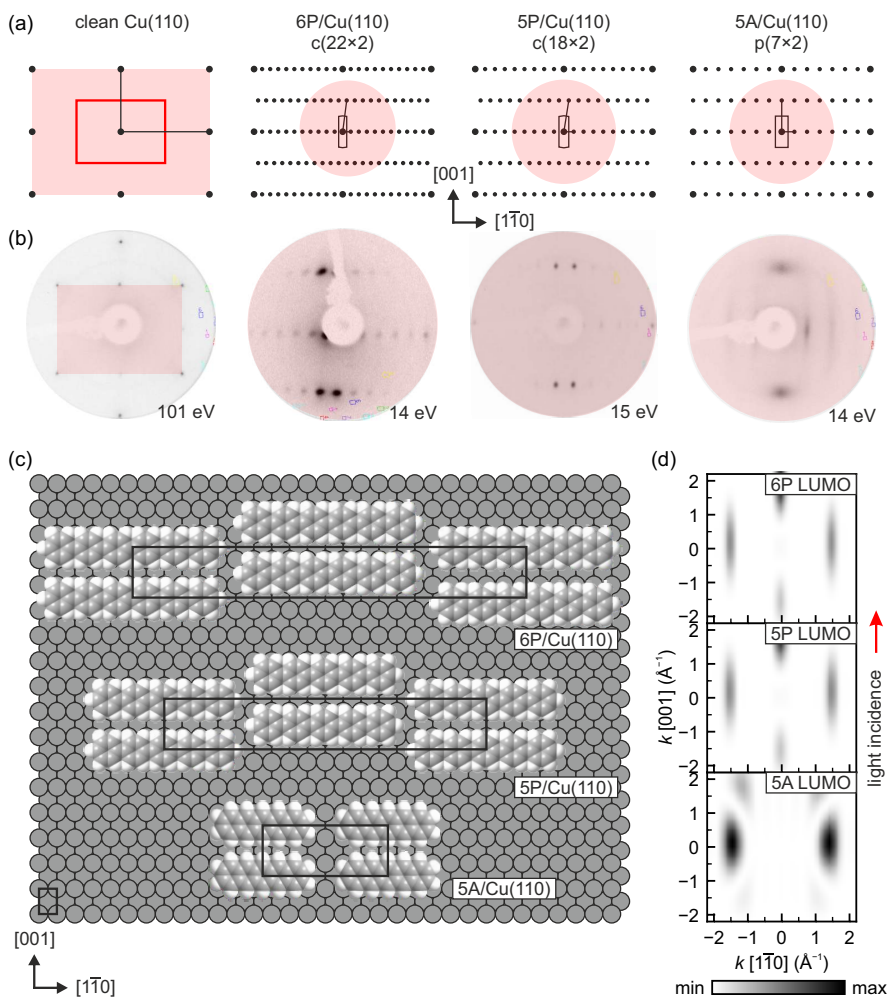


Figure 7.3: Structure models and LEED images of 6P, 5P, and 5A ML on the Cu(110) surface. (a) LEED models. The SBZ and reciprocal vectors of the unit cell for the corresponding superstructure assignments of each system are drawn. (b) LEED images with the electron energy marked aside. The related regions in momentum space between the LEED models and LEED images are marked as pink shaded areas. (c) Real-space structure models with unit cells. (d) Theoretical LUMO k -maps corresponding to the real-space models in (c), with only freestanding molecules taken into account.

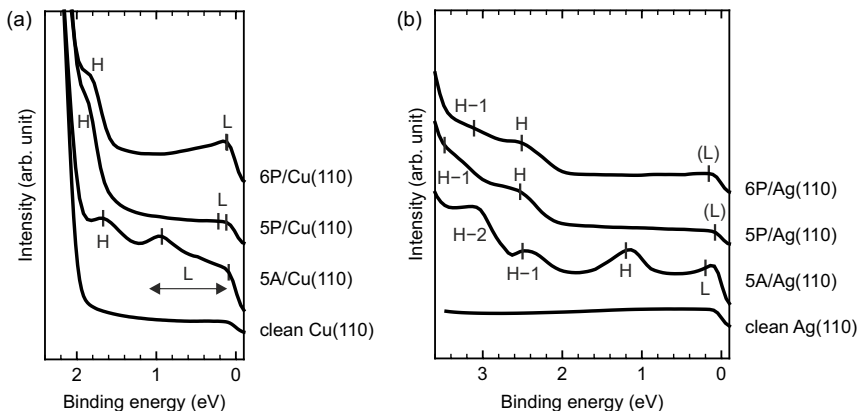


Figure 7.4: Angle-integrated energy distribution curves measured for ML of 6P, 5P, and 5A on (a) Cu(110) and (b) Ag(110). The curves for the clean substrates are also included for reference. The orbital assignments are abbreviated: L for LUMO, H for HOMO and H-1 for HOMO-1, and so on. Note for 5A/Cu(110) the LUMO emission down to 1.2eV below E_F is strongly dispersing as discussed in Section 6.3.3 and drawn with a double-headed arrow. Short vertical lines mark the energy positions at which the k -maps are measured in Figs. 7.5, 7.6, and 7.7 [on Cu(110)] and in Figs. 7.15 and 7.17 [on Ag(110)].

k -Maps and Bandmaps

Figs. 7.5, 7.6, and 7.7 show k -maps measured at the binding energy close to the Fermi level as marked in the EDC curves for 6P, 5P, and 5A on Cu(110), respectively. Comparing to the LUMO k -maps calculated for isolated molecules [Fig. 7.3(d), magnified ones are also presented in Figs. 7.5, 7.6, and 7.7], it is clear that the electronic properties of molecules are strongly influenced by the Cu(110) substrate which is not included in the simulation: the k -positions and intensity distribution of the LUMO main lobes are overall in agreement with the calculations, providing proof that these molecules are indeed lying flat, but within the LUMO lobes there are evidently additional features.

7.4.1 6P/Cu(110) and 5P/Cu(110)

First let us scrutinize the results for 6P/Cu(110) and 5P/Cu(110) due to their similarity (Figs. 7.5 and 7.6). In the k -maps measured at the LUMO energy for 6P and 5P on Cu(110), there are distinct features on top of the four major lobes as shown in Fig. 7.5(d) and Fig. 7.6(d): (1) one ellipse at \bar{Y} , (2) two ellipses with the

same size overlap at $\bar{\Gamma}'$, the center of the neighboring Cu(110) SBZ, (3) elliptical patterns close to \bar{X} and \bar{S} , and (4) two overlapping ellipses at $\bar{\Gamma}$. For features (1)–(3) where the ellipses intersect with the LUMO lobes, the intensity of the latter is curtailed.

At first glance, the similar appearance of intensity distribution at \bar{Y} to the Shockley surface state in Fig. 7.1(a) tempts one to think that the Shockley surface state of Cu(110) remains intact upon molecule adsorption. This is, however, not the case.

The parabolic-shaped Shockley surface state, resulting from the broken symmetry in the z -direction at surfaces, is localized in a hardly visible, so-called projected bulk band gap. Earlier ARPES studies revealed that, when the molecular layer (such as PTCDA, NTCDA, and metal phthalocyanine) is deposited on a clean metal fcc (111) surface, the Shockley surface state is shifted in energy towards E_F , which has been attributed to the Pauli repulsion of surface electrons by adsorbates [265–268]. Coverage-dependent experiments also found that the bottom of the surface state moves to lower binding energy with increasing coverage [269].

On the metal fcc (110) surface, the studies by Nuber et al. [270] exemplified the high sensitivity of the surface state of Au(110) to adsorbates and the surface structure. Compared to the clean Au(110) surface, on the (2×1) reconstructed Au(110) surface no Shockley surface state below E_F can be detected. By adsorption of different amounts of Na and extrapolation to a clean surface, the authors showed that the Shockley surface state of the (2×1) reconstructed Au(110) is shifted above E_F in agreement with calculations. Furthermore, in the measured k -map, the (2×1) reconstructed Au(110) shows an empty projected bulk band gap, which is backfolded to the $\bar{\Gamma}$ point due to the reconstruction. A well-ordered molecular overlayer has a similar effect to the Shockley surface state, as shown in the case of a highly commensurate superstructure of the 6P layer on Cu(110) by Berkebile et al. [9].

The Shockley surface state at \bar{Y} is emptied upon molecule adsorption, and the molecule induces increased intensity that allows the projected bulk band gap to be observable. Interestingly, the scatterings on the 6P overlayer periodicity of the states surrounding this gap are visible all over the k -map where they overlap with the LUMO photoemission signal. We now turn to a detailed separate discussion of 6P/Cu(110) and 5P/Cu(110).

6P/Cu(110)

Compared to the results for 6P/Cu(110) by Berkebile et al. [9], in this thesis not only the Shockley surface states absent at \bar{Y} are precisely reproduced (Fig. 7.5), but also the hybridization at various k -positions, $\bar{\Gamma}'$, \bar{X} , \bar{S} , and $\bar{\Gamma}$, can be determined by the elliptical features.

\bar{Y} Point The fact that the ellipses at \bar{Y} are not the Shockley surface states, but the edge of states surrounding the projected bulk band gap, can be verified in the bandmaps. In Fig. 7.8, the dispersion of the Shockley surface state is indicated by a yellow parabola and the same curve is overlaid on all other bandmaps as yellow, dashed parabolas for comparison. In the bandmaps measured through \bar{Y} for 6P/Cu(110) [Fig. 7.8(b)], the clear dispersion of the Shockley surface state of clean Cu(110) [Fig. 7.8(a)] disappears and the edge of states just below the previous Shockley surface state becomes evident, due to the intensity difference of bulk states and the gap. Because of these changes, at the \bar{Y} point in the k -map, the ellipse of 6P/Cu(110) (states around the projected bulk band gap) has a slightly larger size than the ellipse of clean Cu(110) (Shockley surface state).

$\bar{\Gamma}'$ Point The Cu sp bulk states around \bar{Y} , $(k_{[1\bar{1}0]}, k_{[001]}) = (0 \text{ \AA}^{-1}, 0.87 \text{ \AA}^{-1})$, are scattered to either side of $\bar{\Gamma}'$, $(k_{[1\bar{1}0]}, k_{[001]}) = (\pm 0.11 \text{ \AA}^{-1}, 1.74 \text{ \AA}^{-1})$, in the vicinity of the 6P LUMO major lobe. Note, all three points mentioned above are at the equivalent k -positions in SBZ of the 6P overlayer. The vector from \bar{Y} pointing to $(\pm 0.11 \text{ \AA}^{-1}, 1.74 \text{ \AA}^{-1})$ corresponds to the reciprocal lattice vector of the 6P overlayer (black arrow). The hybridized states close to $\bar{\Gamma}'$ maintain the metallic character as shown in Fig. 7.8(b), the bandmap through $\bar{\Gamma}'$ has two intersecting parabolas separated by 0.22 \AA^{-1} , which subtract intensities from the background of 6P LUMO.

\bar{X} and \bar{S} Points The measured k -map presented in Fig. 7.5 has a wider range of reciprocal space compared to the one reported by Berkebile et al. [9]. One of the new findings here is that, at six different k -positions close to \bar{X} and \bar{S} , two overlapping ellipses can be seen, hinted by the curtailed intensity of the LUMO lobe. One also observes that the bulk sp-bands [shown as short lines close to \bar{S} in Fig. 7.5(c)] are scattered to the outer side of \bar{X} [shown as short dashed lines in Fig. 7.5(c)]. The scattering vectors between these stripe-like features can be attributed to the neighboring SBZ of the 6P overlayer.

$\bar{\Gamma}$ Point At $\bar{\Gamma}$, there are also two overlapping ellipses which appear similar to the other two at $\bar{\Gamma}'$ (with an opposite scattering vector from \bar{Y}). However, a thorough inspection reveals that they are not identical. Superimposing the dispersion of previous Shockley surface state of clean Cu(110) (yellow, dashed parabola) on the bandmap through $\bar{\Gamma}$ in Fig. 7.8(b), it is evident that the measured dispersive intensity is not outside the surface state, as in the bandmap through $\bar{\Gamma}'$. Instead, the intensity sits *on* the parabola of the surface state. This relationship is better illustrated in the enlarged views of k -maps, see Fig. 7.9. The Shockley surface

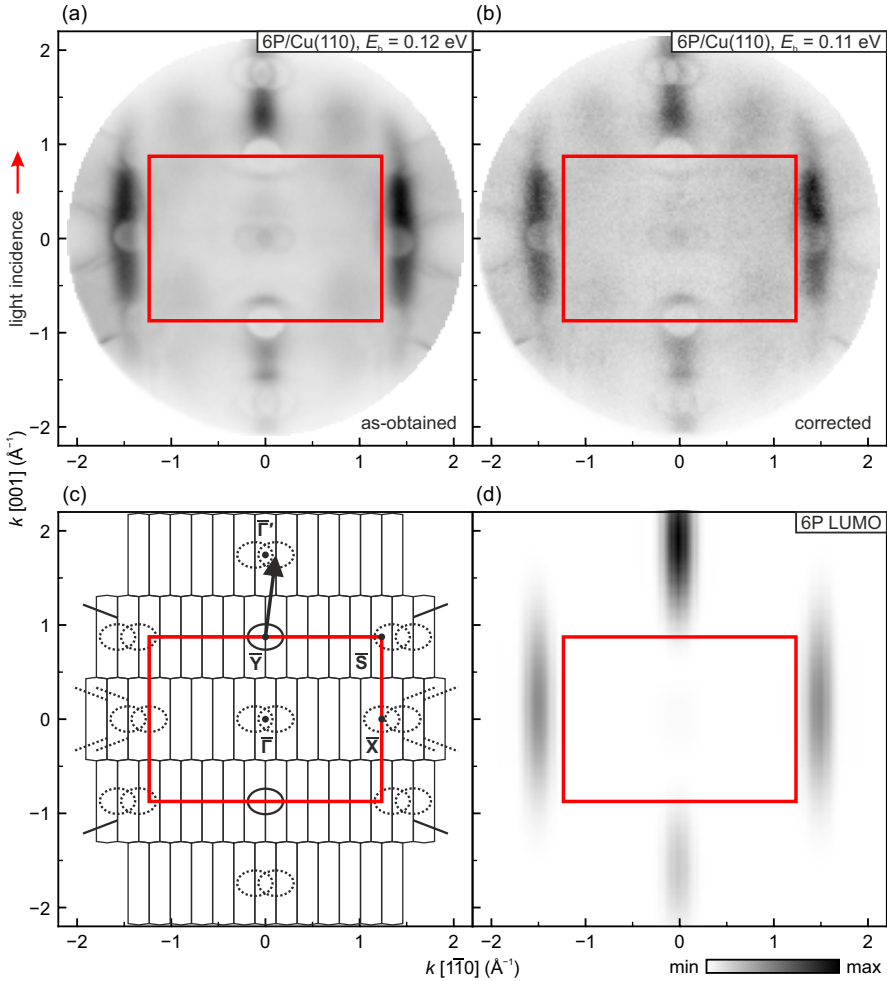


Figure 7.5: 6P ML on Cu(110). (a) As-obtained and (b) corrected experimental k -maps. (c) Brillouin zone boundaries of the molecular overlayer structure, together with the reciprocal lattice vectors (arrows), the states around the gap (ellipses) and the scattering of those (dashed ellipses) for 6P/Cu(110). Also, the Cu sp -bands (short lines) and the scattering of those (short dashed lines) are marked. (d) Theoretical LUMO k -map for 6P as shown in Fig. 7.3(d). In each panel, the SBZ of the clean Cu(110) is drawn as a red rectangle.

7 Momentum-Resolved Hybridization of Molecular and Metal States

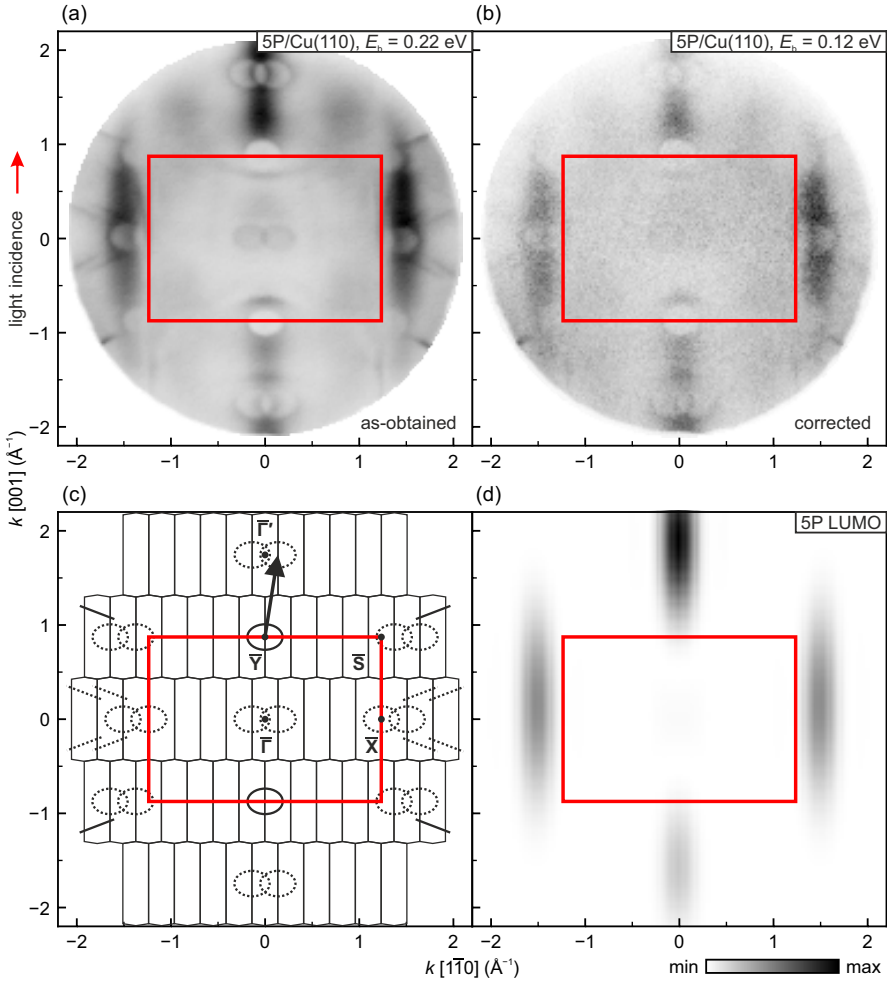


Figure 7.6: 5P ML on Cu(110). (a) As-obtained and (b) corrected experimental k -maps. (c) Brillouin zone boundaries of the molecular overlayer structure, together with the reciprocal lattice vectors (arrows), the states around the gap (ellipses) and the scattering of those (dashed ellipses) for 5P/Cu(110). Also, the Cu sp-bands (short lines) and the scattering of those (short dashed lines) are marked. (d) Theoretical LUMO k -map for 5P as shown in Fig. 7.3(d). In each panel, the SBZ of the clean Cu(110) is drawn as a red rectangle.

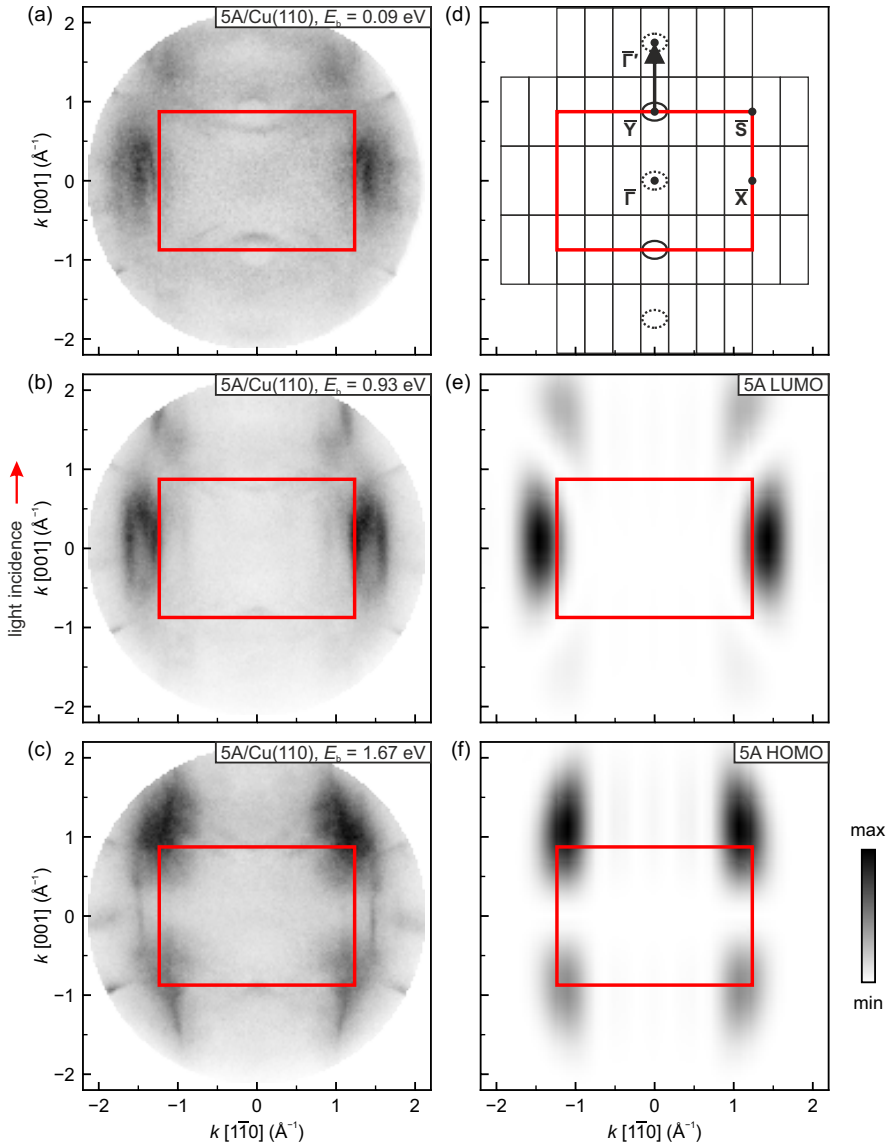


Figure 7.7: 5A ML on Cu(110). (a–c) Corrected experimental k -maps at $E_b = 0.16$ eV, 0.86 eV, and 1.46 eV. (d) Brillouin zone boundaries of the molecular overlayer structure, together with the reciprocal lattice vectors (arrows), the states around the gap (ellipses) and the scattering of those (dashed ellipses) for 5A/Cu(110). (e,f) Theoretical LUMO [cf. Fig. 7.3(d)] and HOMO k -map for 5A. In each panel, the SBZ of the clean Cu(110) is drawn as a red rectangle.

state (yellow ellipse) of the clean Cu(110) in Fig. 7.9(a) is overlaid on the k -maps of 6P/Cu(110) in Fig. 7.9(b) as yellow, dashed ellipse. At $\bar{\Gamma}'$ and \bar{Y} , the intensity is outside the dashed ellipse(s); at $\bar{\Gamma}$ the intensity is along the dashed ellipses. A reasonable assumption would be, it is the surface state previously at \bar{Y} that is scattered to $\bar{\Gamma}$, not the states surrounding the projected bulk band gap, which is the case for the appearance of two ellipses at $\bar{\Gamma}'$.

5P/Cu(110)

All arguments above for 6P/Cu(110) can also be applied to the 5P/Cu(110) system, with one exception: the size of 5P SBZ is by $\sim 22\%$ larger than that of 6P SBZ along $k_{[1\bar{1}0]}$, while along $k_{[001]}$ the sizes are equivalent. This results in a smaller overlap when the states around the gap scatter at $\bar{\Gamma}'$, \bar{X} , \bar{S} , and $\bar{\Gamma}$, see Fig. 7.6. In the corresponding bandmaps through $\bar{\Gamma}'$ and $\bar{\Gamma}$ [cf. Fig. 7.8(b) and (c)], two dispersive parabolas just below the Shockley surface state of clean Cu(110) are separated by 0.22\AA^{-1} and 0.27\AA^{-1} for 6P/Cu(110) and 5P/Cu(110), respectively, corresponding to the sizes of SBZ along $k_{[1\bar{1}0]}$. The same separation is also visible in Fig. 7.9(b) and (c).

7.4.2 5A/Cu(110)

Now let us turn to the results for 5A/Cu(110). In Fig. 7.7, k -maps measured at three different binding energies are shown, Fig. 7.7(a,b) corresponding to LUMO and Fig. 7.7(c) corresponding to HOMO. At \bar{Y} , the ellipses are not Shockley surface state, but the edge of states surrounding the projected bulk band gap, same as 6P/Cu(110) and 5P/Cu(110), see comparison of bandmaps in Fig. 7.8. For the 6P/Cu(110) and 5P/Cu(110) cases, the main LUMO lobes of 6P and 5P are located at $\bar{\Gamma}'$, whereas 5A has its main LUMO lobes close to \bar{X} instead and 5A has a much less contribution of LUMO photoemission at $\bar{\Gamma}'$, see Fig. 7.7(e). There is no obvious appearance of elliptical intensity in the main LUMO lobes of 5A close to \bar{X} . Only at $\bar{\Gamma}'$, $(k_{[1\bar{1}0]}, k_{[001]}) = (0\text{\AA}^{-1}, \pm 1.74\text{\AA}^{-1})$, two scattered ellipses potentially exist, see also Fig. 7.9(d). This can be directly related to the poorer order of the prepared 5A overlayer, as seen in the LEED pattern of 5A/Cu(110) in Fig. 7.3(b): the first reflex along [001] is strongly blurred; along [1 $\bar{1}$ 0], the first and second reflexes have better defined positions, and due to the extension along [001] they appear stripe-like. The former corresponds to the potentially scattered ellipses at $\bar{\Gamma}'$. The latter is seen in the main LUMO lobes of 5A as vertical stripes, see Fig. 7.7(a,b), which possess a periodicity of 5A SBZ in the [1 $\bar{1}$ 0] direction.

In the corresponding bandmap [Fig. 7.13(c)] the large oscillation of LUMO emission, from E_F down to 1.2eV, has the same overlayer periodicity and points at a

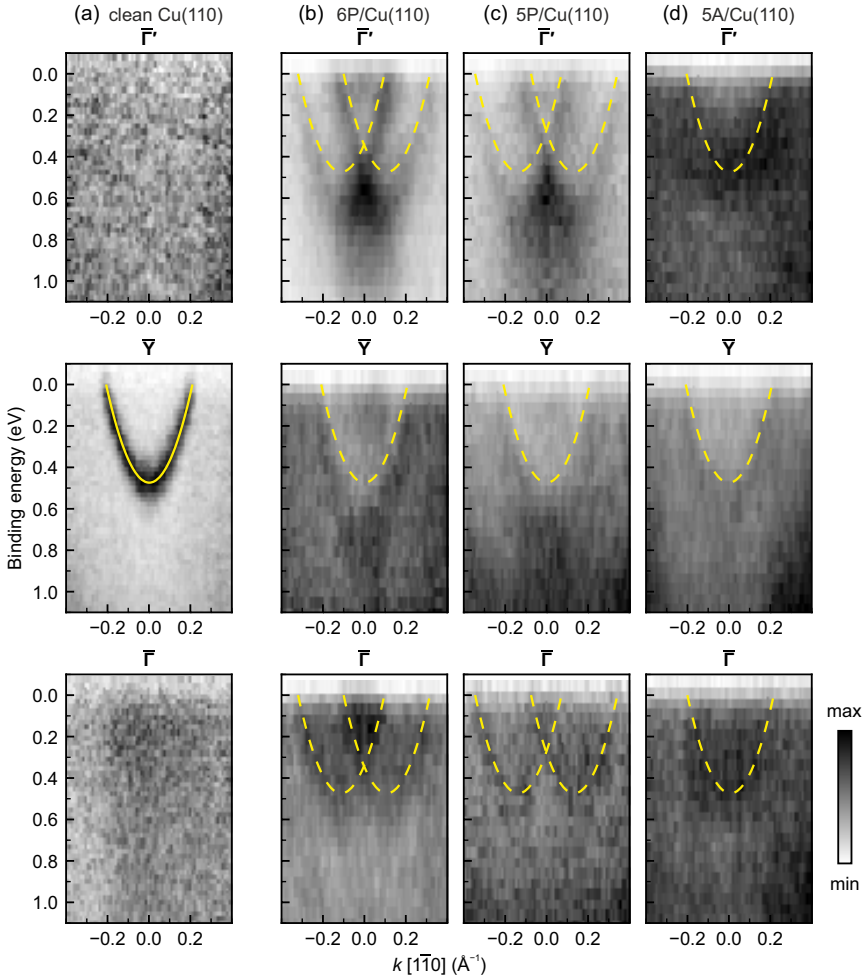


Figure 7.8: Bandmaps measured along $[1\bar{1}0]$ through critical points ($\bar{\Gamma}'$, \bar{Y} , and $\bar{\Gamma}$) for (a) clean Cu(110), (b) 6P/Cu(110), (c) 5P/Cu(110), and (d) 5A/Cu(110). The dispersion of Shockley surface state on clean Cu(110) [yellow parabola in (a)] is overlaid on different features in other bandmaps (yellow, dashed parabola) to guide the eyes for their relationship.

7 Momentum-Resolved Hybridization of Molecular and Metal States

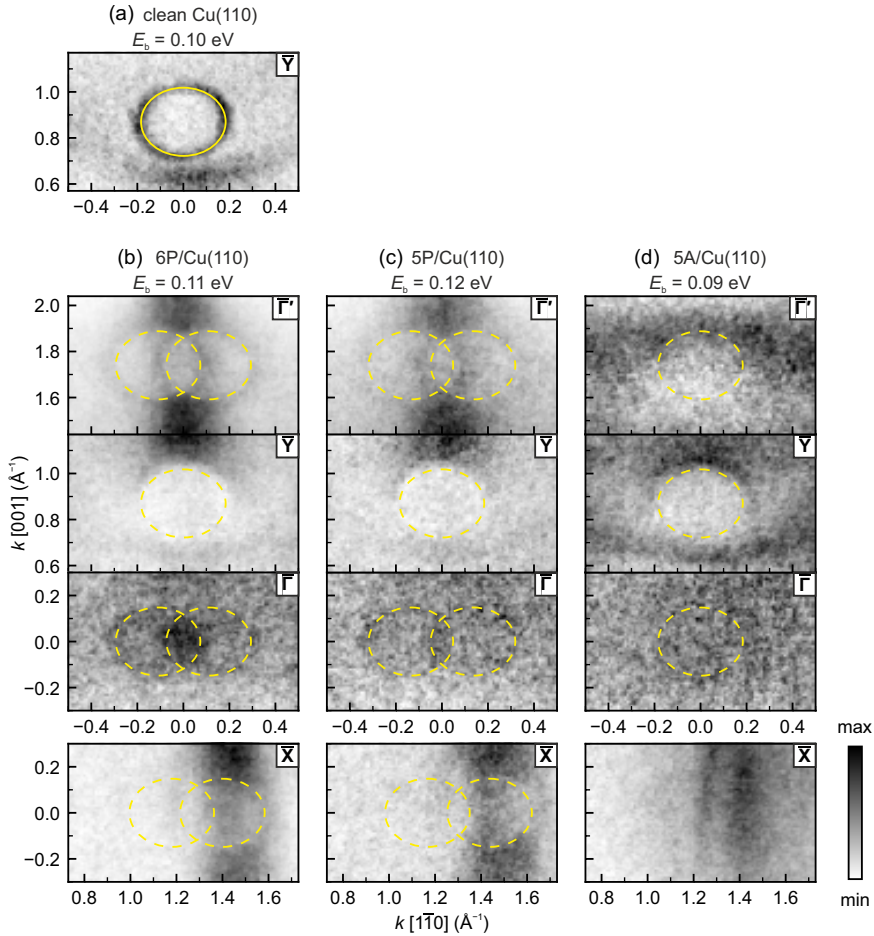


Figure 7.9: Enlarged sections of experimental k -maps at specific points (center of each map is labeled in the upper right corner) for (a) clean Cu(110), (b) 6P/Cu(110), (c) 5P/Cu(110), and (d) 5A/Cu(110). The instrument-intrinsic energy dispersion is corrected for all k -maps and their kinetic energies are chosen to be close to each other. The yellow ellipse corresponds to the cross section of the Shockley surface state of clean Cu(110) in (a). It is overlaid as yellow, dashed ellipse with different features in other maps to estimate their relative sizes. See also Fig. 7.10 for data with a better resolution, where k -maps of clean Cu(110) with different E_{kin} have to be used for comparison because of uncorrected data.

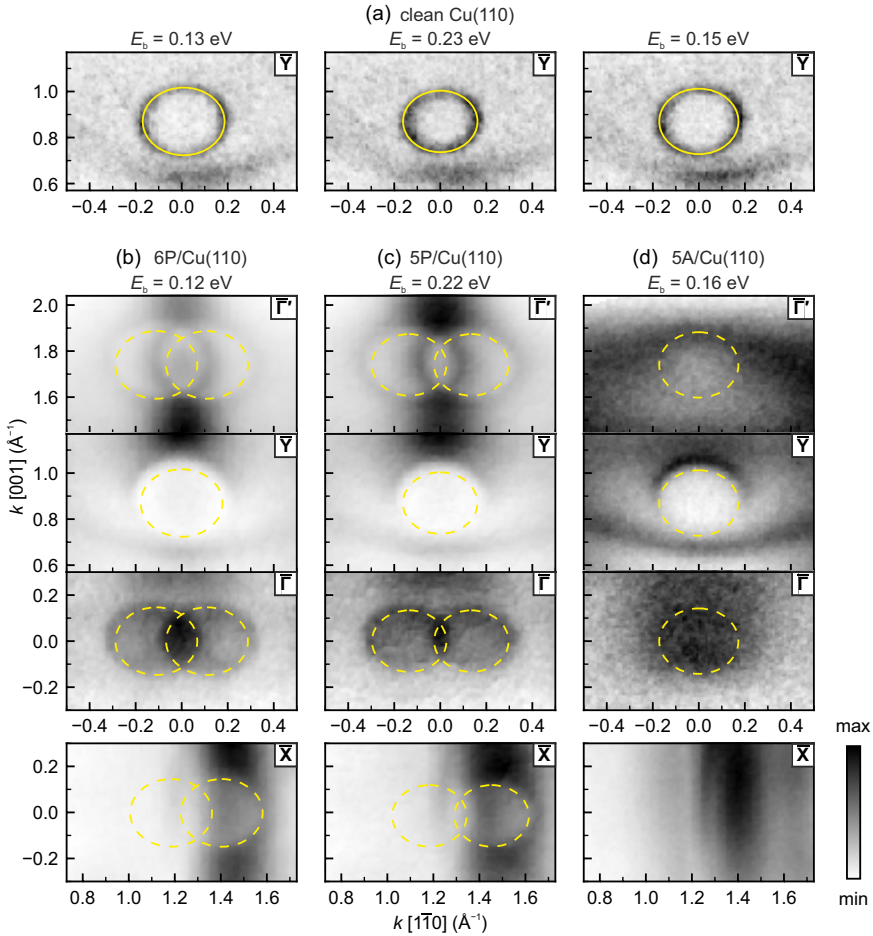


Figure 7.10: Enlarged sections of experimental k -maps at specific points (center of each map is labeled in the upper right corner) for (a) clean Cu(110), (b) 6P/Cu(110), (c) 5P/Cu(110), and (d) 5A/Cu(110). The instrument-intrinsic energy dispersion is *not* corrected, therefore one expects that features of Shockley surface state type would appear with slightly different size at (in the order of larger to smaller): $\bar{\Gamma}'$, \bar{Y} , and $\bar{\Gamma}$. But this does not alter the conclusions drawn from the data presented in Fig. 7.9 where such energy dispersion is eliminated. The yellow ellipse corresponds to the cross section of the Shockley surface state of clean Cu(110) in (a). It is overlaid as yellow, dashed ellipse with different features in other maps to estimate their relative sizes.

7 Momentum-Resolved Hybridization of Molecular and Metal States

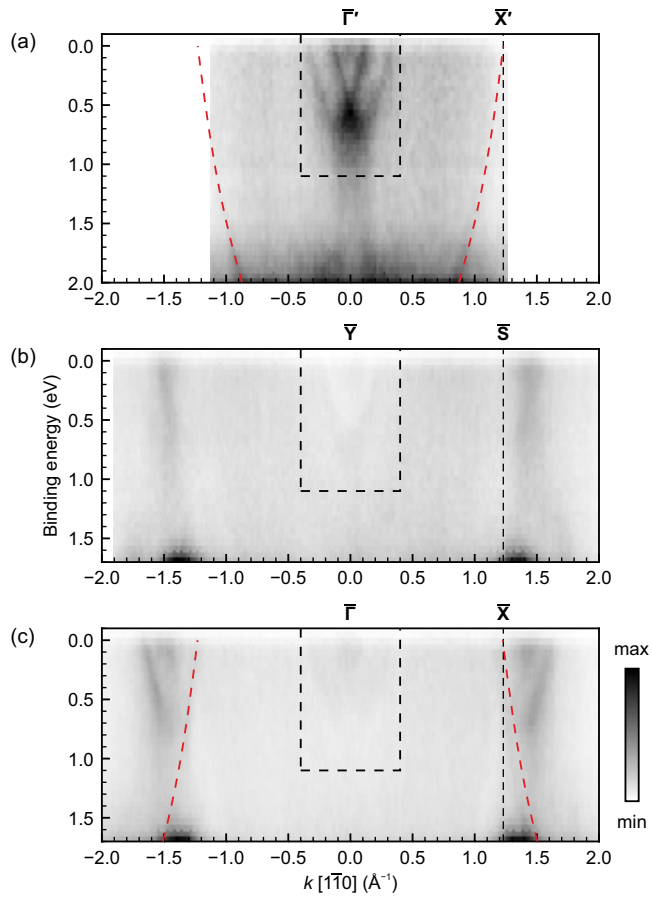


Figure 7.11: Bandmaps of 6P/Cu(110) measured along $[1\bar{1}0]$ through (a) $\bar{\Gamma}'$, (b) \bar{Y} , and (c) \bar{I} , see Fig. 7.5(b). Dashed rectangles mark the enlarged regions shown in Fig. 7.8(b). Red dashed lines guide the eyes for the Cu sp-bands [from Fig. 7.1(b)].

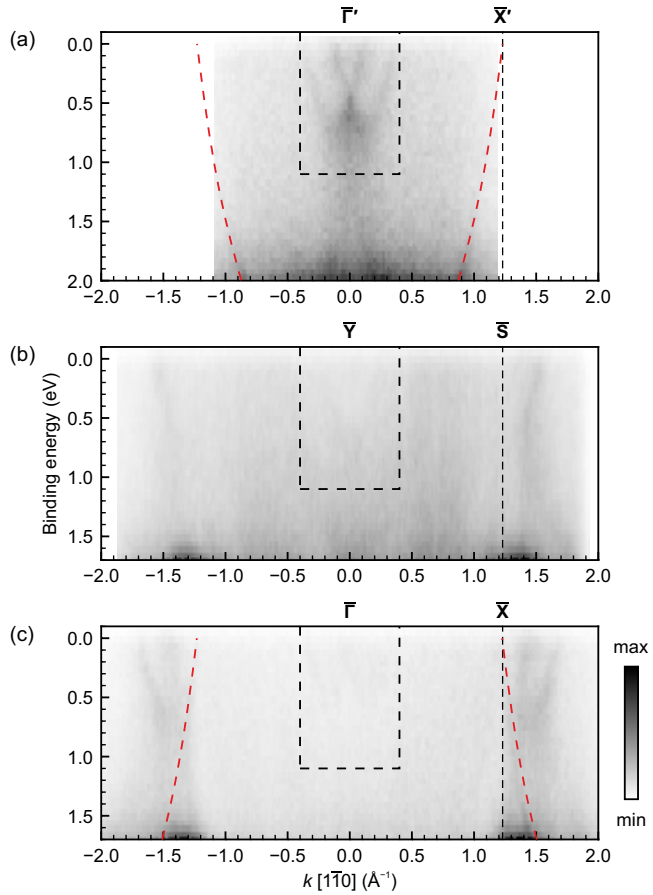


Figure 7.12: Bandmaps of 5P/Cu(110) measured along $[1\bar{1}0]$ through (a) $\bar{\Gamma}'$, (b) \bar{Y} , and (c) $\bar{\Gamma}$, see Fig. 7.6(b). Dashed rectangles mark the enlarged regions shown in Fig. 7.8(c). Red dashed lines guide the eyes for the Cu sp-bands [from Fig. 7.1(b)].

7 Momentum-Resolved Hybridization of Molecular and Metal States

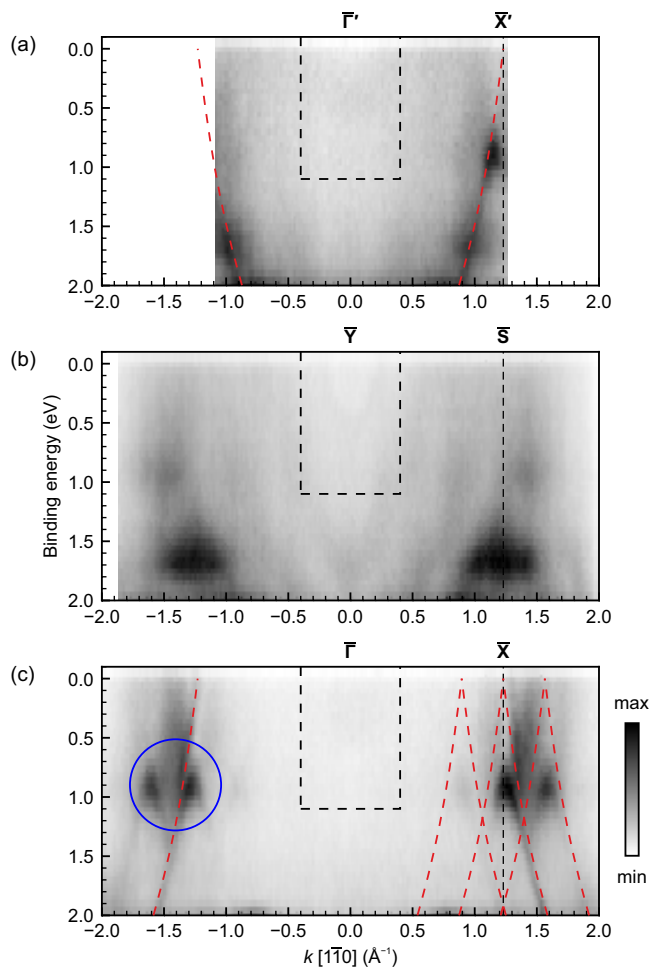


Figure 7.13: Bandmaps of 5A/Cu(110) measured along $[1\bar{1}0]$ through (a) $\bar{\Gamma}'$, (b) \bar{Y} , and (c) $\bar{\Gamma}$, see Fig. 7.7(d). Dashed rectangles mark the enlarged regions shown in Fig. 7.8(d). Red dashed lines guide the eyes for the Cu sp-bands [from Fig. 7.1(b)] and related scatterings. Blue circle marks the region where the sp-band is truncated and hybridizes with the LUMO.

strong intermolecular dispersion, as introduced earlier in Section 2.3.3.5. Note, although the 5A overlayer on Cu(110) prepared in this thesis is not identical to Ules et al. [23] but reminiscent to a mixture of multiple phases (judging from the blurred LEED pattern, cf. Zhang et al. [263]), the LUMO dispersion along $[\bar{1}\bar{1}0]$, i.e. along the molecular long axis, is exactly reproduced because the overlayer periodicity is the same in this direction. The sp-bands from the dispersion of the clean Cu(110) [Fig. 7.1(b)] are overlaid on the bandmaps of 5A/Cu(110) in Fig. 7.13 as red dashed curves. The replicas of these sp-bands display the periodicity of the 5A overlayer, which hints at the molecule–metal hybridization. These bands are not simply the bulk sp-bands scattered by the overlayer, otherwise they are replicated over the entire energy range up to E_F following the red dashed curves [23, 105]. Instead they are truncated at 1.2 eV, just below the onset of the LUMO emissions, see the region marked with a blue circle.

Interestingly, although the LUMO main lobe is not located at $\bar{\Gamma}'$ but close to \bar{X} for 5A/Cu(110), in the bandmaps [Fig. 7.8(d)] there is some indication of a single parabola corresponding to the potentially scattered ellipses at $\bar{\Gamma}'$ (probably also at $\bar{\Gamma}$). Due to the poorer order of the prepared 5A overlayer and the limited energy resolution, the parabola is not very clear. Compared to 6P/Cu(110) and 5P/Cu(110), the overlayer structure of 5A/Cu(110) has primitive unit cells instead of centered ones, see Fig. 7.3. This difference causes varying structures of surface Brillouin zone boundaries [cf. Fig. 7.5(c), Fig. 7.6(c), and Fig. 7.7(d)] so that the bandmaps through $\bar{\Gamma}$ and $\bar{\Gamma}'$ of 5A/Cu(110) do not have two parabolas like the 6P/Cu(110) and 5P/Cu(110) cases, but a single one. Note, photoemission measurement for the monolayer of 5A on Cu(110) prepared by Ules et al. [23] with a rhomboid superstructure $\begin{pmatrix} 6.5 & -1 \\ -0.5 & 2 \end{pmatrix}$ has observed two parabolas close to $\bar{\Gamma}$, each belonging to one of the two mirror domains. But due to the larger size of the overlayer unit cell, these two parabolas do not intersect, see Fig. 4.12 of Ref. [105].

7.5 6P/5P/5A on Ag(110)

LEED

The structures of the prepared 6P/Ag(110), 5P/Ag(110), and 5A/Ag(110) samples are summarized in Fig. 7.14. For both 6P/Ag(110) [34, 105] and 5P/Ag(110), no definite structure has been resolved yet in literature and here the overlayer structures are tentatively assigned to be $\begin{pmatrix} 1 & 6.5 \\ 2 & -2.5 \end{pmatrix}$ and $\begin{pmatrix} 1 & 6 \\ 2 & -2 \end{pmatrix}$, respectively. The $\begin{pmatrix} 3 & -1 \\ -1 & 4 \end{pmatrix}$ unit cell for 5A/Ag(110) is in agreement to the structure reported by

Wang et al. [271] and Ules et al. [23]. Compared to the cases on Cu(110), all three molecules have their long axes rotated by 90° , now across the close-packed row, see Fig. 7.14(c). The orientation of these systems will be verified later in the measured k -maps and bandmaps.

EDC

The EDCs integrated for all k values from the data cube $I(E_{\text{kin}}, k_x, k_y)$ for 6P, 5P, and 5A on Ag(110) are shown in Fig. 7.4(b). For both 6P/Ag(110) and 5P/Ag(110) the population of LUMO is (if any) relatively weak. Ules et al. [23] has recorded partially occupied LUMO for 6P on Ag(110), at 0.1 eV below the Fermi level. The HOMO of 6P/5P is much deeper in binding energy, at around 2.4 eV. For 5A on Ag(110), the LUMO is evidently occupied as has been verified before [23] and deeper orbitals down to HOMO-2 can be observed in this energy range.

In a similar way to the three cases on Cu(110), k -maps for 6P, 5P, and 5A on Ag(110) were measured at chosen energies close to the Fermi level, seen as short vertical lines in Fig. 7.4(b). Due to the low binding energy of the silver Shockley surface state that is very close to the Fermi level ($E_b = \sim 0.1$ eV), in the measured k -maps at binding energies 0.16, 0.08, and 0.20 eV for 6P, 5P, and 5A on Ag(110), respectively, only the bottom of dispersing silver Shockley surface state is observable, see the next section.

k -Maps and Bandmaps

Because of different azimuthal orientations of the molecules on copper and silver substrates, for the Ag(110) surface the LUMO k -maps calculated for isolated molecules [Fig. 7.14(d)] now have the main lobes parallel to $[1\bar{1}0]$. However, due to the marginal occupation of LUMO for 6P/Ag(110) and 5P/Ag(110), their LUMO lobes are hardly seen in the photoemission distribution, see Fig. 7.15(a,b). Measured k -maps for orbitals with higher binding energies [HOMO and HOMO-1, Fig. 7.17(a,b)] confirm that both 6P and 5P are indeed flat-lying and fit the real-space models. For 5A/Ag(110) [Fig. 7.15(c)] the LUMO occupation is clear and in good agreement to the calculated one, which also verifies the real-space model.

What interests us is how the electronic properties of molecules are influenced by the Ag(110) substrate and whether elliptical features at $\bar{\Gamma}$ undergo similar scattering processes as seen in the previous results on Cu(110).

First, compared to Cu(110), Ag(110) has a weaker coupling to the molecular adsorbates (cf. Fig. 7.4): the LUMO for 6P/Ag(110) and 5P/Ag(110) is nearly empty; the LUMO for 5A/Ag(110) is now on the edge of Fermi level. At the $\bar{\Gamma}$ point, the Shockley surface state has maintained its intrinsic character as on the clean Ag(110). The appearance of Shockley surface state dispersion is not greatly al-

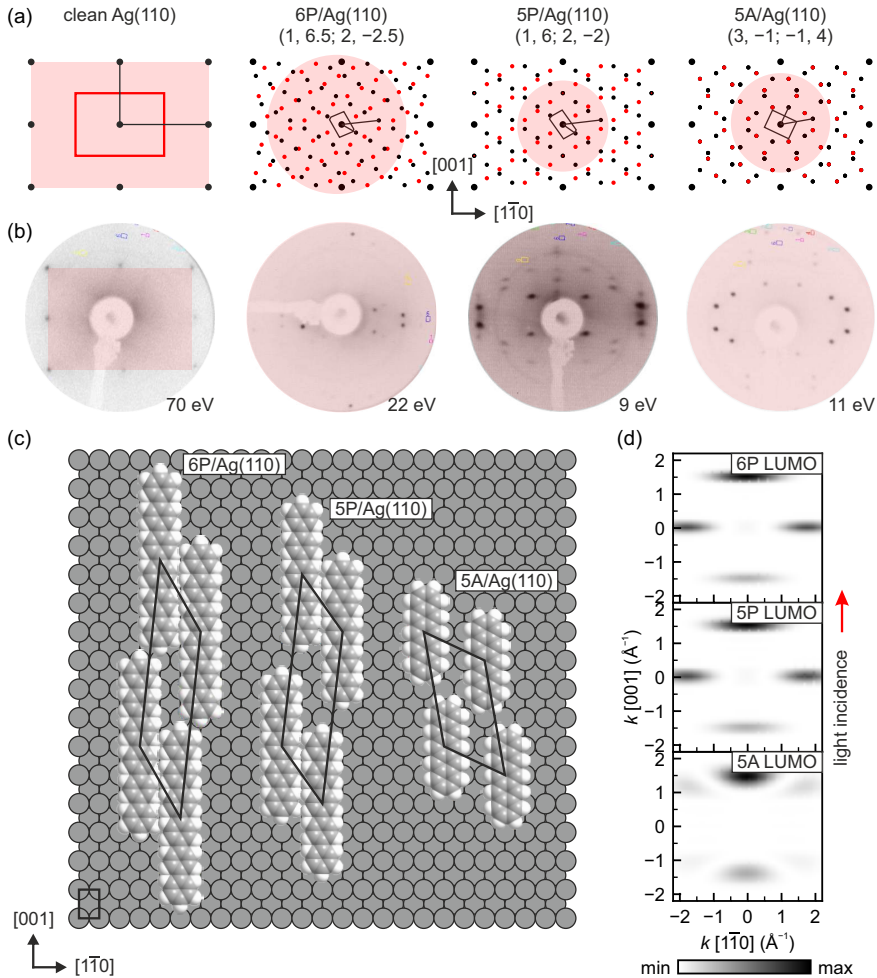


Figure 7.14: Structure models and LEED images of 6P, 5P, and 5A ML on the Ag(110) surface. (a) LEED models. The two mirror domains because of the surface symmetry is drawn in black and red, respectively. The SBZ (belongs to one of the two domains) and reciprocal vectors of the unit cell for the corresponding superstructure assignments of each system are drawn. (b) LEED images with the electron energy marked aside. The related regions in momentum space between the LEED models and LEED images are marked as pink shaded areas. (c) Real-space structure models with unit cell. (d) Theoretical LUMO k -maps corresponding to the real-space models in (c), with only freestanding molecules taken into account.

tered upon the adsorption of molecules, see Fig. 7.16. This is in stark contrast to the cases on Cu(110) where the surface states are completely emptied and one observes the gap in the bulk projected density of states at \bar{Y} (cf. Fig. 7.8). Although the bandmaps of molecules on Ag(110) have a pixelized resolution in Fig. 7.16 due to the small binding energy of Shockley surface state dispersion, the highest intensity maintains to be on the yellow parabola that corresponds to the unperturbed Shockley surface state. There is possibly a small upward shift of the dispersion to E_F resulted by the Pauli repulsion [265–268] as mentioned earlier in Section 7.4.1, but we refrain from making a concrete conclusion because of the limited resolution.

Second, for all three cases 6P/5P/5A on Ag(110), the ellipses at \bar{Y} indeed show some scattering to the left and right hand with k -positions related to the reciprocal vector of the unit cell, which are drawn as black/red dashed ellipses for two symmetry domains, see Fig. 7.15(a–c). This is however very weak so that one can only observe this in the enlarged view, Fig. 7.15(d), a minute indication of the scattered Shockley surface state close to \bar{S} .

7.6 Discussion

There are still several interesting aspects in the data that merit some discussion. Especially, we shall compare the results for molecular overlayers on Cu(110) and on Ag(110) in more detail.

First, what exactly decides where the scattered Shockley surface states or scattered states around the projected bulk band gap are in reciprocal space?

- For Cu(110), upon molecule adsorption the Shockley surface states at \bar{Y} are emptied and one observes an ellipse, whose radius is larger than that of the ellipse measured at the same energy for clean Cu(110) (Fig. 7.9). This strong hybridization is suggested by the erasure of molecular states in the gaps, and the distance between the scattered ellipses and their origin (\bar{Y}) can be related by the reciprocal lattice vector of the overlayer. But why are these scattered ellipses not seen all over the entire reciprocal space? One reasonable hypothesis is that the hybridization occurs only when the involved states overlap in momentum [9].
- For 6P, 5P, and 5A on Cu(110), we can categorize the elliptical features in the k -maps: emptied Shockley surface state at \bar{Y} ; scattered states around the projected bulk band gap at $\bar{\Gamma}$ which hybridize with the molecular state (LUMO); scattered Shockley surface state at $\bar{\Gamma}$. These are clearly fulfilled in the 6P/Cu(110) and 5P/Cu(110) cases. For the 5A/Cu(110) case, it is difficult

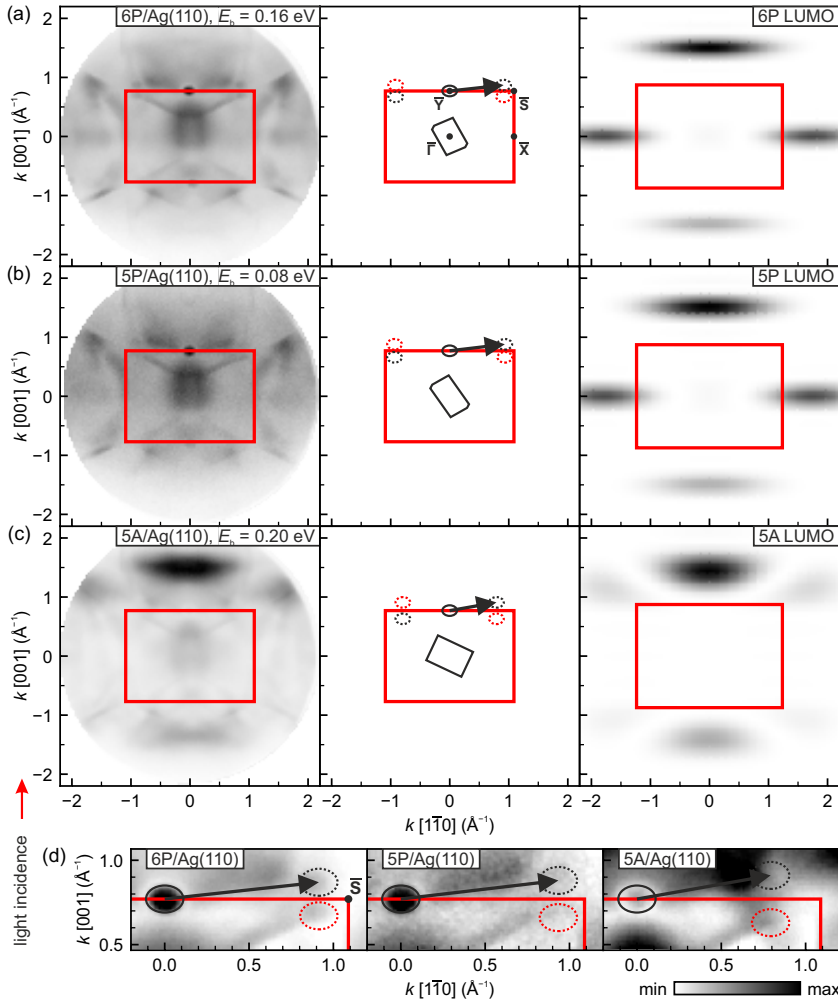


Figure 7.15: k -maps of 6P, 5P, and 5A on Ag(110). (a–c) Left: full k -map of three cases with the SBZ of clean Ag(110) (red rectangle); additionally drawn on the right: Brillouin zone boundary of the molecular overlayer structure (black polygon), reciprocal lattice vector, Shockley surface states (ellipses) and the scattering of those (dashed ellipses, black and red showing different mirror domains). (d) Enlarged sections of (a–c). Experimental k -maps in this figure are not corrected for the instrument-intrinsic energy dispersion.

7 Momentum-Resolved Hybridization of Molecular and Metal States

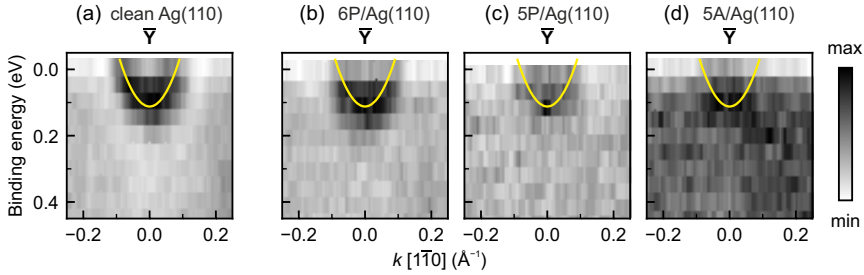


Figure 7.16: Bandmaps measured along $[1\bar{1}0]$ (through \bar{Y}) for (a) clean Ag(110), (b) 6P/Ag(110), (c) 5P/Ag(110), and (d) 5A/Ag(110). The dispersion of the Shockley surface state on clean Ag(110) [yellow parabola in (a)] is overlaid on all other bandmaps to guide the eyes for their relationship.

to make a concrete conclusion for the features at $\bar{\Gamma}'$ and $\bar{\Gamma}$ because of the limited data resolution.

- For Ag(110), the states involved in the hybridization with LUMO is the Shockley surface state only, which is apparently unperturbed judging by the bandmaps through \bar{Y} (Fig. 7.16). There is indication of scattered ellipses near \bar{S} , see Fig. 7.15(d), but this scattering on Ag(110) is much weaker compared to that on Cu(110) (from \bar{Y} to $\bar{\Gamma}$). The region close to \bar{S} , where the ellipses scattered to, hardly overlaps with the LUMO main lobe of 6P, 5P, or 5A. This shows that when the surface state (and not the gap) is scattered, it is not relevant whether there is LUMO intensity but just a matter of band folding.

Another intriguing detail is the appearance of (scattered) ellipses:

- To begin with, dispersing Shockley surface states of the clean Cu(110) and Ag(110) surfaces at \bar{Y} are just above the projected bulk band gap. In k -maps the former appears as an empty ellipse, but the latter is too close to the Fermi level that one sees the bottom of dispersion only, thus appearing as a filled ellipse due to limited energy resolution in this work.
- After 6P/5P/5A is deposited on Cu(110), the surface state dispersion is eliminated and the gap becomes visible, with slightly larger diameters. This is not the case for 6P/5P/5A deposited on Ag(110), because the surface state remains intact and no change in diameters can be observed.
- For 6P/Cu(110) and 5P/Cu(110), when the scattered states around the gap hybridize with the LUMO lobes, the intensity of LUMO is clearly reduced

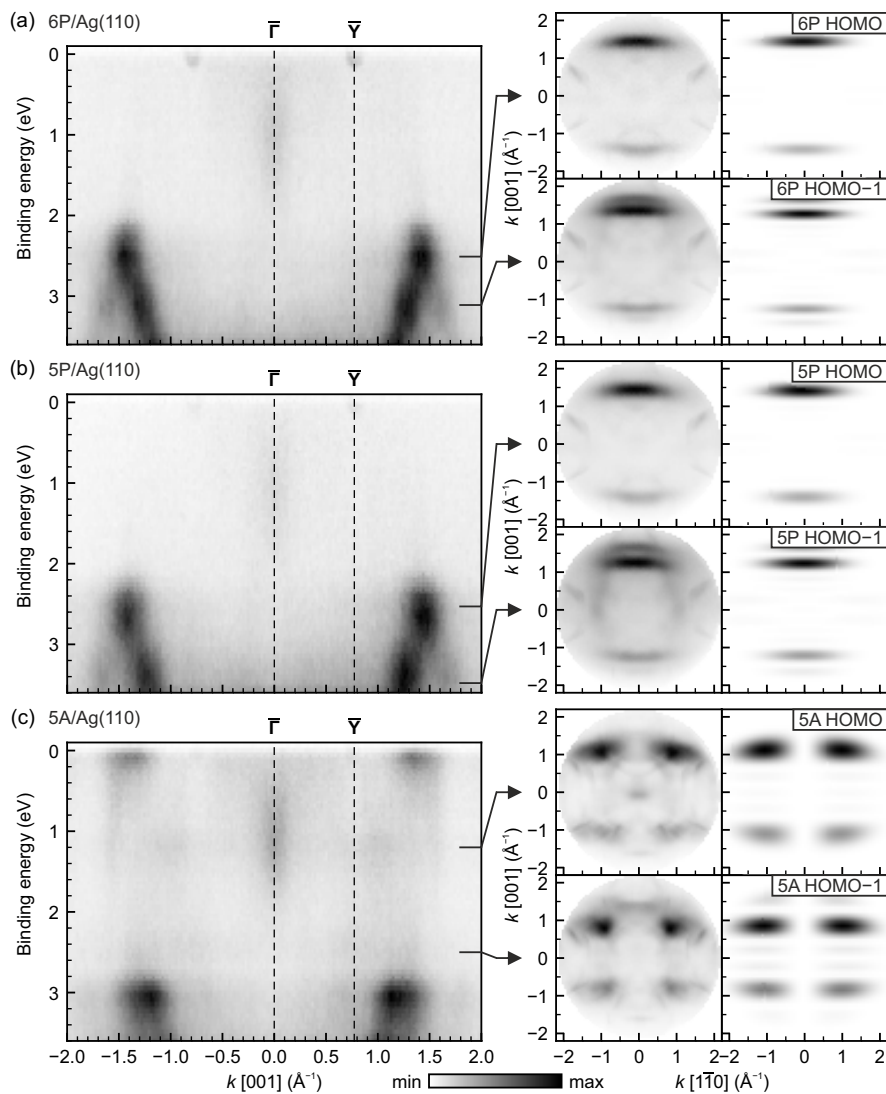


Figure 7.17: Bandmaps measured along [001] (through $\bar{\Gamma}$) of 6P, 5P, and 5A on Ag(110). In each panel, two k -maps corresponding to HOMO and HOMO-1, whose binding energies are marked with arrows from the bandmap, are shown. For comparison, the theoretical k -maps of HOMO and HOMO-1 calculated for isolated molecules are also displayed on the right side. Experimental k -maps in this figure are not corrected for the instrument-intrinsic energy dispersion.

in the elliptical areas near $\bar{\Gamma}'$, the borders of which remain visible, see Fig. 7.5(a) and Fig. 7.6(a). For 5A/Cu(110), the reduction of the LUMO intensity near \bar{X} does not appear as two overlapping ellipses but as stripes along [001], which is a different effect—intermolecular dispersion [Fig. 7.7(a)].

- Judging from the size of elliptical features, we concluded that it is the Shockley surface state that scattered from \bar{Y} to $\bar{\Gamma}$ due to the molecular layer (6P and 5P) on Cu(110). For the clean Cu(110) surface, the Shockley surface state is at \bar{Y} , on top of the project bulk band gap; at $\bar{\Gamma}$ there are only bulk states and no gap. Due to the presence of an ordered molecular superstructure, the surface state is scattered to $\bar{\Gamma}$. The fact that the surface state remains visible at $\bar{\Gamma}$ is extraordinary and it shall be a subject of future studies.

7.7 Conclusion

In this chapter, the monolayers of 6P, 5P, and 5A on Cu(110) and on Ag(110), respectively, are investigated by PT. Compared to the previous work by Berkebile et al. [9], the NanoESCA PEEM employed in this work could capture the images faster and with a better k -space resolution. On Cu(110), the Shockley surface state at the \bar{Y} point of the substrate's SBZ disappears. The electronic states around the projected bulk band gap scatter to $\bar{\Gamma}'$ appearing as ellipses, with a scattering vector following the reciprocal unit cell of the molecular overlayer as determined by LEED measurements. These scattered states overlap with the corresponding LUMO in momentum and the LUMO intensity is curtailed. Interestingly, the surface state that is emptied at \bar{Y} is scattered to $\bar{\Gamma}$ and maintains its dispersive behavior. On Ag(110), the molecular states are altered less as hinted by the unchanged Shockley surface state, which can still scatter with the corresponding reciprocal unit vector of the molecular overlayer.

For molecular adsorbates on a metal surface, PT often only considers a free-standing molecular layer and neglects the momentum distribution of the substrate states. The molecule overlayers investigated in this chapter have shown a dual contribution of the adsorbate LUMO and the surface-related states. We have observed that either the Shockley surface states or the states around the gap (when Shockley surface states are emptied) can be scattered, by reciprocal lattice vectors of the overlayer structure. Such momentum-resolved hybridization can be useful and important in the interpretation of photoemission distribution data for strongly bonding molecule–metal systems, which in turn can serve as a benchmark for DFT calculations that also include the metal substrate in PT studies.

8 Summary and Outlook

In summary, several aspects of the interaction between π -conjugated organic molecular adsorbates and the metal surface were investigated by PT, in particular:

- **Chapter 4** (“Bonded or not”) demonstrated that PT can be successfully used to identify the exact products of chemical reactions at surfaces and their local bonding. This was done using the example of the thermal reaction of precursor molecule DBBA ($C_{28}H_{16}Br_2$) on Cu(110). The debated question, whether the reaction intermediate form covalent bonds with the Cu surface after the removal of Br (debromination) because of the absent H, was approached before with conventional characterization methods—STM and XPS. Instead of measuring specific spatial distribution of the molecular orbitals with STM or fitting peaks in high-resolution XPS spectra, the subtle difference in the local chemical bonds was accurately determined by PT in this work. In the measured k -maps, the transition of diffuse patterns of the as-deposited molecular precursor to defined patterns after annealing to 250 °C shows a clear modification of the orbital structure and indicates that the thermal activated surface reaction occurs. The k -maps of the so synthesized product measured at 0.5, 1.15, and 1.9 eV, respectively, match well with the calculated k -maps of LUMO, HOMO, and HOMO–1 of isolated bisanthene ($C_{28}H_{14}$). Comparison to DFT calculations for three possible reaction intermediates: bisanthene, $C_{28}H_{12}$, and $C_{28}H_8$, the latter two having covalent C–Cu bonds and the first fully hydrogenated, revealed that bisanthene is energetically most favorable, and the H atoms possibly are from the inner sites of anthracene units.
- **Chapter 5** (“Charged or not”) reviewed three different methods to electronically decouple molecular adsorbates from the metal substrate: using dielectric interlayer, oxygen passivation, and 2D materials. The LUMO of PTCDA deposited on a thin layer of MgO grown on Ag(100) was identified with k -map measured by PT, showing that PTCDA receives charge from the metal despite the physical separation with a dielectric interlayer. On the contrary, on oxygen-reconstructed Cu(100), PTCDA is both electronically and physically decoupled. The latter is reflected in the NIXSW experiments that the PTCDA molecule is flat and has a large adsorption height, 3.34 Å, with

respect to the surface copper atoms. The copper surface electrons are stabilized by covalent bonding with oxygen atoms preventing them from being pushed down into the metal bulk. This causes a potential barrier for electrons tunneling from the bulk into the electrophilic PTCDA, but without strongly changing the work function. Another showcase is investigating the electronic decoupling of PTCDA on a monolayer of hexagonal boron nitride grown on the Cu(111) surface. Photoemission spectra show that the frontier orbitals are not altered with respect to those seen for gas-phase spectra, pointing at physisorption of PTCDA.

- **Chapter 6** (“Equally charged or not”) used PT to deal with the charge states in an organic monolayer film composed of tetracene on Ag(110) and Cu(110) surfaces. As a reference, pentacene on the same metal surfaces shows ordinary behaviors of charge transfer that the LUMO of pentacene is occupied which is followed by HOMO, HOMO–1, and so on. However, with one ring short, tetracene on Ag(110) was found to be a special case. Two different tetracene species in the layer have the same orientation with respect to the substrate but behave electronically differently in the sense that one molecule stays neutral while the other one undergoes charge transfer from the substrate. With these coexisting charge states, there are surprisingly two HOMO peaks in the photoemission spectra, at binding energies 1.5 eV and 2.4 eV, which could be easily misinterpreted without the help of PT. Detailed analysis of measured k -maps and coverage-dependence UPS study revealed that the orientation of tetracene molecules changes with increasing coverage up to the saturated monolayer at room temperature ($[001] \rightarrow [1\bar{1}0] \rightarrow [1\bar{1}0]$ misaligned).
- **Chapter 7** (“Scattered or not”) applied PT to study photoelectron angular distributions for highly-hybridized molecule–metal systems, monolayers of p-sexiphenyl, p-quinquephenyl, and pentacene on Cu(110) and on Ag(110), respectively. Bare Cu(110) and Ag(110) surfaces both show Shockley surface states at the \bar{Y} point of the substrate’s surface Brillouin zone, the latter locating at smaller binding energies. With the molecular overlayer on Cu(110), the Shockley surface state disappears at \bar{Y} . The projected bulk band gap, i.e. the absence of the bulk state, can be scattered to multiple k -positions, with a scattering vector following the reciprocal unit cell of the molecular overlayer as determined by LEED measurements. The LUMO intensity is curtailed where the LUMO main lobes are overlapped with these scattered states, clearly visible at $\bar{\Gamma}'$ in the p-sexiphenyl/Cu(110) and p-quinquephenyl/Cu(110) cases. Interestingly, the surface state that is emptied at \bar{Y} is scattered to $\bar{\Gamma}$ and maintains its dispersive behavior. With the

molecular overlayer on Ag(110), the Shockley surface states are not changed but still get scattered with the reciprocal unit vector of the molecular overlayer to k -positions close to \bar{S} . This chapter highlighted the importance of PT to study the interaction of strongly bonding molecule–metal systems, where the momentum-resolved view of photoemission results provides additional information such as the overlayer geometry and the molecule–metal hybridization.

Essentially, PT offers the possibility to obtain images of molecular orbitals in three dimensions. But why PT is emerging as a new powerful tool in molecule–metal systems? The main reason is that PT is capable of approaching molecular orbital $\psi(\mathbf{r})$ and its Fourier transform $\tilde{\psi}(\mathbf{k})$ under the convenient plane wave final state approximation. Compared to scanning probe techniques where two resembling states, $\psi_1(\mathbf{r})$ and $\psi_2(\mathbf{r})$, might be difficult to distinguish (or the detection itself is difficult), the k -maps measured by PT can greatly ease the orbital identification in the momentum space using $\tilde{\psi}_1(\mathbf{k})$ and $\tilde{\psi}_2(\mathbf{k})$.

ARPES-based PT technique is in general easy to conduct experiments and efforts are being made to extend the range of applications with PT, not limited to the few cases reported in this thesis. For instance, one of the prerequisites of PT is the small number of molecular orientations (best would be one or two). One may consult the chemists' expertise to synthesize suitable precursor molecules and perform surface thermal reaction, in order to co-orient all molecules on the surface. Another point to consider when applying PT is the influence of metal substrates, one can still use standard DFT calculations for isolated molecules to study this interaction through the deviation from calculations (Chapter 7). One can also include the substrate into their extended DFT calculation with a simple modeling of evanescent plane wave in the metal layers (Section 2.3.2.2), or find a proper way to decouple molecules from metal if the "intrinsic" molecule properties are of interest (Chapter 5).

A promising direction for future development of the PT method would be adding the time dimension into experiments. As shown in Chapter 4, the surface thermal reaction of precursor molecules is identified via the change of its appearance in k -maps. It would be advantageous to combine the sample preparation equipment (e.g. annealing on the sample holder) with the photoemission measurement system, so that the k -maps are measured in real time while the reaction occurs. PT could also be applied with a pump-probe momentum microscopy, where the ultra-fast structural and electronic dynamics is of interest and the unoccupied states above the Fermi level can be accessed [81].

A Data Analysis Software—Mozi

Introduction

MOZI is a Python-based software written for analyzing the photoemission data measured with the toroidal electron analyzer (Section 3.3), named after the Chinese philosopher (c. 470–391 BC). It substitutes the previous IGOR Pro-based software to have cross-platform compatibility with expanded functionalities, see Fig. A.1. MOZI is capable of the following data analysis for the toroidal electron analyzer:

- “AZI”: k -map mode
 - Plot the middle slice: $I(\theta, \phi)$ or $I(k_x, k_y)$ (k -map)
 - Plot all $I(\theta, \phi)$ slices of data cube $I(E_{\text{kin}}, \theta, \phi)$
 - Calibrate the polar angle θ
 - Plot all k -map $I(k_x, k_y)$ slices of data cube $I(E_{\text{kin}}, k_x, k_y)$
 - Choose certain range of slices and make an averaged k -map
 - Apply symmetrization and rotation on the averaged k -map
 - ROI analysis
 - Extract bandmap from data cube (within energy window ΔE)
- “EDC”: bandmap mode
 - Plot all slices of data cube $I(\text{slice}, \theta, E_{\text{kin}})$
 - Calibrate the “arcwidth”—energy window ΔE
 - Calibrate the polar angle θ
 - Choose certain range of slices and make an averaged bandmap
 - Plot bandmap in both real space $I(\theta, E_{\text{kin}})$ and k -space $I(k_{\parallel}, E_{\text{kin}})$
 - Plot integrated curve of chosen θ or k_{\parallel} range
 - Fit the Fermi level
 - Change display in E_{kin} or E_{b} mode

A Data Analysis Software—Mozi

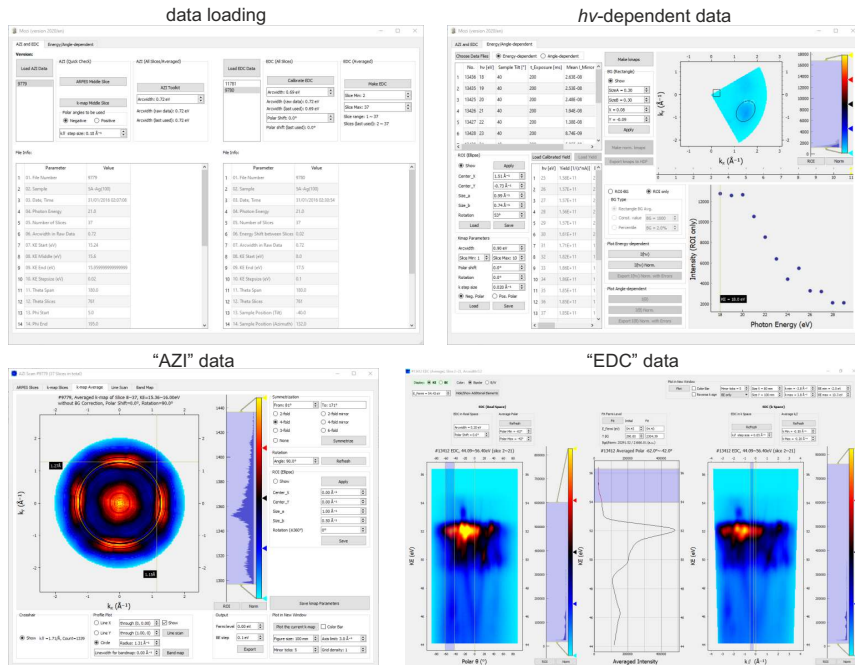


Figure A.1: Screenshot of MOZI.

- $h\nu$ -dependent: batch processing k -maps as a function of photon energy
 - Load a series of AZI data where only photon energies differ
 - Choose parameters for averaging k -maps
 - ROI analysis for all loaded k -maps and plot as a function of the photon energy
 - Normalize with calibrated yield data

The raw data taken with the LabVIEW-based measurement software are TXT files. Reading these by MOZI will collect all experimental parameters as well as the raw data and save them automatically into the compact HDF files, together with the data treatments by user.

Software Server

MOZI is hosted on the internal server of Forschungszentrum Jülich (<https://ibn-pgit.ibn.kfa-juelich.de/xyang/mozi>).

Package Dependencies

MOZI runs with a standard Python 3 installation and the following packages. An environment manager such as Miniconda is recommended.

- h5py
- Matplotlib
- NumPy
- pandas
- PyQt5
- pyqtgraph
- SciPy

Technical Details

Transform Between Real and Reciprocal Space

MOZI uses pyqtgraph to provide an interface that all slices from the data cube can be quickly viewed, *both* in real space $I(E_{\text{kin}}, \theta, \phi)$ and in reciprocal space $I(E_{\text{kin}}, k_x, k_y)$. One difficulty here is, if mathematically transforming the raw data in real space one-to-one to reciprocal space, $I(k_x, k_y)$ does not fall on an equidistant grid of points and cannot be viewed on the screen directly. In order to maintain the fast rendering capacity of pyqtgraph, an interpolation is made: first creating an equidistant grid of points in k -space with the step size defined by user; for each (k_x, k_y) point the corresponding (θ, ϕ) is searched in the raw data.

A code excerpt is shown in [Listing A.1](#). It uses the RegularGridInterpolator from SciPy to interpolate $I(\theta, \phi)$ and for each (k_x, k_y) the corresponding (θ, ϕ) is calculated in a meshgrid. Before applying the interpolator the meshgrid is flattened, and then reshaped to the original shape afterwards.

```

1 import numpy as np
2 from scipy import interpolate
3
4 def ThetaPhi_to_kxky(data_thetaPhi,KE,theta_array,phi_array,k_array,
   polarShift=0.0,rotation=0.0,negativeTheta=True):
5     # shift polar angle theta
6     theta_array = [theta - polarShift for theta in theta_array]
7     # rotate azimuth angle phi
8     phi_array = [phi + rotation for phi in phi_array]
9     k_points = len(k_array)
10    data_kxky = np.zeros([k_points, k_points])
11    f_interp = interpolate.RegularGridInterpolator((theta_array,
   phi_array),data_thetaPhi,bounds_error=False,fill_value=np.nan)
12    KX, KY = np.meshgrid(k_array, k_array, sparse=False)
13    k_magn = (KX**2 + KY**2)**0.5
14    prefactor = 1.95192 / (KE**0.5)
15    # 1.951917539300192 = np.sqrt(hbar**2 / (2*m_e*eV)) * 1e10
16    # sqrt(E[eV])=1.95192*k_parallel[1/Angstrom]
17    if negativeTheta: # negative theta is used
18        x_theta = np.rad2deg(-np.arcsin(prefactor*k_magn)).flatten(order=
   'F')
19    else: # positive theta is used
20        x_theta = np.rad2deg(np.arcsin(prefactor*k_magn)).flatten(order='
   F')
21    y_phi = np.rad2deg(np.arctan2(KY, KX)).flatten(order='F')
22    y_phi = [shifting_phi(phi_array, x) for x in y_phi]
23    points = [(x_theta[i], y_phi[i]) for i in range(len(x_theta))]
24    data_kxky = f_interp(points)
25    data_kxky = np.reshape(data_kxky, (k_points, k_points))
26    return data_kxky

```

Listing A.1: Interpolating $I(\theta, \phi)$ to $I(k_x, k_y)$.

While calculating (k_x, k_y) to (θ, ϕ) , $\pm np.arcsin$ is used to take either the positive or negative polar half for θ . The ϕ angle calculated via $np.arctan2$ returns value ranging in $[-180^\circ, 180^\circ]$, which is not necessarily found in raw data because the measurement software records ϕ e.g. from 180° to 360° . In order to shift it for interpolation the function shown in [Listing A.2](#) is used.

```

1 def shifting_phi(phi_array, phi):
2     phi_min = phi_array[0]
3     if -180.0 < phi_min <= 180.0:
4         if -180.0 <= phi < phi_min:
5             phi += 360.0
6     else:
7         delta_phi = phi_min - 180.0
8         if phi > (-180.0 + delta_phi): # if delta_phi > 0:
9             phi += 360.0
10    elif phi < (-180.0 + delta_phi):
11        phi += 720.0

```

```
12 return phi
```

Listing A.2: Shifting ϕ for interpolation.

Averaging Bandmap

As described in Fig. 3.5, the raw data cube of an “EDC” (bandmap) scan has ~ 40 slices between which the E_{kin} range differs by $\Delta E/(\text{number of slices})$. In MOZI, the user does not have to use all slices. One can choose the slice range of which the bandmap is averaged and specify the “arcwidth” (ΔE) after calibration. While averaging, the program needs to find the common E_{kin} range, i.e. between the lowest E_{kin} of the last slice and the highest E_{kin} of the first slice. Here this new E_{kin} range is also interpolated with the original step size, see Listing A.3.

```
1 # EthetaKE_size is a 3-element list holding the length of slices,
  # theta, and KE.
2 # KE_step is the step size of kinetic energy axis.
3 def get_EDC_avg(EthetaKE_cube, Theta_array, KE_array, slicemin, slicemax,
  arcwidth):
4 # E_step is changed after new arcwidth is given!
5 E_step_new = arcwidth / (EthetaKE_size[0] - 1)
6 KE_start = KE_array[0] - 0.5*arcwidth + (slicemax - 1)*E_step_new
7 KE_end = KE_array[-1] - 0.5*arcwidth + (slicemin - 1)*E_step_new
8 # KE array for averaging EDC has the same stepsize as in raw data.
9 KE_num = (KE_end - KE_start) / KE_step + 1
10 KE_array_forAvg = np.linspace(KE_start, KE_end, num=KE_num)
11 E_num = slicemax - slicemin + 1
12 EthetaKE_size_new = [int(E_num), EthetaKE_size[1], int(KE_num)]
13 EthetaKE_cube_new = np.empty((EthetaKE_size_new))
14 EthetaKE_cube_new[:] = np.nan
15 for i in range(E_num):
16     KE_array_raw = KE_array - 0.5*arcwidth + (slicemin - 1 + i)*
17         E_step_new
18     for j in range(len(Theta_array)):
19         f = interpolate.interpld(KE_array_raw,
20             EthetaKE_cube[slicemin - 1 + i, j])
21         EthetaKE_cube_new[i, j] = f(KE_array_forAvg)
22 ThetaKE_array = np.sum(EthetaKE_cube_new, axis=0)
23 return ThetaKE_array, Theta_array, KE_array_forAvg
```

Listing A.3: Function for averaging the bandmap.

B Data Analysis Software—Neso

Introduction

NESO is a Python-based software written for analyzing the photoemission data measured with the NanoESCA PEEM (Section 3.2.3). Its current form handles a stack of momentum maps measured at different kinetic energies, with a user-friendly graphical interface, see Fig. B.1. NESO is capable of the following data analysis for the NanoESCA data:

- Load a stack of TIF images
- Read or set kinetic energies of each slice
- Calibrate the size and shift in reciprocal space
- Crop data outside of the field of view
- Plot integrated EDC curve and fit the Fermi level
- Dispersion correction
- Line scan and bandmap of chosen line cut
- Save (read) data to (from) HDF format

The raw data taken at the NanoESCA beamline in Elettra are TIF files. Reading these by NESO is performed with the `tiffile` package (see below). The user can save the data and related parameters together into the compact HDF file for later treatments.

Software Server

NESO is hosted on the internal server of Forschungszentrum Jülich (<https://ibn-pgit.ibn.kfa-juelich.de/xyang/neso>).

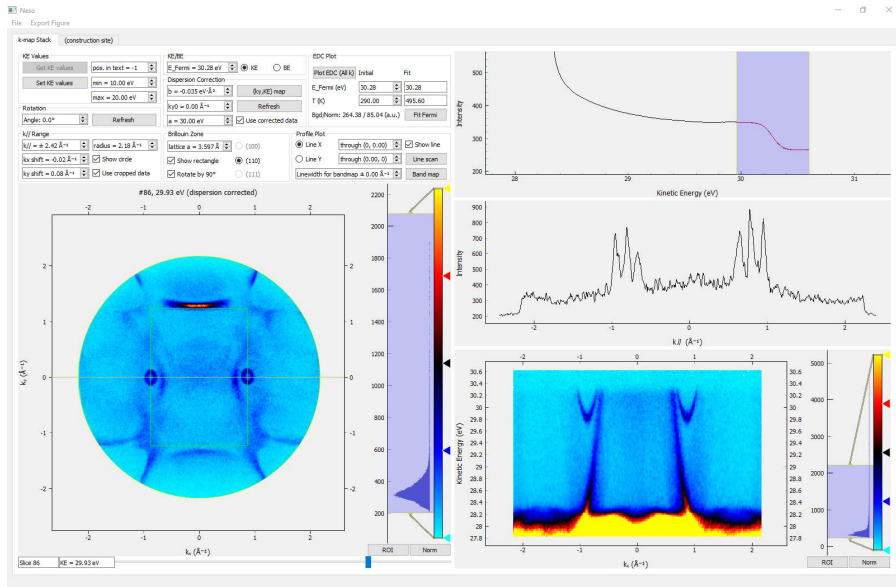


Figure B.1: Screenshot of Neso. A dataset of the clean Cu(110) surface is displayed.

Package Dependencies

Neso runs with a standard Python 3 installation and the following packages. An environment manager such as Miniconda is recommended.

- h5py
- Matplotlib
- NumPy
- pandas
- PyQt5
- pyqtgraph
- SciPy
- skimage
- tiffle

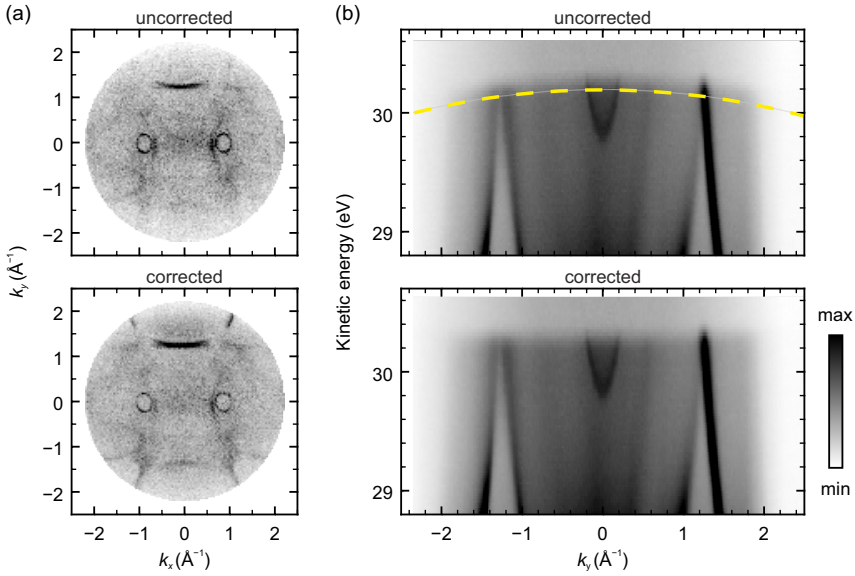


Figure B.2: Dispersion correction in NESO. (a) Momentum map of clean Cu(110) measured at E_{kin} close to the Fermi level. p-polarized light, photon energy 30 eV, angle of incidence 65° . (b) Integrated bandmap $I(k_y, E_{\text{kin}})$ to determine the dispersion necessary for correction. User-defined parabola is displayed as a yellow, dashed curve.

Technical Details

Dispersion Correction

Different from the conventional ARPES technique which measures a 3D data cube in real space $I(E_{\text{kin}}, \theta, \phi)$ before transformed into reciprocal space $I(E_{\text{kin}}, k_x, k_y)$ during data analysis, NanoESCA captures $I(k_x, k_y)$ images—momentum maps—already in the data acquisition stage. However, two hemispherical analyzers in series intrinsically introduce an energy dispersion, see Fig. B.2(a): For a measured Fermi surface k -map it is noticeable the intensity at $k_y = 0 \text{\AA}^{-1}$ is slightly higher than that at $k_y = \pm 2.0 \text{\AA}^{-1}$ because of the kinetic energy difference. This is compensated, if a data cube of $I(E_{\text{kin}}, k_x, k_y)$ is available, by a user-defined parabola near the Fermi level in the integrated bandmap $I(k_y, E_{\text{kin}})$, so that the “bent” Fermi level is straightened [Fig. B.2(b)].

The user defines the b and k_{y0} parameter in the parabola formula,

$$E_{\text{kin}} = b(k_y - k_{y0})^2 + a, \quad (\text{B.1})$$

where a is simply a shift in kinetic energy axis, which is adjustable to align the parabola according to the Fermi level. The whole data cube is then corrected by interpolation, see [Listing B.1](#).

```

1 KEleft = abs(b * (self.ky_axis[0] - ky0)**2)
2 KEright = abs(b * (self.ky_axis[-1] - ky0)**2)
3 KEchange = KEleft if KEleft > KEright else KEright
4 if b < 0:
5     KEmin = self.KE_axis[0] + KEchange
6     KEmax = self.KE_axis[-1]
7 else:
8     KEmin = self.KE_axis[0]
9     KEmax = self.KE_axis[-1] - KEchange
10 self.KE_axis_corrected = np.linspace(KEmin, KEmax, num=int(1 + (KEmax -
    KEmin) / self.KE_stepsize))
11 # interpolation [KE, kx, ky]
12 points = []
13 for _, KE in enumerate(self.KE_axis_corrected):
14     points.append([(b*(ky-ky0)**2+KE, ky) for ky in self.ky_axis])
15 points = np.array(points).reshape([-1, 2])
16 self.data_KEkxky_corrected = np.zeros([len(self.KE_axis_corrected),
    len(self.kx_axis), len(self.ky_axis)])
17 for i in range(len(self.kx_axis)):
18     f_interp = interpolate.RegularGridInterpolator(
19         (self.KE_axis, self.ky_axis), self.data_KEkxky[:, i, :],
20         bounds_error=False, fill_value=np.nan)
21     self.data_KEkxky_corrected[:, i, :] = f_interp(points).reshape(
22         [len(self.KE_axis_corrected), len(self.ky_axis)])

```

Listing B.1: Interpolation for correcting the energy dispersion.

Further Development

Currently the $I(E_{\text{kin}}, k_x, k_y)$ data cube measured on NanoESCA can be read and easily manipulated. For the k -map stack measured at a single kinetic energy one may subtract the MCP background, correct the possible drift, and finally produce averaged results with high statistics. This is currently performed with ImageJ (Fiji) and a plugin called Template Matching, which can be implemented into the cross-platform NESO program in the future.

C Sensitivity of PT for Geometric Information

One strength of photoemission tomography (PT) is its capability to simultaneously determine the electronic and geometric structures of oriented adsorbed layers of organic molecules. In particular, here the sensitivity of PT using momentum maps is demonstrated, where the deviations from a perfectly flat adsorption geometry of the tetracene (4A) molecules and from their azimuthal alignment along the $[1\bar{1}0]$ direction are tested.

Tilting of Tetracene on Ag(110)

Fig. C.1 illustrates the effect of a molecular tilt angle, that is a rotation along the long molecular axis, for the HOMO of tetracene. These simulations clearly indicate that out-of-plane tilt angles larger than approximately 6° would be clearly visible since the four lobes present in the flat geometry start to merge along the $[001]$ direction. Such an appearance is, however, not seen in measurement [Fig. 6.4(b–d)] which excludes significant tilt angles of tetracene. Note that the sensitivity of PT to molecular tilt angles has been demonstrated before for 5A [7, 40] and 6P [17, 30].

Azimuthal Misalignment of Tetracene on Ag(110)

Inspired by the coverage-dependent structural STM and LEED investigations of Takasugi and Yokoyama [250], Fig. C.2 shows how an azimuthal misalignment of tetracene with respect to $[1\bar{1}0]$ would appear in the PT k -maps of the HOMO and the LUMO. Upon increasing the misalignment angle, the four lobes of the HOMO gradually lose their elongated appearance along the $[001]$ direction and become more roundish, before, at angles above 10° , the original lobes split into two separate features. In the coverage-dependent PT results [see Section 6.3.5, Fig. 6.4(b–d)] it is evident that at saturation coverage [Fig. 6.4(d)] there is a $\pm 10^\circ$ misalignment. Note that this finding is fully consistent with the structural study of Tagasugi and Yokoyama, who observed a similar misalignment at the saturated monolayer coverage of 4A on Ag(110) (Fig. 6 of Ref. [250]).

C Sensitivity of PT for Geometric Information

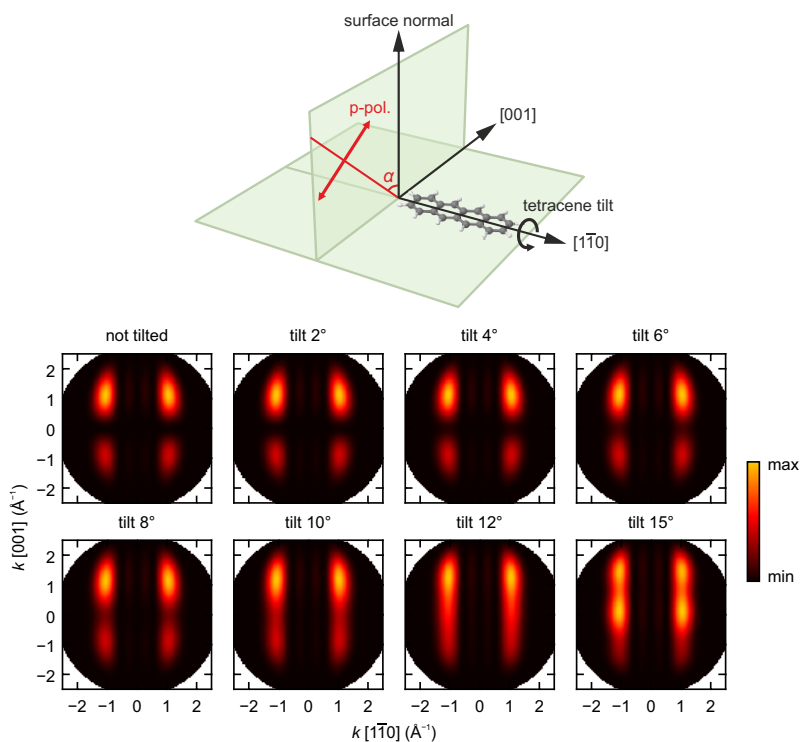


Figure C.1: Theoretical k -maps of HOMO for tetracene (4A) on Ag(110) with tilting around molecules' long axis. Parameters used for simulation: kinetic energy of photoelectrons 28 eV, p-polarized light, angle of incidence $\alpha = 65^\circ$. Taking into account the two-fold symmetry of the substrate, the simulated intensities are a superposition of contributions from 4A molecules tilted by angles $+\alpha$ and $-\alpha$.

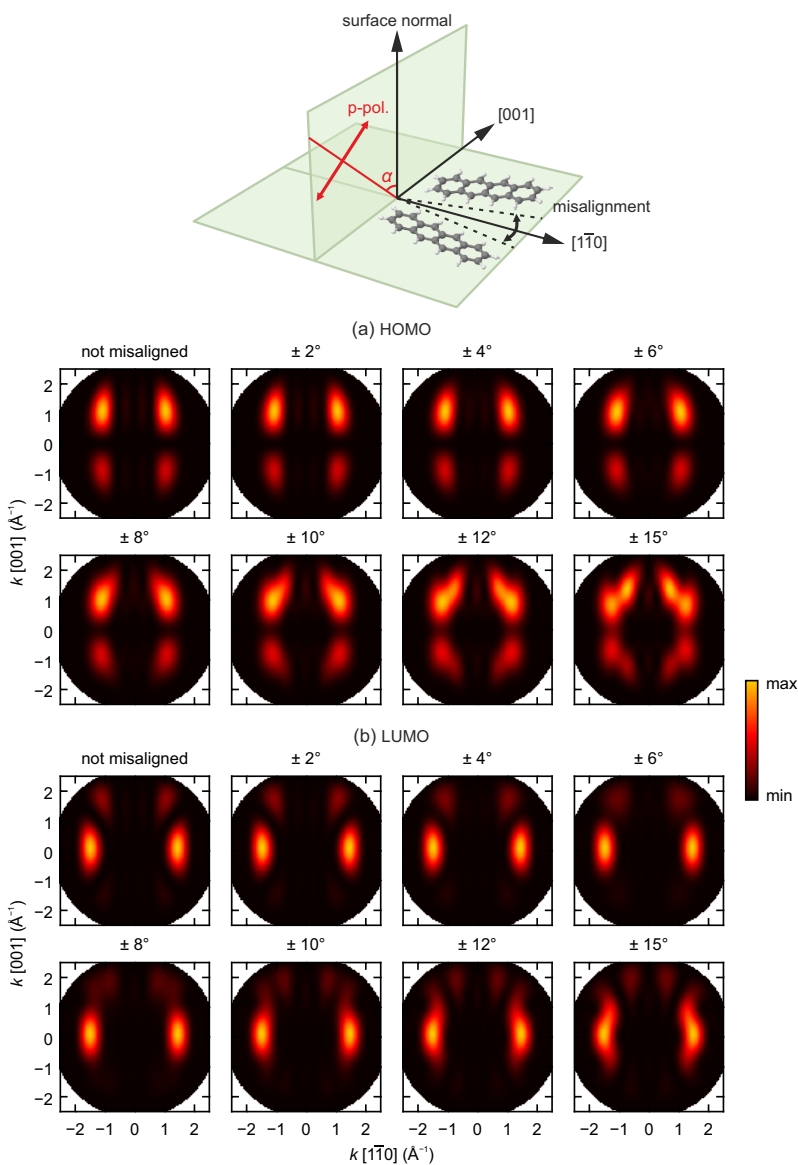


Figure C.2: Theoretical k -maps of HOMO and LUMO for 4A on Ag(110) with misalignment from the $[1\bar{1}0]$ direction. Parameters used for simulation: kinetic energy of photoelectrons 28eV, p-polarized light, angle of incidence $\alpha = 65^\circ$. Upon increasing the misalignment angle, the shape of the main lobe of HOMO changes. This is experimentally observed for the HOMO k -map of the saturated 4A monolayer indicating a misalignment [cf. Fig. 6.4(d)].

D Photon-Energy Dependence of PT

Weiß et al. [46] showed that, for a ML PTCDA on Ag(110), the overall dependence of the photoemission intensity on the photon energy can be well accounted for by assuming a plane wave for the final state (Section 2.3.2). But the experimental data, both for the LUMO and HOMO of PTCDA, exhibit additional modulations attributed to final state scattering effects [46].

Photoemission Intensity Normalization

The photon-energy dependence of a certain molecular orbital is briefly introduced in Section 2.3.3.4. In experiments, the photon-energy dependent photoemission intensities $I(h\nu, E_{\text{kin}}, k_x, k_y)$ as k -maps are recorded, where the kinetic energy E_{kin} of the detector is set to be $h\nu - \Phi - E_b$ each time the photon energy $h\nu$ is changed, Φ being the sample's work function and E_b the binding energy of the molecular orbital of interest. If the toroidal electron analyzer is used, the data needs to be transformed into reciprocal space from $I(h\nu, E_{\text{kin}}, \theta, \phi)$ first, see Section 3.3. If the NanoESCA PEEM (Section 3.2.3) is employed, this transformation step can be neglected.

Subsequently, $I(h\nu)$ should be properly normalized because the photon flux provided by the beamline is not homogeneous throughout a large photon energy range. Basic calibration technique such as gold meshes used in standard synchrotron beamlines is not suitable for a broad spectral range and lacks the absolute calibration. Well-calibrated semiconductor photodiodes in this regard are provided by the U125 insertion device beamline at the Metrology Light Source of Physikalisch-Technische Bundesanstalt (PTB), Berlin, Germany [116] and the normalized intensities $I_n(h\nu)$ are calculated as:

$$I_n(h\nu) = \frac{I(h\nu)}{i_m \eta(h\nu) T}, \quad (\text{D.1})$$

where i_m is the averaged mirror (reference detector in the beamline) current during the measurement, $\eta(h\nu)$ is the calibrated photon yield (Fig. D.1), and T is the camera's acquisition time.

D Photon-Energy Dependence of PT

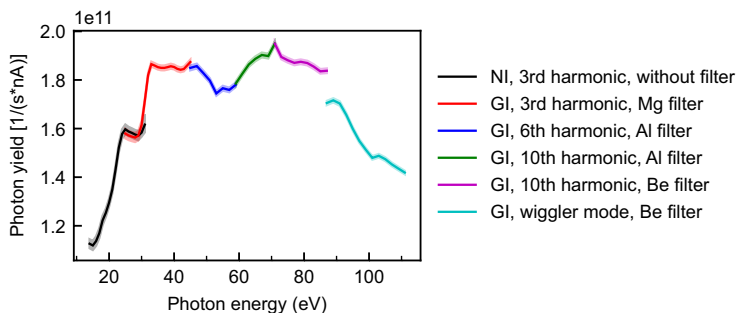


Figure D.1: Calibrated photon yield curve at U125 insertion device beamline, PTB, 2019 April. Error bars are rendered as shaded areas. Colors represent different configurations for monochromator (normal incidence NI or grazing incidence GI), undulator harmonics (or wiggler mode) and filter. Courtesy of A. Gottwald, H. Kaser, and H. Kirschner.

When investigating the photon-energy dependence of a certain molecular orbital, not all photoemission intensities in the measurable k -space are taken into account, but only a small area, normally close to the maxima in the calculated k -map. Comparing with k -maps of larger photon energies, the main lobe in k -maps of small photon energies appear “truncated” by the photoemission horizon. For example, see Fig. D.2(a), the LUMO of PTCDA has its maximum at $(k_x, k_y) = (0 \text{ \AA}^{-1}, 1.35 \text{ \AA}^{-1})$ when $h\nu = 15 \text{ eV}$; at $(0 \text{ \AA}^{-1}, 1.75 \text{ \AA}^{-1})$ when $h\nu = 30 \text{ eV}$. The authors of Ref. [46] had used $|k| = 1.5 \text{ \AA}^{-1}$ and 1.2 \AA^{-1} for PTCDA LUMO and HOMO, respectively [113], so that the chosen region of interest (ROI) is close to the maxima for all photon energies. DFT-calculated wave functions of LUMO and HOMO, considering only isolated PTCDA, are independent of the choice for ROI. The main peak position of $|\tilde{\psi}|$ as a function of k_z for LUMO is marginally larger than that for HOMO (by $\sim 4\%$), see the dotted lines in Fig. D.3.

Plane Wave Final State Prediction

The agreement between the photon-energy dependence of a molecular orbital and the plane wave final state prediction can be checked using the analytic form of the Fourier transform of an atomic p_z orbital for the latter [46]:

$$\tilde{\psi}_{p_z}(k, \theta_k) = \sqrt{8\pi i} \left(\frac{Z}{a_B} \right)^{\frac{7}{2}} \frac{k}{\left(k^2 + \frac{Z^2}{4a_B^2} \right)^3} \cos \theta_k, \quad (\text{D.2})$$

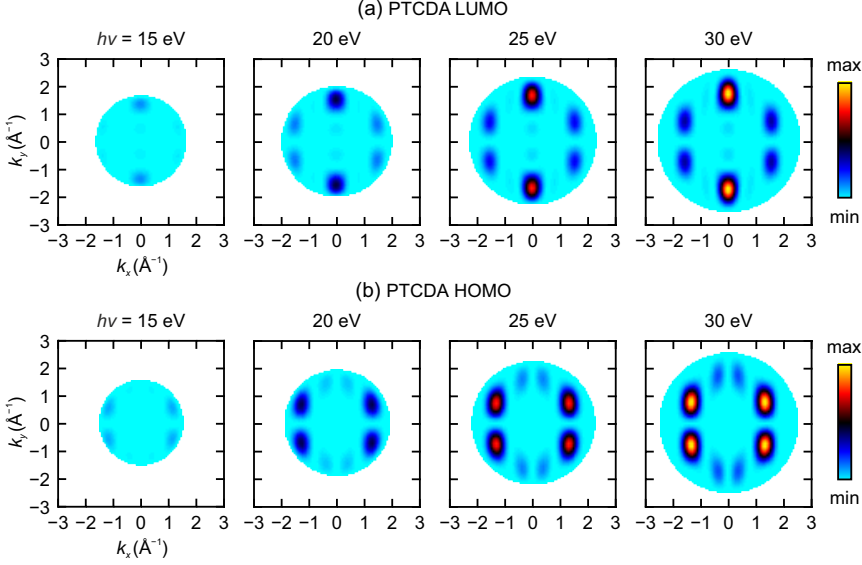


Figure D.2: Photon-energy dependent theoretical k -maps of (a) LUMO and (b) HOMO for PTCDA molecules using the toroidal electron analyzer (p-polarized light, angle of incidence $\alpha = 40^\circ$). Calculations with the help of Ref. [63] and MOZI (Appendix A).

where k and θ_k are the length and the polar angle of wavevector, Z and a_B are the nuclear charge and the Bohr radius. With $\cos\theta_k = k_z/k$, Eq. (D.2) can be reduced to:

$$\tilde{\psi}_{p_z}(k_z) = a_0^2 \frac{k_z}{(k_z^2 + k_0^2)^3}, \quad (\text{D.3})$$

where a_0 and k_0 are fit parameters. With Eq. (2.22), I versus $h\nu$ plots are transferred to $|\tilde{\psi}|$ versus k_z plots and the plane-wave curve fit is conducted using Eq. (D.3), see the PTCDA/Ag(110) example in Fig. D.3.

Essentially both LUMO and HOMO of PTCDA on Ag(110) show similar $h\nu$ -dependence with a peak at around 25 eV ($k_z = 1.3 \text{ \AA}^{-1}$). The plane wave final state fitting also has a good agreement with the DFT-calculated k_z -dependence (dotted lines) for isolated molecules. But there is also clear additional peak/shoulder feature which is unexplained by the plane wave final state prediction (dashed curves) at around 33 eV ($k_z = 2.3 \text{ \AA}^{-1}$) and may result from the scattering of outgoing electrons. It was speculated that the position of this $k_z = 2.3 \text{ \AA}^{-1}$ resonance could be

D Photon-Energy Dependence of PT

related to the adsorption height of PTCDA on Ag(110) (2.56 \AA [142, 204], close to the wavelength of the former).

Results and Discussions

In the following, two further $h\nu$ -dependent datasets of 5A/Ag(100) and bisanthene/Cu(110) are shown, see Figs. D.4 and D.5. Details of sample preparations can be found in Section 6.3.2 and Section 4.3.1, respectively. The agreement between the experimental data and the plane wave final state prediction is somewhat less, e.g. the measured $h\nu$ -dependent LUMO intensity of 5A on Ag(100) exhibits more than two peaks. Aside from arguing how well the concatenations are between different beamline configurations for covering a wide range of photon energies, the fittings for plane wave final state prediction are not good, especially on the small $h\nu$ side. Photoelectrons with very low kinetic energy are generally not easy to detect and the minimum kinetic energy detectable by the toroidal electron analyzer is 10 eV. Therefore, there are less data points to the small $h\nu$ side and this may worsen the fitting for plane wave final state prediction in this energy range.

Another experimental issue one has to take into consideration is the treatment of background intensity. In the data presented in Figs. D.3, D.4, and D.5, the minimum intensity (dark count) of k -maps in each beamline configuration is taken to estimate the background, which then gets subtracted from the ROI intensity for each orbital. This is a relatively rough estimation. The Würzburg group developed a fitting routine where the EDC curve for each pixel in the k -map is split into the contribution of the substrate and the contribution of the LUMO/HOMO orbital [40, 47]. This procedure is only possible with a NanoESCA PEEM system and can “remove” strong substrate features such as sp-bands from the k -map. The photon-energy dependent data of PTCDA/Ag(110) with this fitting routine by Graus et al. [47] is presented in Fig. D.6 and the fitting for plane wave final state prediction is conducted.¹⁰ Comparing with the results on the same system reported by Weiß et al. [46] (Fig. D.3), the data points may be fit with the plane wave final state prediction slightly better, but the main peak position of $|\tilde{\psi}|$ as a function of k_z is shifted by $\sim 30\%$ smaller (to 0.93 \AA^{-1} and 0.89 \AA^{-1} for LUMO and HOMO, respectively). This discrepancy shall be due to the different normalization of measured intensities: Graus et al. [47] used gold meshes and corresponding calibration from the literature; Weiß et al. [46] utilized well-calibrated photodiodes at the Metrology Light Source of PTB which is more accurate. This is reflected by the

¹⁰The authors of Ref. [47] had used $(k_x, k_y) = (0 \text{ \AA}^{-1}, 1.6 \text{ \AA}^{-1})$ for LUMO and $(k_x, k_y) = (0.3 \text{ \AA}^{-1}, 1.8 \text{ \AA}^{-1})$ for HOMO, the latter being the *minor* lobe in simulated k -map. The fitting calculation here also considers the different angle of incidence α (65°) and $\mathbf{A} \cdot \mathbf{k}$ factor.

good agreement between the fitted curves and the DFT calculated k_z -dependence (Fig. D.3).

Overall, the difference between the simple plane wave final state approximation and the measured $h\nu$ -dependent data is still a subject of ongoing discussions, especially the origin of additional modulations in the latter. Up to now we have some doubts whether the position of these modulations (resonances or peaks) can be simply related to the adsorption height of adsorbed molecules. Conclusive results may only be possible if one chooses a system that the molecule–metal interaction is so weak that the substrate can be excluded from the discussion and an extremely heavy DFT calculation involving the molecule and the substrate is avoided. Additionally, the experiment should be conducted at a well-calibrated synchrotron beam line for a reliable intensity normalization.

D Photon-Energy Dependence of PT

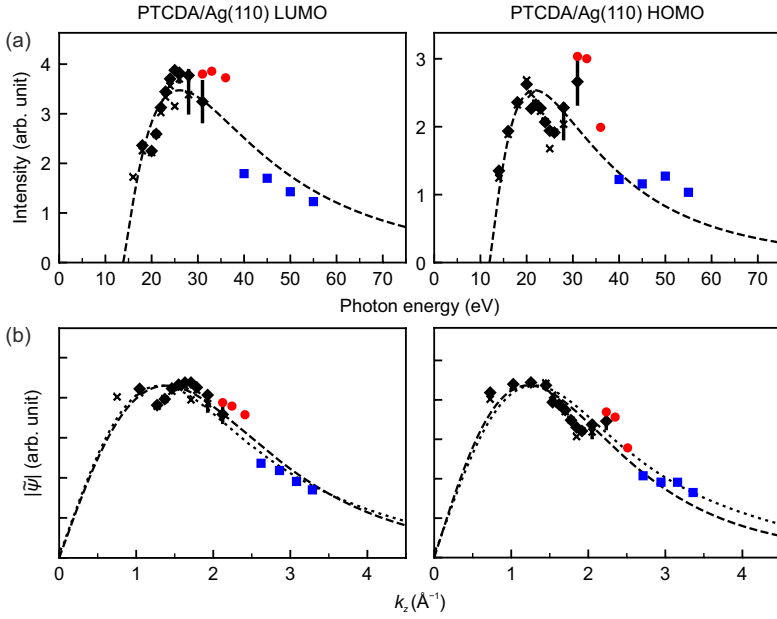


Figure D.3: Photon-energy dependent data of PTCDA/Ag(110). (a) Normalized photoemission intensities of the main LUMO/HOMO lobe as a function of photon energy. (b) k_z -dependence of the Fourier transforms of LUMO/HOMO. Dashed lines correspond to the plane-wave fitting according to Eq. (D.3). Dotted lines show the k_z -dependence of the DFT calculated orbitals in k -space. Colors represent different beamline configurations as in Fig. D.1, except that black crosses for normal incidence, *first* harmonic, without filter. Reproduced from Ref. [46].

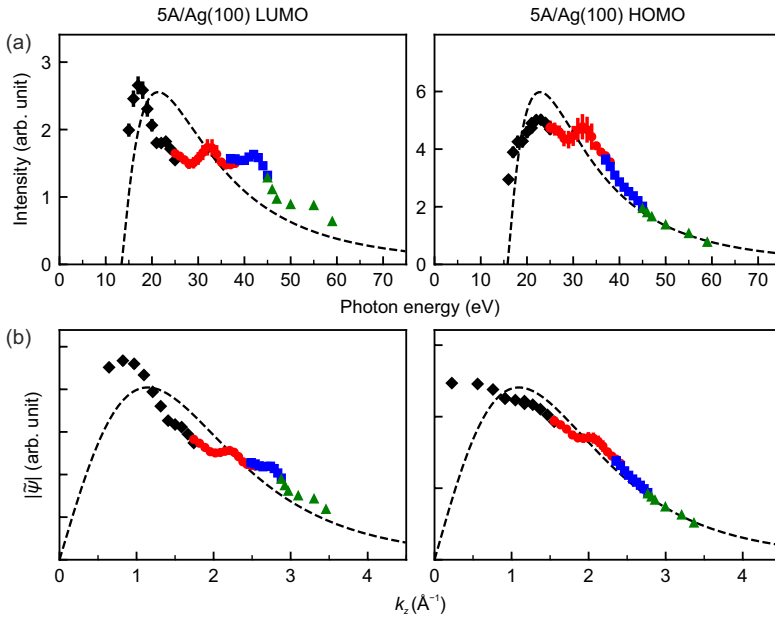


Figure D.4: Photon-energy dependent data of 5A/Ag(100). (a) Normalized photoemission intensities of the main LUMO/HOMO lobe as a function of photon energy. (b) k_z -dependence of the Fourier transforms of LUMO/HOMO. Dashed lines correspond to the plane-wave fitting according to Eq. (D.3). Colors represent different beamline configurations as in Fig. D.1.

D Photon-Energy Dependence of PT

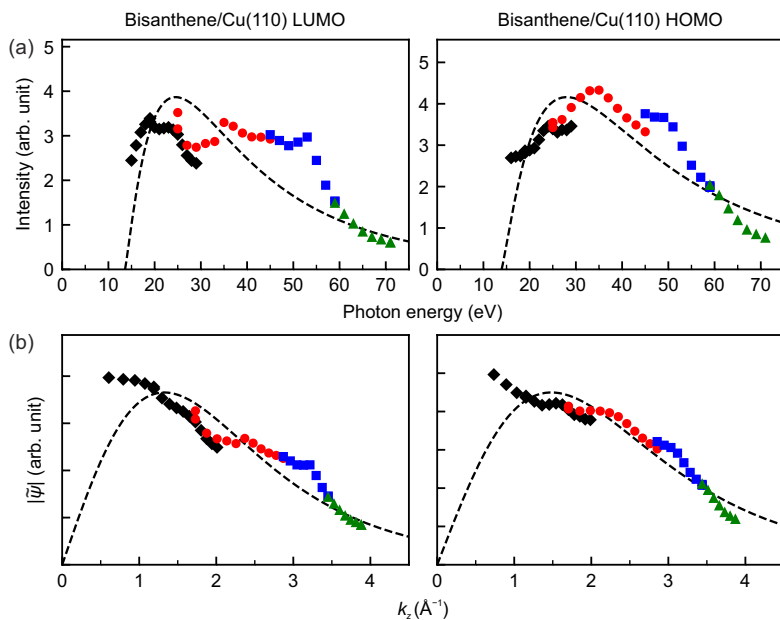


Figure D.5: Photon-energy dependent data of bisanthene/Cu(110). (a) Normalized photoemission intensities of the main LUMO/HOMO lobe as a function of photon energy. (b) k_z -dependence of the Fourier transforms of LUMO/HOMO. Dashed lines correspond to the plane-wave fitting according to Eq. (D.3). Colors represent different beamline configurations as in Fig. D.1.

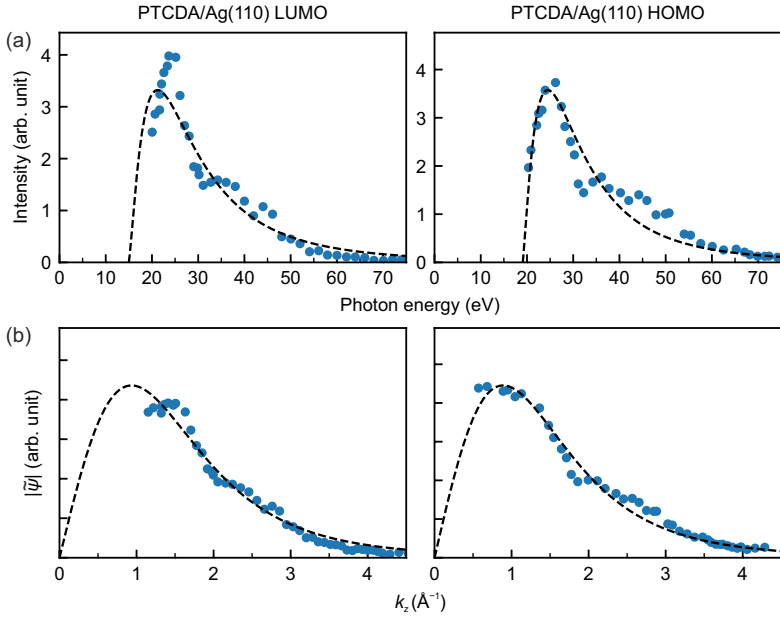


Figure D.6: Photon-energy dependent data of PTCDA/Ag(110). (a) Normalized photoemission intensities of the main LUMO/HOMO lobe as a function of photon energy. Reproduced from Ref. [47]. (b) k_z -dependence of the Fourier transforms of LUMO/HOMO. Dashed lines correspond to the plane-wave fitting according to Eq. (D.3).

Bibliography

- [1] J. Repp, G. Meyer, S. M. Stojković, A. Gourdon, and C. Joachim, *Phys. Rev. Lett.* **94**, 026803 (2005).
- [2] P. Puschnig and M. G. Ramsey, “Photoemission tomography: valence band photoemission as a quantitative method for investigating molecular films”, in *Encyclopedia of interfacial chemistry: surface science and electrochemistry* (Elsevier, 2018), pp. 380–391.
- [3] G. Koller, S. Berkebile, M. Oehzelt, P. Puschnig, C. Ambrosch-Draxl, F. P. Netzer, and M. G. Ramsey, *Science* **317**, 351 (2007).
- [4] S. Berkebile, P. Puschnig, G. Koller, M. Oehzelt, F. P. Netzer, C. Ambrosch-Draxl, and M. G. Ramsey, *Phys. Rev. B* **77**, 115312 (2008).
- [5] S. Berkebile, G. Koller, P. Puschnig, C. Ambrosch-Draxl, F. P. Netzer, and M. G. Ramsey, *Appl. Phys. A* **95**, 101 (2008).
- [6] S. Berkebile, G. Koller, A. Fleming, P. Puschnig, C. Ambrosch-Draxl, K. Emtsev, T. Seyller, J. Riley, and M. Ramsey, *J. Electron Spectrosc. Relat. Phenom.* **174**, 22 (2009).
- [7] P. Puschnig, S. Berkebile, A. J. Fleming, G. Koller, K. Emtsev, T. Seyller, J. D. Riley, C. Ambrosch-Draxl, F. P. Netzer, and M. G. Ramsey, *Science* **326**, 702 (2009).
- [8] J. Ziroff, F. Forster, A. Schöll, P. Puschnig, and F. Reinert, *Phys. Rev. Lett.* **104**, 233004 (2010).
- [9] S. Berkebile, T. Ules, P. Puschnig, L. Romaner, G. Koller, A. J. Fleming, K. Emtsev, T. Seyller, C. Ambrosch-Draxl, F. P. Netzer, and M. G. Ramsey, *Phys. Chem. Chem. Phys.* **13**, 3604 (2011).
- [10] P. Puschnig, E. M. Reinisch, T. Ules, G. Koller, S. Soubatch, M. Ostler, L. Romaner, F. S. Tautz, C. Ambrosch-Draxl, and M. G. Ramsey, *Phys. Rev. B* **84**, 235427 (2011).
- [11] B. Stadtmüller, M. Willenbockel, E. M. Reinisch, T. Ules, F. C. Bocquet, S. Soubatch, P. Puschnig, G. Koller, M. G. Ramsey, F. S. Tautz, and C. Kumpf, *EPL* **100**, 26008 (2012).
- [12] M. Wießner, D. Hauschild, A. Schöll, F. Reinert, V. Feyer, K. Winkler, and B. Krömker, *Phys. Rev. B* **86**, 045417 (2012).
- [13] M. Wießner, N. S. R. Lastra, J. Ziroff, F. Forster, P. Puschnig, L. Dössel, K. Müllen, A. Schöll, and F. Reinert, *New J. Phys.* **14**, 113008 (2012).

Bibliography

- [14] M. Wießner, J. Ziroff, F. Forster, M. Arita, K. Shimada, P. Puschnig, A. Schöll, and F. Reinert, *Nat. Commun.* **4**, 1514 (2013).
- [15] M. Willenbockel, B. Stadtmüller, K. Schönauer, F. C. Bocquet, D. Lüftner, E. M. Reinisch, T. Ules, G. Koller, C. Kumpf, S. Soubatch, P. Puschnig, M. G. Ramsey, and F. S. Tautz, *New J. Phys.* **15**, 033017 (2013).
- [16] M. Wießner, J. Kübert, V. Feyer, P. Puschnig, A. Schöll, and F. Reinert, *Phys. Rev. B* **88**, 075437 (2013).
- [17] E. M. Reinisch, T. Ules, P. Puschnig, S. Berkebile, M. Ostler, T. Seyller, M. G. Ramsey, and G. Koller, *New J. Phys.* **16**, 023011 (2014).
- [18] V. Feyer, M. Graus, P. Nigge, M. Wießner, R. Acres, C. Wiemann, C. Schneider, A. Schöll, and F. Reinert, *Surf. Sci.* **621**, 64 (2014).
- [19] B. Stadtmüller, D. Lüftner, M. Willenbockel, E. M. Reinisch, T. Sueyoshi, G. Koller, S. Soubatch, M. G. Ramsey, P. Puschnig, F. S. Tautz, and C. Kumpf, *Nat. Commun.* **5**, 3685 (2014).
- [20] M. Wießner, D. Hauschild, C. Sauer, V. Feyer, A. Schöll, and F. Reinert, *Nat. Commun.* **5**, 4156 (2014).
- [21] D. Lüftner, M. Milko, S. Huppmann, M. Scholz, N. Ngyuen, M. Wießner, A. Schöll, F. Reinert, and P. Puschnig, *J. Electron Spectrosc. Relat. Phenom.* **195**, 293 (2014).
- [22] M. Dauth, M. Wiessner, V. Feyer, A. Schöll, P. Puschnig, F. Reinert, and S. Kümmel, *New J. Phys.* **16**, 103005 (2014).
- [23] T. Ules, D. Lüftner, E. M. Reinisch, G. Koller, P. Puschnig, and M. G. Ramsey, *Phys. Rev. B* **90**, 155430 (2014).
- [24] M. Willenbockel, D. Lüftner, B. Stadtmüller, G. Koller, C. Kumpf, S. Soubatch, P. Puschnig, M. G. Ramsey, and F. S. Tautz, *Phys. Chem. Chem. Phys.* **17**, 1530 (2015).
- [25] P. Puschnig and D. Lüftner, *J. Electron Spectrosc. Relat. Phenom.* **200**, 193 (2015).
- [26] B. Stadtmüller, M. Willenbockel, S. Schröder, C. Kleimann, E. M. Reinisch, T. Ules, S. Soubatch, M. G. Ramsey, F. S. Tautz, and C. Kumpf, *Phys. Rev. B* **91**, 155433 (2015).
- [27] H. Offenbacher, D. Lüftner, T. Ules, E. M. Reinisch, G. Koller, P. Puschnig, and M. G. Ramsey, *J. Electron Spectrosc. Relat. Phenom.* **204**, 92 (2015).
- [28] B. Stadtmüller, S. Schröder, and C. Kumpf, *J. Electron Spectrosc. Relat. Phenom.* **204**, 80 (2015).
- [29] S. H. Park and S. Kwon, *Anal. Chem.* **88**, 4565 (2016).
- [30] E. M. Reinisch, P. Puschnig, T. Ules, M. G. Ramsey, and G. Koller, *Phys. Rev. B* **93**, 155438 (2016).
- [31] M. Dauth, M. Graus, I. Schelter, M. Wießner, A. Schöll, F. Reinert, and S. Kümmel, *Phys. Rev. Lett.* **117**, 183001 (2016).

- [32] T. Huempfer, M. Hafermann, C. Udhardt, F. Otto, R. Forker, and T. Fritz, *J. Chem. Phys.* **145**, 174706 (2016).
- [33] K. Schönauer, S. Weiss, V. Feyer, D. Lüftner, B. Stadtmüller, D. Schwarz, T. Sueyoshi, C. Kumpf, P. Puschnig, M. G. Ramsey, F. S. Tautz, and S. Soubatch, *Phys. Rev. B* **94**, 205144 (2016).
- [34] T. Ules, D. Lüftner, E. M. Reinisch, G. Koller, P. Puschnig, and M. G. Ramsey, *Phys. Rev. B* **94**, 205405 (2016).
- [35] P. Puschnig, A. D. Boese, M. Willenbockel, M. Meyer, D. Lüftner, E. M. Reinisch, T. Ules, G. Koller, S. Soubatch, M. G. Ramsey, and F. S. Tautz, *J. Phys. Chem. Lett.* **8**, 208 (2017).
- [36] M. Hollerer, D. Lüftner, P. Hurdax, T. Ules, S. Soubatch, F. S. Tautz, G. Koller, P. Puschnig, M. Sterrer, and M. G. Ramsey, *ACS Nano* **11**, 6252 (2017).
- [37] G. Zamborlini, D. Lüftner, Z. Feng, B. Kollmann, P. Puschnig, C. Dri, M. Panighel, G. Di Santo, A. Goldoni, G. Comelli, M. Jugovac, V. Feyer, and C. M. Schneider, *Nat. Commun.* **8**, 335 (2017).
- [38] M. Graus, C. Metzger, M. Grimm, V. Feyer, P. Puschnig, A. Schöll, and F. Reinert, *J. Phys. Soc. Jpn.* **87**, 061009 (2018).
- [39] G. van Straaten, M. Franke, S. Soubatch, B. Stadtmüller, D. A. Duncan, T.-L. Lee, F. S. Tautz, and C. Kumpf, *J. Phys. Chem. C* **122**, 8491 (2018).
- [40] M. Grimm, C. Metzger, M. Graus, M. Jugovac, G. Zamborlini, V. Feyer, A. Schöll, and F. Reinert, *Phys. Rev. B* **98**, 195412 (2018).
- [41] M. Hollerer, S. Pachmajer, D. Lüftner, B. Butej, E.-M. Reinisch, P. Puschnig, G. Koller, M. G. Ramsey, and M. Sterrer, *Surf. Sci.* **678**, 149 (2018).
- [42] J. Felter, J. Wolters, F. C. Bocquet, F. S. Tautz, and C. Kumpf, *J. Phys.: Condens. Matter* **31**, 114003 (2019).
- [43] D. Lüftner, T. Ules, E. M. Reinisch, G. Koller, S. Soubatch, F. S. Tautz, M. G. Ramsey, and P. Puschnig, *Proc. Natl. Acad. Sci. U.S.A.* **111**, 605 (2014).
- [44] P. Kliuiev, T. Latychevskaia, J. Osterwalder, M. Hengsberger, and L. Castiglioni, *New J. Phys.* **18**, 093041 (2016).
- [45] P. Kliuiev, T. Latychevskaia, G. Zamborlini, M. Jugovac, C. Metzger, M. Grimm, A. Schöll, J. Osterwalder, M. Hengsberger, and L. Castiglioni, *Phys. Rev. B* **98**, 085426 (2018).
- [46] S. Weiß, D. Lüftner, T. Ules, E. M. Reinisch, H. Kaser, A. Gottwald, M. Richter, S. Soubatch, G. Koller, M. G. Ramsey, F. S. Tautz, and P. Puschnig, *Nat. Commun.* **6**, 8287 (2015).
- [47] M. Graus, C. Metzger, M. Grimm, P. Nigge, V. Feyer, A. Schöll, and F. Reinert, *Eur. Phys. J. B* **92**, 80 (2019).

Bibliography

- [48] D. Lüftner, S. Weiß, X. Yang, P. Hurdax, V. Feyer, A. Gottwald, G. Koller, S. Soubatch, P. Puschnig, M. G. Ramsey, and F. S. Tautz, *Phys. Rev. B* **96**, 125402 (2017).
- [49] C. Udhardt, F. Otto, C. Kern, D. Lüftner, T. Huempfer, T. Kirchhübel, F. Sojka, M. Meissner, B. Schröter, R. Forker, P. Puschnig, and T. Fritz, *J. Phys. Chem. C* **121**, 12285 (2017).
- [50] J. W. Gadzuk, *Solid State Commun.* **15**, 1011 (1974).
- [51] J. W. Gadzuk, *Phys. Rev. B* **10**, 5030 (1974).
- [52] J. W. Gadzuk, *Surf. Sci.* **53**, 132 (1975).
- [53] W. H. E. Schwarz, *Angew. Chem. Int. Ed.* **45**, 1508 (2006).
- [54] J. Schirmer, *Many-body methods for atoms, molecules and clusters* (Springer International Publishing, 2018).
- [55] A. I. Krylov, *J. Chem. Phys.* **153**, 080901 (2020).
- [56] P. Puschnig, *Fundamentals of electronic structure theory*, Lecture notes (University of Graz, 2018).
- [57] D. G. Truhlar, P. C. Hiberty, S. Shaik, M. S. Gordon, and D. Danovich, *Angew. Chem.* **131**, 12460 (2019).
- [58] J. V. Ortiz, *J. Chem. Phys.* **153**, 070902 (2020).
- [59] J. M. Zuo, M. Kim, M. O’Keeffe, and J. C. H. Spence, *Nature* **401**, 49 (1999).
- [60] C. Brion, G. Cooper, Y. Zheng, I. Litvinyuk, and I. McCarthy, *Chem. Phys.* **270**, 13 (2001).
- [61] J. Itatani, J. Levesque, D. Zeidler, H. Niikura, H. Pépin, J.-C. Kieffer, P. B. Corkum, and D. M. Villeneuve, *Nature* **432**, 867 (2004).
- [62] W.-H. Soe, C. Manzano, A. De Sarkar, N. Chandrasekhar, and C. Joachim, *Phys. Rev. Lett.* **102**, 176102 (2009).
- [63] P. Puschnig, *Organic molecule database*, online (accessed 18-February-2020).
- [64] E. R. Scerri, *J. Chem. Educ.* **77**, 1492 (2000).
- [65] P. Mulder, *HYLE* **17**, 24 (2011).
- [66] B. Q. Pham and M. S. Gordon, *J. Phys. Chem. A* **121**, 4851 (2017).
- [67] M. Dauth, T. Körzdörfer, S. Kümmel, J. Ziroff, M. Wiessner, A. Schöll, F. Reinert, M. Arita, and K. Shimada, *Phys. Rev. Lett.* **107**, 193002 (2011).
- [68] J.-L. Bredas, *Mater. Horiz.* **1**, 17 (2014).
- [69] N. Koch, N. Ueno, and A. T. S. Wee, eds., *The molecule–metal interface* (WileyVCH, 2013).
- [70] P. S. Bagus, V. Staemmler, and C. Wöll, *Phys. Rev. Lett.* **89**, 096104 (2002).

- [71] G. Witte, S. Lukas, P. S. Bagus, and C. Wöll, *Appl. Phys. Lett.* **87**, 263502 (2005).
- [72] H. Vázquez, Y. J. Dappe, J. Ortega, and F. Flores, *J. Chem. Phys.* **126**, 144703 (2007).
- [73] Y. Zou, L. Kilian, A. Schöll, T. Schmidt, R. Fink, and E. Umbach, *Surf. Sci.* **600**, 1240 (2006).
- [74] N. Ueno and S. Kera, *Prog. Surf. Sci.* **83**, 490 (2008).
- [75] S. Hüfner, *Photoelectron spectroscopy* (Springer, 2003).
- [76] A. Damascelli, *Phys. Scr.* **T109**, 61 (2004).
- [77] R. Schlaf, *Calibration of photoemission spectra and work function determination*, Tutorial notes, University of South Florida.
- [78] M. P. Seah and W. A. Dench, *Surf. Interface Anal.* **1**, 2 (1979).
- [79] F. Reinert and S. Hüfner, *New J. Phys.* **7**, 97 (2005).
- [80] F. Bocquet, G. Mercurio, M. Franke, G. van Straaten, S. Weiß, S. Soubatch, C. Kumpf, and F. Tautz, *Comput. Phys. Commun.* **235**, 502 (2019).
- [81] R. Wallauer, M. Raths, K. Stallberg, L. Münster, D. Brandstetter, X. Yang, J. Güdde, P. Puschnig, S. Soubatch, C. Kumpf, F. C. Bocquet, F. S. Tautz, and U. Höfer, *Science* **371**, 1056 (2021).
- [82] P. Kliuiev, “Reconstruction of molecular orbitals from photoemission data with iterative phase retrieval algorithms”, PhD thesis (University of Zurich, 2018).
- [83] H. Becker, E. Dietz, U. Gerhardt, and H. Angermüller, *Phys. Rev. B* **12**, 2084 (1975).
- [84] B. Holland, *Surf. Sci.* **68**, 490 (1977).
- [85] E. W. Plummer and W. Eberhardt, “Angle-resolved photoemission as a tool for the study of surfaces”, in *Advances in chemical physics*, Vol. 49 (John Wiley & Sons, Inc., 1982), pp. 533–656.
- [86] N. V. Richardson, *Chem. Phys. Lett.* **102**, 390 (1983).
- [87] W. D. Grobman, *Phys. Rev. B* **17**, 4573 (1978).
- [88] N. J. Shevchik, *J. Phys. C: Solid State Phys.* **11**, 3521 (1978).
- [89] S. Hasegawa, S. Tanaka, Y. Yamashita, H. Inokuchi, H. Fujimoto, K. Kamiya, K. Seki, and N. Ueno, *Phys. Rev. B* **48**, 2596 (1993).
- [90] S. Narioka, H. Ishii, K. Edamatsu, K. Kamiya, S. Hasegawa, T. Ohta, N. Ueno, and K. Seki, *Phys. Rev. B* **52**, 2362 (1995).
- [91] S. Hasegawa, H. Inokuchi, K. Seki, and N. Ueno, *J. Electron Spectrosc. Relat. Phenom.* **78**, 391 (1996).
- [92] N. Ueno, *J. Electron Spectrosc. Relat. Phenom.* **78**, 345 (1996).

Bibliography

- [93] N. Ueno, A. Kitamura, K. K. Okudaira, T. Miyamae, Y. Harada, S. Hasegawa, H. Ishii, H. Inokuchi, T. Fujikawa, T. Miyazaki, and K. Seki, *J. Chem. Phys.* **107**, 2079 (1997).
- [94] S. Kera, S. Tanaka, H. Yamane, D. Yoshimura, K. Okudaira, K. Seki, and N. Ueno, *Chem. Phys.* **325**, 113 (2006).
- [95] Y. Liu, D. Ikeda, S. Nagamatsu, T. Nishi, N. Ueno, and S. Kera, *J. Electron Spectrosc. Relat. Phenom.* **195**, 287 (2014).
- [96] P. Puschnig, G. Koller, C. Draxl, and M. G. Ramsey, “The structure of molecular orbitals investigated by angle-resolved photoemission”, in *Small organic molecules on surfaces: fundamentals and applications* (Springer, 2013), pp. 3–23.
- [97] S. Goldberg, C. Fadley, and S. Kono, *Solid State Commun.* **28**, 459 (1978).
- [98] M. Scheffler, K. Kambe, and F. Forstmann, *Solid State Commun.* **25**, 93 (1978).
- [99] E. L. Shirley, L. J. Terminello, A. Santoni, and F. J. Himpsel, *Phys. Rev. B* **51**, 13614 (1995).
- [100] A. M. Bradshaw and D. P. Woodruff, *New J. Phys.* **17**, 013033 (2015).
- [101] S. Moser, *J. Electron Spectrosc. Relat. Phenom.* **214**, 29 (2017).
- [102] D. P. Woodruff, *Modern techniques of surface science*, 3rd ed. (Cambridge University Press, 2016).
- [103] P. Aebi, R. Fasel, D. Naumović, J. Hayoz, T. Pillo, M. Bovet, R. Agostino, L. Patthey, L. Schlapbach, F. Gil, H. Berger, T. Kreutz, and J. Osterwalder, *Surf. Sci.* **402–404**, 614 (1998).
- [104] J. Osterwalder, T. Greber, E. Wetli, J. Wider, and H. Neff, *Prog. Surf. Sci.* **64**, 65 (2000).
- [105] T. Ules, “Orbital tomographic investigations of organic molecular films and their interfaces”, PhD thesis (University of Graz, 2014).
- [106] H. Yamane, D. Yoshimura, E. Kawabe, R. Sumii, K. Kanai, Y. Ouchi, N. Ueno, and K. Seki, *Phys. Rev. B* **76**, 165436 (2007).
- [107] A. Ferretti, C. Baldacchini, A. Calzolari, R. Di Felice, A. Ruini, E. Molinari, and M. G. Betti, *Phys. Rev. Lett.* **99**, 046802 (2007).
- [108] K. Müller, A. P. Seitsonen, T. Brugger, J. Westover, T. Greber, T. Jung, and A. Kara, *J. Phys. Chem. C* **116**, 23465 (2012).
- [109] X. Yang, I. Krieger, D. Lüftner, S. Weiß, T. Heepenstrick, M. Hollerer, P. Hurdax, G. Koller, M. Sokolowski, P. Puschnig, M. G. Ramsey, F. S. Tautz, and S. Soubatch, *Chem. Commun.* **54**, 9039 (2018).
- [110] A. Kraft, R. Temirov, S. K. M. Henze, S. Soubatch, M. Rohlfling, and F. S. Tautz, *Phys. Rev. B* **74**, 041402 (2006).

- [111] T. Körzdörfer, S. Kümmel, N. Marom, and L. Kronik, *Phys. Rev. B* **79**, 201205 (2009).
- [112] S. Refaely-Abramson, S. Sharifzadeh, N. Govind, J. Autschbach, J. B. Neaton, R. Baer, and L. Kronik, *Phys. Rev. Lett.* **109**, 226405 (2012).
- [113] P. Puschnig, private communications.
- [114] R. W. Gerchberg and W. O. Saxton, *Optik* **35**, 237 (1972).
- [115] G. Koller, P. Puschnig, A. Gottwald, and F. S. Tautz, *Phys. Unserer Zeit* **47**, 192 (2016).
- [116] A. Gottwald, H. Kaser, and M. Kolbe, *J. Synchrotron Rad.* **26**, 535 (2019).
- [117] L. Egger, B. Kollmann, P. Hurdax, D. Lüftner, X. Yang, S. Weiss, A. Gottwald, M. Richter, G. Koller, S. Soubatch, F. S. Tautz, P. Puschnig, and M. G. Ramsey, *New J. Phys.* **21**, 043003 (2019).
- [118] C. Metzger, M. Graus, M. Grimm, G. Zamborlini, V. Feyer, M. Schwendt, D. Lüftner, P. Puschnig, A. Schöll, and F. Reinert, *Phys. Rev. B* **101**, 165421 (2020).
- [119] N. Haag, D. Lüftner, F. Haag, J. Seidel, L. L. Kelly, G. Zamborlini, M. Jugovac, V. Feyer, M. Aeschlimann, P. Puschnig, M. Cinchetti, and B. Stadtmüller, *Phys. Rev. B* **101**, 165422 (2020).
- [120] M. Graus, M. Grimm, C. Metzger, M. Dauth, C. Tusche, J. Kirschner, S. Kümmel, A. Schöll, and F. Reinert, *Phys. Rev. Lett.* **116**, 147601 (2016).
- [121] A. Haags, A. Reichmann, Q. Fan, L. Egger, H. Kirschner, T. Naumann, S. Werner, T. Vollgraff, J. Sundermeyer, L. Eschmann, X. Yang, D. Brandstetter, F. C. Bocquet, G. Koller, A. Gottwald, M. Richter, M. G. Ramsey, M. Rohlfing, P. Puschnig, J. M. Gottfried, S. Soubatch, and F. S. Tautz, *ACS Nano* **14**, 15766 (2020).
- [122] *SCIENTA R4000 user manual v5.5*, VG Scienta AB (2006).
- [123] L. Broekman, A. Tadich, E. Huwald, J. Riley, R. Leckey, T. Seyller, K. Emtsev, and L. Ley, *J. Electron Spectrosc. Relat. Phenom.* **144–147**, 1001 (2005).
- [124] H. Ibach, *Physics of surfaces and interfaces* (Springer, 2006).
- [125] K. Oura, V. G. Lifshits, A. A. Saranin, A. V. Zotov, and M. Katayama, *Surface science: an introduction* (Springer Science & Business Media, 2003).
- [126] *NanoESCA II: the ultimate PEEM instrument*, Scienta Omicron (2018).
- [127] M. Escher, N. Weber, M. Merkel, C. Ziethen, P. Bernhard, G. Schönhense, S. Schmidt, F. Forster, F. Reinert, B. Krömker, and D. Funnemann, *J. Phys.: Condens. Matter* **17**, S1329 (2005).
- [128] M. Escher, K. Winkler, O. Renault, and N. Barrett, *J. Electron Spectrosc. Relat. Phenom.* **178–179**, 303 (2010).
- [129] M. C. Patt, “Bulk and surface sensitive energy-filtered photoemission microscopy using synchrotron radiation for the study of resistive switching memories”, PhD thesis (University of Duisburg-Essen, 2016).

Bibliography

- [130] G. Zamborlini, “Organic-metal hybrid interfaces at the mesoscopic scale”, PhD thesis (University of Duisburg-Essen, 2018).
- [131] C. Wiemann, M. Patt, I. P. Krug, N. B. Weber, M. Escher, M. Merkel, and C. M. Schneider, *e-J. Surf. Sci. Nanotechnol.* **9**, 395 (2011).
- [132] B. Krömker, M. Escher, D. Funnemann, D. Hartung, H. Engelhard, and J. Kirschner, *Rev. Sci. Instrum.* **79**, 053702 (2008).
- [133] R. Leckey and J. Riley, *Appl. Surf. Sci.* **22–23**, 196 (1985).
- [134] D. P. Woodruff, *Rep. Prog. Phys.* **68**, 743 (2005).
- [135] J. Zegenhagen and A. Kazimirov, *The x-ray standing wave technique* (World Scientific, 2013).
- [136] D. Woodruff, *Prog. Surf. Sci.* **57**, 1 (1998).
- [137] C. J. Fisher, R. Ithin, R. G. Jones, G. J. Jackson, D. P. Woodruff, and B. C. C. Cowie, *J. Phys.: Condens. Matter* **10**, L623 (1998).
- [138] G. van Straaten, M. Franke, F. C. Bocquet, F. S. Tautz, and C. Kumpf, *J. Electron Spectrosc. Relat. Phenom.* **222**, 106 (2018).
- [139] G. J. Jackson, B. C. C. Cowie, D. P. Woodruff, R. G. Jones, M. S. Kariapper, C. Fisher, A. S. Y. Chan, and M. Butterfield, *Phys. Rev. Lett.* **84**, 2346 (2000).
- [140] J. Lee, C. Fisher, D. Woodruff, M. Roper, R. Jones, and B. Cowie, *Surf. Sci.* **494**, 166 (2001).
- [141] G. Mercurio, “Study of molecule-metal interfaces by means of the normal incidence x-ray standing wave technique”, PhD thesis (RWTH Aachen University, 2012).
- [142] O. Bauer, G. Mercurio, M. Willenbockel, W. Reckien, C. H. Schmitz, B. Fiedler, S. Soubatch, T. Bredow, F. S. Tautz, and M. Sokolowski, *Phys. Rev. B* **86**, 235431 (2012).
- [143] S. Weiß, I. Krieger, T. Heepenstrick, S. Soubatch, M. Sokolowski, and F. S. Tautz, *Phys. Rev. B* **96**, 075414 (2017).
- [144] X. Gonze, B. Amadon, P.-M. Anglade, J.-M. Beuken, F. Bottin, P. Boulanger, F. Bruneval, D. Caliste, R. Caracas, M. Côté, T. Deutsch, L. Genovese, P. Ghosez, M. Giantomassi, S. Goedecker, D. Hamann, P. Hermet, F. Jollet, G. Jomard, S. Leroux, M. Mancini, S. Mazevet, M. Oliveira, G. Onida, Y. Pouillon, T. Rangel, G.-M. Rignanese, D. Sangalli, R. Shaltaf, M. Torrent, M. Verstraete, G. Zerah, and J. Zwanziger, *Comput. Phys. Commun.* **180**, 2582 (2009).
- [145] M. Valiev, E. Bylaska, N. Govind, K. Kowalski, T. Straatsma, H. V. Dam, D. Wang, J. Nieplocha, E. Apra, T. Windus, and W. de Jong, *Comput. Phys. Commun.* **181**, 1477 (2010).
- [146] J. P. Perdew, K. Burke, and M. Ernzerhof, *Phys. Rev. Lett.* **77**, 3865 (1996).
- [147] G. Kresse and J. Hafner, *Phys. Rev. B* **47**, 558 (1993).

- [148] G. Kresse and D. Joubert, *Phys. Rev. B* **59**, 1758 (1999).
- [149] C. Freysoldt, P. Eggert, P. Rinke, A. Schindlmayr, and M. Scheffler, *Phys. Rev. B* **77**, 235428 (2008).
- [150] J. Neugebauer and M. Scheffler, *Phys. Rev. B* **46**, 16067 (1992).
- [151] H. J. Monkhorst and J. D. Pack, *Phys. Rev. B* **13**, 5188 (1976).
- [152] M. Methfessel and A. T. Paxton, *Phys. Rev. B* **40**, 3616 (1989).
- [153] P. E. Blöchl, *Phys. Rev. B* **50**, 17953 (1994).
- [154] A. Tkatchenko and M. Scheffler, *Phys. Rev. Lett.* **102**, 073005 (2009).
- [155] V. G. Ruiz, W. Liu, E. Zojer, M. Scheffler, and A. Tkatchenko, *Phys. Rev. Lett.* **108**, 146103 (2012).
- [156] X. Yang, L. Egger, P. Hurdax, H. Kaser, D. Lüftner, F. C. Bocquet, G. Koller, A. Gottwald, P. Tegeder, M. Richter, M. G. Ramsey, P. Puschnig, S. Soubatch, and F. S. Tautz, *Nat. Commun.* **10**, 3189 (2019).
- [157] A. D. McNaught and A. Wilkinson, eds., *IUPAC compendium of chemical terminology* (Blackwell Scientific Publications, 1997).
- [158] D. G. de Oteyza, P. Gorman, Y.-C. Chen, S. Wickenburg, A. Riss, D. J. Mowbray, G. Etkin, Z. Pedramrazi, H.-Z. Tsai, A. Rubio, M. F. Crommie, and F. R. Fischer, *Science* **340**, 1434 (2013).
- [159] A. B. Zrimsek, N. Chiang, M. Mattei, S. Zaleski, M. O. McAnally, C. T. Chapman, A.-I. Henry, G. C. Schatz, and R. P. Van Duyne, *Chem. Rev.* **117**, 7583 (2017).
- [160] S. Nemšák, A. Shavorskiy, O. Karslioglu, I. Zegkinoglou, A. Rattanachata, C. S. Conlon, A. Keqi, P. K. Greene, E. C. Burks, F. Salmassi, E. M. Gullikson, S.-H. Yang, K. Liu, H. Bluhm, and C. S. Fadley, *Nat. Commun.* **5**, 5441 (2014).
- [161] J. Cai, P. Ruffieux, R. Jaafar, M. Bieri, T. Braun, S. Blankenburg, M. Muoth, A. P. Seitsonen, M. Saleh, X. Feng, K. Müllen, and R. Fasel, *Nature* **466**, 470 (2010).
- [162] Y.-C. Chen, D. G. de Oteyza, Z. Pedramrazi, C. Chen, F. R. Fischer, and M. F. Crommie, *ACS Nano* **7**, 6123 (2013).
- [163] S. Weiß, D. Gerbert, A. Stein, A. K. Schenk, X. Yang, C. Brülke, R. Kremring, S. Feldmann, F. C. Bocquet, M. Gille, S. Hecht, M. Sokolowski, P. Tegeder, S. Soubatch, and F. S. Tautz, *Phys. Rev. B* **98**, 075410 (2018).
- [164] C. Sánchez-Sánchez, T. Dienel, O. Deniz, P. Ruffieux, R. Berger, X. Feng, K. Müllen, and R. Fasel, *ACS Nano* **10**, 8006 (2016).
- [165] S. Linden, D. Zhong, A. Timmer, N. Aghdassi, J. H. Franke, H. Zhang, X. Feng, K. Müllen, H. Fuchs, L. Chi, and H. Zacharias, *Phys. Rev. Lett.* **108**, 216801 (2012).
- [166] K. A. Simonov, N. A. Vinogradov, A. S. Vinogradov, A. V. Generalov, E. M. Zagrebina, G. I. Svirskiy, A. A. Cafolla, T. Carpy, J. P. Cunniffe, T. Taketsugu, A. Lyalin, N. Mårtensson, and A. B. Preobrajenski, *ACS Nano* **9**, 8997 (2015).

Bibliography

- [167] D. Lüftner, “Orbital tomography: understanding photoemission of organic molecular films”, PhD thesis (University of Graz, 2015).
- [168] J. Tersoff and D. R. Hamann, *Phys. Rev. Lett.* **50**, 1998 (1983).
- [169] C. Brülke, T. Heepenstrick, I. Krieger, B. Wolff, X. Yang, A. Shamsaddinlou, S. Weiß, F. C. Bocquet, F. S. Tautz, S. Soubatch, and M. Sokolowski, *Phys. Rev. B* **99**, 121404 (2019).
- [170] V. J. Langlais, R. R. Schlittler, H. Tang, A. Gourdon, C. Joachim, and J. K. Gimzewski, *Phys. Rev. Lett.* **83**, 2809 (1999).
- [171] C. Bock, D. V. Pham, U. Kunze, D. Käfer, G. Witte, and C. Wöll, *J. Appl. Phys.* **100**, 114517 (2006).
- [172] A. Rastgoo-Lahrood, J. Björk, M. Lischka, J. Eichhorn, S. Kloft, M. Fritton, T. Strunskus, D. Samanta, M. Schmittel, W. M. Heckl, and M. Lackinger, *Angew. Chem. Int. Ed.* **55**, 7650 (2016).
- [173] A. Baby, M. Gruenewald, C. Zwick, F. Otto, R. Forker, G. van Straaten, M. Franke, B. Stadtmüller, C. Kumpf, G. P. Brivio, G. Fratesi, T. Fritz, and E. Zojer, *ACS Nano* **11**, 10495 (2017).
- [174] J. Repp, G. Meyer, S. Paavilainen, F. E. Olsson, and M. Persson, *Science* **312**, 1196 (2006).
- [175] J. Repp, G. Meyer, F. E. Olsson, and M. Persson, *Science* **305**, 493 (2004).
- [176] I. Swart, T. Sonnleitner, and J. Repp, *Nano Lett.* **11**, 1580 (2011).
- [177] G. Kresse, M. Schmid, E. Napetschnig, M. Shishkin, L. Köhler, and P. Varga, *Science* **308**, 1440 (2005).
- [178] T. W. White, “The development of model organic decoupling films for use on strongly-interacting metal surfaces”, PhD thesis (University of Warwick, 2014).
- [179] G. Pacchioni, L. Giordano, and M. Baistrocchi, *Phys. Rev. Lett.* **94**, 226104 (2005).
- [180] M. Sterrer, T. Risse, U. Martinez Pozzoni, L. Giordano, M. Heyde, H.-P. Rust, G. Pacchioni, and H.-J. Freund, *Phys. Rev. Lett.* **98**, 096107 (2007).
- [181] M. Hollerer, “Charge transfer through thin dielectric films: organic molecules on MgO(001)/Ag(001)”, PhD thesis (University of Graz, 2019).
- [182] J. Pal, M. Smerieri, E. Celasco, L. Savio, L. Vattuone, and M. Rocca, *Phys. Rev. Lett.* **112**, 126102 (2014).
- [183] S. Schintke and W.-D. Schneider, *J. Phys.: Condens. Matter* **16**, R49 (2004).
- [184] E. Zojer, T. C. Taucher, and O. T. Hofmann, *Adv. Mater. Interfaces* **6**, 1900581 (2019).
- [185] F. Besenbacher and J. K. Nørskov, *Prog. Surf. Sci.* **44**, 5 (1993).
- [186] M. Oehzelt, L. Grill, S. Berkebile, G. Koller, F. P. Netzer, and M. G. Ramsey, *ChemPhysChem* **8**, 1707 (2007).

- [187] N. Tsukahara, K. Noto, M. Ohara, S. Shiraki, N. Takagi, Y. Takata, J. Miyawaki, M. Taguchi, A. Chainani, S. Shin, and M. Kawai, *Phys. Rev. Lett.* **102**, 167203 (2009).
- [188] L. Sun, G. Weidlinger, M. Denk, R. Denk, M. Hohage, and P. Zeppenfeld, *Phys. Chem. Chem. Phys.* **12**, 14706 (2010).
- [189] J. Gall, P. Zeppenfeld, L. Sun, L. Zhang, Y. Luo, Z. Dong, C. Hu, and P. Puschnig, *Phys. Rev. B* **94**, 195441 (2016).
- [190] A. Picone, D. Giannotti, A. Brambilla, G. Bussetti, A. Calloni, R. Yivlialin, M. Finazzi, L. Duò, F. Ciccacci, A. Goldoni, A. Verdini, and L. Floreano, *Appl. Surf. Sci.* **435**, 841 (2018).
- [191] M. Tiba, O. Kurnosikov, C. Flipse, B. Koopmans, H. Swagten, J. Kohlhepp, and W. de Jonge, *Surf. Sci.* **498**, 161 (2002).
- [192] A. Carrera, L. J. Cristina, S. Bengiό, A. Cossaro, A. Verdini, L. Floreano, J. D. Fuhr, J. E. Gayone, and H. Ascolani, *J. Phys. Chem. C* **117**, 17058 (2013).
- [193] V. C. Zoldan, R. Faccio, C. Gao, and A. A. Pasa, *J. Phys. Chem. C* **117**, 15984 (2013).
- [194] B. Warner, F. El Hallak, H. Prüser, J. Sharp, M. Persson, A. J. Fisher, and C. F. Hirjibehedin, *Nat. Nanotechnol.* **10**, 259 (2015).
- [195] H. Zeng, R. McFarlane, and K. Mitchell, *Surf. Sci.* **208**, L7 (1989).
- [196] M. Wuttig, R. Franchy, and H. Ibach, *Surf. Sci.* **213**, 103 (1989).
- [197] M. Kittel, M. Polcik, R. Terborg, J.-T. Hoeft, P. Baumgärtel, A. Bradshaw, R. Toomes, J.-H. Kang, D. Woodruff, M. Pascal, C. Lamont, and E. Rotenberg, *Surf. Sci.* **470**, 311 (2001).
- [198] W. Liu, K. Wong, H. Zeng, and K. Mitchell, *Prog. Surf. Sci.* **50**, 247 (1995).
- [199] T. Fujita, Y. Okawa, Y. Matsumoto, and K. Tanaka, *Phys. Rev. B* **54**, 2167 (1996).
- [200] H. Iddir, D. D. Fong, P. Zapol, P. H. Fuoss, L. A. Curtiss, G.-W. Zhou, and J. A. Eastman, *Phys. Rev. B* **76**, 241404 (2007).
- [201] X. Duan, O. Warschkow, A. Soon, B. Delley, and C. Stampfl, *Phys. Rev. B* **81**, 075430 (2010).
- [202] S. Gärtner, B. Fiedler, O. Bauer, A. Marele, and M. M. Sokolowski, *Beilstein J. Org. Chem.* **10**, 2055 (2014).
- [203] A. Schöll, Y. Zou, M. Jung, T. Schmidt, R. Fink, and E. Umbach, *J. Chem. Phys.* **121**, 10260 (2004).
- [204] G. Mercurio, O. Bauer, M. Willenbockel, N. Fairley, W. Reckien, C. H. Schmitz, B. Fiedler, S. Soubatch, T. Bredow, M. Sokolowski, and F. S. Tautz, *Phys. Rev. B* **87**, 045421 (2013).
- [205] *CasaXPS manual 2.3.15*, Casa Software Ltd (2009).

Bibliography

- [206] A. Gerlach, S. Sellner, F. Schreiber, N. Koch, and J. Zegenhagen, *Phys. Rev. B* **75**, 045401 (2007).
- [207] S. K. Henze, O. Bauer, T. L. Lee, M. Sokolowski, and F. S. Tautz, *Surf. Sci.* **601**, 1566 (2007).
- [208] A. Hauschild, R. Temirov, S. Soubatch, O. Bauer, A. Schöll, B. C. C. Cowie, T.-L. Lee, F. S. Tautz, and M. Sokolowski, *Phys. Rev. B* **81**, 125432 (2010).
- [209] F. Habraken, C. Mesters, and G. Bootsma, *Surf. Sci. Lett.* **97**, A247 (1980).
- [210] A. Spitzer and H. Lüth, *Surf. Sci.* **118**, 121 (1982).
- [211] P. O. Gartland, S. Berge, and B. J. Slagsvold, *Phys. Rev. Lett.* **28**, 738 (1972).
- [212] S. Duhm, A. Gerlach, I. Salzmann, B. Bröker, R. Johnson, F. Schreiber, and N. Koch, *Org. Electron.* **9**, 111 (2008).
- [213] C. Brülke, T. Heepenstrick, N. Humberg, I. Krieger, M. Sokolowski, S. Weiß, F. S. Tautz, and S. Soubatch, *J. Phys. Chem. C* **121**, 23964 (2017).
- [214] F. Schulz, R. Drost, S. K. Hämäläinen, and P. Liljeroth, *ACS Nano* **7**, 11121 (2013).
- [215] P. Erler, P. Schmitt, N. Barth, A. Irmler, S. Bouvron, T. Huhn, U. Groth, F. Pauly, L. Gagnaniello, and M. Fonin, *Nano Lett.* **15**, 4546 (2015).
- [216] S. Koslowski, D. Rosenblatt, A. Kabakchiev, K. Kuhnke, K. Kern, and U. Schlickum, *Beilstein J. Nanotechnol.* **8**, 1388 (2017).
- [217] J. I. Urgel, M. Schwarz, M. Garnica, D. Stassen, D. Bonifazi, D. Ecija, J. V. Barth, and W. Auwärter, *J. Am. Chem. Soc.* **137**, 2420 (2015).
- [218] M. Schwarz, D. A. Duncan, M. Garnica, J. Ducke, P. S. Deimel, P. K. Thakur, T.-L. Lee, F. Allegretti, and W. Auwärter, *Nanoscale* **10**, 21971 (2018).
- [219] M. Corva, F. Mohamed, E. Tomsic, M. Rinaldi, C. Cepek, N. Seriani, M. Peressi, and E. Vesselli, *J. Phys. Chem. C* **123**, 3916 (2019).
- [220] Q. H. Wang and M. C. Hersam, *Nat. Chem.* **1**, 206 (2009).
- [221] J. Cho, J. Smerdon, L. Gao, Ö. Süzer, J. R. Guest, and N. P. Guisinger, *Nano Lett.* **12**, 3018 (2012).
- [222] R. Forker, D. Kasemann, T. Dienel, C. Wagner, R. Franke, K. Müllen, and T. Fritz, *Adv. Mater.* **20**, 4450 (2008).
- [223] G. S. Painter and D. E. Ellis, *Phys. Rev. B* **1**, 4747 (1970).
- [224] N. Dori, M. Menon, L. Kilian, M. Sokolowski, L. Kronik, and E. Umbach, *Phys. Rev. B* **73**, 195208 (2006).
- [225] P. Hurdax, M. Hollerer, P. Puschnig, D. Lüftner, L. Egger, M. G. Ramsey, and M. Sterrer, *Adv. Mater. Interfaces* **7**, 2000592 (2020).
- [226] X. Yang, L. Egger, J. Fuchsberger, M. Unzog, D. Lüftner, F. Hajek, P. Hurdax, M. Jugovac, G. Zamborlini, V. Feyer, G. Koller, P. Puschnig, F. S. Tautz, M. G. Ramsey, and S. Soubatch, *J. Phys. Chem. Lett.* **10**, 6438 (2019).

- [227] J. Hermann, R. A. DiStasio, and A. Tkatchenko, *Chem. Rev.* **117**, 4714 (2017).
- [228] J. B. Neaton, M. S. Hybertsen, and S. G. Louie, *Phys. Rev. Lett.* **97**, 216405 (2006).
- [229] S. Soubatch, C. Weiss, R. Temirov, and F. S. Tautz, *Phys. Rev. Lett.* **102**, 177405 (2009).
- [230] R. Temirov, S. Soubatch, A. Luican, and F. S. Tautz, *Nature* **444**, 350 (2006).
- [231] C. H. Schwalb, S. Sachs, M. Marks, A. Schöll, F. Reinert, E. Umbach, and U. Höfer, *Phys. Rev. Lett.* **101**, 146801 (2008).
- [232] N. Gonzalez-Lakunza, I. Fernández-Torrente, K. J. Franke, N. Lorente, A. Arnau, and J. I. Pascual, *Phys. Rev. Lett.* **100**, 156805 (2008).
- [233] H. Yamane, K. Kanai, Y. Ouchi, N. Ueno, and K. Seki, *J. Electron Spectrosc. Relat. Phenom.* **174**, 28 (2009).
- [234] M. Marks, N. L. Zaitsev, B. Schmidt, C. H. Schwalb, A. Schöll, I. A. Nechaev, P. M. Echenique, E. V. Chulkov, and U. Höfer, *Phys. Rev. B* **84**, 081301 (2011).
- [235] M. C. E. Galbraith, M. Marks, R. Tonner, and U. Höfer, *J. Phys. Chem. Lett.* **5**, 50 (2014).
- [236] W. Erley and H. Ibach, *Surf. Sci.* **178**, 565 (1986).
- [237] I. G. Hill, A. Rajagopal, A. Kahn, and Y. Hu, *Appl. Phys. Lett.* **73**, 662 (1998).
- [238] H. Ishii, K. Sugiyama, E. Ito, and K. Seki, *Adv. Mater.* **11**, 605 (1999).
- [239] S. Braun and W. R. Salaneck, *Chem. Phys. Lett.* **438**, 259 (2007).
- [240] S. Braun, W. R. Salaneck, and M. Fahlman, *Adv. Mater.* **21**, 1450 (2009).
- [241] G. Heimel, S. Duhm, I. Salzmann, A. Gerlach, A. Strozecka, J. Niederhausen, C. Bürker, T. Hosokai, I. Fernandez-Torrente, G. Schulze, S. Winkler, A. Wilke, R. Schlesinger, J. Frisch, B. Bröker, A. Vollmer, B. Detlefs, J. Pflaum, S. Kera, K. J. Franke, N. Ueno, J. I. Pascual, F. Schreiber, and N. Koch, *Nat. Chem.* **5**, 187 (2013).
- [242] G. Zamborlini, M. Jugovac, A. Cossaro, A. Verdini, L. Floreano, D. Lüftner, P. Puschnig, V. Feyer, and C. M. Schneider, *Chem. Commun.* **54**, 13423 (2018).
- [243] O. T. Hofmann, P. Rinke, M. Scheffler, and G. Heimel, *ACS Nano* **9**, 5391 (2015).
- [244] S. Erker and O. T. Hofmann, *J. Phys. Chem. Lett.* **10**, 848 (2019).
- [245] Q. Chen, A. J. McDowall, and N. V. Richardson, *Langmuir* **19**, 10164 (2003).
- [246] B. Lu, H. J. Zhang, H. Huang, H. Y. Mao, Q. Chen, H. Y. Li, P. He, and S. N. Bao, *Appl. Surf. Sci.* **245**, 208 (2005).
- [247] W. Dou, N. Li, D. Guan, F. Song, H. Huang, H. Zhang, H. Li, P. He, S. Bao, Q. Chen, and W. Zhou, *J. Chem. Phys.* **127**, 224709 (2007).
- [248] H. Huang, F. Song, B. Lu, H. Zhang, W. Dou, H. Li, P. He, S. Bao, Q. Chen, and W. Zhou, *J. Phys.: Condens. Matter* **20**, 315010 (2008).

Bibliography

- [249] Y. Tao, H. Mao, H. Zhang, and P. He, *Surf. Sci.* **641**, 135 (2015).
- [250] K. Takasugi and T. Yokoyama, *J. Chem. Phys.* **144**, 104702 (2016).
- [251] P. Yannoulis, K.-H. Frank, and E. E. Koch, *Surf. Sci.* **243**, 58 (1991).
- [252] S. Soubatch, I. Kröger, C. Kumpf, and F. S. Tautz, *Phys. Rev. B* **84**, 195440 (2011).
- [253] S. Lukas, G. Witte, and C. Wöll, *Phys. Rev. Lett.* **88**, 028301 (2002).
- [254] Z. Liang, Q. Tian, H. Zhang, J. Hu, P. He, H. Li, S. Bao, P. Wang, H. Huang, and F. Song, *Crystals* **10**, 13 (2020).
- [255] C. Baldacchini, C. Mariani, M. G. Betti, I. Vobornik, J. Fujii, E. Annese, G. Rossi, A. Ferretti, A. Calzolari, R. Di Felice, A. Ruini, and E. Molinari, *Phys. Rev. B* **76**, 245430 (2007).
- [256] A. Bendounan, F. Forster, A. Schöll, D. Batchelor, J. Ziroff, E. Umbach, and F. Reinert, *Surf. Sci.* **601**, 4013 (2007).
- [257] A. Scheybal, K. Müller, R. Bertschinger, M. Wahl, A. Bendounan, P. Aebi, and T. A. Jung, *Phys. Rev. B* **79**, 115406 (2009).
- [258] J. Jiang, S. S. Tsirkin, K. Shimada, H. Iwasawa, M. Arita, H. Anzai, H. Namatame, M. Taniguchi, I. Y. Sklyadneva, R. Heid, K.-P. Bohnen, P. M. Echenique, and E. V. Chulkov, *Phys. Rev. B* **89**, 085404 (2014).
- [259] A. Gerlach, G. Meister, R. Matzdorf, and A. Goldmann, *Surf. Sci.* **443**, 221 (1999).
- [260] M. Wagner, S. Berkebile, F. P. Netzer, and M. G. Ramsey, *ACS Nano* **9**, 12070 (2015).
- [261] J. Martínez-Blanco, M. Ruiz-Osés, V. Joco, D. I. Sayago, P. Segovia, and E. G. Michel, *J. Vac. Sci. Technol. B* **27**, 863 (2009).
- [262] K. Müller, A. Kara, T. K. Kim, R. Bertschinger, A. Scheybal, J. Osterwalder, and T. A. Jung, *Phys. Rev. B* **79**, 245421 (2009).
- [263] L. Zhang, C. Y. Liu, X. Fu, L. D. Sun, and P. Zeppenfeld, *Phys. Rev. B* **89**, 035428 (2014).
- [264] M. Sauvage-Simkin, A. Coati, Y. Garreau, A. Vlad, K. Müller, A. Bendounan, and A. Kara, *J. Phys. Chem. C* **118**, 27815 (2014).
- [265] N. Nicoara, E. Román, J. M. Gómez-Rodríguez, J. A. Martín-Gago, and J. Méndez, *Org. Electron.* **7**, 287 (2006).
- [266] J. Ziroff, P. Gold, A. Bendounan, F. Forster, and F. Reinert, *Surf. Sci.* **603**, 354 (2009).
- [267] H. Yamane and N. Kosugi, *J. Phys. Chem. C* **120**, 24307 (2016).
- [268] H. Yamane, A. Carlier, and N. Kosugi, *Mater. Chem. Front.* **2**, 609 (2018).
- [269] E. Annese, J. Fujii, I. Vobornik, and G. Rossi, *J. Phys. Chem. C* **115**, 17409 (2011).

- [270] A. Nuber, M. Higashiguchi, F. Forster, P. Blaha, K. Shimada, and F. Reinert, *Phys. Rev. B* **78**, 195412 (2008).
- [271] Y. L. Wang, W. Ji, D. X. Shi, S. X. Du, C. Seidel, Y. G. Ma, H.-J. Gao, L. F. Chi, and H. Fuchs, *Phys. Rev. B* **69**, 075408 (2004).

Eidesstattliche Erklärung

Xiaosheng Yang, M. Sc., erklärt hiermit, dass diese Dissertation und die darin dargelegten Inhalte die eigenen sind und selbstständig, als Ergebnis der eigenen originären Forschung, generiert wurden.

Hiermit erkläre ich an Eides statt

1. Diese Arbeit wurde vollständig oder größtenteils in der Phase als Doktorand dieser Fakultät und Universität angefertigt;
2. Sofern irgendein Bestandteil dieser Dissertation zuvor für einen akademischen Abschluss oder eine andere Qualifikation an dieser oder einer anderen Institution verwendet wurde, wurde dies klar angezeigt;
3. Wenn immer andere eigene- oder Veröffentlichungen Dritter herangezogen wurden, wurden diese klar benannt;
4. Wenn aus anderen eigenen- oder Veröffentlichungen Dritter zitiert wurde, wurde stets die Quelle hierfür angegeben. Diese Dissertation ist vollständig meine eigene Arbeit, mit der Ausnahme solcher Zitate;
5. Alle wesentlichen Quellen von Unterstützung wurden benannt;
6. Wenn immer ein Teil dieser Dissertation auf der Zusammenarbeit mit anderen basiert, wurde von mir klar gekennzeichnet, was von anderen und was von mir selbst erarbeitet wurde;
7. Ein Teil oder Teile dieser Arbeit wurden zuvor veröffentlicht und zwar in:
 - X. Yang, I. Krieger, D. Lüftner, S. Weiß, T. Heepenstrick, M. Hollerer, P. Hurdax, G. Koller, M. Sokolowski, P. Puschnig, M. G. Ramsey, F. S. Tautz, and S. Soubatch, *Chem. Commun.* **54**, 9039 (2018).
 - C. Brülke, T. Heepenstrick, I. Krieger, B. Wolff, X. Yang, A. Shamsaddinlou, S. Weiß, F. C. Bocquet, F. S. Tautz, S. Soubatch, and M. Sokolowski, *Phys. Rev. B* **99**, 121404 (2019).
 - X. Yang, L. Egger, P. Hurdax, H. Kaser, D. Lüftner, F. C. Bocquet, G. Koller, A. Gottwald, P. Tegeder, M. Richter, M. G. Ramsey, P. Puschnig, S. Soubatch and F. S. Tautz, *Nat. Commun.* **10**, 3189 (2019).
 - X. Yang, L. Egger, J. Fuchsberger, M. Unzog, D. Lüftner, F. Hajek, P. Hurdax, M. Jugovac, G. Zamborlini, V. Feyer, G. Koller, P. Puschnig, F. S. Tautz, M. G. Ramsey, and S. Soubatch, *J. Phys. Chem. Lett.* **10**, 6438 (2019).

7. September 2021

Xiaosheng Yang

Band / Volume 58

Element-Selective Investigation of Femtosecond Spin Dynamics in $\text{Ni}_x\text{Pd}_{1-x}$ Magnetic Alloys using Extreme Ultraviolet Radiation

S. Gang (2019), 93, xx pp

ISBN: 978-3-95806-411-9

Band / Volume 59

Defect engineering in oxide thin films

F. V. E. Hensling (2019), 10, 164 pp

ISBN: 978-3-95806-424-9

Band / Volume 60

Chemical control of the electrical surface properties of *n*-doped transition metal oxides

M. Andrä (2019), X, 150, XXXVIII pp

ISBN: 978-3-95806-448-5

Band / Volume 61

Digital Signal Processing and Mixed Signal Control of Receiver Circuitry for Large-Scale Particle Detectors

P. Muralidharan (2020), xv, 109 pp

ISBN: 978-3-95806-489-8

Band / Volume 62

Development of Electromagnetic Induction Measurement and Inversion Methods for Soil Electrical Conductivity Investigations

X. Tan (2020), ix, 124 pp

ISBN: 978-3-95806-490-4

Band / Volume 63

Novel System Approach for a mm-range Precision Indoor Positioning System

R. Xiong (2020), xi, 144 pp

ISBN: 978-3-95806-517-8

Band / Volume 64

Quantitative investigation of group III-nitride interfaces by a combination of scanning tunneling microscopy and off-axis electron holography

Y. Wang (2021), 102 pp

ISBN: 978-3-95806-534-5

Band / Volume 65

Scalable Control Electronics for a Spin Based Quantum Computer

L. Geck (2021), xiv, 114, xv-xxxiii

ISBN: 978-3-95806-540-6

Band / Volume 66

DNA-capped silver nanoparticles for stochastic nanoparticle impact electrochemistry

L. Nörbel (2021), VI, 142 pp

ISBN: 978-3-95806-541-3

Band / Volume 67

Development, characterization, and application of intraretinal implants

V. Rincón Montes (2021), XII, 173 pp

ISBN: 978-3-95806-553-6

Band / Volume 68

Optogenetic and electrical investigation of network dynamics in patterned neuronal cultures

T. J. J. Hondrich (2021), x, 177 pp

ISBN: 978-3-95806-555-0

Band / Volume 69

Disentangling parallel conduction channels by charge transport measurements on surfaces with a multi-tip scanning tunneling microscope

S. Just (2021), xii, 225 pp

ISBN: 978-3-95806-574-1

Band / Volume 70

Nanoscale four-point charge transport measurements in topological insulator thin films

A. Leis (2021), ix, 153 pp

ISBN: 978-3-95806-580-2

Band / Volume 71

Investigating the Interaction between π -Conjugated Organic Molecules and Metal Surfaces with Photoemission Tomography

X. Yang (2021), xviii, 173 pp

ISBN: 978-3-95806-584-0

Information

Band / Volume 71

ISBN 978-3-95806-584-0